Semiconductors, Vol. 36, No. 4, 2002, pp. 363–366. Translated from Fizika i Tekhnika Poluprovodnikov, Vol. 36, No. 4, 2002, pp. 385–388.

ATOMIC STRUCTURE AND NONELECTRONIC PROPERTIES OF SEMICONDUCTORS

Changes in the State of Phosphorus Atoms in the Silicon Lattice as a Result of Interaction with Radiation Defects

V. V. Bolotov*, G. N. Kamaev, and L. S. Smirnov****

** Institute of Sensor Microelectronics, Siberian Division, Russian Academy of Sciences,*
pr. Mira 55, Omsk, 644077 Russia

*** Institute of Semiconductor Physics, Siberian Division, Russian Academy of Sciences,*
pr. Akademika Lavrent'eva 13, Novosibirsk, 630090 Russia

e-mail: kamaev@isp.nsc.ru

Submitted September 18, 2001; accepted for publication September 20, 2001

Abstract—Interaction of radiation defects with phosphorus atoms in silicon crystals subjected to electron irradiation and thermal treatments was studied under conditions of various degrees of supersaturation with respect to the equilibrium concentration of impurities and point defects. It is shown that, in the course of silicon irradiation, the electron-dose dependences of the phosphorus concentration at the lattice sites (P_s) level off (tend toward a constant value). This constant value is governed by the irradiation temperature. The stages of recovery of the concentration P_s as a result of heat treatments correlate with temperature intervals of dissociation of the vacancy complexes. The results indicate that there are two processes. One process involves the interaction of dopant atoms with silicon self-interstitials and the emergence of interstitial complexes; i.e., this process corresponds to the radiation-stimulated decomposition of a supersaturated solution of an impurity as a result of point-defect generation and ionization. The other process consists in the recombination of interstitial impurities with vacancies at sufficiently high temperatures or in the annihilation of vacancies released during heat treatments with interstitial atoms incorporated into composite defect complexes with the involvement of phosphorus atoms. *© 2002 MAIK "Nauka/Interperiodica".*

1. INTRODUCTION

Silicon crystals are typically doped with impurities at high temperatures with subsequent, comparatively rapid cooling, which gives rise to a supersaturated solid solution. Understandably, the resulting concentrations of electrically active impurities exceed the equilibrium concentrations at low temperatures. The degree of supersaturation may exceed 10^4 in the temperature range of 20–100°C [1]. An increase in the impurity concentration leads to the fact that, in heavily doped semiconductors, a discrepancy between the concentration of the introduced impurity and the charge-carrier concentration is observed if the doping level exceeds a certain value [2]. This discrepancy may be caused by the redistribution of the impurity between the regular and interstitial lattice sites [3] and by the formation of associations of impurity atoms and advanced precipitates and precipitates of the second-phase particles [4–6]. The state of a supersaturated solid solution is thermodynamically unstable, and the system tends toward the equilibrium state via decomposition of the supersaturated solid solution. This is a multistage process; the decomposition may be restricted to the existence of intermediate phases for a fairly long time. In the semiconductor crystals (for the impurity concentration lower than the highest one defined by the liquidus curve), spontaneous decomposition is inhibited [1, 7]. Therefore, any subsequent treatment result in changes in the electrical and structural parameters of the doped crystal [8–10].

For a crystal to be transformed into a new equilibrium state, the mobile point defects should be present. It is especially interesting to study the relaxation processes in initially nonequilibrium crystals and structures under the conditions of point-defect generation and ionization at low temperatures. Irradiation not only leads to the formation of nonequilibrium radiation defects; it also promotes the approach of nonequilibrium crystal to the state of thermodynamic equilibrium [11, 12]. In particular, if the impurity concentration exceeds the solubility limit at a specified temperature, impurity atoms can be removed from the lattice sites as a result of irradiation, with subsequent formation of associated complexes [11]. This process may be regarded as the first stage of decomposition of the dopant supersaturated solution in silicon.

Previously [13, 14], we studied the changes in the concentration of phosphorus and boron atoms at the lattice sites as a result of electron irradiation in the temperature range T_{irr} = 20–700°C. An analysis of the results for the temperatures below and above the temperature corresponding to dissociation of the vacancy-related complexes, the results of experiments with irradiation of silicon containing various concentrations of

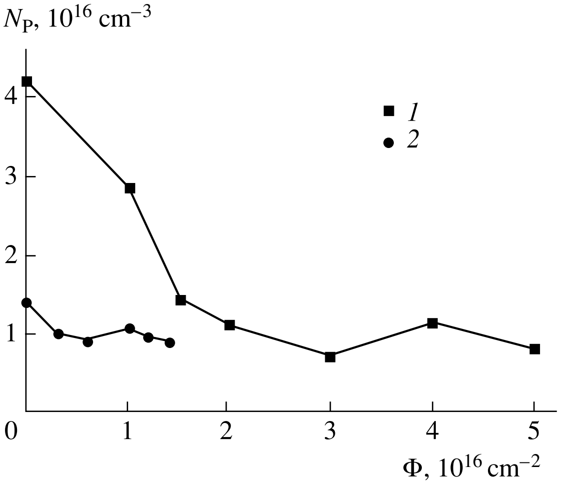

Fig. 1. The dose dependences of concentration of phosphorus atoms at the lattice sites for *n*-Si:P with ρ = (*1*) 0.15 and (*2*) 0.5 Ω cm. T_{irr} = 20°C.

carbon and oxygen, and the data on the recovery of the substitutional-impurity concentration as a result of heat treatments made it possible to conclude that phosphorus and boron atoms effectively interact with silicon self-interstitials within the entire temperature range under consideration.

In this paper, we report the results of studying the interaction of radiation effects with phosphorus atoms in silicon crystals under conditions of various degrees of supersaturation with respect to the equilibrium concentrations of impurities and point defects.

2. EXPERIMENTAL

In our experiments, we used samples of P-doped Si with resistivities ranging from $\rho \approx 0.15$ to ≈ 1 Ω cm and with various concentrations of oxygen and carbon. The samples were irradiated with electrons at an energy E = 3.5 MeV; a Microtron pulsed accelerator was used. The concentration of phosphorus atoms at the lattice sites after irradiation and after subsequent heat treatments was determined from the measurements of infrared (IR) absorption by 1*s*–2*p* electron transitions ($m = \pm 1$) in the hydrogen-like series at k = 318 cm^{-1} related to the shallow levels of substitutional phosphorus [15]. The temperature of the samples during measurements was 78 K. The concentration of phosphorus atoms at lattice sites (N_P) was calculated using the following formula:

$$N_P = \sigma S/f_e. \quad (1)$$

Here, f_e is the function that describes the occupancy of the phosphorus level with electrons at 78 K and is calculated on the basis of the Hall measurements; S (expressed in cm^{-2}) is the area under the absorption curve and is determined from the IR absorption spectra recalculated using the transmission spectra; and σ (expressed in cm^{-1}) is a calibration factor calculated using experimental data obtained from a number of measurements for original (unirradiated) samples.

Since the shallow levels of phosphorus atoms are completely ionized in the as-grown samples at room temperature, the free-carrier concentration n_k is equal to the concentration of phosphorus atoms at the lattice sites N_P; i.e.,

$$n_k = N_P. \quad (2)$$

In view of (1), we then obtain

$$\sigma = k_k f_e/S. \quad (3)$$

The calibration factor σ calculated using (3) was found to be equal to 3.7×10^{13} cm^{-1}.

Prior to optical measurements, the samples were subjected to conventional etching in a solution of CP-4A. Ohmic contacts for electrical measurements were formed by depositing Au in an electric discharge.

3. RESULTS AND DISCUSSION

In Fig. 1, we show the concentration of phosphorus atoms at the silicon lattice sites N_P as a function of the irradiation dose Φ. As can be seen, the concentration of phosphorus atoms at the lattice sites decreases as the irradiation dose increases; the dose dependences then level off (the concentrations tend to a constant asymptotic value). It is noteworthy that this asymptotic value is the same for *n*-Si:P with ρ = 0.5 Ω cm and for *n*-Si:P with ρ = 0.15 Ω cm with the concentrations of P atoms at the lattice sites equal to $\sim 1.6 \times 10^{16}$ and $\sim 4.0 \times 10^{16}$ cm^{-3}, respectively.

A similar effect was observed previously [14] as the result of electron irradiation of silicon ($N_P \approx 5 \times 10^{15}$ cm^{-3}) in the temperature range T_{irr} = 20–500°C, in which case the dose dependences also leveled off at $T_{irr} > 300$°C. Notably, the number of phosphorus atoms removed from the lattice sites decreased with increasing temperature. All of this indicates that the steady-state concentrations of the doping impurity in the lattice-site (P_s) and intersitial (P_i) states are attained under the given irradiation conditions. Indeed, since the number of impurity atoms remaining at interstices depends on the rate of two reactions, one of which is related to the occupation of interstices (I) by impurity atoms and the other consists in recombination of interstitial atoms with vacancies (V),

$$P_s + I \longrightarrow P_i,$$

$$P_i + V \longrightarrow P_s,$$

a variation in the ratio between the unoccupied interstices I and free vacancies V at the temperatures when the concentrations of the free I and V sites are still low should profoundly affect the resulting concentration of the impurity at interstices.

In Fig. 2, we show the data on the recovery of the concentration of the phosphorus atoms at the lattice sites and of the free-electron concentration as a result of isochronous heat treatments of floating-zone (FZ) silicon crystals irradiated with electrons with a dose $\Phi = 6 \times 10^{15}$ cm^{-2} at 20°C. We show the dependences $f(T_{\text{ann}})$, where $f = (n_0 - n_{\text{ann}})/(n_0 - n_{\text{irr}})$ is the unrecovered fraction of the concentration after heat treatment, n_0 is the concentration before irradiation, n_{irr} is the concentration after irradiation, and n_{ann} is the concentration after heat treatment. As can be seen from Fig. 2, two pronounced stages of recovery of phosphorus atoms at the lattice sites are observed: at the annealing temperatures of T_{ann} = 80–110 and 130–170°C. The stages of the P_s recovery correlate with those of the recovery of the free-carrier concentration measured at room temperature. At the first stage, nearly 20% of the free-carrier concentration and 40% of the phosphorus concentration at the lattice sites are recovered, which amounts to $\sim 7 \times 10^{14}$ and $\sim 1 \times 10^{15}$ cm^{-3}, respectively; by the end of the second stage, $\sim 1.7 \times 10^{15}$ cm^{-3} of the charge carriers and $\sim 1.2 \times 10^{15}$ cm^{-3} of the phosphorus atoms at the lattice sites are recovered.

As shown previously [13], in silicon crystals grown by the floating-zone method, the variation in the P_s concentration as a result of irradiation with high-energy electrons exceeds by more than two times the concentration of the forming *E* centers, which dominate over the other known vacancy-related complexes. It has been concluded that the recovery of the concentration of phosphorus at the lattice sites in silicon with low oxygen concentration is governed not only by the dissociation of *E* centers but also by the release of phosphorus atoms from other complexes. Once the second-stage temperature coincides with the temperature range within which the *E* centers are annealed out, more complex defects may then be annealed out in the first stage. According to the previous data [16], variations in the lifetime of the minority charge carriers as a result of irradiation of the FZ Si crystals are also annealed out in two stages. Shallow-level defects, in addition to the deep-level *E* centers, can manifest themselves in the recombination processes at high injection levels. Formation of the above defects correlates with the concentration of phosphorus atoms in the samples; possibly, it is these defects that are responsible for the first annealing stage.

In Fig. 3, we show the data on the recovery of the substitutional phosphorus concentration as a result of isochronous heat treatments of the Czochralski-grown silicon crystals after electron irradiation at temperatures of 20 and 180°C. After irradiation at T_{irr} = 20°C, we observe a poorly pronounced stage of recovery of substitutional phosphorus at T_{ann} = 180°C, a pronounced annealing stage at T_{ann} = 260°C, a reverse-annealing stage in the vicinity of T_{ann} = 320°C, and the final recovery of P_s at 340–380°C. The annealing stages at T_{ann} = 180, 260, and 320°C correlate with the stages of annealing of the vacancy defects in silicon: the *E* centers, divacancies, and the *A* centers, respectively. After irradiation at T_{irr} = 180°C, the formation of new defect complexes containing phosphorus atoms is observed as the heat-treatment temperature increases. The annealing temperature of T_{ann} = 300°C corresponds to the highest concentration of defects. An almost complete recovery of the substitutional phosphorus concentration occurs after heat treatment at temperatures higher than 320°C.

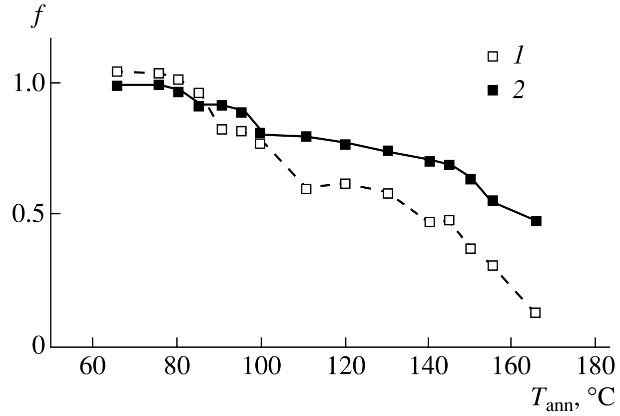

Fig. 2. Recovery of concentration of (*1*) phosphorous atoms at the lattice sites and (*2*) electrons as a result of isochronous (15 min) heat treatments after irradiation at T_{irr} = 20°C. The material under investigation was floating-zone *n*-Si:P with ρ = 1 Ω cm.

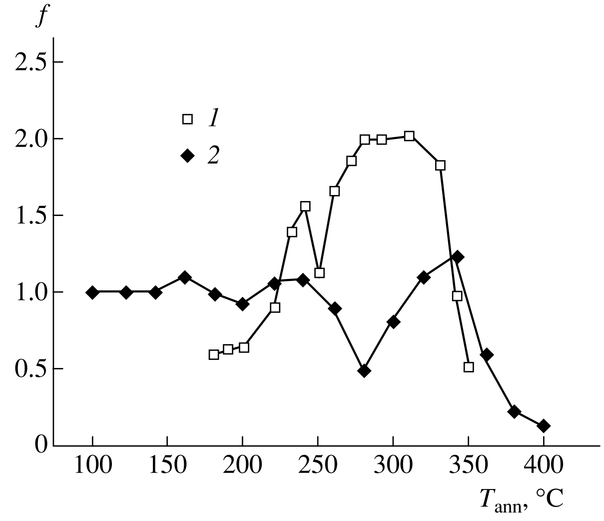

Fig. 3. Recovery of the concentrations of electrons and substitutional phosphorus atoms as a result of isochronous (15 min) heat treatments after irradiation at T_{irr} = (*1*) 180 and (*2*) 20°C. The material under investigation was *n*-Si:P with ρ = 1 Ω cm.

Experimental data on the recovery of the concentration of phosphorus atoms at the lattice sites as a result of the isochronous heat treatment of Czochralski-grown silicon show that the contribution of the *E* centers to the changes in the concentration of substitutional phosphorus is insignificant compared to the floating-zone silicon. This is consistent with the data obtained by deep-level transient spectroscopy, according to which the concentration of forming *E* centers is lower by an order of magnitude than the variation in the concentration of the electrically active phosphorus impurity [13]. The stage of reverse annealing observed in the curves of recovery of the substitutional phosphorus concentration after irradiation at T_{irr} = 180°C is probably caused by the release of interstitial silicon atoms from the sites of their residence as a result of dissociation. This is shown by the extended range of annealing stages (from 200 to 300°C).

Experimental data on the recovery of the concentration of phosphorus atoms at the lattice sites as a result of isochronous heat treatments after irradiation at T_{irr} = 20°C show that the major annealing stage is within the temperature range of T_{ann} = 340–360°C for silicon grown by the Czochralski method and within T_{ann} = 100–180°C for silicon grown by the floating-zone method. It is noteworthy that the recovery of phosphorus atoms at the lattice sites is related to the temperature ranges in which the major vacancy complexes (the *A* centers in the crucible-grown Si and the *E* centers in Si grown by the floating-zone method) are annealed out. As a result of dissociation of the vacancy-containing complexes, the mobile-vacancy concentration becomes higher than the corresponding steady-state concentration. This leads to the predominance of reactions (2) and to the interaction of vacancies with interstitial-type complexes containing phosphorus atoms. The emergence of an excess concentration of mobile interstitial-type defects promotes the reactions of type (1), which manifests itself in the stage of reverse annealing in the curves of recovery of the concentration of phosphorus atoms at the lattice sites.

CONCLUSION

Thus, the above results can be interpreted taking into account the following two processes: (i) interaction of the dopant atoms with silicon self-interstitials and origination of interstial-related complexes containing dopant atoms; this is equivalent to the radiation-induced decomposition of a supersaturated dopant solution as a result of the generation of point defects and ionization at comparatively low temperatures (the stage of formation of associated complexes [1, 7]); and (ii) recombination of interstitial impurity atoms with vacancies at fairly high temperatures or annihilation of the vacancies (released during heat treatment) with interstitial atoms incorporated into defect complexes containing phosphorus atoms.

REFERENCES

1. V. I. Fistul’, *Decomposition of Oversaturated Semiconductor Solid Solutions* (Metallurgiya, Moscow, 1977).
2. S. S. Gorelik and M. Ya. Dashevskiĭ, *Material Science of Semiconductors and Insulators* (Metallurgiya, Moscow, 1988).
3. V. P. Shapovalov and V. A. Gorodkin, Fiz. Tverd. Tela (Leningrad) **25**, 614 (1983) [Sov. Phys. Solid State **25**, 351 (1983)].
4. R. O. Schwenker, E. S. Pan, and R. F. Lever, J. Appl. Phys. **42**, 3195 (1971).
5. M. L. Joshi and S. Dash, IBM Syst. J. **5**, 271 (1967).
6. R. J. Jaccordine, J. Appl. Phys. **39**, 3105 (1968).
7. S. V. Bulyarskiĭ and V. I. Fistul’, *Thermodynamics and Kinetics of Interacting Defects in Semiconductors* (Nauka, Moscow, 1997).
8. R. M. Bayazitov, V. E. Borisenko, D. A. Konovalov, *et al.*, Fiz. Tekh. Poluprovodn. (Leningrad) **21**, 1505 (1987) [Sov. Phys. Semicond. **21**, 917 (1987)].
9. V. I. Obodnikov and E. G. Tishkovskiĭ, Fiz. Tekh. Poluprovodn. (St. Petersburg) **32**, 417 (1998) [Semiconductors **32**, 372 (1998)].
10. J. Xia, T. Saito, R. Kim, *et al.*, Jpn. J. Appl. Phys. **38**, 2319 (1999).
11. L. S. Smirnov, V. V. Bolotov, and A. V. Vasil’ev, Fiz. Tekh. Poluprovodn. (Leningrad) **13**, 1443 (1979) [Sov. Phys. Semicond. **13**, 845 (1979)].
12. V. V. Bolotov, V. A. Korotchenko, A. P. Mamontov, *et al.*, Fiz. Tekh. Poluprovodn. (Leningrad) **14**, 2257 (1980) [Sov. Phys. Semicond. **14**, 1337 (1980)].
13. V. V. Bolotov, G. N. Kamaev, and L. S. Smirnov, Fiz. Tekh. Poluprovodn. (Leningrad) **22**, 210 (1988) [Sov. Phys. Semicond. **22**, 129 (1988)].
14. V. D. Akhmetov, V. V. Bolotov, G. N. Kamaev, and L. S. Smirnov, Fiz. Tekh. Poluprovodn. (Leningrad) **24**, 72 (1990) [Sov. Phys. Semicond. **24**, 44 (1990)].
15. A. K. Ramdas and S. Rodrigues, Rep. Prog. Phys. **44**, 1297 (1981).
16. I. D. Konozenko, A. K. Semenyuk, and V. I. Khivrich, *Radiation Effects in Silicon* (Naukova Dumka, Kiev, 1974).

Translated by A. Spitsyn

Semiconductors, Vol. 36, No. 4, 2002, pp. 367–369. Translated from Fizika i Tekhnika Poluprovodnikov, Vol. 36, No. 4, 2002, pp. 389–391.
Original Russian Text Copyright © 2002 by Ostrovskiĭ, Nadtochiĭ, Podolyan.

ATOMIC STRUCTURE AND NONELECTRONIC PROPERTIES OF SEMICONDUCTORS

Ultrasonically Stimulated Low-Temperature Redistribution of Impurities in Silicon

I. V. Ostrovskiĭ, A. B. Nadtochiĭ, and A. A. Podolyan
Shevchenko State University (Physical Faculty), Kiev, 03127 Ukraine
e-mail: gogi@mail.univ.kiev.ua

Submitted October 17, 2001; accepted for publication October 18, 2001

Abstract—The effect of an ultrasonic treatment on the content of metal impurities in Si surface layers was studied by using secondary-ion mass spectrometry and the photoconductivity relaxation method. It is shown that ultrasound treatment increases the content of K and Na in Si surface layers at room temperature. *© 2002 MAIK “Nauka/Interperiodica”.*

Silicon is presently widely used in microelectronics. The electrical parameters of Si devices are governed, among other factors, by defects in Si wafers. As a rule, undesirable defects are introduced into Si during its growth and subsequent treatments [1]. One of a number of perspective methods used to control defects in Si is ultrasonic treatment (UST) [2, 3].

In spite of general agreement that UST affects defects in Si, it still remains unclear via what mechanisms it does so. In particular, the effect of UST on the chemical composition of an impurity in dislocation-free semiconductors has not been investigated. In this study, we attempt to clarify the matter.

We used KÈF Si wafers (i.e., n-Cz-Si:P, $\rho = 16\ \Omega$ cm) cut out of the central part of an ingot. In order to remove the damaged surface layers, the wafers were subjected to mechanical polishing and subsequent chemical polishing with a CP solution ($3HNO_3 : 1HF : 1CH_3COOH$). The presence of dislocations was checked by chemical etching, which showed that the samples were nearly dislocation-free. After the polishing, the samples were $3 \times 4 \times 11$ mm^3 in size. Seven samples were investigated in total, and similar results were obtained for all the samples. The samples were subjected to UST using the procedure described in [4]. The UST was carried out in air in the frequency range of 0.4–1 MHz. The duration of the UST was as long as 6.5 h.

The types and concentrations of impurities in the surface layers of the Si samples were determined by secondary-ion mass spectrometry (SIMS). The thickness of the surface layer was controlled by the depth at which the surface was etched by an argon beam while recording the SIMS spectrum. It did not exceed a few micrometers under the measurement conditions. Before the measurements, each sample, being installed in a vacuum chamber, was etched by an argon beam for 5 min to remove contaminants brought onto the surface from air. The error of the SIMS measurements did not exceed 5%. Several spectra were recorded subsequently from each sample, which allowed us to approximately determine the depth distribution of the impurities.

In addition, the kinetics of photoconductivity decay was measured to analyze the effect of the UST on Si. Since this method is sensitive to the change in the concentration of recombination centers [5], it can serve as an independent test to analyze the effect of ultrasound on a semiconductor. In order to measure the photoconductivity kinetics, ohmic contacts to samples were formed by depositing In–Ga paste on the Si surface. The fact that the contacts were ohmic was verified by their linear current–voltage characteristics. During the measurements, the contact area was shielded. Pulses of light from a GaAs light-emitting diode ($\lambda \approx 0.95\ \mu$m) were used to generate nonequilibrium charge carriers in the samples. The duration of the pulses was 500 μs Under these conditions, the photocurrent attained the steady-state value in the course of the pulse. The error of the photoconductivity measurements did not exceed 10%.

All ultrasonic treatments and subsequent measurements were conducted at room temperature.

Figure 1 shows typical SIMS spectra of the same Si sample (a) before and (b) after UST. The table gives the number of counts for elements and complexes detected in several successively obtained ion-mass spectra before and after UST. As can be seen, the content of elements we identify with K and Na increases in the surface layer after UST. We also observed a slight increase in the content of a complex with an atomic mass of 44 amu, which we identify with the SiO complex. The decrease in the content of an element with an atomic mass of 40 amu (^{40}Ca) by 20% (see table) seems to be due to the specific form of its depth distribution. As for K and Na, we observed that their content decreased with the distance from the surface, but drastically increased after UST (see table).

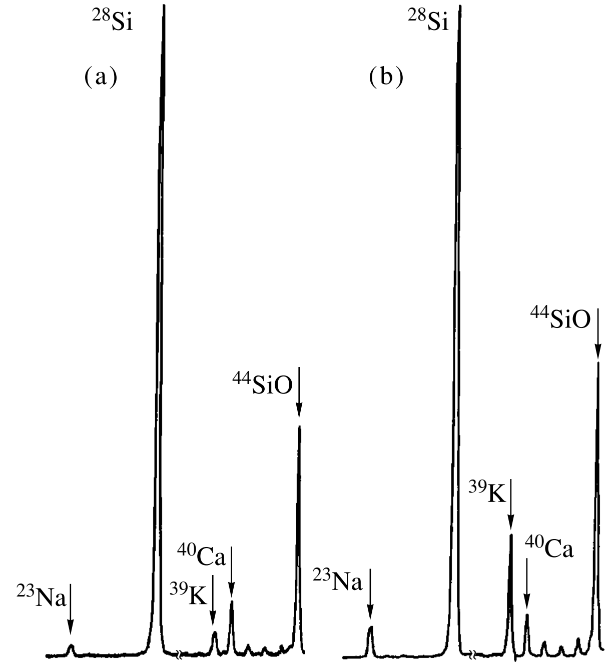

Fig. 1. SIMS spectra of the surface layer of a *n*-Cz-Si sample (*n*-Si-*2k-2*) (a) before and (b) after the UST.

Figure 2 shows the results of the photoconductivity relaxation measurements in the Si samples before and after UST. The photocurrent decay curves can be simulated fairly well by two exponentials

$$i_p(t) = A_1 \exp(-t/\tau_1) + A_2 \exp(-t/\tau_2), \qquad (1)$$

where τ_1 and τ_2 are the characteristic times of the relaxation process.

The rapid initial decay corresponding to the characteristic time τ_1 may be attributed to the recombination processes and redistribution of charge carriers on the surface and in the thin surface layer immediately after the light is switched off [6, 7]. It can be assumed that the thickness of the layer is equal to the effective screening length of the electric field, which is related to the surface band bending [8]. For the Si samples under investigation, the screening length is ~0.3 μm. The other (flatter) portion in the photocurrent decay curves is directly related to the lifetime of nonequilibrium charge carriers [6, 9]; i.e.,

$$\tau_2^{-1} = \tau_b^{-1} + [d^2/\pi^2 D]^{-1}, \qquad (2)$$

where τ_b and D are the bulk lifetime and diffusion coefficients of minority charge carriers, respectively; and d is the sample thickness. Under experimental conditions, the characteristic time τ_2 of the slower photocurrent component was governed by the bulk lifetime of minority charge carriers, τ_b [6]. In the measurements we conducted, the absorption length of light (~34 μm) was much smaller than the diffusion length of minority charge carriers, i.e., holes (~255 μm). Therefore, the diffusion length of minority charge carriers $L_{\text{eff}} \approx 255$ μm can be identified with the effective length within which the recombination of the charge carriers is analyzed [8]. The results obtained show that the characteristic times $\tau_{1,2}$ corresponding to both regions in the photocurrent decay curves increase as a result of UST. We should mention the results of our previous investigations, which showed that ultrasound has the most profound effect on surface layers of Si [4]. The thickness of such layers is ~100 μm. Therefore, the change in the photoconductivity relaxation is most likely caused by the UST.

Number of counts per each SIMS-recorded ion mass

Atomic mass, amu (element)	Number of counts			
	before UST		after UST	
	no. 1	no. 2	no. 3	no. 4
23 (Na)	2233	1095	7176	2915
28 (Si)	600000	600000	600000	600000
39 (K)	432	229	2603	1139
40 (Ca)	667	511	428	414
44 (SiO)	2798	2104	2897	2728

Note: Nos. 1 and 2 correspond to successively recorded SIMS spectra before the UST; nos. 3 and 4 correspond to successively recorded SIMS spectra after the UST. The duration of each recording was about 10 min.

In our opinion, the most probable cause of the changes in the SIMS spectra and photocurrent decay kinetics measured in the UST-subjected Si samples is the migration of K and Na from the bulk to the surface, which is stimulated by ultrasound. In fact, if UST causes the diffusion of light metal atoms to the surface, their content in the layer of thickness L_{eff} should increase. As shown in [7], the increase in the Na content results in the increase in the charge carrier lifetime. A similar effect can be expected from the increase in the K content in the layer of thickness L_{eff}. At the same time, metals can passivate surface recombination centers, which, in turn, slows down the surface recombination (increase in τ_1). We also observed an increase in the steady-state value of the photocurrent (see Fig. 2). In the linear approximation [10] that is applicable to the experiments we conducted, this is indicative of an increase in the lifetime of nonequilibrium charge carriers. This also indicates that, on the whole, the recombination centers affect the charge carriers to a lesser extent.

There exists the possibility of another explanation for the results obtained. For example, the changes in the SIMS spectra can be caused by changes in the material composition that are not due to diffusion. The peaks in the SIMS spectra, which we attribute to Na, K, and Ca, can be related to complexes formed by lighter elements (for example, by C, B, and O that are present in Cz-Si in rather large amount [1]) either with each other or

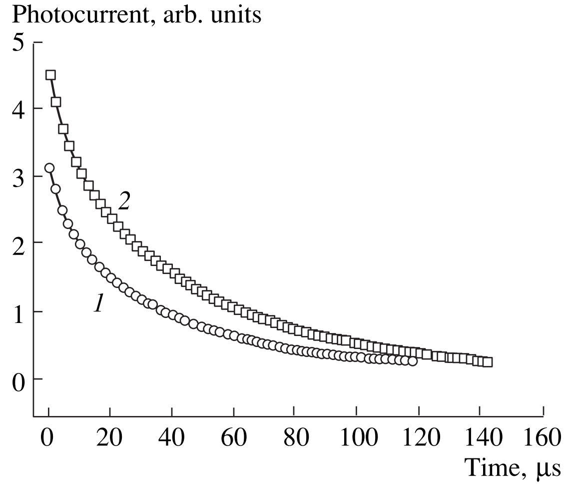

Fig. 2. Photocurrent decay curves for a *n*-Cz-Si sample (*n*-Si-*2k-2*) (*1*) before the UST (τ_1 = 7 μs, τ_2 = 44 μs) and (*2*) after the UST (τ_1 = 8 μs, τ_2 = 56 μs). The solid lines represent the results of a computer simulation using the least-squares method approximation.

with Si. The UST may result in either the formation or decomposition of these complexes, which should cause changes in the SIMS spectra and photocurrent decay kinetics. However, compared with ordinary diffusion, these processes require more energy and, therefore, in our opinion are less probable. Furthermore, the apparent increase in the impurity content may be related to the formation of some complexes in the beam plasma, but, in this case, the content of lighter components should also increase, which was not observed.

It is worth noting that the extent and features of the UST effect on Si should depend on the UST parameters, i.e., on the duration and intensity of the ultrasound. Although these rather time-consuming investigations were beyond this study, we did fix different changes in $\tau_{1,2}$ for different UST durations. The data given in Fig. 2 are typical of the UST duration on the order of tens of hours. The amplitude of the relative ultrasound-induced strain was on the order of 10^{-5}.

Thus, using two independent complementary methods, we attempted to show experimentally that the ultrasonic treatment of Si can stimulate diffusion processes in it at room temperature.

REFERENCES

1. V. S. Vavilov, V. F. Kiselev, and B. N. Mukashev, *Defects in the Bulk and at the Surface of Silicon* (Nauka, Moscow, 1990).
2. R. E. Bell, S. Ostapenko, and J. Lagowski, Mater. Res. Soc. Symp. Proc. **378**, 647 (1995).
3. I. B. Ermolovich, V. V. Milenin, R. V. Konakova, *et al.*, Fiz. Tekh. Poluprovodn. (St. Petersburg) **31**, 503 (1997) [Semiconductors **31**, 427 (1997)].
4. I. V. Ostrovskiĭ, L. P. Steblenko, and A. B. Nadtochiĭ, Fiz. Tekh. Poluprovodn. (St. Petersburg) **34**, 257 (2000) [Semiconductors **34**, 251 (2000)].
5. A. Hangleiter, Phys. Rev. B **35**, 9149 (1987).
6. M. Saritas and H. D. McKell, J. Appl. Phys. **63**, 4561 (1988).
7. F. Shimura, T. Okui, and T. Kusama, J. Appl. Phys. **67**, 7168 (1990).
8. G. E. Pikus, *Foundations of Theory of Semiconductor Devices* (Nauka, Moscow, 1965).
9. V. Grivitskas, E. Gaubas, A. Kanyava, *et al.*, Litov. Fiz. Sb. **32**, 589 (1992).
10. J. Auth, D. Genzow, and K. H. Hermann, *Photoelektrische Erscheinungen* (Akademie-Verlag, Berlin, 1977; Mir, Moscow, 1980).

Translated by Yu. Sin'kov

Semiconductors, Vol. 36, No. 4, 2002, pp. 370–374. Translated from Fizika i Tekhnika Poluprovodnikov, Vol. 36, No. 4, 2002, pp. 392–396.

ATOMIC STRUCTURE AND NONELECTRONIC PROPERTIES OF SEMICONDUCTORS

Simulation of Low-Temperature Arsenic Diffusion from a Heavily Doped Silicon Layer

O. V. Aleksandrov

University of Electrical Engineering, St. Petersburg, 197376 Russia

e-mail: aleks_ov@mailbox.alkor.ru

Submitted June 29, 2001; accepted for publication October 18, 2001

Abstract—Low-temperature (500–800°C) diffusion of As from a heavily doped Si layer was simulated on the basis of a dual pair mechanism. The anomalously high diffusion rate is attributed to excess self-interstitials accumulated in the layer during the preceding high-temperature diffusion stage. The shift of the concentration profile in the region of intermediate values of concentrations is caused by the presence of a maximum in the concentration dependence of the diffusivity. This shift is attributed to the considerable role that negatively charged self-interstitials play in the arsenic diffusion process ($f_I^- \approx 0.4$). *© 2002 MAIK "Nauka/Interperiodica".*

1. INTRODUCTION

Diffusion of As into Si is widely used to fabricate microwave transistors and integrated circuits, because it makes it possible to obtain heavily doped emitters whose important advantages are shallow depth and a steep impurity gradient. Another advantage of arsenic emitters in comparison with phosphorus ones is that they virtually cause no emitter-push effect; i.e., the collector–base junction does not shift away from the surface under the arsenic emitter [1]. However, on low-temperature treatments of transistor structures (from 500 to 800°C), anomalously fast diffusion of both As and B (base dopant) under an emitter is observed. This results in undesirable changes in the parameters of transistors during their testing and operation [3, 4]. Two mechanisms were suggested as possible causes of the anomalously fast diffusion: (1) generation of excess vacancies during the decay of a solid solution, due to the displacement of As atoms from their lattice sites [2] and (2) climb of dislocation loops during the formation of precipitates [3]. No quantitative model of the phenomenon has been developed to date. It is known presently that B diffuses in Si via an indirect interstitial mechanism, while As diffuses via a mixture of vacancy and interstitial mechanisms [5]. The enhancement of the diffusion of both substitutional impurities, B and As, during a low-temperature treatment may be caused only by excess self-interstitials. We assume that, as well as in the case of phosphorus [6], excess self-interstitials arise during low-temperature treatment (mainly in pairs with As atoms), due to their accumulation in the heavily doped Si layer during the preceding high-temperature diffusion (HTD).

The aim of this study is to develop a quantitative model of the low-temperature diffusion (LTD) of As from a heavily doped Si layer.

2. MODEL EQUATIONS

We assume that the diffusion of As, as well as that of P, can be described in terms of a dual pair mechanism. This mechanism can be considered as a mixture of two simpler mechanisms: a vacancy mechanism, via which As atoms diffuse in pairs with vacancies (As–V), and an indirect interstitial mechanism, via which As atoms diffuse in pairs with self-interstitials (As–I). We also assume that neutral As–I pairs can migrate to long distances during low-temperature treatments. As shown in [6], the diffusion of impurity can be described in this case by two diffusion equations for impurity-containing and self-interstitial-containing components; i.e.,

$$\frac{\partial A_F}{\partial t} = \frac{\partial}{\partial x}\left(D_{AF}\frac{\partial A_F}{\partial x}\right), \tag{1}$$

$$\frac{\partial F_I}{\partial t} = \frac{\partial}{\partial x}\left(D_{FI}\frac{\partial F_I}{\partial x}\right). \tag{2}$$

Here, t is time; x is the depth; A_F is the net concentration of As atoms and neutral As–I pairs; $A_F = A + F$; F_I is the net concentration of neutral As–I pairs and self-interstitials; $F_I = F + I^0$, D_{AF} and D_{FI} are the diffusion coefficients of As-containing and self-interstitial-containing components, respectively; and

$$D_{AF} = \frac{D_A A + D_F F}{A_F}, \quad D_{FI} = \frac{D_F F + D_I I^0}{F_I}, \tag{3}$$

where D_A, D_F, and D_I are the diffusion coefficients of As atoms, neutral As–I pairs, and self-interstitials, respectively.

When high-temperature diffusion (HTD) is followed by low-temperature diffusion (LTD), the thermodynamic equilibrium concentration of self-interstitials decreases. This should result in a corresponding decrease in the concentration of As–I pairs at the surface. In this case, As–I pairs and self-interstitials accumulated in the bulk of the diffusion layer during the HTD serve as a source of excess self-interstitials. The initial conditions for Eqs. (1) and (2) are the distributions of As-containing and self-interstitial-containing components immediately after the HTD; i.e.,

$$A_F(x,0) = A_{FH}(x), \quad F_I(x,0) = F_{IH}(x) \cong F_{IHS}, \tag{4}$$

where the subscript H denotes the HTD, and the subscript S denotes the surface concentration. The boundary conditions we used are as follows: for the net concentration of As-containing components there is a reflection at both boundaries of the solution region ($x = 0$ and $x = L$); for the net concentration of neutral self-interstitial-containing components there is a reflection at the far boundary ($x = L$), while the concentration at the surface ($x = 0$) corresponds to the equilibrium concentration of self-interstitials ($I_S^0 = I_{eq}^0$)

$$\begin{gathered}\frac{\partial A_F(0,t)}{\partial x} = \frac{\partial A_F(L,t)}{\partial x} = 0, \\ F_I(0,t) = F_{Ieq}, \quad \frac{\partial F_I(L,t)}{\partial x} = 0.\end{gathered} \tag{5}$$

At the diffusion temperatures, the concentration of As–I pairs is much lower than the concentration of As atoms; i.e., $F \ll A$. Therefore, $A_F \cong A$, and Eq. (1) can be used as a diffusion equation for As. The concentrations of other diffusion components can be found from the solution for Eq. (2) by using the relations for local equilibrium $I^- = k_I I^0 n$ and $F = k_F A^+ I^-$, where k_I is the equilibrium reaction-rate constant for the formation of negatively charged self-interstitials, k_F is the equilibrium reaction-rate constant for the formation of neutral As$^+$–I^- pairs, A^+ is the concentration of ionized As atoms, and n is the electron concentration.

In the initial stage of LTD, self-interstitials are redistributed between the self-interstitial-containing components in accordance with the conditions of the local equilibrium at the new (lower) temperature. As a result, a nonuniform initial distribution of neutral self-interstitials with depth is established; i.e.,

$$I^0(x,0) = \frac{F_{IH}(x)}{1 + k_{IF}A^+ n}, \tag{6}$$

where $k_{IF} = k_I k_F$. From (6), we can derive the dependence of the initial supersaturation of self-interstitials on the concentration and depth

$$a_I(x,0) = \frac{1 + k_{IFH}A_S^+ n_S I_{eqH}^0}{1 + k_{IF}A^+ n I_{eq}^0} \tag{7}$$

and the value of the initial supersaturation of self-interstitials at the tail of the concentration profile at low As concentrations, $A^+ \ll 1/(k_{IF}n_i)$:

$$a_{It}(0) = (1 + k_{IFH}A_S^+ n_S)\frac{I_{eqH}^0}{I_{eq}^0}. \tag{8}$$

As the LTD proceeds, the number of self-interstitials accumulated during the HTD decreases due to the drain of excess self-interstitials and As–I pairs to the surface until quasi-stationary depth distributions $F(x)$ and $I^0(x)$ and supersaturation $a_I(x)$, which is determined only by the As concentration and LTD temperature, are established there:

$$a_I(x,\infty) = \frac{1 + k_{IF}A_S^+ n_S}{1 + k_{IF}A^+ n}. \tag{9}$$

For low concentrations of As, the supersaturation of self-interstitials tends to reach its steady-state value at the tail of the concentration profile

$$a_{It}(\infty) = 1 + k_{IF}A_S^+ n_S. \tag{10}$$

3. SIMULATION PARAMETERS

The simulation parameters are the concentration dependence of the diffusion coefficient of As (D_A), the equilibrium constant for the reaction of formation of negatively charged self-interstitials (k_I), the equilibrium rate constant for the reaction of formation of neutral As–I pairs (k_F), self-interstitial formation energy (E_{fI}), and the diffusion coefficients of neutral As–I pairs (D_F) and self-interstitials (D_I).

The concentration dependence of the diffusion coefficient of As in Si at equilibrium with respect to intrinsic point defects (IPDs) for isoconcentration diffusion conditions is given in [5]. It has the form

$$D^* = D^0 + D^- = D_i^0 + D_i^-\left(\frac{n}{n_i}\right), \tag{11}$$

where D_i^0 and D_i^- are the partial intrinsic coefficients of diffusion involving IPDs in neutral and charged states, respectively; and n_i is the intrinsic-carrier concentration. Under nonisoconcentration conditions, the internal electric field and formation of clusters affect the diffusion. In this case, $D_A^* = D^* f_E f_C$, where f_E is the factor of diffusion enhancement due to the internal electric field [7], and f_C is the factor of the diffusion retardation due to the formation of clusters, $f_C = A^+/A$ [8, 9].

In the absence of equilibrium with respect to IPDs, one should take into account relative supersaturations (undersaturations) of self-interstitials and vacancies, as well as the relative contributions of indirect interstitial and vacancy mechanisms of As diffusion for different

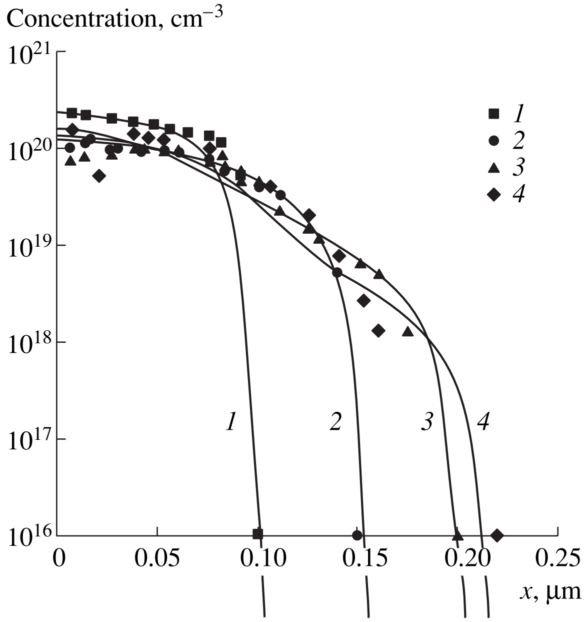

Fig. 1. Concentration profiles of electrically active As after (*1*) HTD for 0.12 h at 1000°C and (*2*–*4*) subsequent LTD. The LTD temperatures are (*2*) 700, (*3*) 600, and (*4*) 500°C; the LTD times are (*2*) 24, (*3*) 170, and (*4*) 336 h. Solid lines represent the simulation results; circles, squares, triangles, and diamonds represent the experimental data [2, 3].

charge states of IPDs. For the dual pair mechanism, the diffusion coefficient of As can be represented as a sum $D_A = D^*_{AV} a_V + D^*_{AI} a_I$, where D^*_{AV} and D^*_{AI} are the coefficients of As diffusion via vacancy and self-interstitial mechanisms (i.e., in the form of As–*V* and As–*I* pairs), respectively, in equilibrium with respect to IPDs ($D^*_A = D^*_{AV} + D^*_{AI}$); a_V and a_I are the relative supersaturations (or undersaturations) of vacancies and self-interstitials, respectively, $a_V = V/V_{eq}$, $a_I = I/I_{eq}$; and V_{eq} and I_{eq} are, respectively, the concentrations of vacancies and self-interstitials in thermodynamic equilibrium. If there is local equilibrium between vacancies and self-interstitials, we have $IV = I_{eq}V_{eq}$, which yields $a_V = 1/a_I$. The contribution of different charge states and types of pairs to the diffusion can be taken into account by using partial diffusion coefficients of As, and relative fractions of vacancy- and interstitial-related diffusion components, $D^*_{AV} = f^0_V D^0 + f^-_V D^-$, $D^*_{AI} = f^0_I D^0 + f^-_I D^-$, where f^0_V and f^-_V are the relative fractions of the components of diffusion via vacancies in corresponding charge states, and f^0_I and f^-_I are the relative fractions of the components of diffusion via self-interstitials in corresponding charge states. In this model, $f^0_V + f^0_I = 1$ and $f^-_V + f^-_I = 1$. If $A \ll n_i$ (Si:As is close to intrinsic Si), the relative fraction of the component diffusing via the indirect interstitial mechanism in the temperature range of 950–1100°C, f_I, was evaluated at $0.28 < f_I < 0.44$ [5] and $f_I = 0.45$ [10]. Since, according to [5], $D^0_i \cong D^-_i$ under these conditions, we assume that $f^0_I \cong f^-_I \cong 0.4$.

The recharging constant for self-interstitials, k_I, depends on the position of the energy level introduced by negatively charged self-interstitials into the band gap, $(k_I)^{-1} = N_C \exp[-(E_C - E_I)/kT]$, where N_C is the effective density of states in the conduction band, k is the Boltzmann constant, T is the absolute temperature, and $E_C - E_I$ is the position of the energy level of a negatively charged self-interstitial relative to the bottom of the conduction band. According to evaluations made in [11], $E_I \cong E_C - 0.4$ eV.

The self-interstitial formation energy, the formation constant of neutral As–*I* pairs, and the diffusion coefficients of neutral self-interstitials and As–*I* pairs were determined from a comparison of the simulation results with the experimental data [2, 3]. The self-interstitial formation energy governs the temperature dependence of the initial supersaturation of self-interstitials [see (7) and (8)]. This energy was found by analyzing the initial regions in the kinetics of *p*–*n* junction displacement at different LTD temperatures, $E_{fI} = 2.9$ eV. The constant k_F that, along with the constant k_I, determines the degree of self-interstitial supersaturation for long LTD times [see (9) and (10)] was found by analyzing the kinetics of the *p*–*n* junction displacement during long LTD times: $k_F = 1.1 \times 10^{-30} \exp(1.65/kT)$, cm^3. The diffusion coefficients of self-interstitials and As–*I* pairs determine the rate of the decrease in the self-interstitial supersaturation and, accordingly, the rate at which the kinetics of the *p*–*n* junction displacement levels off, while D_F also determines the form of the concentration profile; $D_I = 7.0 \times 10^{-12} \exp(-0.3/kT)$ cm^2/s, and $D_F = 1.0 \times 10^{-9} \exp(-1.0/kT)$ cm^2/s. It is worth noting that, compared with the LTD of P [6], we have the same formation energy (2.9 eV) and similar (on the order of magnitude) values of self-interstitial diffusion coefficients at LTD temperatures. However, the values of k_F and D_F for As are by more than two orders of magnitude smaller than those for P for the same bonding energies (1.65 eV) and migration energies (1.0 eV) for dopant-atom–interstitial pairs. This result may be attributed to the large size of ionized As atoms compared with P atoms, which, evidently, impedes the formation of As–*I* pairs and their migration through the Si lattice.

The additional factor that affects the diffusion coefficient of As for long LTD times is the decrease in the concentration of electrically active As atoms in the heavily doped region due to the decomposition of the As solid solution in Si. The parameters of the decomposition kinetics were taken from [3].

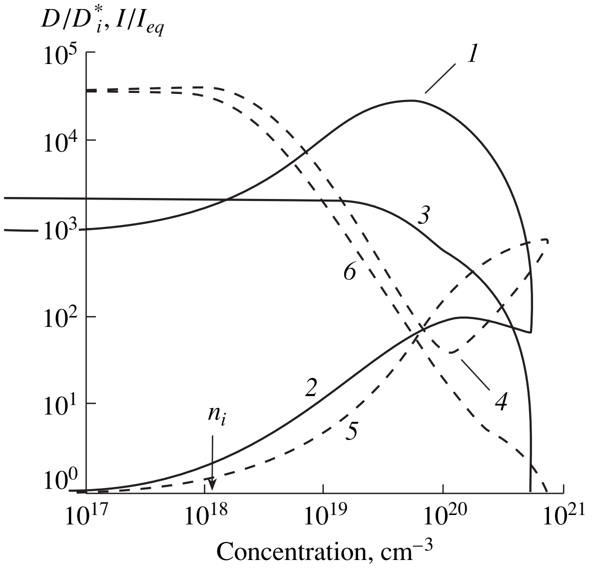

Fig. 2. (*1*, *2*, *4*, *5*) Relative diffusion coefficients and (*3*, *6*) the degrees of self-interstitial supersaturation as functions of the net impurity concentration at LTD for (*1*–*3*) As and (*4*–*6*) P (the HTD temperature, T_H, is 1000°C, the LTD temperature, T, is 700°C, the LTD duration, t, is 1 h). The diffusion coefficients *2* and *5* are calculated at $a_V = a_I = 1$, the diffusion coefficient *4* and supersaturation *6* are calculated using the model from [6].

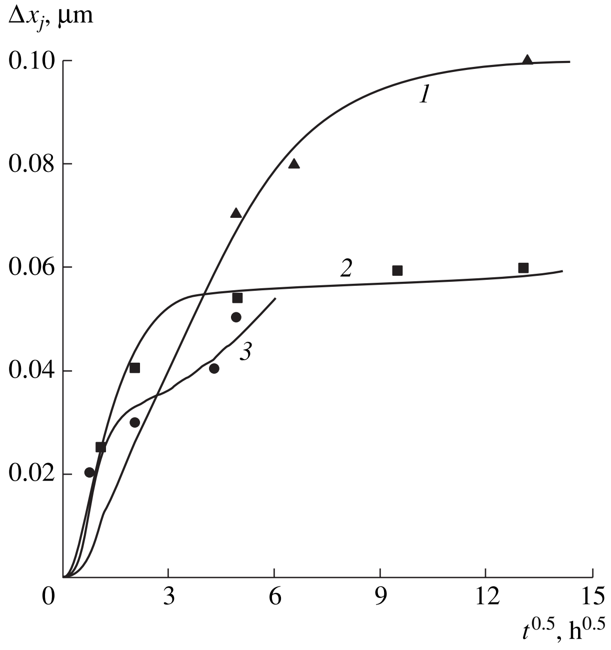

Fig. 3. The depth of a *p*–*n* junction as a function of the LTD duration. The LTD temperatures are (*1*) 600, (*2*) 700, and (*3*) 800°C. The solid lines represent the simulation results; circles, squares, and triangles represent the experimental data [3].

4. RESULTS AND DISCUSSION

Diffusion Eqs. (1) and (2) with the concentration-dependant diffusion coefficients (3), initial conditions (4), and boundary conditions (5) were solved numerically by the finite difference method using the implicit scheme. The simulation results were compared with the experimental concentration profiles and kinetics of the *p*–*n* junction displacement during the LTD, which were taken from [2, 3].

Figure 1 shows the simulation results (solid lines) and experimental concentration profiles of electrically active As^+ after the HTD at 1000°C and subsequent anneals at 500, 600, and 700°C. It can be seen that the simulation satisfactorily describes the displacement of the As profile from the surface at LTD. Unlike the LTD of P, the displacement of the As profile occurs in the intermediate portion of the profile rather than in the tail region. Figure 2 shows the concentration dependence of the relative diffusion coefficients (curves *1* and *2*) and self-interstitial supersaturation (curve *3*) for the LTD of As compared with corresponding dependences for the LTD of P (curves *4*–*6*). The values of the diffusion coefficients were divided into corresponding values of the intrinsic diffusion coefficients in the conditions of IPD equilibrium ($D_i^* = D_i^0 + D_i^-$). As can be seen, the concentration dependence of the diffusion coefficient of As (curve *1*) has a maximum and that of the diffusion coefficient of P (curve *4*) has a minimum for almost the same impurity concentrations, while the concentration dependences of the self-interstitial supersaturation (curves *3*, *6*) behave similarly. This can be attributed to the fact that the As fraction diffusing via the interstitial mechanism (in pairs with negatively charged self-interstitials) is rather large ($f_I^-(\mathrm{As}) \cong 0.4$), while, as it was shown in [6], $f_I^- \cong f_I^{2-} = 0$ for P. As a result, the diffusion coefficient of As does not decrease with decreasing As concentration, as it does in the case of P, but increases. The diffusion coefficient increases until the concentration dependence of a_I levels off, after which, in accordance with the concentration dependence of the diffusion coefficient of As given by (11) (curve *2*), D_A decreases until the As concentration becomes of the same order of magnitude as the intrinsic concentration of charge carriers, n_i, at the LTD temperature.

Figure 3 shows the simulation results (solid lines) compared with the kinetics of the *p*–*n* junction displacement Δx_j during the LTD at 600, 700, and 800°C. As can be seen, the simulation results satisfactorily describe the kinetics of the *p*–*n* junction displacement during the LTD. The increase in Δx_i is steep at the initial stage of the LTD but then slows down because the degree of self-interstitial supersaturation decreases as the LTD duration increases. The degree of self-interstitial supersaturation at the distribution tail is shown in Fig. 4 as a function of the LTD duration. As can be seen, the degree of supersaturation decreases in the course of

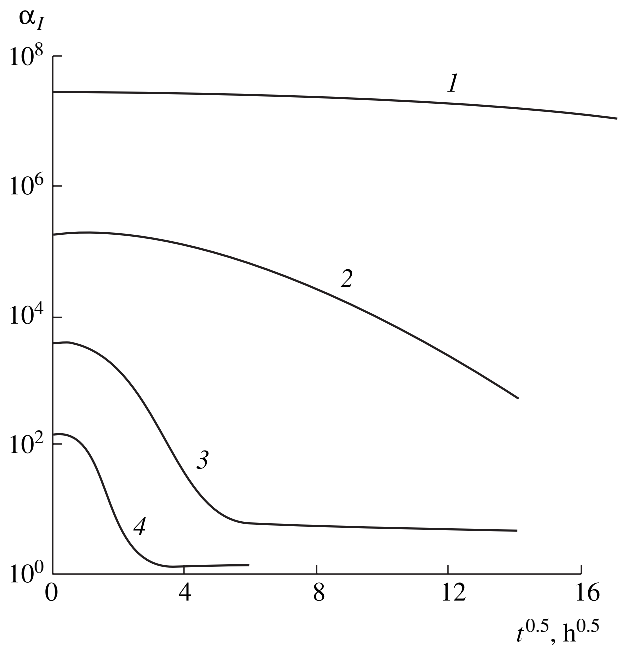

Fig. 4. The degree of supersaturation of self-interstitials as a function of the LTD time. The LTD temperatures are (*1*) 500, (*2*) 600, (*3*) 700, and (*4*) 800°C.

LTD from the initial value determined by formula (8) to the steady-state value defined by formula (10). This decrease in the degree of supersaturation is attributed to the drain of the excess self-interstitials and As–*I* pairs, accumulated during the preceding HTD, to the surface. An increase in the LTD temperature enhances the drain limited by the diffusion of self-interstitials and As–*I* pairs.

5. CONCLUSION

A numerical simulation of low-temperature diffusion of As from a heavily doped Si layer was performed on the basis of the dual pair mechanism. The anomalously high diffusion rate is attributed to the excess self-interstitials accumulated in the heavily doped layer during the preceding HTD, mainly in the form of As–*I* pairs. The concentration profiles of As differ from those obtained for P, which is attributed to the fact that a considerable fraction of As atoms diffuse via the interstitial mechanism, i.e., in pairs with negatively charged self-interstitials (f_I^-(As) ≅ 0.4). This results in a maximum in the concentration dependence of the diffusion coefficient and a shift of the profile in the intermediate-concentration region. The slowing down of the *p*–*n* junction displacement in time and the enhancement of this process with the increase in the temperature is attributed to the drain of excess self-interstitials and As–*I* pairs, accumulated during the preceding HTD, to the surface.

REFERENCES

1. S. M. Hu, in *Atomic Diffusion in Semiconductors,* Ed. by D. Shaw (Plenum, London, 1973; Mir, Moscow, 1975), Chap. 5.
2. H. Shibayama, H. Masaki, and H. Hashimoto, Appl. Phys. Lett. **27**, 230 (1975).
3. H. Shibayama, H. Masaki, H. Ishikawa, and H. Hashimoto, J. Electrochem. Soc. **123**, 742 (1976).
4. N. G. Vevyurko and G. I. Yusupova, Élektron. Tekh., Ser. 2, No. 1 (136), 63 (1980).
5. M. Fahey, P. B. Griffin, and J. D. Plummer, Rev. Mod. Phys. **61**, 289 (1989).
6. O. V. Aleksandrov, Fiz. Tekh. Poluprovodn. (St. Petersburg) **35**, 1289 (2001) [Semiconductors **35**, 1231 (2001)].
7. R. Sh. Malkovich, *Mathematics of Diffusion in Semiconductors* (Nauka, St. Petersburg, 1999), Chap. 5.
8. S. Solmi and D. Nobili, J. Appl. Phys. **83**, 2484 (1998).
9. K. Tsukamoto, Y. Akasaka, and K. Kijima, Jpn. J. Appl. Phys. **19**, 87 (1980).
10. A. Ural, P. B. Griffin, and J. D. Plummer, J. Appl. Phys. **85**, 6440 (1999).
11. W. Frank, Inst. Phys. Conf. Ser. **23**, 23 (1975).

Translated by Yu. Sin'kov

Semiconductors, Vol. 36, No. 4, 2002, pp. 375–378. Translated from Fizika i Tekhnika Poluprovodnikov, Vol. 36, No. 4, 2002, pp. 397–400.
Original Russian Text Copyright © 2002 by Klimenko, Migal'.

ELECTRONIC AND OPTICAL PROPERTIES OF SEMICONDUCTORS

Generalized Character of the Dielectric Response of CdTe Crystals Grown from the Melt

I. A. Klimenko and V. P. Migal'
Zhukovsky National Aerospace Institute KhAI, ul. Chkalova 17, Kharkov, 61070 Ukraine

Submitted August 23, 2001; accepted for publication September 27, 2001

Abstract—It was found that the specific features of the photodielectric response of CdTe crystals grown from the melt are determined by ensembles of macroscopic growth defects. The analysis of diagrams $\varepsilon^*(\lambda)$ and $\varepsilon^*(X)$, which characterize the dependences of the complex dielectric constant on the wavelength and coordinates, as graphic images of sequences of induced states of the crystal was carried out. It was demonstrated that such analysis allows for the identification of the ensembles of macroscopic defects, which are the sources of internal fields. *© 2002 MAIK "Nauka/Interperiodica".*

The CdTe crystals grown from the melt are promising high-resistivity semiconductor materials for gamma spectroscopy. They usually contain various macroscopic growth defects, which comprise the sources of internal interrelated elastic and electric fields and substantially affect transport properties [1]. The uncovering and identification of such defects, as well as determining their charge states by investigation techniques commonly used for semiconductors, is hampered due to the high resistivity of the material. Elastic and electric fields are generated by macroscopic growth defects in piezoelectric II–VI crystals. These fields determine the specific features of the real (ε') and imaginary (ε'') parts of the complex dielectric constant (ε^*) on the photoexcitation wavelength (λ) and temperature (T). These specific features are represented most comprehensively by diagrams $\varepsilon^*(\lambda)$ and $\varepsilon^*(T)$ on the phase plane $\{\varepsilon', \varepsilon''\}$ [2–4]. It was demonstrated that the form of the diagrams $\varepsilon^*(\lambda)$ depends on the photoexcitation intensity as well as on the size and coordinates of the optical probe [2]. The complexity of energy and relaxation spectra for these crystals, as well as the specificity of their dielectric response, necessitates the development of a generalized approach to treatment and analysis of experimental results. Such development was the main purpose of this study.

The CdTe crystals grown in various conditions of vertical crystallization from the melt under high pressure of the inert gas (as high as 100 atm) were investigated. Macroscopic growth defects were revealed and investigated using etching, IR microscopy, and shadow methods. The residual stresses induced by growth defects in the samples investigated were determined using the optical-polarization method. The In–Ga or Au contacts were deposited on the opposite face of the samples; these contacts were $11 \times 11 \times 2$ and $5 \times 5 \times 2$ mm^3 in size, respectively. The dielectric constant ε' and the dielectric loss factor ε'' were determined in the frequency range $f = 10^2$–10^7 Hz using the capacitance technique. The photodielectric response was investigated in the region of low-frequency dispersion. The resistivity ρ of the samples was measured using a four-point probe technique ($\rho < 10^{10}\ \Omega$ cm).

It is found that the growth conditions substantially affect the shape of the crystallization front and determine the multiplicity of the types of the macroscopic growth defect. For the CdTe crystals grown with a large curvature of the crystallization front, the precipitates of Te and Cd, as well as cylindrical and spherical pores, are observed. These crystals also possess a variety of two-dimensional structure defects (impurity-decorated grain interfaces, twins, slip bands, etc.) and composition fluctuations. These features are revealed by etching and in shadow and optical-polarization patterns [1].

The character of the distribution of macroscopic growth defects and interrelated elastic and electric fields, which are generated by these defects, determines the specific features of the low-frequency dielectric response of CdTe crystals [3]. This determines the individuality of the $\varepsilon^*(\lambda)$ diagrams for each single sample [3, 4]. The multiplicity of macroscopic growth defects in the samples can be revealed by optical and other methods. The $\varepsilon^*(\lambda)$ diagrams obtained during the integrated photoexcitation of the sample as a whole consist of various bow-shaped segments (Fig. 1, curve *1*). These diagrams can also contain separated partial diagrams as well as the domains, for which $d\varepsilon''/d\varepsilon' < 0$. Substantial distinctions of the diagrams are observed even for the samples cut from the same ingot. However, the diagrams of the samples, which are prepared from neighboring regions of the ingot, are often similar. It turned out that it was possible to use the criteria of geometric similarity for the comparative analysis of the diagrams. In this case, the $\varepsilon^*(\lambda)$ diagrams are considered as peculiar graphic images, which characterize the generalized photodielectric response of the crystal. The

1063-7826/02/3604-0375$22.00 © 2002 MAIK "Nauka/Interperiodica"

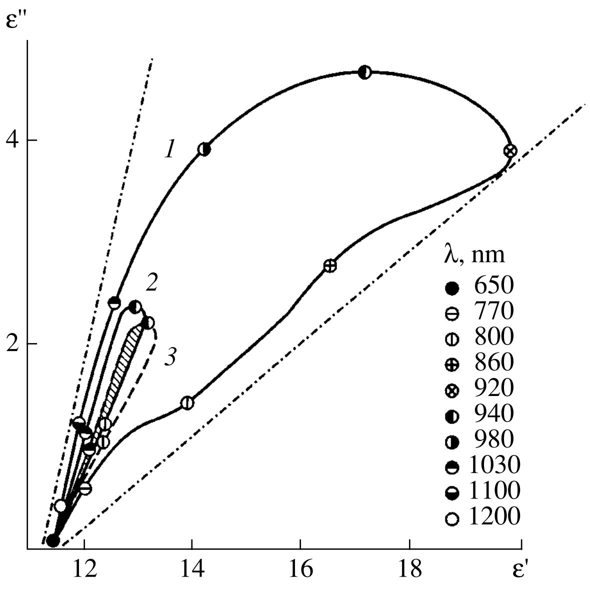

Fig. 1. Diagrams (*1*) $\varepsilon^*(\lambda)$ obtained with the photoexcitation of the entire sample as well as diagrams (*2, 3*) $\varepsilon^*_X(\lambda)$ obtained with the probe photoexcitation. The frequency $f = 10^3$ Hz, and the temperature $T = 293$ K. The wavelengths λ are indicated.

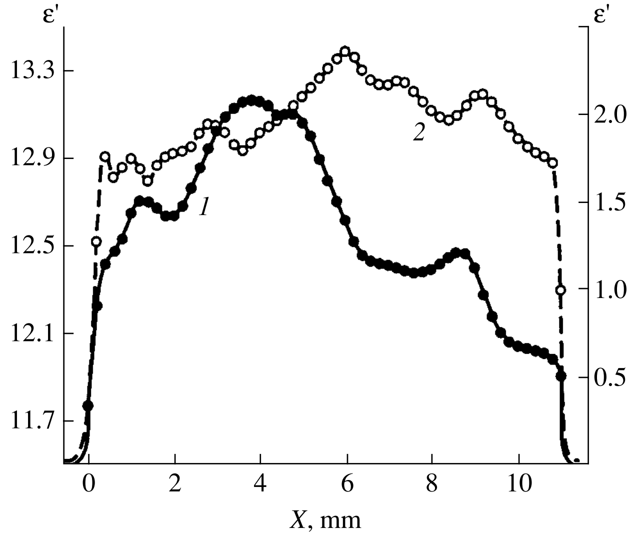

Fig. 2. Dependences (*1*) $\varepsilon'(X)$ and (*2*) $\varepsilon''(X)$ for the CdTe sample, which are obtained with the probe photoexcitation. The frequency $f = 10^3$ Hz, the temperature $T = 293$ K, and the probe width is 100 μm. The points correspond to various probe positions with the step of 0.2 mm.

diagrams $\varepsilon^*_X(\lambda)$, which were obtained with the photoexcitation of neighboring regions of the crystal by the monochromatic probe with the width less than 100 μm, are more similar geometrically compared to the diagrams measured with the excitation of spatially separated regions or various samples. The geometric shape of these diagrams is simpler and more symmetric compared to the diagrams obtained with the integrated photoexcitation (Fig. 1, curves *2, 3*). Such diagrams differ only by increments of ε' and ε" under illumination, as well as by the regions outlined by them in the phase plane. The diagrams ΔS were obtained with the photoexcitation of neighboring regions X_n and X_{n+1} of the sample (shaded region in Fig. 1). In this case, the area of their overlapping varies with the probe coordinate X in a complex manner. It was also found that, as the probe width increases, the similarity of $\varepsilon^*_X(\lambda)$ diagrams ceases to exist. This suggests that the specific features of these diagrams are associated with the effect of internal fields, which are generated by macroscopic growth defects, on the charged state of complex centers responsible for the photosensitivity. Thus, the coordinate dependences $\varepsilon'(X)$ and $\varepsilon''(X)$, which are obtained by scanning the optical probe with the width of 100 μm and the wavelength in the vicinity of the intrinsic photosensitivity peak, contain a number of local extrema. The number and distribution of extrema are the individual characteristics of the crystal (Fig. 2, curves *1, 2*). In this case, the diagrams $\varepsilon^*(X)$ in the phase plane, which are obtained based on these dependences, comprise the collection of macroscopic domains of various character, namely, linear, steplike, bow-shaped, and looplike amongst others (Fig. 3). Note that certain domains are the isolated partial diagrams. These domains are marked with arrows in Fig. 3. This allows one to consider these regions as mappings of the specific ensembles of macroscopic growth defects. An increase in the photoexcitation intensity leads to a variation in the $\varepsilon^*(X)$ diagrams. In this case, the geometric similarity is retained up to a certain critical intensity level Φ_c.

Such a character of the variation in the dielectric response over the sample, which is mapped by the diagram $\varepsilon^*(X)$, is indicative of the zoned distribution of certain aggregations of macroscopic growth defects. This is partially confirmed by the results of optical-polarization and shadow investigations. The complex individual character of diagrams and their dependence on many factors necessitates the search for a generalized approach to the analysis of the dielectric response of such crystals. Specifically, such an approach may be based on the notions about metastable and induced states of the crystal. The reason is that all the samples from the CdTe ingot are in various metastable states. These states are mapped by the set of the points ε^*_T in the sector of the phase plane and can be varied by thermal treatment [4]. At the same time, the external effect F (photoexcitation, thermal effect, pressure, etc.) induce the state in the ZnSe crystal, which is also mapped by the point ε^*_T in the phase plane. In this case, the $\varepsilon^*(F)$ diagrams are also the characteristic signs of the metastable state [5]. In this case, we can assume that the set of points in the region outlined by the diagram $\varepsilon^*(\lambda)$ (Fig. 1, curve *1*) is also the subset of energetically allowed induced states, which is mapped by the corresponding graphic image in the phase plane. Consequently, the area *S*, which is outlined by the diagram $\varepsilon^*_X(\lambda)$, which is obtained with the local photoexcitation (Fig. 1, curve *1*), is the region or the subset of possible induced states ε^*_1, ε^*_2, …, which have their own graphic image. Actually, by varying the wavelength and decreasing the probe intensity, we can obtain any ε^*_i value from this subset. In the context of these notions, the ratio of the overlapping area ΔS of two neighboring diagrams $\varepsilon^*_X(\lambda)$ to their average area $(S_1 + S_2)/2$, i.e., $2\Delta S/(S_1 + S_2)$ is a certain correlation parameter *K*, which determines the fraction of common induced states. It is evident that it characterizes the degree of interrelation between definite agglomerations of macroscopic growth defects.

With the probe photoexcitation, the *i*th state is induced in the crystal, which is represented by the $\varepsilon^*(X_i)$ point in the phase plane. In this case, the sequence of $\varepsilon^*(X_i)$ values within the limits of the above-mentioned domain comprises the subset of coordinate-allowed induced states. In the context of this approach, the subset of induced states can be brought into correspondence with each of the above-mentioned regions of the $\varepsilon^*(X)$ diagram. In this case, the corresponding graphic image is associated with each such subset. The shape of the image (line, loop, arc, etc.) is determined by the character of interaction of the aggregation of macroscopic growth defects. This makes it possible to identify the ensembles of macroscopic growth defects from the shape of the graphic image as well as to determine the coordinates of similar ensembles. Thus, the domains marked by the arrows in the $\varepsilon^*(X)$ diagram (Fig. 3), which are mapped by isolated graphic images, can be naturally associated with inclusions. The loop-like regions of the diagram, which are characterized by the direct (clockwise) or inverse sequence of induced states, are worthy of special attention. The inverse sequence can be considered as the opposite charge state of the aggregation of macroscopic growth defects. These regions of the crystal act as the sinks or the sources of internal fields, which are generated by the aggregation of macroscopic growth defects. Macroscopic regions of the crystal, which are in correspondence with the separated domains of the $\varepsilon^*(X)$ diagram, also differ by the form of distribution of complex centers responsible for the photosensitivity. It is also evident that the form of distribution of these centers and their charge state are controlled by the sequence of macroscopic growth defects for the specific region of the sample. We note that elements of similarity of graphic images in $\varepsilon^*(X)$ diagrams are retained with increasing probe intensity Φ up to a certain critical Φ_c value. This value is the individual characteristic of each sample. New induced states are also found within the sector shown in Fig. 1 by the dash-and-dot line.

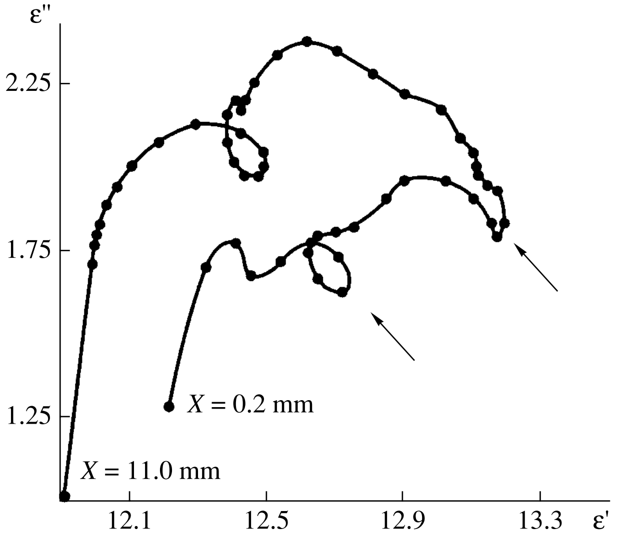

Fig. 3. Diagram $\varepsilon^*(X)$ for the CdTe sample. The frequency $f = 10^3$ Hz, the temperature $T = 293$ K, and the probe width is 100 μm. The points correspond to various probe positions with the step of 0.2 mm.

For the series of samples, certain domains of the $\varepsilon^*(X)$ diagram are transformed with increasing the probe intensity to $\Phi > \Phi_c$. This transformation includes the smoothing and combining of certain domains, as well as loop transformation, into the partial diagram or vice versa. It was also found that the same domains of diagrams transform with heating of the samples. Apparently, the crystal as a system counteracts the variation in its metastable state according to the Le Chatelier principle or the piezoelectric analogue of the Lenz law. A cause–effect relation between the set of ensembles of macroscopic growth defects and growth conditions exists. These ensembles are mapped by the subsets of individual states. This relation manifests itself in the character of the sequence of graphic images, i.e., in the diagram $\varepsilon^*(X)$. Structuring of separate ensembles also takes place. This structuring is mapped by definite graphic images, for example, loops. It can be seen that the decomposition of the system of the actual crystal can be carried out by dividing the $\varepsilon^*(X)$ diagram into a sequence of domains. Each of these domains is mapped by the corresponding image in the phase plane. A comparative analysis makes it possible (1) to determine the number of ensembles of macroscopic growth defects in the sample (ingot) and the presence of similar ensembles in them; (2) to reveal the sinks and sources of the fields, which are created by a certain aggregation of macroscopic growth defects; (3) to determine the coordinates of ensembles of macroscopic growth defects, which change their properties under the intensive load; and (4) to reveal the elements of structuring of macroscopic growth defects of CdTe crystals, which are associated with highly nonequilibrium growth conditions.

Thus, a variety of macroscopic growth defects in the crystals under consideration and an apparently random form of their distribution in the bulk are observed. In spite of this, the approach developed for the analysis of the generalized dielectric response offers the possibility of identifying the separate aggregations of macroscopic growth defects. It is possible to identify these aggregations not only from their graphic images and functional characteristics, but also from their sequence and its variation under intensive loads. It is also possible to reveal the growth factors which predominately affect the formation of the electrical properties of these crystals. All these facts are especially important for functional piezoelectric crystals, whose investigation by known techniques yields ambiguous results. The above results form the basis of the technique for the identification of growth defects and assessment of quality of these crystals.

REFERENCES

1. V. Komar, A. Gektin, D. Nalivaiko, *et al.*, Nucl. Instrum. Methods Phys. Res. A **458**, 113 (2001).
2. I. A. Klimenko, V. K. Komar’, V. P. Migal’, and D. P. Nalivaĭko, Fiz. Tekh. Poluprovodn. (St. Petersburg) **35** (2), 139 (2001) [Semiconductors **35**, 135 (2001)].
3. I. A. Klimenko, V. K. Komar’, V. P. Migal’, and D. P. Nalivaĭko, Fiz. Tekh. Poluprovodn. (St. Petersburg) **35** (4), 403 (2001) [Semiconductors **35**, 391 (2001)].
4. I. A. Klimenko and V. P. Migal, Funct. Mater. **8** (2), 395 (2001).
5. V. P. Migal’, Fiz. Tekh. Poluprovodn. (St. Petersburg) **35** (10), 1188 (2001) [Semiconductors **35**, 1135 (2001)].

Translated by N. Korovin

Semiconductors, Vol. 36, No. 4, 2002, pp. 379–381. Translated from Fizika i Tekhnika Poluprovodnikov, Vol. 36, No. 4, 2002, pp. 401–403.
Original Russian Text Copyright © 2002 by Arutyunyan.

ELECTRONIC AND OPTICAL PROPERTIES OF SEMICONDUCTORS

Effect of the Radial Electric Field on Absorption in a Quantized Spherical Layer

V. A. Arutyunyan

State Armenian Engineering University, 377503 Gyumree, The Republic of Armenia

Submitted August 22, 2001; accepted for publication August 29, 2001

Abstract—Electronic states in the quantized spherical layer under the presence of a static radial field are considered. Expressions for the energy spectrum and the wave functions of carriers are obtained. The electroabsorption coefficient has a resonance nature; electric-field induced oscillations are observed in each subband. The external field leads also to a shift of the absorption edge to shorter wavelengths. A weak rise of the absorption coefficient is observed in each quantum-well subband with increasing field. © *2002 MAIK “Nauka/Interperiodica”*.

Various multilayer nanoheterostructures with a spherical symmetry are now being intensively studied along with many low-temperature semiconductors (see, for example, [1–5]). For this reason, it is of interest to consider the properties of a “unit” structure of this kind; i.e., a quantized spherical layer. Of particular interest is the effect of various static electric fields on the physical parameters of a sample. The geometric features of a sample allows us to trace the action not only of external fields but of fields induced by a source located inside the sample [10]; e.g., a charged impurity, an ion, or a charged microsphere, coated with a nanocrystalline spherical shell.

Here, we consider the effect of the radial static electric field on the shape of the optical absorption band in the spherically symmetric quantized layer.

1. ELECTRON STATES IN A LAYER UNDER THE PRESENCE OF A RADIAL FIELD

If the layer is approximated by an infinitely deep potential well, the motion of the carriers within the layer can be described as the motion in a field with the following model potential:

$$U(r) = \begin{cases} \infty, & \text{when } r \le R_1, r \ge R_2 \\ \dfrac{\gamma}{r}, & \text{when } R_1 < r < R_2, \end{cases} \tag{1}$$

where R_1 and R_2 are, respectively, the inner and outer radii of the layer, and γ is the constant of interaction of the charged particle with the field source. Representing the radial wave function as

$$\psi(r) = \frac{\chi(r)}{r} \tag{2}$$

for the related Schrödinger equation in the isotropic effective mass approximation, we obtain

$$\frac{\hbar^2}{2m}\chi'' + E\chi - \frac{\hbar^2 l(l+1)}{2mr^2}\chi - \frac{\gamma}{r}\chi = 0, \tag{3}$$

where m is the effective mass of the isotropic carrier, E is the particle energy and l is the orbital quantum number. Hereafter we will be interested in the case of a “thin” layer, when its thickness L is much less than the 3D-exciton Bohr radius a_0:

$$L \ll a_0. \tag{4}$$

At the same time, we assume that the layer is distant enough from the source; i.e., the following condition holds:

$$L \ll R_1. \tag{5}$$

In other words, the effective Bohr energy γ/R_1 is much less in this case than the quantum confinement energy. Introducing the variable $\rho = r - R_1$ and restricting our consideration to the first order in the parameter $\rho/R - 1$, we obtain, taking (4) and (5) into account,

$$\chi''(\rho) + \frac{2m}{\hbar^2}(\mathcal{E} + F\rho)\chi(\rho) = 0 \tag{6}$$

instead of (3) with the following designations introduced:

$$\left.\begin{aligned} \mathcal{E} &= E - \frac{\hbar^2 l(l+1)}{2mR_1^2} - \frac{\gamma}{R_1} \\ FL &= \frac{\hbar^2 l(l+1)}{2mR_1^2}\frac{2L}{R_1} + \frac{\gamma}{R_1}\frac{L}{R_1} \end{aligned}\right\}. \tag{7}$$

Passing to the dimensionless variable

$$\xi = \left(\rho + \frac{\mathcal{E}}{F}\right)\left(\frac{2mF}{\hbar^2}\right)^{1/3}, \tag{8}$$

we arrive at the equation

$$\chi''(\chi) + \xi\chi(\xi) = 0. \tag{9}$$

As is known [11], its solutions are given by the linear combination of the Airy functions of the first ($Ai(\xi)$) and second ($Bi(\xi)$) kinds:

$$\chi(\xi) = C_1 Ai(-\xi) + C_2 Bi(-\xi), \tag{10}$$

where C_1 and C_2 are normalization constants.

The carrier energy spectrum is determined from the boundary conditions:

$$\begin{cases} C_1 Ai(-\xi_0) + C_2 Bi(-\xi_0) = 0 \\ C_1 Ai(-\xi_L) + C_2 Bi(-\xi_L) = 0, \end{cases} \tag{11}$$

where ξ_0 and ξ_L are the values of the variable ξ at the layer boundaries $\rho = 0$ and $\rho = L$, respectively. One can see from (7) that $FL \ll \mathscr{E}$.

On the other hand, if we represent ξ_0 and ξ_L as

$$\begin{aligned} \xi_0 &= \pi^{\frac{2}{3}} \frac{\mathscr{E}}{F} \left(\frac{FL}{\varepsilon_1} \right)^{\frac{1}{3}}, \\ \xi_L &= \pi^{\frac{2}{3}} \left(1 + \frac{\mathscr{E}}{FL} \right) \left(\frac{FL}{\varepsilon_1} \right)^{\frac{1}{3}}, \end{aligned} \tag{12}$$

where $\varepsilon_1 = \dfrac{\pi^2 \hbar^2}{2mL^2}$ is the first quantum confinement energy level of radial motion, then for ξ_0 and ξ_L, we obtain

$$\xi_0, \xi_L \gg 1. \tag{13}$$

Using the asymptotic expansion of Airy functions for large argument values [11], after simple calculations we obtain the following expression for the carrier energy spectrum:

$$\begin{aligned} \mathscr{E}_{n,\,l} &\cong \varepsilon_1 n^2 - \frac{FL}{2} \quad (n = 1, 2, \ldots), \\ E_{n,\,l} &\cong \varepsilon_1 n^2 + \frac{\hbar^2 l(l+1)}{2mR_1^2} \left(1 + \frac{L}{R_1} \right)^{-1} + \frac{\gamma}{R_1} \left(1 + \frac{L}{R_1} \right)^{-\frac{1}{2}}. \end{aligned} \tag{14}$$

Correspondingly, for the radial wave function we obtain

$$\psi_{n,\,l}(\rho) \cong \sqrt{\frac{2}{L}} (1 + \alpha_{n,\,l}\rho) \frac{\sin(\beta_{n,\,l}\rho L)}{\rho + R_1}, \tag{15}$$

where the parameters $\alpha_{n,\,l}$ and $\beta_{n,\,l}$ are given by

$$\alpha_{n,\,l} = \frac{F}{4\mathscr{E}_{n,\,l}}; \quad \beta_{n,\,l} = \frac{\pi}{L} \left(\frac{\mathscr{E}_{n,\,l}}{\varepsilon_1} \right)^{1/2}. \tag{16}$$

Thus, within the framework of the model under consideration, the energy of the carrier in the layer is a sum of three terms related to, respectively, the quantized radial motion, the orbital motion, and the energy imparted to the particle by the external field. It is easy to see that, at $R_1 \longrightarrow \infty$, (14) and (15) reduce to the case of a "conventional" film (see, for example, [12]).

2. INTERBAND TRANSITIONS

Let us now calculate the electroabsorption coefficient for the interband optical transitions in the layer within the dipole approximation. We assume that the light wave is incident along the x axis and is linearly polarized (along the z-axis). Then we have, within the dipole approximation, for a perturbation related to the light wave

$$\hat{V} = i\hbar \frac{|e| A_0}{m_0 c} \left(\cos\vartheta \frac{\partial}{\partial r} - \frac{\sin\vartheta}{r} \frac{\partial}{\partial r} \right), \tag{17}$$

where m_0 is the free electron mass, e is the elementary charge, q is the photon wave number, c is the speed of light in free space, A_0 is the incident light wave amplitude, and ϑ is the polar angle. The total electron wave function is a product of the radial functions (15) and the spherical functions $Y_{l,\,m}(\vartheta, \varphi)$. Their form is well known (see, for example, [13]) and will not be presented here. Integration over the angular variables leads to the following selection rules: only transitions between the states for which $m_c = m_v$, $l_c = l_v + 1$, where m_k is the azimuthal quantum number, are subscripts v and c related to the valence and conduction bands, respectively. For the interband transition matrix element, we obtain

$$\begin{aligned} M_{c,\,v} &= \hbar \frac{2|e|A_0}{m_0 c} \frac{2}{L} \sqrt{\frac{(l_v + 1)^2 - m_v^2}{(2l_v + 3)(2l_v + 1)}} \\ &\times \left\{ \frac{1}{2R_1} (1 + l_v - \alpha_v R_1) f_1(\beta_c, \beta_v) + \beta_v (\alpha_c + \alpha_v) \right. \\ &\left. \times \left(\frac{L}{2} f_3(\beta_c, \beta_v) - f_2(\beta_c, \beta_v) \right) - \beta_v f_4(\beta_c, \beta_v) \right\}, \end{aligned} \tag{18}$$

where the functions $f_i(\beta_c, \beta_v)$ read

$$\begin{aligned} f_1(\beta_c, \beta_v) &= \frac{\sin(\beta_c - \beta_v)L}{\beta_c - \beta_v} - \frac{\sin(\beta_c + \beta_v)L}{\beta_c + \beta_v}, \\ f_2(\beta_c, \beta_v) &= \frac{\sin(\beta_c + \beta_v)L}{(\beta_c + \beta_v)^2} - \frac{\sin(\beta_c - \beta_v)L}{(\beta_c - \beta_v)}, \\ f_3(\beta_c, \beta_v) &= \frac{\cos(\beta_c + \beta_v)L}{\beta_c + \beta_v} - \frac{\cos(\beta_c - \beta_v)L}{\beta_c - \beta_v}, \\ f_4(\beta_c, \beta_v) &= \frac{\sin^2 \frac{1}{2}(\beta_c + \beta_v)L}{\beta_c + \beta_v} + \frac{\sin^2 \frac{1}{2}(\beta_c - \beta_v)L}{\beta_c - \beta_v}. \end{aligned} \tag{19}$$

The definition of α_i, β_i implies that the last term makes the dominating contribution to (18) (the first two terms are first-order corrections to $\beta_\nu f_4(\beta_c, \beta_\nu)$. Correspondingly, for the absorption coefficient we obtain

$$K(\omega) = \frac{16\pi^2}{V}\frac{e^2\hbar^2}{\nu m_0^2 cL\omega}$$

$$\times \sum_{n_c, n_\nu} \sum_{l_\nu, m_\nu} \frac{(l_\nu+1)^2 - m_\nu^2}{(2l_\nu+3)(2l_\nu+1)} \delta(\hbar\omega - E_g - E_{n_c, l_c} - E_{n_\nu, l_\nu}) \tag{20}$$

$$\times \left| \frac{1}{2R_1}(1 + l_\nu - \alpha_\nu R_1) f_1(\beta_c, \beta_\nu) + \beta_\nu(\alpha_c + \alpha_\nu) \right.$$

$$\left. \times \left(\frac{L}{2} f_3(\beta_c, \beta_\nu) - f_2(\beta_c, \beta_\nu) - \beta_\nu f_4(\beta_c, \beta_\nu) \right) \right|^2,$$

where ω is the incident light frequency, ν is the refractive index, V is the volume of the system, $\delta(x)$ is the Dirac delta function, and E_g is the energy gap of the bulk semiconductor; the energy is reckoned from the middle of the gap in the bulk.

3. DISCUSSION OF RESULTS

We obtained the following pattern of interband optical transitions within the framework of the proposed model.

1. The radial electric field widens the energy gap, with the absorption edge shifted to the shorter wavelengths by

$$\Delta = \frac{2\gamma}{R_1}\left(1 + \frac{L}{R_1}\right)^{-\frac{1}{2}}.$$

2. The interband absorption has a resonance character with respect to the incident light frequency because of the strict discreteness of the energy spectrum of carriers.

3. Only transitions between orbital states with $l_\nu \longrightarrow l_c = l_\nu + 1$ and equal azimuthal quantum numbers are allowed; a steep decay of the absorption curve is observed with increasing l_ν.

4. The presence of the electric field leads to the absence of a selection rule on the radial quantum number $n_{c,\nu}$; transitions between arbitrary quantum confined states of radial motion are possible during absorption. The presence of the electric field also leads to an explicit dependence of the absorption coefficient on the carrier effective mass (via the parameter $\beta_{c,\nu}$).

5. Analysis of the dominant term $\beta_\nu f_4(\beta_c, \beta_\nu)$ reveals that the absorption coefficient shows an oscillating electric field dependence at the fixed resonance frequency $\omega_{c\nu}$. A slow rise ($\propto(1+x)^{1/2}$ at $x \ll 1$) of the oscillation amplitude envelope function for the "partial" absorption coefficient related to transitions between quantum-well subbands with increasing field is observed. In the limit of zero field (at $R_1 \longrightarrow \infty$), the quantity $\beta_\nu f_4(\beta_c \beta_\nu)$ simply reduces to the factor $n_c m n_\nu / n_c^2 - n_\nu^2$, which is characteristic of absorption in films.

REFERENCES

1. J. W. Haus, H. S. Zhou, I. Honma, and H. Komiyama, Phys. Rev. B **47**, 1359 (1993).
2. D. Schooss, A. Mews, A. Eychuller, and H. Wollex, Phys. Rev. B **49**, 17072 (1994).
3. A. Mews, A. V. Kadavanich, U. Banin, and A. P. Alivisateos, Phys. Rev. B **53**, R13242 (1996).
4. N. V. Tkach, Fiz. Tverd. Tela (St. Petersburg) **39**, 1109 (1997) [Phys. Solid State **39**, 995 (1997)].
5. N. V. Tkach, V. A. Holovatsky, and O. N. Voĭtsekhivska, Fiz. Tekh. Poluprovodn. (St. Petersburg) **34**, 602 (2000) [Semiconductors **34**, 583 (2000)].
6. V. A. Sinyak, Zh. Tekh. Fiz. **65** (1), 195 (1995) [Tech. Phys. **40**, 110 (1995)].
7. E. Cassado and C. Trallero-Giner, Phys. Status Solidi B **196**, 335 (1996).
8. D. Ahn and S. L. Chang, Phys. Rev. B **35**, 4199 (1987).
9. V. A. Arutyunyan, S. L. Arutyunyan, A. A. Dzhivanyan, and G. O. Demirchyan, Izv. Akad. Nauk Arm., Fiz. **30**, 245 (1995).
10. V. A. Arutyunyan, S. L. Arutyunyan, and S. A. Mkrtchyan, Izv. Akad. Nauk Arm., Fiz. **31**, 158 (1996).
11. *Handbook of Mathematical Functions,* Ed. by M. Abramowitz and I. A. Stegun (Dover, New York, 1971; Nauka, Moscow, 1979).
12. B. A. Tavger and V. Ya. Demikhovskiĭ, Usp. Fiz. Nauk **96**, 61 (1968) [Sov. Phys. Usp. **11**, 644 (1969)].
13. L. D. Landau and E. M. Lifshitz, *Course of Theoretical Physics,* Vol. 3: *Quantum Mechanics: Non-Relativistic Theory* (Nauka, Moscow, 1974; Pergamon, New York, 1977).

Translated by S. Ktitorov

Semiconductors, Vol. 36, No. 4, 2002, pp. 382–384. Translated from Fizika i Tekhnika Poluprovodnikov, Vol. 36, No. 4, 2002, pp. 404–406.
Original Russian Text Copyright © 2002 by Andrievskiĭ, Gorelenok, Zagorel’skaya, Kamanin, Shmidt.

Photoelectric *C–V* Profiling of Majority Charge Carriers and Effective Lifetimes of Minority Charge Carriers in Gettered GaAs Wafers

V. F. Andrievskiĭ, A. T. Gorelenok*, N. A. Zagorel’skaya**, A. V. Kamanin*, and N. M. Shmidt***

** Ioffe Physicotechnical Institute, Russian Academy of Sciences,*
Politekhnicheskaya ul. 26, St. Petersburg, 194021 Russia
e-mail: kamanin@ffm.ioffe.rssi.ru
*** Institute of Electronics, Belarussian National Academy of Sciences, Minsk, 220090 Belarus*

Submitted August 21, 2001; accepted for publication August 29, 2001

Abstract—The procedure for photoelectrochemical *C–V* profiling of the concentration of majority charge carriers and effective lifetimes of minority charge carriers in high-resistivity thick (1.6 mm) GaAs wafers subsequently to their gettering is described. Gettering was performed by both one-side and two-side coating of the wafers with a Y film and subsequent thermal treatment at 700 and 800°C. It was demonstrated that the concentration profile N_d–N_a and the effective lifetime for minority charge carriers throughout the wafer are rather uniform in both cases. This procedure makes it possible to measure the charge carrier concentration as low as 10^{12} cm^{-3}. *© 2002 MAIK “Nauka/Interperiodica”.*

INTRODUCTION

Several techniques for the determination of the concentration of majority charge carriers in semiconductors exist, e.g., Hall measurements [1] and *C–V* measurements [2] at the Schottky barrier metal–semiconductor [2] or electrolyte–semiconductor. For concentration profiling, the *C–V* technique in the electrolyte–semiconductor system is more advantageous, since the electrolyte can simultaneously serve as the chemical etchant. Due to this, the process of concentration profiling can be automated [3]. In this case, the profile is recorded simultaneously with continuous etching. In addition, using the irradiation of the electrolyte–semiconductor interface with photons with $h\nu > E_g$ and maintaining a constant photocurrent, it is possible to record the distribution profile of the effective lifetime of minority charge carriers. The lifetime is proportional to the photocurrent across the Schottky barrier. It is noteworthy that the accuracy of determining the concentration profile is higher for the continuous etching relative to the discrete one.

The purpose of this study was to demonstrate the potential of the photoelectrochemical technique for *C–V* profiling of the majority carrier concentration and effective lifetimes of minority carriers. The technique is applied to thick (1.6 mm) high-resistivity GaAs wafers, which were obtained via gettering by one-side and two-side coating with a Y film with subsequent thermal treatment at 700 and 800°C.

EXPERIMENTAL

In this study, undoped GaAs grown by the Czochralski technique [4] using Ga and As of 99.99999% purity grade was used as the starting material for gettering. The electron concentration was $(1–3) \times 10^{15}$ cm^{-3}, and the electron mobility was 1500–2000 cm^2 V^{-1} s^{-1} at 300 K. It was demonstrated that this charge-carrier concentration is determined by the shallow donor level with the activation energy 10–12 meV and deep donor level with the activation energy ~150 meV [5]. In this case, the degree of compensation of 40% was apparently determined by the concentration of intrinsic defects and their complexes. Thick (~1.6 mm) GaAs(111) wafers were used for gettering. The wafers were covered on one or both sides with 1000 Å-thick Y film using the method of vacuum thermal deposition. Then, the wafers were thermally treated in purified hydrogen at 700°C for 0.25 h and at 800°C for 0.5 h. Subsequent to thermal treatment, Y films were removed by plasma etching in a RIBES Rokappa installation.

The electron concentration in wafers subjected to gettering was determined from Hall measurements [1], and the electron distribution in the depth of the wafer was determined by *C–V* profiling using electrochemical [6] or photochemical [7] techniques in the chemical cell (Fig. 1). The cell design allowed for illumination of the electrolyte–insulator interface through the transparent window *2*. The sulfuric acid etchant $H_2SO_4 : H_2O_2 : H_2O$ (1 : 8 : 1) with a constant etching rate (4 μm/min) for several days was used as the polishing electrolyte etchant. The contact area was determined by the seal ring with a diameter of 3 mm. The charge-carrier concentration was determined from expression [6]:

$$N(x) = -\frac{C^3}{e\varepsilon\varepsilon_0 A^2}\left(\frac{\Delta C}{\Delta V}\right)^{-1}. \qquad (1)$$

Here, C is the capacitance of the space charge region (SCR) in GaAs; e is the elementary charge; ε is the permittivity; ε_0 is the permittivity of free space; A is the area of the Schottky contact; and ΔC and ΔV are the increments of capacitance and voltage, respectively.

In the case of irradiation of the interface between the electrolyte and high-resistivity GaAs with photons with $h\nu > E_g$ for GaAs, the photocurrent generated in this system is proportional to the effective hole lifetime [2]. Consequently, with chemical etching of high-resistivity GaAs, the measurement of the photocurrent gives a qualitative distribution of the effective lifetime of minority carriers.

During the measurements of the concentration profile in the depth of the wafer, as the electrolytic contact moves deeper into the wafer, the contact area increases due to the formation of cylindrical lateral regions in the local zone of etching. This zone also contacts the electrolyte and makes a contribution to the measured capacitance. Thus, the measured capacitance consists of two components, namely, the capacitance of the lateral region and the capacitance of the etching bottom. For this reason, when calculating the charge-carrier concentration, we used the capacitance determined by the difference between the measured capacitance of the SCR and the capacitance corresponding to the lateral region [8].

RESULTS AND DISCUSSION

A preliminary investigation of the charge-carrier concentration using the Hg–GaAs Schottky barrier with layer-by-layer etching of GaAs in the etchant $H_2SO_4 : H_2O_2 : H_2O$ (1 : 8 : 50) at an etching rate of 1000 Å/min^{-1} was carried out. It should be noted that the investigation demonstrated that, in the case of thermal treatment of the Y–GaAs structures at 800°C for 0.25 h with subsequent plasma-induced removal of the Y film, the wafer surface is of the *p*-type conduction with $p \simeq 10^{16}$ cm^{-3} to the depth of ~0.5 μm. At the same time, in the case of one-side gettering, the surface unprotected by the Y film also had the *p*-type conduction with $p \simeq 10^{17}$ cm^{-3} after thermal treatment at 800°C for 0.25 h. The depth of the *p*-type layer was several μm, and the inversion of the conduction type occurred at a large depth from both sides, the electron concentration being no higher than ~10^{13} cm^{-3}.

The distribution of the majority-carrier concentration ($N_d - N_a$) and the effective lifetime of minority charge carriers in GaAs subjected to gettering at 800°C for 0.5 h are shown in Figs. 2 and 3, respectively. The distributions are nearly uniform. A slight decrease in $N_d - N_a$ at a depth of more than 600 μm is associated with a large error of the capacitance measurement due to nonuniform etching for various crystallographic directions.

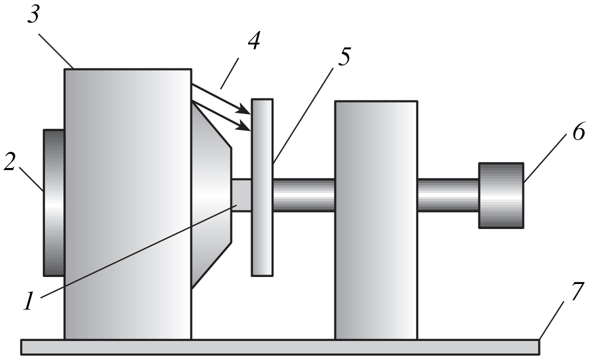

Fig. 1. Photoelectrochemical cell: (*1*) seal ring, (*2*) transparent window for optical excitation, (*3*) reservoir for electrolyte, (*4*) clamping contacts, (*5*) semiconductor wafer, (*6*) clamping device, and (*7*) base.

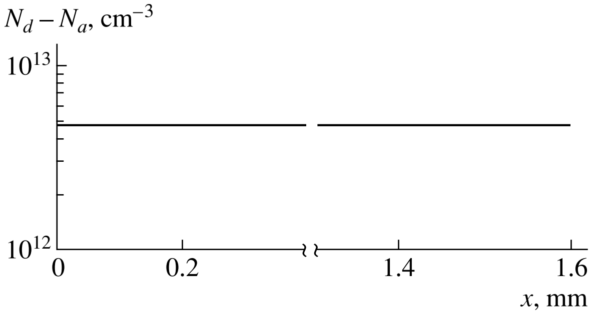

Fig. 2. Distribution profile $N_d - N_a$ subsequent to the one-side gettering at 800°C for 0.5 h.

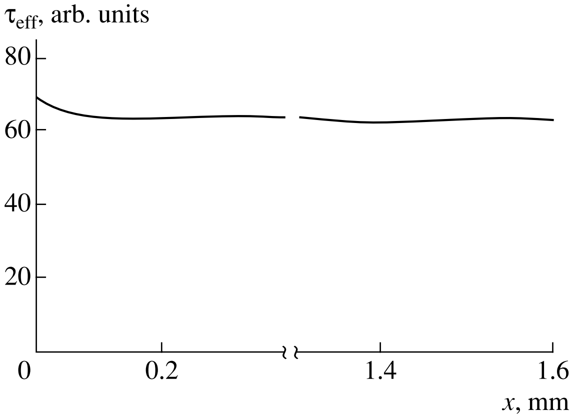

Fig. 3. Distribution profile of the effective lifetime of minority charge carriers subsequent to the one-side gettering at 800°C for 0.5 h.

For both the one-side and two-side gettering subsequent to thermal treatment at 700°C for 0.25 h followed

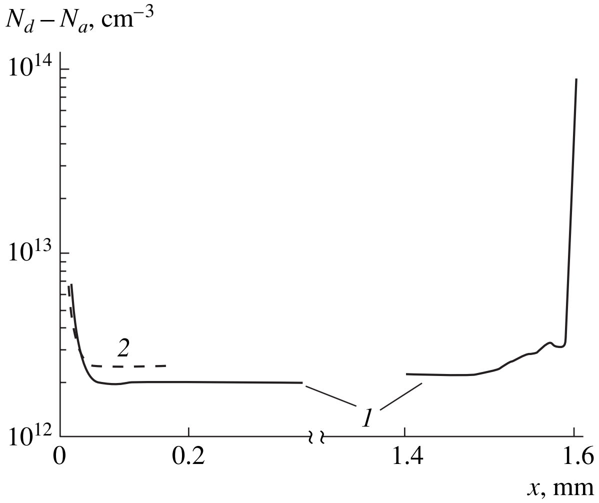

Fig. 4. Distribution profiles $N_d - N_a$ subsequent to the one-side gettering: (*1*) at 800°C for 0.5 h and (*2*) at 700°C for 0.25 h. The depth 1.6 mm corresponds to the second uncoated surface of the wafer.

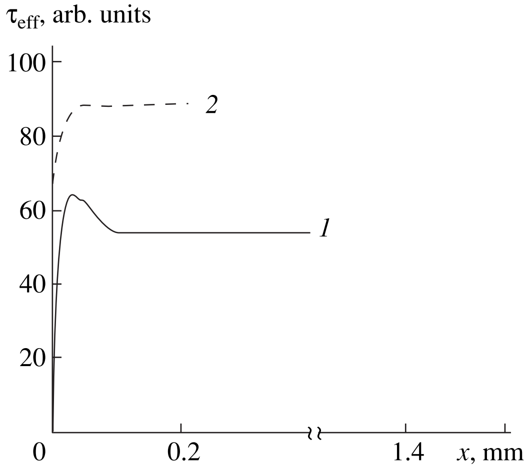

Fig. 5. Distribution profiles of the effective lifetime of minority charge carriers subsequent to the one-side gettering: (*1*) at 800°C for 0.5 h and (*2*) at 700°C for 0.25 h.

by the plasma-induced removal of Y films from both sides, the surface layer had the *n*-type conduction with $n \simeq 10^{13}$–10^{14} cm^{-3}. This layer was several μm thick, whereas at a larger depth the concentration decreased to 10^{12} cm^{-3} and lower depending on the thermal treatment mode (Fig. 4). It can be concluded from Figs. 4 and 5 that gettering has a bulk character even for the wafer coated on one side with the Y film. However, the uncoated surface apparently makes its own contribution to the gettering effect. It can be seen from Fig. 5 that the distribution of τ_{eff} is also uniform over the depth for thermal treatment both at 700 and 800°C, and τ_{eff} for 700°C is 30% larger compared to that for 800°C. The above data on the concentration profile $N_d - N_a$ allow us to assume that antisite defects As_{Ga} and Ga_{As} and, possibly, intrinsic defects of various types, namely, V_{Ga}, V_{As}, I_{Ga}, and I_{As}, are generated during gettering. The spatial separation of antisite defects and the formation of complexes with their participation rather than their direct annihilation apparently plays a major role in the gettering process. As a result, the charge-carrier concentration decreases to 10^8 cm^{-3} [2].

CONCLUSION

It is demonstrated that the surface gettering for the one-side and two-side getter coating has a bulk character and can be accomplished at relatively low temperatures (700°C). At 700°C, τ_{eff} is by 30% larger compared to that obtained after thermal treatment at 800°C. This makes it possible to obtain high-resistivity GaAs wafers with uniform distributions of $N_d - N_a$ and τ_{eff} for minority charge carriers over the depth of a wafer of up to 1.5 mm thick. In this case, the electron mobility in GaAs can be as high as 7000 cm^2 V^{-1} s^{-1} at 300 K [5]. This material holds promise for high-voltage power devices, detectors of X-ray and nuclear radiation and particles, including neutrinos, as well as for ultra-high-speed optoelectronic VLSIs. In this case, the technology of obtaining such material is very simple and involves conventional technology for preparing substrates with the inclusion of only two additional operations, namely, the deposition of a gettering coating and thermal treatment.

ACKNOWLEDGMENTS

We thank M. Mezdrogina for deposition of Y films and Yu. Zadiranov for their plasma-induced removal.

This study was supported by the Russian Foundation for Basic Research, project no. 00–02–17026.

REFERENCES

1. L. J. van der Pauw, Philips Tech. Rev. **20**, 220 (1958/59).
2. S. Sze, *Physics of Semiconductor Devices* (Wiley, New York, 1981; Mir, Moscow, 1984), Vol. 1.
3. T. Ambridge and M. M. Factor, Electron. Lett. **10**, 204 (1974).
4. A. V. Markov, A. Y. Polyakov, N. B. Smirnov, *et al.*, Nucl. Instrum. Methods Phys. Res. A **439**, 651 (2000).
5. N. Shmidt, A. Gorelenok, V. Emtsev, *et al.*, Solid State Phenom. **69–70**, 279 (1999).
6. J. Reichman, Appl. Phys. Lett. **36**, 574 (1980).
7. V. F. Andrievskiĭ, *Theory, Methods, and Instrumentation for Measurements and Control of Parameters of Magnetic Materials, Semiconductors, and Insulators* (Novocherkassk, 2000), Part 4, p. 24.
8. V. F. Andrievskiĭ, E. V. Yakimenko, and O. K. Muravitskiĭ, USSR Inventor's Certificate No. 1611075, G 01 NL 27/22 (1989), Byull. Izobret. (1990).

Translated by N. Korovin

Semiconductors, Vol. 36, No. 4, 2002, pp. 385–389. Translated from Fizika i Tekhnika Poluprovodnikov, Vol. 36, No. 4, 2002, pp. 407–411.
Original Russian Text Copyright © 2002 by Bogdanova, Davletkil'deev, Semikolenova, Sidorov.

ELECTRONIC AND OPTICAL PROPERTIES OF SEMICONDUCTORS

Effective Electron Mass in Heavily Doped GaAs in the Ordering of Impurity Complexes

V. A. Bogdanova, N. A. Davletkil'deev*, N. A. Semikolenova, and E. N. Sidorov
Institute of Sensor Microelectronics, Siberian Division, Russian Academy of Sciences, Omsk, 644077 Russia
** e-mail: davlet@univer.omsk.su*

Submitted July 9, 2001; accepted for publication September 27, 2001

Abstract—Spectra of edge photoluminescence (PL) at 300 K have been studied in a set of Czochralski-grown Te-doped GaAs single crystals with a free carrier density of $n_0 = 10^{17}$–10^{19} cm^{-3}. The carrier density dependences of the chemical potential and band gap narrowing are obtained by analyzing the PL spectral line profiles. The dependence of the effective mass of electrons at the bottom of the conduction band on their density, $m_0^*(n_0)$, is calculated. It is shown that the nonmonotonic $m_0^*(n_0)$ dependence correlates with data on electron scattering in the material under study and results from the ordering of impurity complexes. © *2002 MAIK "Nauka/Interperiodica".*

1. INTRODUCTION

Semiconductor properties are strongly affected by complexes comprising atoms of the main substance, dopant atoms, and intrinsic structural point defects. Association of these complexes at their critical concentrations gives rise to fundamentally new effects. Systematic studies of the doping of III–V compounds with Group VI elements revealed nonmonotonic dependences of a number of parameters on impurity concentration in the range of heavy doping ($10^{18} < N_{\text{imp}} < 10^{19}$ cm^{-3}) [1–4]. The appearance of singularities in concentration dependences of electrical and optical parameters at some critical concentration indicates crossing of phase boundaries. It is assumed that the Coulomb and elastic interactions lead to ordering of the impurity subsystem with the formation of a superstructure with long-range order. The formation of a long-period superstructure in GaAs:Te single crystals at free carrier densities $n_0 = (3–4) \times 10^{18}$ cm^{-3} has been confirmed by direct experiments [4, 5].

The ordering of the impurity subsystem must modify the electronic spectrum. A conventional method for studying the effect of heavy doping on the electronic structure of a material is analysis of the edge photoluminescence (PL) spectrum. In heavily doped semiconductors, the electron–electron and electron–impurity interactions strongly distort the parabolic dispersion law of an ideal Fermi gas in a pure semiconductor. This distortion is interpreted as a steady "rigid" shift of the conduction band toward the valence band (band gap narrowing) and as a distortion of the density of states. In addition, the random distribution of impurities results in the formation of density-of-state tails. Commonly, analysis of the edge PL line shape yields dependences of the band gap narrowing, associated with many-particle effects, and the rms fluctuation of the impurity potential, characterizing the effect of band-tail formation, on the doping level [6–14]. In [15], the effective mass at the conduction band bottom, m_0^*, was determined by analyzing the edge PL spectrum. The observed increase in m_0^* with growing electron density was attributed by the authors to the distortion of the dispersion law at the center of the Brillouin zone by the electron–impurity interaction.

This paper presents the results of an analysis of edge PL spectra and the obtained dependence of the effective mass at the conduction band bottom on the doping level of GaAs:Te single crystals.

2. EXPERIMENTAL PROCEDURE AND DATA ANALYSIS

Czochralski-grown GaAs:Te single crystals with a free carrier density $n_0 = 10^{17}$–10^{18} cm^{-3} found from Hall-effect measurements were studied. The PL was excited with a He–Ne laser at an excitation intensity of $L = 5 \times 10^{19}$ quanta cm^{-2} s^{-1}. Edge PL spectra obtained at room temperature for different doping levels were analyzed.

The spectrum of edge emission from heavily doped semiconductors consists of a broad structureless band commonly attributed to the band-to-band recombination. The low-energy wing of this band is related to band gap narrowing and the formation of a density-of-states tail; the high-energy wing reflects the band filling with majority carriers and gives information on the position of the chemical potential. In analysis of n^+-GaAs PL spectra, it is commonly assumed that, first, the matrix element of transition is independent of quasi-momentum, and, second, the quasi-momentum

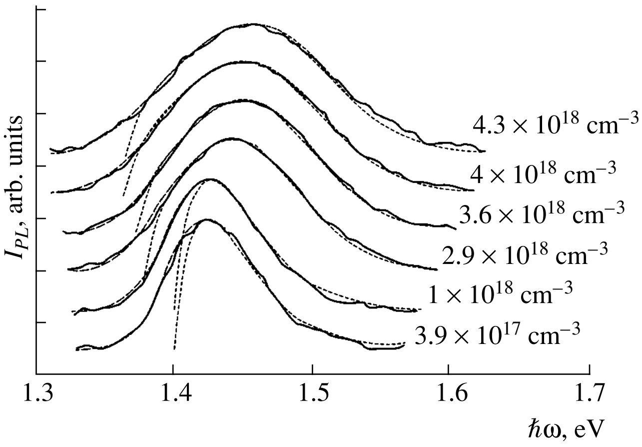

Fig. 1. PL spectra of GaAs:Te single crystals at $T = 300$ K. Solid lines, experiment; short-dash lines, fitting with account of the conduction band nonparabolicity; long-dash lines, fitting with account of both the nonparabolicity and the statistical effect. Electron density in GaAs samples is shown in the figure.

selection rule is completely lifted by the electron–electron and electron–impurity scattering. The latter circumstance results in that all occupied states in the conduction band may be involved in radiative transitions to empty states of the valence band. Therefore, if the details of the hole distribution in the valence band are disregarded, the spectrum shape can be directly related to the density of states in the conduction band, $\rho(E)$ [16]:

$$I(\hbar\omega) \propto \rho(E) f(E). \qquad (1)$$

The Fermi–Dirac distribution $f(E)$ is used as the distribution function, since the energy relaxation time for electrons is much shorter than their recombination time:

$$f(E) = \left[1 + \exp\left(\frac{E-\mu}{kT}\right)\right]^{-1}. \qquad (2)$$

Here, the chemical potential μ is reckoned from the conduction band edge. Presently, there is no simple analytical expression for $\rho(E)$ that can account for the many-particle and statistical effects, along with the electron–impurity interaction, in terms of a unified model and that can be used in the fitting of PL spectra. The density-of-states tail defined by a random distribution of impurities is described using Kane's expression:

$$\rho(E) \sim \int_{-\infty}^{E} \rho_0(E-z)\exp\left(-\frac{z^2}{\gamma^2}\right)dz, \qquad (3)$$

where the electron energy E is reckoned from the band edge, and γ is the rms fluctuation of the impurity potential. The unperturbed density of states, ρ_0, can be calculated in a simple way for a nonparabolic band in terms of the standard $\mathbf{k} \cdot \mathbf{p}$ theory:

$$\rho_0(E) = \frac{1}{2\pi^2}\left(\frac{2m_0^*}{\hbar^2}\right)^{3/2}\left(E^{1/2} + \frac{5\beta}{2E_g^0}E^{3/2}\right), \qquad (4)$$

where E_g^0 is the band gap of the undoped material, and β is the nonparabolicity parameter.

In the present study, the spectra were fitted using relations (1)–(4), in which, in terms of the "rigid" shift of bands,

$$E = \hbar\omega - \hbar\omega_{\min}, \quad \hbar\omega_{\min} = E_g - \Delta E_g,$$

where ΔE_g is the band gap narrowing. The μ, ΔE_g, γ, and β values were determined by means of spectrum fitting. It is noteworthy that Eq. (1) yields μ without using m_0^* and n_0, because these latter do not define the PL line shape. The m_0^* value was determined using the obtained μ and the relation

$$n_0 = \int_0^{\infty} \rho(E) f(E) dE. \qquad (5)$$

3. RESULTS AND DISCUSSION

Figure 1 shows the experimental spectra of several GaAs:Te samples, illustrating the evolution of the spectra with electron density in accordance with the Burstein–Moss effect, and also the theoretical PL spectra calculated using relations (1)–(4). Figure 2 presents the fitting parameter ΔE_g for the samples studied (ΔE_g calculated with E_g^0 taken to be 1.424 eV [17]) and the theoretical dependence of the band gap narrowing on carrier density, associated with many-particle effects (i.e. the sum of exchange and correlation energies E_{xc}) for $T = 0$ K [18]. In the "rigid" band shift approximation, the dependence $\Delta E_g(n_0)$ must correlate well with $E_{xc}(n_0)$, which is observed in analysis of the PL spectra of n^+-GaAs [15]. Such an agreement takes place in our samples in the free carrier density range $n_0 < 2 \times 10^{18}$ cm^{-3}. At $n_0 > 2 \times 10^{18}$ cm^{-3}, ΔE_g values are not described by the $E_{xc}(n_0)$ dependence, which indicates the presence of additional contributions to the "rigid" band shift. Some authors [19–21] use the "non-rigid" band shift approximation; however, the result of analysis depends on the selected theoretical approach. As regards the experimental aspect of this approximation, there is no unambiguous answer to the question as to what is the origin of the part of the spectrum with $\hbar\omega < E_g$. Application of relation (3) assumes that this part of the spectrum is related to the density-of-states tail caused by the statistical effect. However, as stated in [22], the band tails observed in the PL spectra of heavily doped semiconductors differ fundamentally from the exponential band tails associated with a random distribution of impurities. The reason for this is the uncertainty in transition energy stemming from electron–electron and electron–impurity interactions. Therefore, one should be careful in interpreting the dependence of the fitting parameter, $\gamma(n_0)$, presented for our samples in Fig. 3. In the material under study, γ weakly depends on the free carrier density. Figure 3 also shows a theoretical dependence of the rms fluctuation of the impurity potential [23].

The interpretation of the high-energy part of the PL spectrum, which reflects the conduction band filling, is more unambiguous. Figure 4 presents the chemical potential obtained by fitting for the samples under study and also the theoretical dependences of chemical potential for the standard ($\mu_0(n_0)$) and nonstandard band ($\mu(n_0)$), calculated for $m_0^* = 0.063m_e$ using the relations

$$n_0 = N_c F_{1/2}\left(\frac{\mu_0}{kT}\right); \quad \mu = \mu_0\left(1 - \beta\frac{\mu_0}{E_g^0}\right), \tag{6}$$

where N_c is the effective density of states in the conduction band, and $F_{1/2}$ is the Fermi–Dirac integral.

The filling of states in the conduction band tail can also lower the chemical potential. However, the position of the chemical potential in heavily doped uncompensated semiconductors is close to that observed for an ideal degenerate gas of carriers with $n_0 = N_{\text{imp}}$ [24]. The correction for the filling of the fluctuation states can be evaluated using the relation [23]

$$\Delta\mu = \frac{1}{8}\frac{\gamma^2}{\mu}. \tag{7}$$

In the case in question, $\Delta\mu \approx 0.004$ eV in the range $n_0 = 8 \times 10^{17}$–10^{19} cm^{-3}. Figure 4 shows the chemical potential obtained by fitting with only relation (4) used to calculate $\rho(E)$. As seen, the position of the chemical potential is hardly modified by the statistical effect, and, therefore, it was ignored in the calculation of m_0^*.

Figure 5 presents the dependence of the effective mass at the conduction band bottom, m_0^*, on the free carrier density for the samples studied. Near the conduction band bottom, the kinetic energy of electrons is low, so the electron–electron and electron–impurity interactions become the key factor. As shown in [25], the effective mass slightly decreases with doping because of the exchange interaction; it was noted, however, that this result is valid only for the electron energies near the Fermi level. On the other hand, the calculation of the impurity pseudopotential taking the contribution from the central cell [26] into account demonstrated that the electron–impurity scattering leads to a linear increase in m_0^* at $N_{\text{imp}} < 10^{20}$ cm^{-3}. The rise in m_0^* with increasing doping level was observed in n^+-GaAs in [15]. Based on the performed analysis, the authors concluded that the increase in m_0^* results from the distortion of the conduction band bottom, caused by the electron–impurity interaction. It should be emphasized that the empirical dependence $m_0^*(n_0)$ from [15] (Fig. 5, curve *2*) stems from the electron interaction with isolated impurity ions (epitaxial MOCVD-grown GaAs:Se films were studied, with the metal-organic phase characterized by a superlinear relation between n_0 and the mole fraction of H$_2$Se, which indicates the absence of complexation).

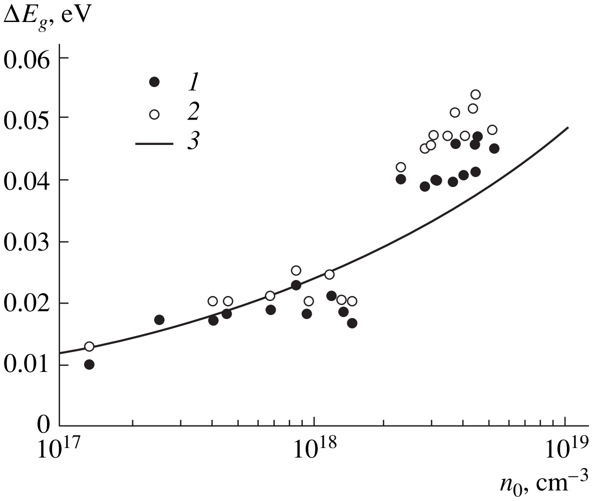

Fig. 2. Band gap narrowing vs. electron density in GaAs:Te single crystals at $T = 300$ K: (*1*) fitting with account of the conduction band nonparabolicity, (*2*) fitting with account of both the nonparabolicity and the statistical effect, and (*3*) theoretical dependence for ΔE_g due to many-particle phenomena [18].

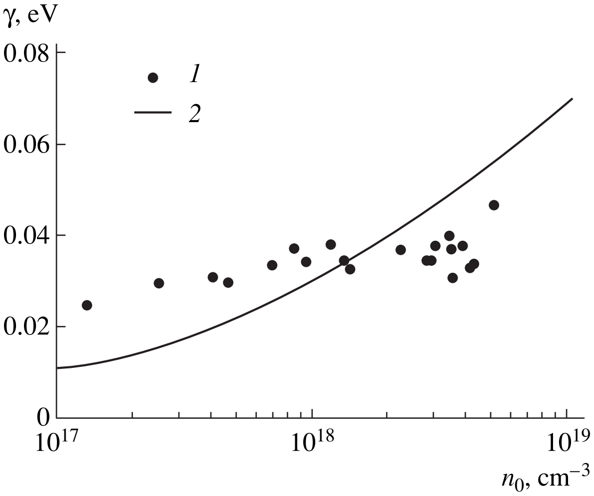

Fig. 3. Rms fluctuation of the impurity potential vs. free carrier density in GaAs:Te single crystals at $T = 300$ K: (*1*) fitting and (*2*) theory [23].

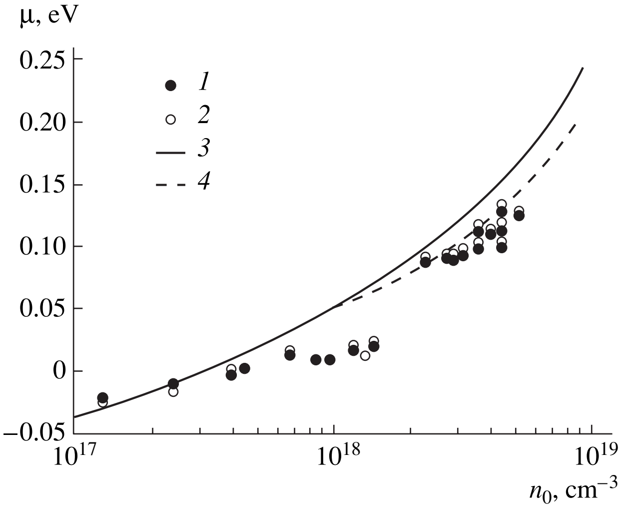

Fig. 4. Chemical potential vs. free carrier density in GaAs:Te single crystals at T = 300 K: (*1*) fitting with account of the conduction band nonparabolicity, (*2*) fitting with account of both the nonparabolicity and the statistical effect, (*3*) theoretical values for a standard conduction band, and (*4*) theoretical values for a nonparabolic conduction band.

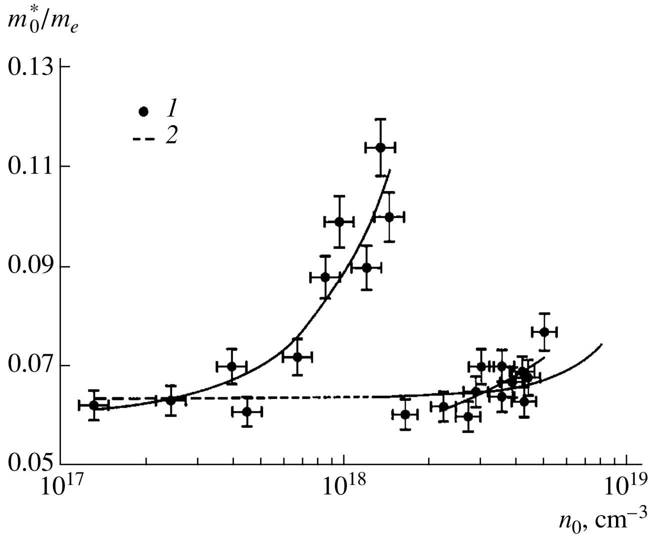

Fig. 5. Effective electron mass at the conduction band bottom vs. free carrier density in n^+-GaAs at T = 300 K: (*1*) GaAs:Te, data of the present study, and (*2*) GaAs:Se, data of [15].

The nonmonotonic dependence $m_0^*(n_0)$ obtained in the present study correlates with the data on electron scattering in the material studied. The analysis of the IR absorption by free carriers has shown that the dominant mechanism of free carrier scattering on local heterogeneities of a crystal changes abruptly at $n_0 > 2 \times 10^{18}$ cm^{-3} [27]. The dependence of the free carrier absorption coefficient on wavelength is commonly approximated by the power law $\alpha \propto \lambda^n$, with the spectral parameter n characterizing the mechanism of carrier scattering in a crystal. Fair agreement between the experimental and calculated $n(n_0)$ dependences was observed for samples with $n_0 < 5 \times 10^{17}$ cm^{-3}, which indicates that scattering by the polar optical mode of lattice vibrations is the dominant mechanism. In the range 5×10^{17} cm^{-3} $< n_0 <$ 1.5×10^{18} cm^{-3}, the experimental $n(n_0)$ values are higher than those calculated, which indicates the appearance of additional sources of scattering, i.e., complexes comprising impurity ions and intrinsic point defects. At $n_0 > 2 \times 10^{18}$ cm^{-3}, the calculated $n(n_0)$ exceed the experimental values, which points to suppression of scattering on impurity defects and an increasing contribution of scattering on defects with a weaker spectral dependence of the absorption coefficient. At $n_0 > 2 \times 10^{18}$ cm^{-3}, the Coulomb and elastic interactions between the complexes lead to their ordering and the formation of a periodic superstructure. This process reduces the contribution of scattering on ionized impurity atoms. In the range of ordering, the scattering on phonons becomes dominant again. This concept is consistent with the carrier density dependence of the average electron momentum relaxation time, obtained by analysis of reflection in the IR spectral range [28].

The $m_0^*(n_0)$ dependence obtained for our samples is also related to the redistribution of complexes: in the range 5×10^{17} cm^{-3} $< n_0 < 1.5 \times 10^{18}$ cm^{-3}, impurity complexes make a significant contribution to the free electron scattering, thus strongly distorting the dispersion law; in the range of complex ordering, the effectiveness of scattering on complexes and the distortion of the dispersion law decrease.

4. CONCLUSION

The edge PL spectra have been studied for a set of Czochralski-grown Te-doped GaAs single crystals with free carrier density $n_0 = 10^{17}$–10^{19} cm^{-3}. Dependences of the chemical potential and the band gap narrowing on the electron density were obtained by analysis of the PL spectra. The density dependence of the effective electron mass at the conduction band bottom, $m_0^*(n_0)$, was calculated. It is shown that the nonmonotonic $m_0^*(n_0)$ dependence correlates with the data on the electron scattering and is caused, in the range 5×10^{17} cm^{-3} $< n_0 <$ 1.5×10^{18} cm^{-3}, by substantial electron scattering by impurity complexes, which strongly distort the dispersion law; in the range of complex ordering, both the effectiveness of scattering on complexes and the distortion of the dispersion law decrease.

REFERENCES

1. N. M. Bogatov, A. L. Petrov, and É. N. Khabarov, Fiz. Tekh. Poluprovodn. (Leningrad) **16**, 353 (1982) [Sov. Phys. Semicond. **16**, 222 (1982)].
2. V. A. Bogdanova and N. A. Semikolenova, Fiz. Tekh. Poluprovodn. (St. Petersburg) **26**, 818 (1992) [Sov. Phys. Semicond. **26**, 460 (1992)].
3. V. V. Prudnikov, I. A. Prudnikova, and N. A. Semikolenova, Phys. Status Solidi B **181**, 87 (1994).
4. V. A. Bogdanova, N. A. Semikolenova, and A. S. Semikolenov, Phys. Status Solidi A **120**, K121 (1990).
5. V. A. Bogdanova, V. I. Dubovik, V. V. Prudnikov, and N. A. Semikolenova, in *Extended Abstracts of the International Conference on Solid State Devices and Materials, Osaka, Japan, 1995*, p. 1057.
6. H. C. Casey, Jr. and F. Stern, J. Appl. Phys. **47**, 631 (1976).
7. D. Olego and M. Cardona, Phys. Rev. B **22**, 886 (1980).
8. J. De-Sheng, Y. Machita, K. Ploog, and H. J. Queisser, J. Appl. Phys. **53**, 999 (1982).
9. G. Borhgs, K. Bhattacharyya, K. Deneffe, *et al.*, J. Appl. Phys. **66**, 4381 (1989).
10. T. Lideiskis and G. Treideris, Semicond. Sci. Technol. **4**, 938 (1989).
11. S. I. Kim, M. S. Kim, S. K. Min, and C. Lee, J. Appl. Phys. **74**, 6128 (1993).
12. N.-Y. Lee, K. Y. Lee, C. Lee, *et al.*, J. Appl. Phys. **78**, 3367 (1995).
13. G. C. Jiang, Y. Chang, L.-B. Chang, *et al.*, Jpn. J. Appl. Phys. **34**, 42 (1995).
14. V. A. Vil’kotskiĭ, D. S. Domanevskiĭ, S. V. Zhokhovets, and M. V. Prokopenya, Fiz. Tekh. Poluprovodn. (Leningrad) **18**, 2193 (1984) [Sov. Phys. Semicond. **18**, 1368 (1984)].
15. D. M. Szmyd, P. Porro, A. Majerfeld, and S. Lagomarsino, J. Appl. Phys. **68**, 2367 (1990).
16. H. B. Bebb and E. W. Williams, in *Semiconductors and Semimetals* (Academic, New York, 1972), p. 276.
17. M. E. Levinshtein, S. L. Rumyantsev, and M. Shur, in *Handbook Series on Semiconductor Parameters* (World Scientific, London, 1996), Vol. 1, p. 79.
18. S. C. Jain and D. J. Roulston, Solid-State Electron. **34**, 453 (1991).
19. R. A. Abram, G. N. Childs, and P. A. Saunderson, J. Phys. C **17**, 6105 (1984).
20. B. E. Sernelius, Phys. Rev. B **33**, 8582 (1986).
21. H. S. Bennett, J. Appl. Phys. **60**, 2866 (1986).
22. P. Van Mieghem, Rev. Mod. Phys. **64**, 755 (1992).
23. B. I. Shklovskiĭ and A. L. Efros, *Electronic Properties of Doped Semiconductors* (Nauka, Moscow, 1979; Springer-Verlag, New York, 1984).
24. V. L. Bonch-Bruevich and S. G. Kalashnikov, *Physics of Semiconductors* (Nauka, Moscow, 1977).
25. P. A. Wolff, Phys. Rev. **126**, 405 (1962).
26. A. Glodeanu, Rev. Roum. Phys. **26**, 945 (1981).
27. E. A. Balagurova, Yu. B. Grekov, A. F. Kravchenko, *et al.*, Fiz. Tekh. Poluprovodn. (Leningrad) **19**, 1566 (1985) [Sov. Phys. Semicond. **19**, 963 (1985)].
28. N. A. Semikolenova, Fiz. Tekh. Poluprovodn. (Leningrad) **22**, 137 (1988) [Sov. Phys. Semicond. **22**, 84 (1988)].

Translated by D. Mashovets

Semiconductors, Vol. 36, No. 4, 2002, pp. 390–393. Translated from Fizika i Tekhnika Poluprovodnikov, Vol. 36, No. 4, 2002, pp. 412–415.

ELECTRONIC AND OPTICAL PROPERTIES OF SEMICONDUCTORS

Determination of the Matrix Element of the Quasi-Momentum Operator in the Zero-Gap Semiconductor HgSe by the Field-Effect Method in Electrolyte

O. Yu. Shevchenko*, V. F. Radantsev, A. M. Yafyasov*, V. B. Bozhevol'nov*, I. M. Ivankiv*, and A. D. Perepelkin***

** Institute of Physics, St. Petersburg State University, ul. Ul'yanovskaya 1, Petrodvorets, 199164 Russia*

e-mail: yafyasov@desse.phys.spbu.ru

*** Ural State University, pr. Lenina 51, Yekaterinburg, 620083 Russia*

Submitted May 30, 2001; accepted for publication September 27, 2001

Abstract—The field-effect method in electrolyte was used to study the zero-gap semiconductor HgSe–electrolyte (saturated solution of KCl) system by measuring the capacitance–voltage and current–voltage characteristics. A technique for the estimation of the matrix element P of the quasi-momentum operator from capacitance–voltage characteristics was proposed, and the value of P for HgSe was determined at T = 295 K. *© 2002 MAIK "Nauka/Interperiodica".*

Interest in interfaces in the systems of narrow- and zero-gap semiconductors based on binary and ternary mercury telluride and selenide compounds is stimulated by the use of these materials in infrared devices in the range of the atmospheric window [1] and in quantum interference structures for nanoelectronics [2]. Progress in these fields significantly depends on the technology for production of the surface and heterostructures with a low density of surface states and reproducible electrical parameters of the surface and subsurface layer. We note that compounds based on mercury telluride have been studied in sufficient detail; compounds based on mercury selenides call for further investigation. The fact that there are only a few papers dedicated to HgSe surface properties is explained by methodical difficulties in forming stable insulating and passivating coatings at the material surface. This, in turn, does not allow the efficient application of sophisticated conventional methods based on the analysis of MIS structures or Schottky barriers to study the electrical properties of the material surface.

Moreover, the papers dedicated to the bulk HgSe band parameters (as a rule, such data involve low-temperature measurements) do not offer a unified concept of these parameters (we recall the recent discussion about the HgSe band structure [3–5]). For example, the effective electron mass is $m_e^* = 0.05m_0$ at $T = 300$ K at the Kane band gap $E_g = -0.2$ eV [6]; $m_e^* = (0.015–0.019)m_0$ and $E_g = -0.2$ eV [7]; $m_e^* = 0.019m_0$ at T = 95 K and $E_g = -0.22$ eV at T = 300 K [8]; and $m_e^* = 0.019m_0$ and $E_g = -0.22$ eV at T = 300 K [9]. According to [10], the parameters for the $HgS_xSe_{(1-x)}$ ternary compound at T = 300 K are $E_g = -0.18$ eV, $m_e^* = 0.007m_0(x = 0.05)$ and $E_g = -0.2$ eV, $m_e^* = 0.008m_0(x = 0.1)$. According to [11], the matrix element of the quasi-momentum operator for HgSe is $P = 7.5 \times 10^{-8}$ eV cm.

In this study, we measured and analyzed the electrical properties of the HgSe surface and subsurface regions (the volume density of electrons in a studied sample was determined from the Shubnikov–de Haas oscillation as $n = N_A - N_D = 4.1 \times 10^{17}$ cm^{-3}) using the field-effect method in electrolyte. This technique, applied earlier to many semiconductors [12], including binary and ternary compounds based on mercury tellurides [13, 14], has shown itself as an efficient method for analyzing and producing ultrathin insulating coatings. This technique makes it possible to study the semiconductor surface in a wide range of surface potentials, including the region of band bendings corresponding to electron and hole degeneracy at the surface. This method can also yield information on many semiconductor band parameters at room temperature [15], which is often impossible with conventional techniques. The method is simple and does not require the preparation of MIS structures and/or the use of low-temperature measurements, which makes it rather promising as applied to the nondestructive rapid determination of the semiconductor surface and subsurface layer parameters.

The electrical and band parameters of the HgSe space charge region (SCR) were determined by capacitance–voltage (C–V) characteristics in the system of HgSe and a saturated aqueous solution of KCl. Simultaneously with *C*–*V* characteristics, current–voltage (*I*–*V*) characteristics were measured to control currents through the semiconductor–electrolyte interface. All the measurements were carried out in a constant-temperature (at $T = 295$ K) electrochemical cell. The HgSe sample surface was polished with diamond paste and then chemicomechanically polished in an 8% bromine solution in methanol. Immediately before measurements, the surface was etched in a 2–8% bromine solution in methanol. The differential capacitance was measured using a rectangular pulsed signal with the test pulse duration $\tau = 1$ μs at a cyclic sweep of the electrode potential φ at the rate of 10–30 mV s^{-1} according to the technique outlined in [16]. The electrode potential was measured in reference to a carbon–graphite electrode.

All the *C*–*V* measurements were carried out in the electrode potential range, for which

(i) the current through the interface was negligible; i.e., there was no significant contribution of the current component caused by electrochemical reactions proceeding when the semiconductor–electrolyte interface was polarized due to the field effect;

(ii) the *C*–*V* characteristics remained unchanged during the multiple cyclic variation of the electrode potential (for a few hours);

(iii) the HgSe–electrolyte interface had no surface states recharged within relaxation times $\tau \geq 10^{-5}$ s;

(iv) no capacitance saturation was observed, which would indicate formation of a surface oxide with a thickness comparable to the Debye screening radius in HgSe. If such a layer exists at the semiconductor surface, its thickness is comparable to the Helmholtz layer thickness (i.e., thinner than 0.2–0.4 nm [12]) and certainly thinner than the SCR width. If these conditions are met, the total change of the electrode potential when sweeping the voltage over the cell falls within the HgSe SCR ($|\Delta\varphi| = |\Delta V_s|$, where V_s is the surface potential), and the measured capacitance is the differential capacitance of the semiconductor SCR.

One can see from the figure that the experimental *C*–*V* characteristic is linearized in the range of sufficiently high negative electrode potentials (electron portion of the characteristic). It can be readily shown that exactly such a dependence of the specific capacitance of the semiconductor SCR should be observed for Kane semiconductors in the region of band bendings exceeding the Kane band gap E_g. The slope of the *C*–*V* characteristic is directly defined by the matrix element *P* of the quasi-momentum operator. Indeed, for pronounced band bendings, the dispersion law in the two-band approximation

$$E = \sqrt{2P^2k^2/3 + E_g^2/4} - E_g/2$$

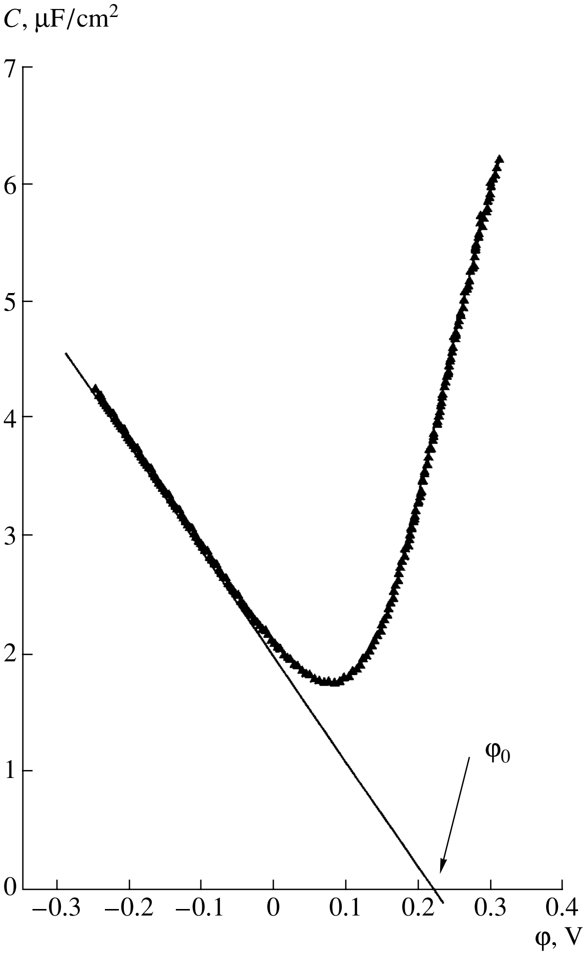

Experimental capacitance–voltage characteristic of the system consisting of HgSe and saturated solution of KCL.

is reasonably adequate for narrow- and zero-gap semiconductors and is close to linear for most of the enriched-layer electrons involved in screening, i.e., $E \approx \sqrt{2/3}\,Pk - |E_g/2|$ [17]. Hence, the density of states

$$D(E) = \frac{2}{(2\pi)^3}\int_S \frac{dS}{\nabla_k E}$$

in the conduction band takes the form

$$D(E) = (3/2)^{3/2}\frac{(E + |E_g/2|)^2}{\pi^2 P^3}.$$

The latter expression includes only the first-order terms in the series expansion in the parameter $E_g/2E$; *dS* is the isoenergetic surface element in the quasi-wave vector space. Since the conditions of pronounced degeneracy $\mu_s \geq \mu \geq \mu_b \gg kT$ ($\mu_s = eV_s + \mu_b$, μ, and μ_b are, respectively, the Fermi energies at the surface, in the SCR, and in the bulk of the semiconductor) are met in almost the entire enriched layer of the considered material, the local carrier concentration is given by

$$n(\mu) = \int_0^{\mu} D(E)dE = (3/8)^{1/2}\frac{(\mu + |E_g/2|)^3}{\pi^2 P^3}.$$

Within this approximation, which is adequate in a wide range of experimental conditions, the SCR differential capacitance is written as

$$C = \frac{dQ_s}{dV_s},$$

where the surface charge density in the SCR

$$Q_s = \varepsilon_0\varepsilon_{sc}\frac{dV}{dz}\bigg|_{V = V_s} = \frac{\varepsilon_0\varepsilon_{sc}}{e}\frac{d\mu}{dz}\bigg|_{\mu = \mu_s}$$

(ε_{sc} is the static dielectric constant of the semiconductor) is defined by the first integral of the Poisson equation,

$$\frac{d\mu}{dz}\bigg|_{\mu = \mu_s} = \sqrt{\frac{2e^2}{\varepsilon_0\varepsilon_{sc}}}\left[\int_{\mu_b}^{\mu_s} n(\mu)d\mu\right]^{1/2}.$$

Elementary calculations then yield the following formula for C:

$$C = \beta\frac{(eV_s + \mu_b + |E_g/2|)^3}{\sqrt{(eV_s + \mu_b + |E_g/2|)^4 - (\mu_b + |E_g/2|)^4}}.$$

Here,

$$\beta = \sqrt{\frac{e^2\varepsilon_0\varepsilon_{sc}}{(2/3)^{1/2}\pi^2 P^3}}.$$

Expanding the above expression for the capacitance in series in the small parameter $(\mu_b + |E_g/2|)/eV_s$, we arrive at the simple expression

$$C \approx \beta(eV_s + \mu_b + |E_g/2|)\left[1 + \frac{1}{2}\left(\frac{\mu_b + |E_g/2|}{eV_s}\right)^3\right].$$

Since the correction, related to a deviation from the quasi-ultrarelativistic limit $E_g = 0$, $\mu_b = 0$ [17], arises only in the third order with respect to $(\mu_b + |E_g/2|)/eV_s$, the contribution of the second term in parentheses is insignificant even at relatively small band bendings and decreases rapidly as V_s increases and we arrive at the sought-for linear dependence

$$C \approx \beta(eV_s + \mu_b + |E_g/2|).$$

The derivative dC/dV_s, measured in the linear electron portion of the C–V characteristic, is defined by only two material parameters, i.e., the matrix element P of the quasi-momentum operator and the dielectric constant. This is ultimately a direct consequence of the ultrarelativistic character of electron motion in the enriched layer, whose dispersion $E \approx \sqrt{2/3}Pk$ is described by the single parameter P. Using the experimental value $dC/d\varphi = dC/dV_s$ for the electron portion of the C–V characteristic (see figure) and the dielectric constant $\varepsilon_{sc} = 25.6$ from [6], we find that the matrix element of the quasi-momentum operator is $P = 8.2 \times 10^{-8}$ eV cm for HgSe. This value conforms well to the data of [11] for HgSe at low temperatures and is close to P in HgTe.

On the assumption that the zero electrode potential corresponds to the condition of flat bands, $\varphi_{fb} = V_s = 0$, the cutoff potential $\varphi|_{C = 0} = 0.220$ V, found by extrapolation of the linear portion of the C–V characteristic to $C = 0$, can be used to estimate $\mu_b + |E_g/2|$. If we use the Kane band gap $E_g = -0.220$ eV [8, 9], the Fermi energy in the bulk is $\mu_b \approx 0.110$ eV, which conforms well to the value $\mu_b = 0.095$ eV, determined from the electroneutrality equation with the above values of P, E_g, and $N_D - N_A$.

ACKNOWLEDGMENTS

This study was supported by the Ministry of Education of the Russian Federation, project no. E00-3.4-278, and the Federal Program "Russian Universities—Basic Research", project no. 99-27-32.

REFERENCES

1. P. Tribolet, J. P. Chatard, P. Costa, and A. Manissadjian, J. Cryst. Growth **184–185**, 1262 (1998).
2. G. Nimtz, J. X. Huang, J. Lange, *et al.*, Semicond. Sci. Technol. **6**, C130 (1991).
3. K.-U. Gawlik, L. Kipp, M. Skibowski, *et al.*, Phys. Rev. Lett. **78**, 3165 (1997).
4. M. von Truchsess, A. Pfeuffer-Jeschke, C. R. Becker, *et al.*, Phys. Rev. B **61**, 1666 (2000).
5. D. Eich, D. Huebner, R. Fink, *et al.*, Phys. Rev. B **61**, 12666 (2000).
6. *Tables of Physical Quantities: A Handbook*, Ed. by I. K. Kikoin (Énergoizdat, Moscow, 1991).
7. P. I. Baranskiĭ, V. P. Klochkov, and I. V. Potykevich, *Semiconductor Electronics. Properties of Materials. A Handbook* (Naukova Dumka, Kiev, 1975).
8. I. M. Tsidil'kovskiĭ, *Energy-Band Structure of Semiconductors* (Nauka, Moscow, 1978).
9. V. M. Askerov, *Electronic Transport Phenomena in Semiconductors* (Nauka, Moscow, 1985).
10. I. I. Berchenko, V. E. Krevs, and V. G. Sredin, *Semiconductor Solid Solutions and Their Applications. Reference Tables* (Voenizdat, Moscow, 1982).

11. I. Stolpe, O. Portugall, N. Puhlmann, *et al.*, Physica B (Amsterdam) **294–295**, 459 (2001).
12. V. A. Myamlin and Yu. V. Pleskov, *Electrochemistry of Semiconductors* (Nauka, Moscow, 1965).
13. A. M. Yafyasov, A. D. Perepelkin, and V. B. Bozhevol’nov, Fiz. Tekh. Poluprovodn. (St. Petersburg) **26**, 633 (1992) [Sov. Phys. Semicond. **26**, 360 (1992)].
14. A. M. Yafyasov, V. B. Bozhevol’nov, and A. D. Perepelkin, Fiz. Tekh. Poluprovodn. (Leningrad) **21**, 1144 (1987) [Sov. Phys. Semicond. **21**, 697 (1987)].
15. A. M. Yafyasov, V. V. Monakhov, and O. V. Romanov, Vestn. Leningr. Univ., Ser. 4: Fiz., Khim. **1**, 104 (1986).
16. V. B. Bozhevol’nov and A. M. Yafyasov, Vestn. Leningr. Univ., Ser. 4: Fiz., Khim. **1**, 18 (1989).
17. V. F. Radantsev, Pis’ma Zh. Éksp. Teor. Fiz. **46**, 157 (1987) [JETP Lett. **46**, 197 (1987)].

Translated by A. Kazantsev

Semiconductors, Vol. 36, No. 4, 2002, pp. 394–397. Translated from Fizika i Tekhnika Poluprovodnikov, Vol. 36, No. 4, 2002, pp. 416–419.
Original Russian Text Copyright © 2002 by Dzhabbarov.

ELECTRONIC AND OPTICAL PROPERTIES OF SEMICONDUCTORS

Energy Transfer of $Ce^{3+} \longrightarrow Eu^{2+}$ in the $CaGa_2S_4$ Compound

R. B. Dzhabbarov
Institute of Physics, Azerbaijan Academy of Sciences, Baku, 370143 Azerbaijan
e-mail: azerpl@lan.ab.az

Submitted June 2, 2001; accepted for publication September 27, 2001

Abstract—Photoluminescence of $CaGa_2S_4$:Eu^{2+}, $CaGa_2S_4$:Ce^{3+}, and $CaGa_2S_4$:(Eu^{2+}, Ce^{3+}) is shown to be caused by intracenter transitions of Eu^{2+} and Ce^{3+} ions. It is ascertained that an energy transfer with an efficiency of 0.43 takes place from Ce^{3+} to Eu^{2+}. © *2002 MAIK “Nauka/Interperiodica”.*

Introduction of rare-earth element (REE) impurities is necessary to achieve a higher quantum yield during optical and electric pumping of $CaGa_2S_4$ crystals and to ensure an efficient energy transfer from excited carriers to 4*f*-electrons. Rare-earth elements can be excited via wide absorption bands of the host, which in turn lowers the excitation threshold, thus increasing the luminescence efficiency.

The diversity of REE radiative transitions makes it possible to attain any glow color, as well as lasing [1]. An important feature of these materials consists in the absence of pronounced concentrational quenching (up to 7 mol % of impurity) for a number of levels involved in generation [2, 3].

$CaGa_2S_4$:Eu^{2+} compounds are characterized by weak electroluminescence (EL); however, their admixture to commercial electroluminophor ZnS:Cu leads to a drastic enhancement in brightness. A 5-fold and 50-fold increase in brightness in reference to commercial and $CaGa_2S_4$:Eu^{2+} luminophors is achieved, respectively. In our opinion, the marked nonadditivity is caused by an increase in the concentration of primary electrons accelerated for impact excitation of luminescence centers; this increase is due to light reabsorption in commercial electroluminophors [4].

Currently, the cathodoluminescence (CL) phenomenon is widely used in almost all black-and-white and color electron beam tubes [5]. Cathodoluminescence is used to study various objects together with other spectroscopic techniques, such as photoluminescence and streamer luminescence among others. Since the light generation mechanisms in semiconductors, related to recombination of nonequilibrium carriers, are identical for various excitation methods, the results should be similar although slightly different. Light emission during CL is caused by all the radiative recombination mechanisms in the semiconductor. Variation of the energy of incident electrons, hence, their penetration depth, allows one to gain information from a certain crystal depth.

The CL spectra were measured at a temperature of 300 K using the technique described in [6]. The samples were excited by a pulsed electron beam with an energy up to 40 keV at a pulse duration of 6×10^{-7} s. The number of pulses per second is 200, the current density in a pulse is 0.4–0.2 A/cm^2, and the beam penetration depth is 5–8 μm. Figure 1 shows the CL spectrum of the $CaGa_2S_4$:Eu^{2+} crystal at a current density of 1.5×10^{-3} A/cm^2. One can see that the CL spectrum consists of a single peak at the photon energy $h\nu \approx$ 2.21 eV (the wavelength $\lambda \approx 560$ nm). The spectrum has virtually no fine structure, and the CL band is rather broad. This is caused by the efficient electron–phonon interaction at radiative transitions of electrons from excited Eu^{2+} levels. An analysis of the data shows the observed peak to be caused by the $4f^65d \longrightarrow 4f^7$ electron transition of Eu^{2+} ions.

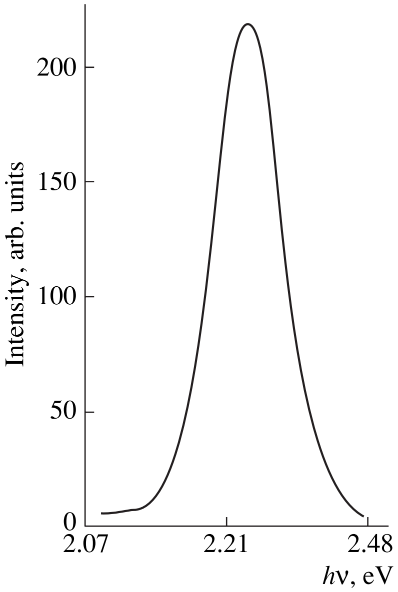

Fig. 1. Cathodoluminescence spectrum of the $CaGa_2S_4$:Eu^{2+} crystal at T = 300 K.

Cathodoluminescence in $CaGa_2S_4$:Eu^{2+} compounds is characterized by a rather short decay time (shorter than 5×10^{-7} s) and a high specific light yield (32–40 lm W^{-1}).

The photoluminescence (PL) excitation spectrum of $CaGa_2S_4$:Eu^{2+} is an extremely broad band overlapped in a wide visible range of the spectrum with the emission spectrum (see Fig. 2). The observed excitation spectrum is explained by the absorption of Eu^{2+} ions, since unactivated $CaGa_2S_4$ does not absorb in this spectral region. The emission spectrum represents a narrow band with a peak at $h\nu = 2.21$ eV and a half-width of 0.23 eV at 300 K. The position of the emission peak of $CaGa_2S_4$:Eu^{2+} crystals depends on the activator concentration. The emission quantum efficiency η is 30% at the excitation energy of 2.81 eV [7]. The high value of η and the peak position $h\nu = 2.21$ eV make this phosphor rather interesting from the practical standpoint. The high performance of this compound, in comparison with commercial phosphors, is also caused by its high adhesion and stability. The short decay time (400 ns) offers promise to apply these phosphors to manufacture kinescope screens fluorescing under electron beams.

Figure 3 displays the PL excitation and emission spectra of $CaGa_2S_4$:Ce^{3+} crystals. The excitation spectrum consists of the short-wavelength (3.45 eV or 359 nm) and long-wavelength (2.9 eV or 427 nm) peaks. Unactivated phosphor does not actively absorb near the long-wavelength peak, while the activated Ce^{3+} crystal strongly absorbs in this region. At 3.45 eV, active absorption by both activated and unactivated phosphors is observed. It may be assumed that Ce^{3+} ions absorb in the long-wavelength range (2.9 eV), while the luminescent material host absorbs in the short-wavelength range.

The emission spectrum consists of two bands with peaks at 2.65 eV (467 nm) and 2.4 eV (516 nm). As the temperature varies within $T = 77$–150 K, the peak positions remain unchanged. A further temperature increase affects the peak heights so that their integrated intensity remains approximately unchanged. In this case, the emission bands are caused by the electron transitions $5d \longrightarrow {}^2F_{5/2}$ and $5d \longrightarrow {}^2F_{7/2}$, respectively.

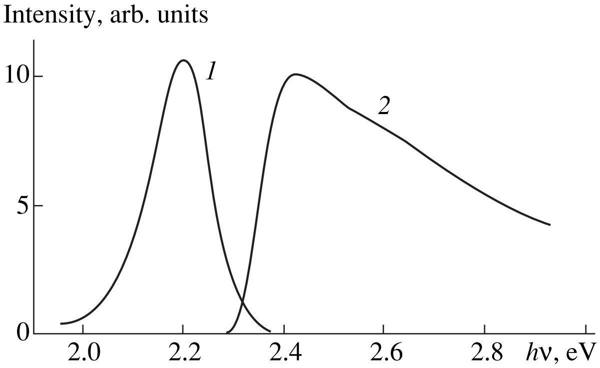

Fig. 2. The photoluminescence emission (*1*) and excitation (*2*) spectra of the $CaGa_2S_4$:Eu^{2+} crystal at $T = 77$ K.

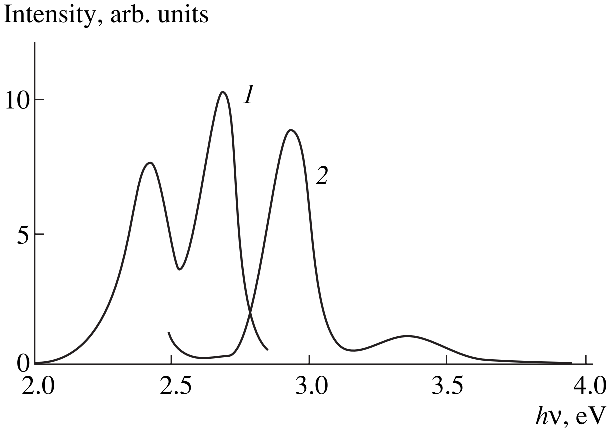

Fig. 3. The photoluminescence emission (*1*) and excitation (*2*) spectra of the $CaGa_2S_4$:Ce^{3+} crystal at $T = 300$ K.

If a system contains more than one rare-earth element, nonadditive effects can arise due to REE interaction. Due to rearrangement of the system of energy levels, this interaction can manifest itself as changes in the absorption and emission spectra, excited state duration, energy transition probability, and some other properties. At high concentrations, or in the case of a deviation of the REE distribution in the lattice from the statistical one, other indications of the interaction are observed. These are shifts of lines and their energy redistribution, the appearance of new lines, and the disappearance of previous ones. One of the theories developed in this line of inquiry [8–11] is focused on the problem of sensitized luminescence, at which the energy of an allowed sensitizer level is transferred to a forbidden activator level.

The strong overlap of the Eu^{2+} excitation and Ce^{3+} emission spectra can cause energy transfer from Ce^{3+} to Eu^{2+}. Therefore, we studied $CaGa_2S_4$:(Eu^{2+}, Ce^{3+}) PL excited by a pulsed N_2 laser (the wavelength λ is 337 nm, pulse duration is 10 ns, pulse-repetition rate is 1000 Hz, and power density is 20 kW cm^{-2}).

Figure 4 shows the PL spectra of $CaGa_2S_4$:(Eu^{2+}, Ce^{3+}) at 77 and 300 K. The spectrum consists of a single peak at 2.21 eV (560 nm) with a half-width of 0.08 and 0.10 eV at 77 and 300 K, respectively. The peaks characteristic of the $CaGa_2S_4$:Ce^{3+} spectrum are not detected in this case.

As the theory [12] shows, the resonance energy transfer arises when the overlap integral is nonzero,

$$\int_0^{\infty} \left(\frac{V}{\nu}\right)^4 I(\nu)\alpha(\nu)d\nu \neq 0, \qquad (1)$$

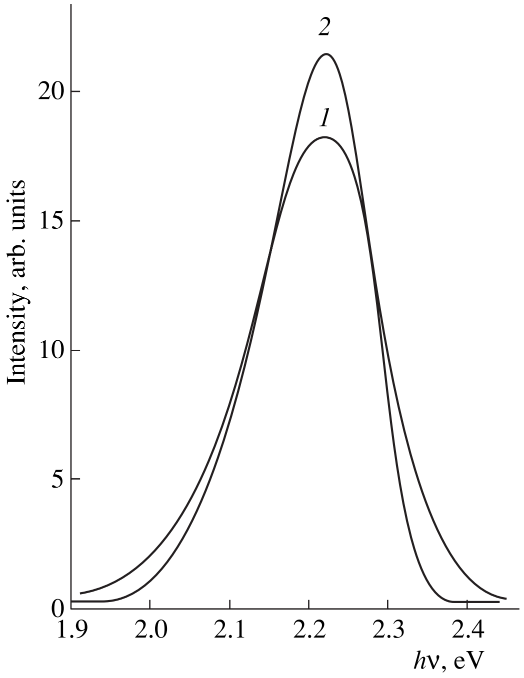

Fig. 4. Photoluminescence spectra of the $CaGa_2S_4$:(Eu^{2+}, Ce^{3+}) crystal at T = (*1*) 300 and (*2*) 77 K.

where $\bar{\nu}$ is the average frequency in the range of overlapping emission and absorption spectra, $\alpha(\nu)$ is the absorptivity per center, and $I(\nu)$ is the emission spectrum normalized to unity.

In this case, the probability of the energy transfer W_{SA} in the approximation of dipole interaction of centers spaced by the distance R_{SA} is proportional to R_{SA}^{-6}. Thus, W_{SA} decreases abruptly as the distance between interacting centers grows (see [11]),

$$W_{SA} = \frac{3\hbar^4 c^4 Q_A}{4\pi K^2 \tau_S}\left[\frac{1}{R_{SA}}\right]^6 \int \frac{f_S(E) f_A(E)}{E^4} dE, \qquad (2)$$

where τ_S is the lifetime in the sensitizer in the absence of activator, R_{SA} is the distance between sensitizer and activator ions, K is the crystal dielectric constant, E is the energy transfer, and

$$\Omega = \int f_S(E) f_A(E) \frac{dE}{E^4} \qquad (3)$$

is defined by overlap of the normalized Ce^{3+} emission spectrum $f_S(E)$ and the Eu^{2+} absorption spectrum $f_A(E)$.

The first excited level of the configuration $4f^7(^6P_J)$, whose position is about 27500 cm^{-1} [13], is not detected in the optical spectra of most of the crystals activated by Eu^{2+} ions. This is caused by the fact that this region includes a group of broad levels of the mixed $4f^65d$ configuration (^8H, ^8G, ^8F), related to allowed optical transitions with the ground state $^8S_{7/2}$. As was indicated in [14], the levels ^8H, ^8G, ^8F shift to higher energies as the crystal field weakens, thus providing conditions favorable to observe narrow-band f–f transitions. The electron shell $4f$ of the Ce^{3+} ion, screened by the filled shell $5s^25p^6$, has only one electron. The spectrum of the free Ce^{3+} ion was studied in [15]. It is caused mainly by the three terms ^2F, ^2D, and ^2S, of which ^2F is the ground one, and the others are excited. The excitation energies correspond to 51000 and 87000 cm^{-1}. The spin–orbit interaction splits the terms ^2F and ^2D into two pairs of levels, $^2F_{7/2}$ and $^2F_{5/2}$, and $^2D_{5/2}$ and $^2D_{3/2}$, with intervals of 2250 and 2500 cm^{-1}. The crystal field has a much stronger impact on excited $5d$-electrons than on $4f$ electrons; i.e., the field markedly lowers the energy position of excited $5d$ levels. Therefore, an electron easily occupies this level. The interaction of centers also has an appreciable impact on the luminescence decay kinetics. The lifetime of excited levels is 228 ns. The energy transfer efficiency calculated by the formula $\eta = 1 - \tau/\tau_0$ [16] is equal to 0.43. Here, τ_0 is the observed lifetime of the Eu^{2+} ion in the absence of Ce^{3+}, and τ is the observed lifetime of Eu^{2+} in the excited state in the presence of the Ce^{3+} ion.

The excited Eu^{2+} levels are pronouncedly split in the crystal field. The absence of the lines inherent in $CaGa_2S_4$:Ce^{3+} in the $CaGa_2S_4$:(Eu^{2+}, Ce^{3+}) spectrum may be caused by the nonradiative energy transfer of these states to the Eu^{2+} excited level. Then, the nonradiative transition to the luminescence level and the transition ($4f^65d \longrightarrow 4f^7$) accompanied by emission are observed.

REFERENCES

1. S. Iida, T. Matsumoto, N. T. Mamedov, *et al.*, Jpn. J. Appl. Phys., Part 2 **36** (7A), L857 (1997).
2. B. G. Tagiev, V. A. Dzhalilov, T. A. Gyul'maliev, *et al.*, Neorg. Mater. **28** (12), 2269 (1992).
3. B. A. Tagiev, M. G. Shakhtakhtinskiĭ, V. A. Dzhalilov, *et al.*, Neorg. Mater. **29** (10), 1392 (1993).
4. B. G. Tagiev, A. B. Abdullaev, O. B. Tagiev, *et al.*, Zh. Prikl. Spektrosk. **62** (3), 145 (1995).
5. V. I. Petrov, Usp. Fiz. Nauk **166** (8), 859 (1996) [Phys. Usp. **39**, 807 (1996)].
6. M. V. Chukichev, D. M. Sabri, V. I. Sokolov, and T. P. Surkova, Opt. Spektrosk. **68** (1), 200 (1990) [Opt. Spectrosc. **68**, 114 (1990)].
7. T. Matsumoto, S. Iida, N. T. Mamedov, *et al.*, in *Proceedings of the 11th International Conference on Ternary and Multinary Compounds, Salford, 1997,* p. 1001.

8. Y. Tan and C. Shi, J. Phys. Chem. Solids **60**, 1805 (1999).
9. M. D. Shinn and W. A. Sibley, Phys. Rev. B **29** (7), 3834 (1984).
10. J. O. Rubio, A. F. Minoz, C. Zaldo, and H. S. Murrieta, Solid State Commun. **65** (4), 251 (1988).
11. R. Capelletti, M. Manfredi, R. Gywinski, *et al.*, Phys. Rev. B **36** (10), 5124 (1987).
12. V. M. Agranovich and M. D. Galanin, *Electronic Excitation Energy Transfer in Condensed Matter* (Nauka, Moscow, 1978; North-Holland, Amsterdam, 1982).
13. P. P. Feofilov, in *Spectroscopy of Crystals* (Moscow, 1966), p. 87.
14. G. Blasse, Phys. Status Solidi B **55**, k131 (1973).
15. N. V. Starostin, P. F. Gruzdev, V. A. Ganin, and T. E. Chebotareva, Opt. Spektrosk. **35** (3), 476 (1973).
16. R. R. Jacobs, C. B. Layne, and M. J. Webber, J. Appl. Phys. **47** (5), 2020 (1976).

Translated by A. Kazantsev

Semiconductors, Vol. 36, No. 4, 2002, pp. 398–403. Translated from Fizika i Tekhnika Poluprovodnikov, Vol. 36, No. 4, 2002, pp. 420–425.
Original Russian Text Copyright © 2002 by Deĭbuk, Voznyĭ, Sletov.

Features of Optical Properties of $Al_xGa_{1-x}N$ Solid Solutions

V. G. Deĭbuk*, A. V. Voznyĭ, and M. M. Sletov**
National University, Chernovtsy, 58012 Ukraine
*e-mail: * vdei@chdu.cv.ua; ** avozny@elegance.cv.ua*

Submitted September 3, 2001; accepted for publication September 27, 2001

Abstract—It is shown that optical reflectance spectra of $Al_{0.1}Ga_{0.9}N$ thin films deposited on sapphire substrates exhibit some special features in the range of 4.0–5.5 eV, which is confirmed by modulation and photosensitivity spectra. These special features can be explained taking into account the biaxial strain when calculating the dielectric function in the pseudopotential approximation. *© 2002 MAIK “Nauka/Interperiodica”.*

INTRODUCTION

In the last few years, great progress has been made in development of optical and electronic devices based on the Group III nitrides AlN, GaN, and InN. Active optoelectronic devices operating in the green, blue, and ultraviolet regions of the spectrum have been developed [1], as well as high-frequency and high-temperature electronic devices, i.e., field-effect transistors, heterojunction bipolar transistors, tunnel diodes, etc. [2].

A prominent feature of ternary nitride alloys both in the bulk and epitaxial cases is the presence of internal local strains caused by mismatched lattice constants and different thermal expansion coefficients of initial compounds. For example, the mismatch of the GaN and AlN lattices is 2.5 and 4.5% for the hexagonal lattice constants a and c, respectively. The thermal expansion coefficients vary between $5.6(3.2) \times 10^{-6}$ and $4.2(5.3) \times 10^{-6}\,K^{-1}$ for directions corresponding to $a(c)$ in hexagonal GaN and AlN [3]. The difference of lattice constants and thermal expansion coefficients gives rise to significant internal strains. In unordered alloys, such strains, similar to the hydrostatic ones, cause proportional changes in the lattice constants with no appreciable changes in the crystal symmetry in general. This in turn causes proportional energy shifts of major peaks of many optical functions with a certain redistribution of their relative intensities. At the same time, epitaxial layers of corresponding ternary alloys pseudomorphically grown on different substrates are subject to additional biaxial deformation. The latter leads to a tetragonal distortion of the lattice; hence, the selection rules for interband electron transitions are changed. Therefore, radical changes of optical functions in such systems would be expected.

Impact of the above factors on the structural and thermodynamic properties, electron spectrum, exciton structure, and some optical characteristics of nitrides and their solid solutions have been actively studied in recent years [4–6] as related to one more possibility of improving the device parameters.

In this study, we investigate the effect of internal local and biaxial strains on the electron spectrum and dielectric function of bulk crystals and epitaxial layers of $Al_xGa_{1-x}N$ solid solutions. The observed special features in the reflectance spectra of $Al_{0.1}Ga_{0.9}$ thin films on sapphire in the energy range E = 4.0–5.5 eV are theoretically explained taking into account biaxial strains in the film.

EXPERIMENTAL

We studied the optical properties of $Al_{0.1}Ga_{0.9}N$ epitaxial layers, with a thickness up to 5 μm, deposited onto sapphire substrates with the (0001) orientation. The layers were grown by the pyrolysis of inorganic ammonium compounds of aluminum and gallium halides [7]. The composition of solid solutions was determined by X-ray spectral analysis using an IXA microanalyzer and by studying the long-wavelength edge of optical absorption. According to the electron and X-ray diffraction data, the layers had a single-crystal structure. X-ray topography, rocking curve, two-wave and multiwave diffractometry techniques showed that structure imperfections were caused mainly by the mismatch of the lattice parameters of epitaxial layers and sapphire. Near the long-wavelength edge, the dependence of the absorptivity α on the photon energy E is described by the known expressions for direct interband transitions,

$$\alpha(h\nu) = \alpha_0(E_g - E)^{1/2}, \tag{1}$$

where E_g is the band gap and α_0 is a parameter independent of E. According to (1), $\alpha^2 = f(E)$ is approximated by a linear dependence within five orders of variation in α.

Optical reflection was studied in the range $E \geq E_g$ by the known method using an MDR-23 diffraction monochromator, an optical chopper, and a synchronous detection system [8]. The layers were preliminarily treated in a 1% $(NH_4)_2S$ solution in isopropyl alcohol [9]. To reveal the special features, which are hardly detected in spectra measured by conventional technique, the λ-modulation method was used when studying the reflectance spectra [10]. In particular, this method made it possible to obtain $E_g = 3.61$ eV, i.e., the value conforming to that determined by extrapolation of the linear dependence $\alpha^2 = f(E)$ to the photon energy axis.

Figure 1 displays the experimental reflectance R spectra measured by the conventional technique (curve *1*) and the spectra $(1/R)(dR/dE)$ measured using λ-modulation (curve *2*). One can see the spectral features in the energy range $E = 4.0$–5.5 eV. We note that their positions correlate with the peaks in the photosensitivity spectra (Fig. 2) of Au–$Al_xGa_{1-x}N$ diode structures produced on the same heterolayers by the explosive evaporation of a semitransparent Au film.

SIMULATION OF THE DIELECTRIC FUNCTION SPECTRUM

The electron band structure, necessary to describe the optical properties, was calculated by the model empirical pseudopotential method described in [11].

Local strains arise in growing GaAlN solid solutions due to different lattice constants of constituent binary compounds. Epitaxial samples also exhibit mismatch strains. To take them into account, we used a functional form of the pseudopotential [12], which is continuous in the reciprocal space and depends on the strain ϵ. The strain-independent pseudopotentials, which yield the band structure in an equilibrium state (e.g., for bulk crystals), have some disadvantages when describing strained systems, since the pseudopotential $V_a(\mathbf{k}, 0)$ form contains no information on the local atomic surroundings. This disadvantage does not arise in self-consistent screened potentials, since these are calculated on the basis of charge redistribution under deformation. To describe changes in the atomic surroundings, we simulate the dependence of the pseudopotential on ϵ using the trace of the strain tensor $\mathrm{Tr}(\epsilon)$; i.e.,

$$V_\alpha(\mathbf{k}, \epsilon) = a_{0\alpha}\frac{(\mathbf{k}^2 - a_{1\alpha})}{a_{2\alpha}\exp(a_{3\alpha}\mathbf{k}^2) - 1}[1 + a_{4\alpha}\mathrm{Tr}(\epsilon)], \quad (2)$$

where $a_{i\alpha}$ $(i = 0, 1, 2, 3, 4)$ are adjustable parameters.

The functional form is chosen so that we have sufficient versatility in describing the maximum possible set of physical properties and do not have to deal with many parameters, which is important for the selection process. Initially, the parameters a_0, a_1, a_2, and a_3 in (2) were determined by an approximation procedure using the known form factors taken from [13]. Finally, the parameters were selected so as to ensure a satisfactory fit of the calculated band structure, optical properties, and deformation potentials to the known experimental data [5, 14–16]. The parameters $a_{i\alpha}$ of the pseudopotential form factors used in this study are listed in Table 1.

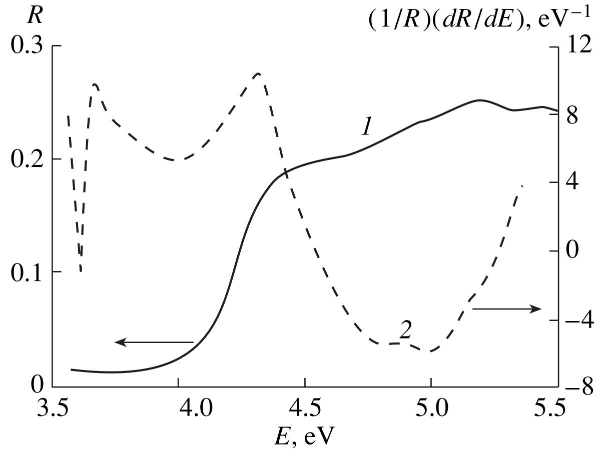

Fig. 1. Experimental reflectance spectra of the $Al_xGa_{1-x}N$ thin film: (*1*) the reflectance R spectrum measured by the conventional technique and (*2*) the λ-modulation spectrum. $(1/R)(dR/dE)$.

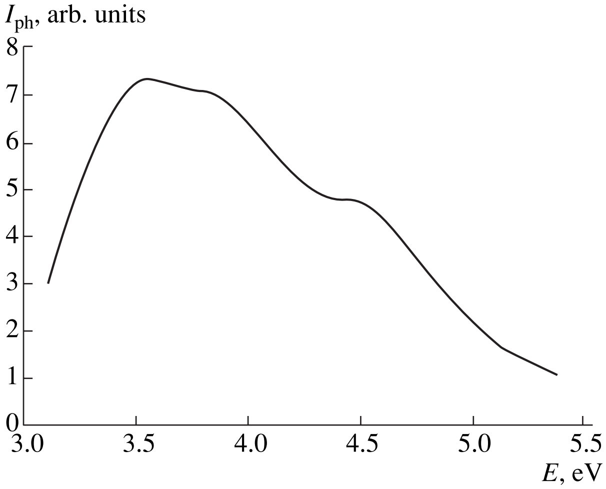

Fig. 2. Photosensivity I_{ph} spectrum of the diode structure.

The GaN and AlN lattice constants in the calculations were taken equal to the experimentally determined ones: $a_{GaN} = 3.190$ Å, $c_{GaN} = 5.189$ Å, $u_{GaN} = 0.377$, $a_{AlN} = 3.111$ Å, $c_{AlN} = 4.978$ Å, and $u_{AlN} = 0.382$ [17, 18].

Table 1. Parameters of the screened atomic pseudopotentials in GaN and AlN

Form factor parameters	a_0	a_1	a_2	a_3	a_4
Ga	20.9	1.68	216	0.144	15
N in GaN	60.9	7.62	77.8	0.543	0
Al	10	2.39	28.5	0.23	12
N in AlN	23.2	7.05	84.2	0.251	0

Table 2. Allowed transitions at the point Γ in different polarization directions (**e** ⊥ **c**–*xy*; **e** || **c**–**z**)

Point Γ	Γ_{1C}	Γ_{2C}	Γ_{3C}	Γ_{4C}	Γ_{5C}	Γ_{6C}
Γ_{1V}	*z*					*xy*
Γ_{2V}		*z*				*xy*
Γ_{3V}			*z*		*xy*	
Γ_{4V}				*z*	*xy*	
Γ_{5V}			*xy*	*xy*	*z*	*xy*
Γ_{6V}	*xy*	*xy*			*xy*	*z*

The optical characteristics of materials can be calculated if one knows their dielectric function, whose imaginary part ε_2 is defined by the band structure (see [17])

$$\varepsilon_2(E) = \frac{\hbar^2 e^2}{3\pi m^2 E^2}\sum_{ij}\int\limits_{E_{ij}=E}|M_{ij}(\mathbf{k})|^2\frac{dS}{|\nabla_k E_{ij}(\mathbf{k})|}, \quad (3)$$

where *i* and *j* are the indices of bands between which transitions occur, and $M_{ij}(\mathbf{k})$ is the oscillator strength for interband transitions. Transitions from 8 valence bands in 12 lower conduction bands were considered.

The real ε_1 and imaginary ε_2 parts of the dielectric function are related by the Kramers–Kronig formula:

$$\varepsilon_1(E) = 1 + \frac{2}{\pi}\int_0^\infty \frac{E'\varepsilon_2(E')}{E'^2 - E^2}dE'. \quad (4)$$

Integration in (3) over the constant-energy surface $E_{ij} = E$ in the Brillouin zone was carried out by the method of tetrahedra [19]. We determined the energies in the grid of 726 points, which were then used for integration in the 3000 obtained tetrahedra.

Conventional calculations of optical properties imply that the matrix elements $M_{ij}(\mathbf{k})$ remain unchanged irrespective of positions in the Brillouin zone. The necessity to calculate the matrix elements for the wurtzite structure is caused by a change of the energy dependence of the dielectric function for various polarization directions [15, 16] and by zero matrix elements for most of the transitions [20].

The calculated pseudowave functions allow us to pass to the determination of the matrix elements,

$$M_{ij}(\mathbf{k}) = \frac{1}{V_{\text{crystal}}}\int\limits_{V_{\text{crystal}}}\Psi_i^*(\mathbf{k},\mathbf{r})\cdot(\mathbf{e}\nabla_k)\Psi_j(\mathbf{k},\mathbf{r})d^3\mathbf{r}, \quad (5)$$

where **e** is the polarization vector of an incident electromagnetic wave. Taking into account the explicit form of the pseudowave functions, (5) can be transformed to the form

$$M_{ij}(\mathbf{k}) = \frac{1}{V_{\text{cell}}}\sum_{mn}^{N} C_{im}^* C_{jn} i[(\mathbf{k}+\mathbf{G}_m)\mathbf{e}] \times \int\limits_{V_{\text{cell}}}\exp[i(\mathbf{G}_n-\mathbf{G}_m)\mathbf{k}]d^3\mathbf{r}, \quad (6)$$

where C_{im} are the Bloch amplitudes and $\mathbf{G}_m$ are the reciprocal lattice vectors. Due to the lattice periodicity, the integral in (6) has nonzero values only at $\mathbf{G}_m = \mathbf{G}_n$. In this case, the integrand is unity. Then, we have

$$M_{ij}(\mathbf{k}) = \sum_{m}^{N} C_{im}^* C_{jm} i[(\mathbf{k}+\mathbf{G}_m)\mathbf{e}]. \quad (7)$$

The accuracy of the matrix element calculation is confirmed by the results of a group theory analysis at the point Γ (see Table 2) [20].

The obtained spectra of the dielectric function for GaN and AlN in polarization *xy* are shown in Figs. 3 and 4. For both materials, three groups of peaks can be

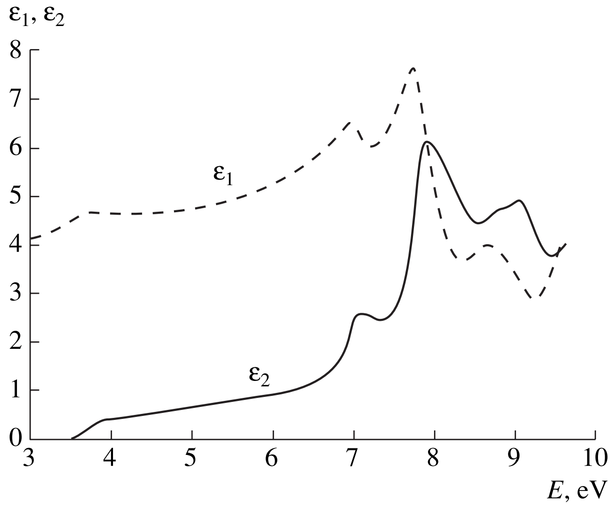

Fig. 3. Calculated spectrum of the dielectric function of GaN for polarization **e** ⊥ **c**.

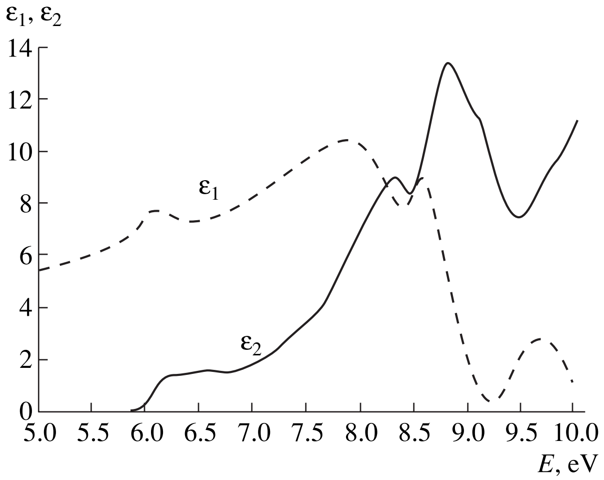

Fig. 4. Calculated spectrum of the dielectric function of AlN for polarization **e** ⊥ **c**.

Table 3. Comparison of the experimental peaks in the imaginary part of the dielectric function of GaN and AlN with the calculated electron transitions

Peak		Experiment [15]	LMTO [16] (T = 300 K)		Our calculation (model pseudopotential) (T = 0 K)		
		energy, eV ($\mathbf{e} \perp \mathbf{c}$, T = 130 K)	energy, eV	transition	energy, eV	transition, $\mathbf{e} \perp \mathbf{c}$	transition $\mathbf{e} \parallel \mathbf{c}$
GaN	E_0	3.4	3.6	Γ: 8–9	3.5	Γ: 7,8–9	Γ: 6–9
	E_1	7.1	6.2	*U*: 8–9	7	*A*: 5,6–9; 7,8–9	
				M: 8–10			
	E_2	8	7.2	*M*: 8–10	8	*L*: 5–10; 6,7–9	*L*: 7,8–9,10
				Σ': 7,8–9,10		*U*: 8–9; *M*: 8–10	*U*: 7–9
	E_3	9.1	8.2	*M*: 6–9	9	*H*: 7,8–9,10	*H*: 7–10; 8–9
				Σ: 6–10; *H*: 8–9			
AlN	E_0	6.1	4.9	Γ: 8–9	6	Γ: 6,7–9	Γ: 8–9
	E_1	7.9	7.1	*L*: 7,8–9,10	8.3	*M*: 8–10; *H*: 8–9	*H*: 7–10; 8–9
						U: 8–9	*U*: 7–9
	E_2	9.05	8.1	*R*: 7,8–9,10	8.8	*M*, Σ: 6–9	
				U': 6–10; *M*: 6–10			

distinguished in the spectrum of the imaginary part of the dielectric function (in the ranges of 7–9 (8–9), 9.5–10.5 (9.5–11.5), and 12–14 eV for GaN (AlN)), which conforms to other calculations [15, 16].

To date, few papers concerned with experimentally measured dielectric functions of GaN and AlN [14, 15] have been published. In the first group of peaks for GaN, three peaks stand out: E_1, E_2, and E_3 with energies of 7, 8, and 9.1 eV (at 130 K), respectively [15]. In our calculations, the positions of these peaks are 7, 8, and 9 eV (at 0 K), which is the best result in comparison with the LMTO calculations (6.2, 7.3, and 8.2 eV) [16] and the tight binding method (6.4, 7.5, and 8.4 eV) [6]. However, the accurate distribution of the peak intensity was found only in the *ab initio* calculations by the density functional method taking into account the electron–hole interaction [15].

For AlN, two peaks are observed at energies 7.9 and 9.05 eV in the first group; the calculated values are 8.3 and 8.8 eV, respectively.

In Table 3, the optical transitions (on the basis of the calculated matrix elements) are identified with the peaks in the spectrum of the imaginary part of the dielectric function; the results of other calculations [16] and experimental data [15] are also given.

Our calculations of the matrix elements show that the selection rules are independent of form factors, but are defined only by the problem symmetry, though the relative position of allowed transitions can vary.

The band structure and the dielectric function of the $Al_xGa_{1-x}N$ solid solution was simulated in the virtual crystal approximation [11], which is justified by a small difference between the pseudopotentials of binary compounds.

EFFECT OF STRAINS ON OPTICAL PROPERTIES

To explain the special features of the experimentally measured reflectance spectra in the range E = 4–5.5 eV, we took into account both local and biaxial strains that arose in the pseudomorphic $Al_{0.1}Ga_{0.9}N$ epitaxial film grown on a sapphire substrate. These strains are caused by the difference in the lattice constant of starting compounds (local strains), mismatch of the lattice constants of the film and substrate (biaxial strains), and the difference in the thermal expansion coefficients of the film and substrate.

To take into account the effect of local strain, which is similar to hydrostatic strain, the form factor parameters a_4 (see Table 1) were selected so that the calculated deformation potentials

$$a_g = V\frac{\partial E_g}{\partial V} \tag{8}$$

were equal to the experimental values: –7.8 and –8.8 eV for GaN and AlN, respectively [5, 16]. In this case, diagonal elements of the deformation tensor were set equal: $\epsilon_{xx} = \epsilon_{yy} = \epsilon_{zz}$. The effect of local strain on the dielectric function of alloy was found to be insignificant.

In order to take into account the biaxial strain, we set the lattice constant of alloy $a(x)$ in the plane xy equal to the substrate lattice constant a_{sub}. In this case, we have

$$\epsilon_{\parallel} = \epsilon_{xx} = \epsilon_{yy} = \frac{a_{\text{sub}} - a(x)}{a(x)}, \tag{9}$$

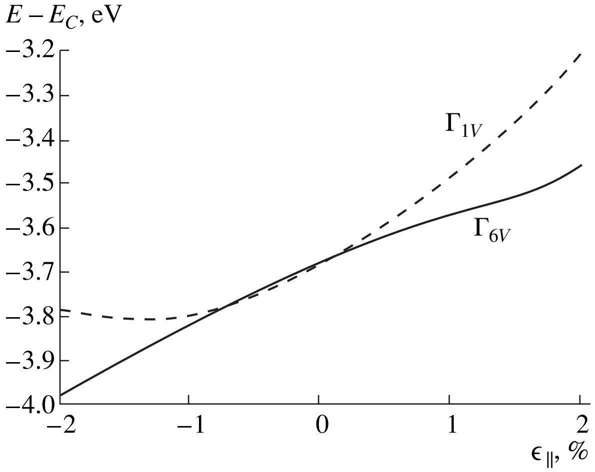

Fig. 5. Splitting of the upper valence band versus the biaxial strain.

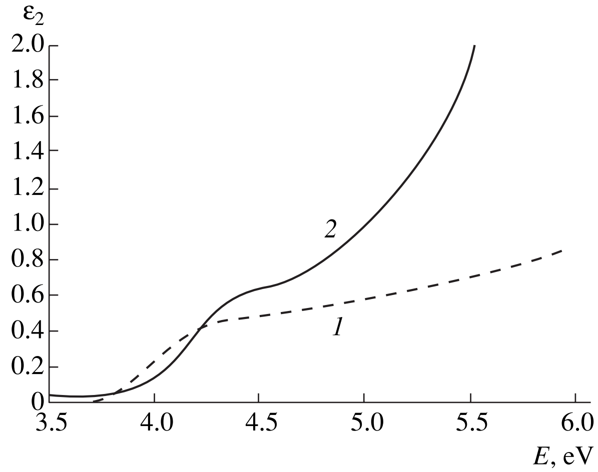

Fig. 6. Calculated imaginary part of the dielectric function of $Al_{0.1}Ga_{0.9}N$ solid solution (*1*) neglecting the film strain and (*2*) taking into account the biaxial strain $\epsilon_{\parallel} = 4\%$.

and the z component of the strains is given by

$$\epsilon_{\perp} = \epsilon_{zz} = \frac{c_l - c(x)}{c(x)}, \quad (10)$$

where c_l is the lattice constant in the z-direction of the strained film and $c(x)$ is the lattice constant of the unstrained film.

For hexagonal crystals, the z component of the stress and the strain tensor are related as (see [21])

$$\tau_3 = C_{13}\epsilon_{xx} + C_{13}\epsilon_{yy} + C_{33}\epsilon_{zz}, \quad (11)$$

where C_{13} and C_{33} are the alloy elastic constants determined by linear interpolation of the elastic constant of binary compounds. Setting $\tau_3 = 0$, we obtain

$$\epsilon_{\perp} = \frac{-2C_{13}}{C_{33}}\epsilon_{\parallel}. \quad (12)$$

From (10) and (12) we find the strained lattice constant

$$c_l = c(x)\left(1 - \frac{2C_{13}}{C_{33}}\epsilon_{\parallel}\right). \quad (13)$$

The obtained strain tensor components were used in (2) to calculate the band structure.

Due to the inclusion of biaxial strain, the band structure of the considered alloy will change somewhat. In particular, in the absence of spin–orbit interaction, the upper valence band will split into doubly and singly degenerate states Γ_{6V} and Γ_{1V}, respectively (see Fig. 5), which conform to the data calculated *ab initio* [5]. The consideration of biaxial strain also leads to a change in the selection rules for the allowed interband transitions [20].

Figure 6 shows the calculated imaginary part $\varepsilon_2(E)$ of the dielectric function of the studied $Al_{0.1}Ga_{0.9}N$ solid solution in the energy range E = 3.5–6 eV, taking into account and ignoring the film biaxial strains. The inclusion of the biaxial strain leads to the appearance of a characteristic peak at 4.5 eV, which is mainly caused by the interband electron transitions Γ_{5V}–Γ_{1C} and Γ_{6V}–Γ_{3C}. These transitions become permissible when there is a biaxial strain. Furthermore, such transitions shift the main spectral peaks to lower energies. The calculated dependence $\varepsilon_2(E)$ allows for the explanation of the experimentally observed special features in the reflectance spectrum of the $Al_{0.1}Ga_{0.9}N$ epitaxial film on the sapphire substrate.

CONCLUSION

The optical reflectance spectra of the $Al_{0.1}Ga_{0.9}N$ thin films deposited on sapphire substrate exhibit special features in the energy range E = 4.0–5.5 eV, which was confirmed by the modulation and photosensivity spectra. These special features can be explained by taking biaxial strain into consideration when calculating the dielectric function in the pseudopotential approximation.

REFERENCES

1. Shuji Nakamura, *Introduction to Nitride Semiconductor Blue Lasers and Light Emitting Diodes* (Taylor & Francis, London, 2000).
2. H. Markoc, *Nitride Semiconductors and Devices* (Springer-Verlag, Berlin, 1999).
3. *Data in Science and Technology: Semiconductors*, Ed. by O. Madelung (Springer-Verlag, Berlin, 1991).
4. L. K. Teles, J. Furthmüller, L. M. R. Scolfaro, *et al.*, Phys. Rev. B **62**, 2475 (2000).
5. D. Volm, K. Oettinger, T. Streibl, *et al.*, Phys. Rev. B **53**, 16543 (1996).
6. Z. Yang and Z. Xu, Phys. Rev. B **54**, 17577 (1996).

7. A. V. Dobrynin, M. M. Sletov, and V. V. Smirnov, Zh. Prikl. Spektrosk. **55**, 861 (1991).
8. Yu. V. Vorob’ev, V. I. Dobrovol’skiĭ, and V. I. Strikha, *Methods for Study of Semiconductors* (Vyshcha Shkola, Kiev, 1989).
9. Yu. V. Zhilyaev, M. E. Kompan, E. V. Konenkova, *et al.*, Pis’ma Zh. Tekh. Fiz. **24** (24), 90 (1998) [Tech. Phys. Lett. **24**, 986 (1998)].
10. A. N. Georgobiani, Yu. V. Ozerov, and I. M. Tiginyanu, Tr. Fiz. Inst. Akad. Nauk SSSR **163**, 3 (1985).
11. V. G. Deĭbuk, A. V. Voznyĭ, and M. M. Sletov, Fiz. Tekh. Poluprovodn. (St. Petersburg) **34**, 36 (2000) [Semiconductors **34**, 35 (2000)].
12. T. Matilla, L.-W. Wang, and Z. Zunger, Phys. Rev. B **59**, 15270 (1999).
13. S. Bloom, J. Phys. Chem. Solids **32**, 2027 (1971).
14. S. Logotetidis, J. Petalas, M. Cardona, and T. D. Moustakas, Phys. Rev. B **50**, 18017 (1994).
15. L. X. Benedict, T. Wethkamp, K. Wilmers, *et al.*, Solid State Commun. **112**, 129 (1999).
16. N. E. Christensen and I. Gorczyca, Phys. Rev. B **50**, 4397 (1994).
17. M. L. Cohen and J. R. Chelikowsky, *Electronic Structure and Optical Properties of Semiconductors* (Springer-Verlag, Berlin, 1988).
18. A. Chen and A. Sher, *Semiconductor Alloys: Physics and Material Engineering* (Plenum, New York, 1995).
19. J. Rath and A. J. Freeman, Phys. Rev. B **11**, 2109 (1976).
20. P. Tronc, Yu. E. Kitaev, G. Wang, *et al.*, Phys. Status Solidi B **216**, 599 (1999).
21. G. L. Bir and G. E. Pikus, *Symmetry and Strain-Induced Effects in Semiconductors* (Nauka, Moscow, 1972; Wiley, New York, 1974).

Translated by A. Kazantsev

Semiconductors, Vol. 36, No. 4, 2002, pp. 404–409. Translated from Fizika i Tekhnika Poluprovodnikov, Vol. 36, No. 4, 2002, pp. 426–432.
Original Russian Text Copyright © 2002 by Gasan-zade, Strikha, Staryĭ, Shepel'skiĭ, Boĭko.

ELECTRONIC AND OPTICAL PROPERTIES OF SEMICONDUCTORS

Increase in Quantum Efficiency of IR Emission in Elastically Strained Narrow-Gap Semiconductors

S. G. Gasan-zade*, M. V. Strikha, S. V. Staryĭ, G. A. Shepel'skiĭ, and V. A. Boĭko
Institute of Semiconductor Physics, National Academy of Sciences of Ukraine, 01650 Kiev, Ukraine
**e-mail: gassan@class.semicond.kiev.ua; fax: (38044) 265 8342*

Submitted May 8, 2001; accepted for publication October 9, 2001

Abstract—The rate of radiative band-to-band recombination in elastically strained direct-band narrow-gap semiconductors increases owing to the valence band transformation. At the same time, the rate of nonradiative band-to-band transitions (Auger recombination) decreases dramatically. As a result, the quantum efficiency of IR emission in the range of band-to-band transitions can be essentially raised and, as calculation shows, tends to limiting values close to unity. Experimental data were obtained for InSb crystals under strong excitation. *© 2002 MAIK "Nauka/Interperiodica".*

Direct-band narrow-gap semiconductors, like InSb and $Cd_xHg_{1-x}Te$, are the basic materials for mid-IR range (5–12 μm) photodetectors. However, fundamental difficulties are encountered in designing efficient emitters on the basis of these semiconductors. It is well known that the main impediment to obtaining efficient emitters on the basis of narrow-gap semiconductors is the intensive channel of nonradiative transitions in the form of band-to-band impact recombination (Auger recombination). This important kind of nonradiative recombination cannot, in principle, be eliminated because the recombination characteristics are governed by the parameters of the intrinsic band spectrum (in the first place, the narrow band gap $\mathcal{E}_g$ and the large ratio between the effective masses of heavy holes and electrons in the conduction band, $m_h/m_c \gg 1$), rather than by the presence of impurity or defect energy levels in the band gap. The Auger recombination is effective in narrow-gap semiconductors in the actual temperature range. For example, the Auger recombination is significant in InSb even at low excitation levels at $T \gtrsim 250$ K [1], i.e., in the intrinsic conduction range, and in $Cd_xHg_{1-x}Te$ with $x = 0.20$ it becomes dominant already in the extrinsic conduction range ($T \gtrsim 77$ K) [2].

Under high-intensity excitation, when the nonequilibrium carrier density significantly exceeds the equilibrium value, $\delta n = \delta p \gg n_0, p_0$, the importance of Auger recombination sharply increases. This is related to the stronger (cubic) dependence of the Auger recombination rate on density, compared with the quadratic dependence for the rate of radiative recombination. This circumstance imposes fundamental constraints on the limiting theoretical values of the IR emitter parameters.

It is shown in the present study that a dramatic decrease in the rate of Auger recombination occurs in an elastically strained narrow-gap semiconductor along with an increase in the rate of radiative band-to-band transitions. As a result, the quantum efficiency of IR emission in the range of band-to-band transitions increases manyfold, and, according to calculations, tends to values close to unity. The proposed method of suppression of the band-to-band Auger recombination is based on the high sensitivity of the energy spectrum of a narrow-gap semiconductor to uniaxial elastic stress.

As is known, uniaxial stress (in what follows, we consider compression along the [001] crystallographic axis; the results for other axes are similar) strongly modifies the band spectrum $\mathcal{E}(k)$ of a narrow-gap semi-

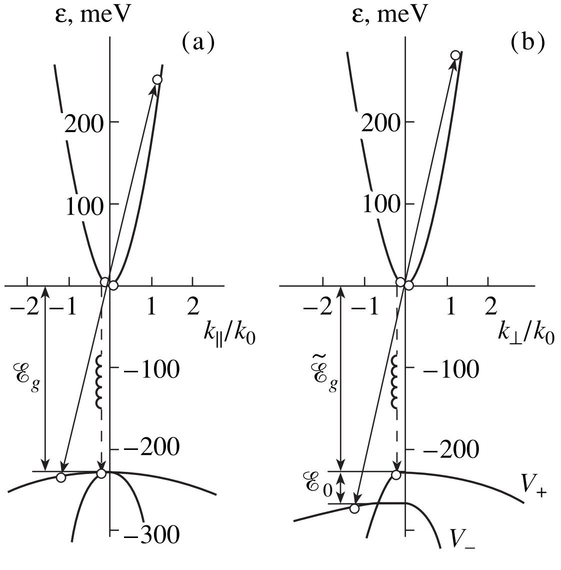

Fig. 1. Transformation of the InSb energy spectrum under uniaxial elastic stress: (a) $P = 0$ and (b) $P = 4$ kbar. Arrows show band-to-band recombination transitions; solid lines, Auger transitions; dashed lines, radiative transitions. $k_0 \approx 4 \times 10^{-6}$ cm^{-1}.

1063-7826/02/3604-0404$22.00 © 2002 MAIK "Nauka/Interperiodica"

conductor [3–6] (see Fig. 1). States of heavy and light holes are mixed (in this case, it is convenient to discuss V_+ and V_- bands), and the degeneracy of the valence band at the Γ_8 point is lifted. An energy gap appears between the top edges of the V_+ and V_- subbands; according to the model of Bir and Pikus [7], its width $\mathcal{E}_0$ is proportional to the applied compression P and, for the direction $\mathbf{P} \parallel [100]$, can be represented as $\mathcal{E}_0 = \chi P = 2|b|(S_{11} - S_{12})P$, where b is the deformation potential constant, and S_{11} and S_{12} are components of the elastic compliance tensor.

It is noteworthy that in these conditions the band gap (and, consequently, the long-wavelength edge of the band-to-band emission) changes only slightly: at P = 4 kbar, the change in $\mathcal{E}_g$ of InSb does not exceed 3 meV. This is due to the mutual compensation of two quantities: the increase in the energy gap, caused by the hydrostatic component of the uniaxial stress, and its decrease by $(1/2)\mathcal{E}_0(P)$ because of the upward shift of the V_+ subband. In this case, the gap width renormalized by the uniaxial compression can be represented, in the simplest case of compression along the [001] axis, as $\tilde{\mathcal{E}}_g = \mathcal{E}_g + (\zeta/3 - \chi/2)P$. For InSb, the constants related to the hydrostatic and shear components of the uniaxial stress are $\zeta = 15.3$ and $\zeta = 0.9$ meV kbar^{-1}, respectively [3]. The calculated energy shifts and splittings correlate well with the experimental data obtained from the polarization-spectral measurements of photocurrent in uniaxially strained InSb and $\mathrm{Cd}_x\mathrm{Hg}_{1-x}\mathrm{Te}$ [8].

It should be noted that the recombination rates may change substantially even at relatively small P values, since the compression-induced gap $\mathcal{E}_0$ in a narrow-gap semiconductor reaches the average thermal energy of holes $(3/2)k_BT$ (k_B is the Boltzmann constant) at liquid nitrogen temperature (77 K) already at compressions of ~0.5 kbar. In this situation, the effective masses in the $V_\pm$ bands become anisotropic under uniaxial compression, being equal to, respectively, $m_0/(\gamma_1 \pm 2\gamma)$ and $m_0/(\gamma_1 \mp \gamma)$ for the longitudinal and transverse directions relative to the compression axis. Here m_0 is the free electron mass, and γ_1 and γ are the parameters of the isotropic Luttinger model.

Hence, the averaged effective mass of holes decreases substantially, compared with the heavy hole mass in the initial crystal. Consequently, with increasing $\mathcal{E}_0$, the majority of holes thermalize in the small momentum range, and direct radiative transitions of electrons from the conduction band become more effective. This results in that the rate of radiative band-to-band recombination grows with increasing stress, which can in itself raise the intensity of the recombination emission.

Without deformation, the nonradiative process with the electron transition to the heavy hole band is characterized by a very low energy threshold in view of the smallness of the effective mass ratio: $m_c/m_h \ll 1$ [9]. In a uniaxially strained state, the Coulomb matrix element of the band-to-band transition is barely modified. However, the considerable decrease in the hole effective masses in the subbands results in a dramatic increase in the energy thresholds for the Auger transitions. This refers to all cases, with the exception of electron rebound to the V_- band in the momentum direction parallel to the compression axis. This state—the only one in the split valence band—is characterized by an effective mass close to the heavy hole mass m_h in an undeformed crystal. However, the hole density in the V_- band will decrease exponentially with increasing energy gap $\mathcal{E}_0$ between the subbands, i.e., with growing stress P. Therefore, the rate of Auger recombination will decrease, in contrast to that of radiative recombination. In terms of Kane's three-band model and the theoretical model developed in [10, 11], the deformation dependence of the lifetimes of nonequilibrium holes with respect to the radiative (τ_R) and Auger recombination (τ_A) in an n-type material can be represented as

$$\frac{\tau_R(\mathcal{E}_0)}{\tau_R(0)} = \frac{4(\gamma_1/2\gamma - 1)^{3/2}}{\sqrt{\pi}(e^{-\mathcal{E}_0/2k_BT} + e^{\mathcal{E}_0/2k_BT}}J(\gamma_1/2\gamma, \mathcal{E}_0/k_BT), \quad (1)$$

$$\frac{\tau_A(\mathcal{E}_0)}{\tau_A(0)} = \frac{2(\gamma_1/2\gamma - 1)^{3/2}}{\sqrt{\pi}e^{-\mathcal{E}_0/2k_BT}}J(\gamma_1/2\gamma, \mathcal{E}_0/k_BT). \quad (2)$$

The dimensionless integral in (1), (2) is defined by

$$J(\gamma_1/2\gamma, \mathcal{E}_0/k_BT) = \sum_{\pm}\int_0^\infty x^2dx\int_{-1}^{1}du\,\exp$$
$$\times\left\{-\gamma_1x^2/2\gamma \pm \left[x^4 + \frac{\mathcal{E}_0}{2k_BT}x^2\frac{3u^2-1}{2} + \left(\frac{\mathcal{E}_0}{2k_BT}\right)^2\right]\right\}. \quad (3)$$

It is noteworthy that relations (1)–(3) are derived for the case of nondegenerate holes, with arbitrary degeneracy of electrons.

Figure 2 presents the results of the numerical calculation of Eqs. (1) and (2) for narrow-gap semiconductors with the parameters of InSb ($\gamma_1/2\gamma = 1.044$) and $\mathrm{Cd}_{0.2}\mathrm{Hg}_{0.8}\mathrm{Te}$ ($\gamma_1/2\gamma = 1.10$). As seen, uniaxial compression may lead to a significant (by an order of magnitude) change in the radiative to Auger recombination lifetime ratio. This may, in turn, substantially change the quantum efficiency of emission from a narrow-gap semiconductor.

Experimental dependences of the carrier lifetimes on the elastic stress $\tau(P)$ were obtained by measuring the steady-state photoconductivity at a low excitation level in n-$\mathrm{Cd}_x\mathrm{Hg}_{1-x}\mathrm{Te}$ samples with $x \approx 0.30$ ($\mathcal{E}_g = 0.25$ meV) and $x \le 0.2$ ($\mathcal{E}_g \le 0.1$ meV) under compression P = 0–2 kbar in the temperature range T = 77–250 K [4]. The composition choice was due to the fact that, in the temperature range of intrinsic conduction, the carrier lifetime is governed by the radiative channel for the sam-

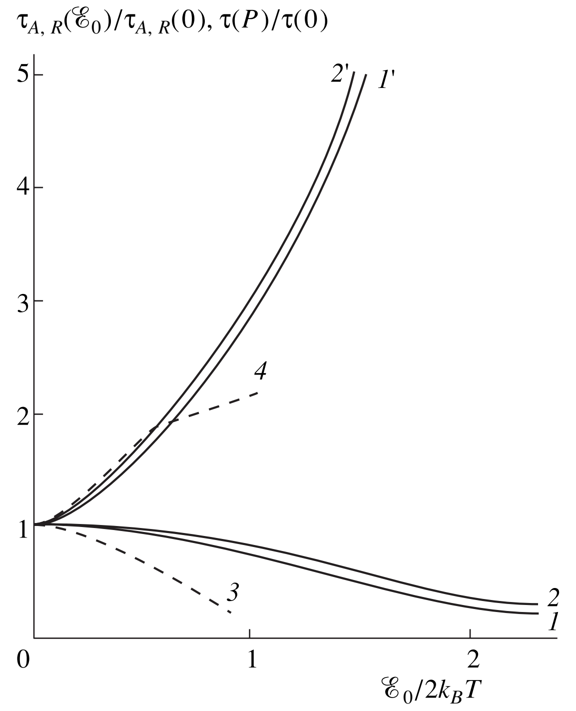

Fig. 2. Deformation dependences of lifetimes. Solid lines—calculation: (*1*, *2*) $\tau_R(P)/\tau_R(0)$ and (*1*', *2*') $\tau_A(P)/\tau_A(0)$ for (*1*, *1*') InSb and (*2*, *2*') $Cd_xHg_{1-x}Te$. Dashed lines—experimental $\tau(P)/\tau(0)$ dependences for $Cd_xHg_{1-x}Te$: (*3*) $x = 0.29$, $T = 170$ K; (*4*) $x = 0.20$, $T = 120$ K.

ples with $x \approx 0.3$ and by the Auger recombination for $x \leq 0.2$, which was confirmed by the run of the temperature dependences of τ at $P = 0$. This allowed us to neglect recombination via impurities in the temperature range $T > 160$ K for the first case and at $T > 100$ K for the second.

In the experiment, a decrease in τ with increasing stress was observed for samples with $x \approx 0.3$, at least in the temperature range 150–240 K. By contrast, τ markedly increased with growing P for samples with $x \approx 0.2$ at $T \gtrsim 100$ K (Fig. 2, dashed lines). The obtained experimental curves reasonably correlate with the theory. Some quantitative differences are apparently associated with the possible contribution to τ from the impurity recombination, which was disregarded in the calculation. Changes in τ by a factor of 2–2.5 correspond to the ratio $\mathcal{E}_0/k_BT \approx 2.5$ implemented in the experiment. It is important that the nature of τ variation (increase or decrease) with stress unambiguously indicates by itself the dominant recombination mechanism. On the other hand, it is evident that a situation may occur in which the dominant recombination mechanism will change on reaching certain P values. Let us consider such a possibility for InSb and $Cd_{0.2}Hg_{0.8}Te$. Our attention will be, in the first place, focused on variation with deformation of the emission quantum efficiency in the range of band-to-band transitions. As is known, the temperature dependence of the emission quantum efficiency $\eta(T)$ in InSb is markedly nonmonotonic. In sufficiently pure undoped crystals, $\eta(T)$ has a maximum (~0.2) in the range 200 K < T < 250 K and then sharply falls to ~0.05 with decreasing temperature. As the temperature is lowered further, η grows again and, at $T = 77$ K, it may reach values close to 0.50 in doped crystals with donor concentration $N_D \gtrsim 5 \times 10^{15}$ cm^{-3}. It was suggested in [12] that this η value is, altogether, the highest achievable in InSb at $T = 77$ K and the optimal doping level.

Table 1 presents calculated deformation dependences of τ_R, τ_A, and η. The calculation took into account that $\mathcal{E}_0 = \chi P$, where $\chi = 9$ meV kbar^{-1} for InSb and 12 meV kbar for $Cd_{0.2}Hg_{0.8}Te$, [6]. Without deformation, τ_R is 5.6×10^{-7} and 5.0×10^{-5} s and $\eta = 0.4$ and 0.04, respectively, for these materials [2, 12]. It is noteworthy that no account was taken, over the entire range of elastic stresses under study, of the possible contribution from the impurity Shockley–Read recombination. This assumption may be not quite justified at low excitation levels.

As seen from Table 1, the Auger recombination dominates at $P < 0.5$ kbar in InSb and at $P < 2.2$ kbar in $Cd_{0.2}Hg_{0.8}Te$. However, the radiative recombination becomes dominant at a higher elastic stress. In the P range under study, the resulting lifetime $\tau = 1/(1/\tau_A + 1/\tau_R)$ varies relatively weakly, being represented by a smooth curve with a peak in the P range corresponding to the change of the dominant recombination mechanism. However, the quantum efficiency grows steadily with increasing P and tends to values close to unity.

The calculated values of τ_R, τ_A, and η, presented in the table, correspond to low excitation levels ($\delta n, \delta p < n_0, p_0$). Much more important from the practical standpoint is the case of high excitation levels, taking place in semiconductor light-emitting diodes and lasers. In the present study, such a level of electron–hole pair excitation in the sample was ensured by external laser irradiation.

At a high excitation level ($\delta n = \delta p \approx 5 \times 10^{17}$ cm^{-3}) in InSb, $\tau = (1–1.5) \times 10^{-9}$ s and $\eta = 0.025–0.030$ [13]. It is necessary to note that at these electron–hole pair densities and $T = 77$ K, electrons are strongly degenerate, while the condition for strong degeneracy of holes is not satisfied yet. Therefore, approximate relations (1) and (2) can be used. The results of calculation are presented in Table 2. The resulting lifetime τ grows rather substantially in the P range studied, owing to the suppression of the dominant Auger recombination channel. In this situation, the peak in $\tau(P)$ is observed in that range of stresses near which a sample may already disintegrate. However, the quantum efficiency grows steadily with increasing P to become more than an order of magnitude higher.

Interestingly, on passing to the case of strongly degenerate holes, a situation may occur in which all the holes are accumulated in the upper of the two split valence bands ($\mathcal{E}_F < \mathcal{E}_0$ limit, where $\mathcal{E}_F$ is the Fermi energy). In this case, Auger transitions will be forbidden by virtue of the impossibility of simultaneous energy and momentum conservation, due to the lack of holes with energies exceeding the threshold for transitions to the upper of the split bands. Under these conditions, the quantum efficiency rises steeply. A numerical estimate shows that this situation may occur in InSb at liquid helium temperature.

Deformation dependences of the quantum efficiency of band-to-band IR emission were investigated in *n*-InSb crystals. At $T = 77$ K, the electron density of the crystals was $n = (2–4) \times 10^{13}$ cm^{-3} and the mobility was $\mu_n = (3–5) \times 10^5$ cm^2 V^{-1} s^{-1}. A sample under study was placed, together with a device for uniaxial compression, directly in a cryostat with liquid nitrogen. The sample was excited with a Nd laser in pulse mode. The emission was detected with a cooled Ge:Au detector.

Figure 3 shows the emission intensity *I* as a function of the excitation level *L* for an InSb sample at several values of elastic stress *P*. Characteristic bends observed in the curves (shown by arrows) indicate a change of the dominant recombination mechanism. The slope of curves in the log–log scale is about 0.5 in the range $L = 5 \times 10^{22}–3 \times 10^{23}$ photon cm^{-2} s^{-1} and 1.5–1.6 for different samples at lower *L*. It is noteworthy also that the excitation level *L* corresponding to the bending point grows with increasing *P*. Reasoning from the fact that the bend in the *I*(*L*) dependence shows a change of the principal recombination channel, we may assume that the Auger recombination dominates at high excitation levels ($\delta n = \delta p \gg n_0, p_0$). Let us consider the carrier distribution for the case of nonuniform excitation of a crystal with strongly absorbed light, which is described by the continuity equation of the form [12, 13]

$$D_a \frac{d^2 \delta n}{dx^2} - B(\delta n)^{\beta(x)} = 0, \tag{4}$$

with the boundary condition

$$-D_a \frac{d\delta n}{dx^2} = L - s\delta n. \tag{5}$$

Here, $\Delta a = A(\delta n)^{\alpha(x)}$ is the ambipolar diffusion coefficient, with $\alpha = 0$ for the simple case of nondegenerate carriers; and $B(\delta n)^{\beta(x)}$ is the recombination term. For nondegenerate carriers, $\beta = 1$ if the lifetime of nonequilibrium holes is governed by the Shockley–Reed recombination, $\beta = 2$ if the radiative band-to-band recombination dominates, and $\beta = 3$ for the case of Auger recombination. In the boundary condition, *s* is the surface recombination rate. It is necessary to note that, in the case of strongly degenerate carriers, the coefficients α and β may differ significantly from the above simple values. However, the theoretical and experimental data are somewhat contradictory for strongly degenerate InSb [13].

Table 1. Deformation dependences of recombination parameters at low excitation levels

InSb

P, kbar	τ_R, 10^{-7} s	τ_A, 10^{-6} s	τ, 10^{-7} s	η, %
0	5.6	0.37	2.2	40
0.37	5.5	0.48	2.6	47
0.74	5.0	0.62	2.8	55
1.13	4.5	0.81	2.9	64
1.50	3.9	1.1	2.9	74
2.24	2.7	1.9	2.4	88
2.98	1.9	3.5	1.8	95
4.47	1.0	13	0.99	99

Cd$_{0.2}$Hg$_{0.8}$Te

P, kbar	τ_R, 10^{-5} s	τ_A, 10^{-5} s	τ, 10^{-6} s	η, %
0	5.0	0.20	1.9	4
0.28	4.8	0.25	2.4	5
0.56	4.5	0.35	3.3	7
0.84	4.0	0.45	4.0	10
1.12	3.5	0.60	5.1	15
1.68	2.7	1.1	7.3	29
2.26	2.0	2.2	11	52
3.35	1.2	9.8	11	89
4.46	0.85	49	8.4	99.7

In what follows, we assume that the sample thickness *d* greatly exceeds the diffusion length $l_d = \sqrt{D_a \tau_p}$ (τ_p is the hole lifetime). We also consider the intensity of external excitation *L* to be high enough, so that $\delta n = \delta p \gg n_0 \gg p_0$ in Eq. (4). In the limit of the low surface recombination rate (ensured in the experiment by thor-

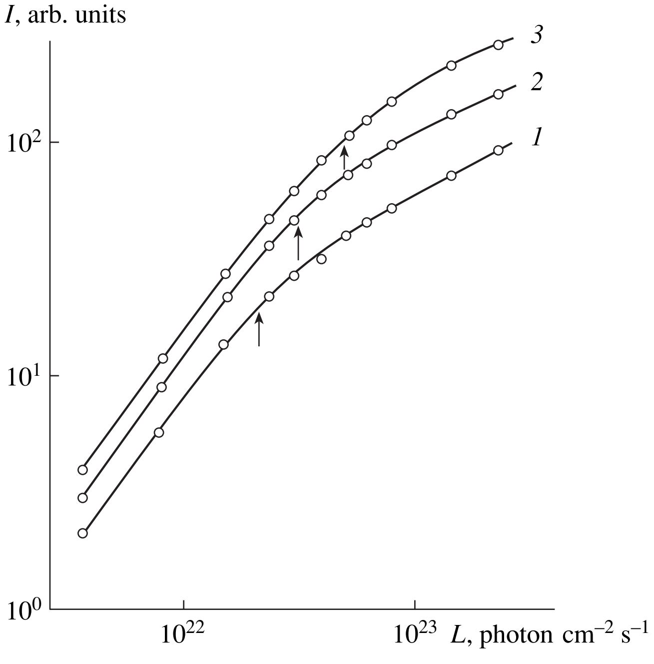

Fig. 3. Intensity of recombination emission in *n*-InSb vs. the excitation level *L*. Elastic stress *P*: (*1*) 0, (*2*) 2.6, and (*3*) 4.5 kbar.

Table 2. Deformation dependences of recombination parameters at high excitation levels

InSb				
P, kbar	τ_R, 10^{-8} s	τ_A, 10^{-9} s	τ, 10^{-9} s	η, %
0	5.0	1.5	1.5	3
0.37	4.9	1.9	1.8	4
0.74	4.5	2.5	2.4	5
1.13	4.0	3.3	3.1	8
1.50	3.5	4.4	3.9	11
2.24	2.5	7.8	6.0	24
2.98	1.7	14	7.7	46
4.47	0.9	54	7.7	86

ough etching of the InSb surface), the solution to Eq. (4) with the boundary condition (5) is easily obtained. Using this solution, we represent the intensity of radiative band-to-band recombination, I, as a function of the excitation level L:

$$I = B_R\int_0^{\infty}[\delta p(x)]^2 dx \propto A^{(\beta-2)/(\alpha+\beta+1)} \times B^{(-\alpha-3)/(\alpha+\beta+1)} L^{(\alpha-\beta+5)/(\alpha+\beta+1)}. \qquad (6)$$

Here, B_R is the coefficient of radiative band-to-band recombination; $B_R = 1/\delta n\tau_R$.

Comparison of (6) with the experimental data in Fig. 3 shows that the Shockley–Reed recombination dominates at relatively low excitation levels, $L < L_0$, where L_0 corresponds to an excess carrier density $\delta n \approx (5–7) \times 10^{16}$ cm^{-3}, and $\beta = 1$. The deviation of the experimental curve from the $I \propto L^2$ dependence given by simple theory can be understood with account of the $D_a = D_p(1 + \mathcal{E}_F/T)$ dependence, where $\mathcal{E}_F$ is the Fermi energy for electrons, and D_p is the diffusion coefficient for holes. When the electron density is relatively low and the conduction band can be considered parabolic, $D_a \propto \delta n^{3/2}$. Hence, the relation $I \propto L^{1.7}$ follows, which is close to the experimentally observed dependence. However, at higher excitation levels, the experimental curve $I \propto L^{0.5}$ corresponds with good precision to $\alpha \approx 0$, $\beta \approx 3$. Apparently, this is accounted for by the fact that the Kane spectrum of the conduction band strongly deviates from the quadratic dependence at high electron densities, tending towards a linear one. Consequently, the $\mathcal{E}_F(\delta n)$ dependence is essentially weaker than that for the parabolic band. Thus, that portion of the $I(L)$ curve which is characterized by the $L^{0.5}$ dependence can be reliably related to the predominance of the Auger recombination. As stated above, the rate of Auger recombination decreases with increasing elastic stress. Evidently, this is exactly the reason why the bending points in the curves in Fig. 3 shift to a higher excitation level with increasing P.

Equation (6) allows estimation of the $I(P)$ dependence for a given L value. For the L range, in which the Auger recombination dominates, we obtain from (6)

$$I(P) \propto B_R/B_A^{3/4} \propto (\tau_A^{3/4}/\tau_R)\delta n^{1/2}. \qquad (7)$$

Here, B_A is the Auger coefficient, and $B_A = 1/\delta n^2\tau_A$. As stated above, B_R grows with increasing P (see Eq. (1)). Let us consider in more detail the deformation dependence of B_A. At high excitation levels, $B_A = B_{An} + B_{Ap}$. Here, the two summands describe the processes with an energy transfer of about $\mathcal{E}_g$ to, respectively, an electron and a hole. Without deformation, $B_{An}/B_{Ap} \sim \mathcal{E}_g/k_BT$, because B_{Ap} is defined by the process involving a hole transition between the light and heavy hole subbands. The low probability of such a transition is determined by the small value of the overlap integral between the states of heavy and light hole subbands. At the same time, a similar overlap integral between two electron states for the process described by B_{An} is close to unity. Therefore, Auger processes with energy transfer to a hole are insignificant at $T = 77$ K. As mentioned above, B_{An} decreases with increasing P. Thus, it follows from the relations presented above that the intensity of IR band-to-band emission must grow with increasing P.

In the range of high L, where the Auger recombination is dominant, Eq. (7) can be written in an illustrative form:

$$I(P) \propto (\eta/\tau_A^{1/4})\delta n^{1/2}. \qquad (8)$$

Consequently, the rise in the recombination radiation intensity with increasing elastic stress is closely associated with the increase in the quantum efficiency η. However, as soon as the stress causes a change of the dominant recombination mechanism and the quantum efficiency tends to unity, the rise in $I(P)$ becomes slower and the function levels off. As seen from the data presented in Tables 1 and 2, this change occurs at a lower compression for relatively low excitation intensities. At the same time, for high excitation intensity, the mentioned stresses are close to the ultimate strength of the crystal. Therefore, according to (8), the $I(P)$ dependence must be represented by a curve with levelling off, at relatively low excitation levels, while at high L the intensity of recombination emission grows with increasing P in virtually the entire experimentally accessible range of elastic stresses.

The experimental deformation dependences $I(P)$ presented in Fig. 4 correlate well with the relations given above. Noteworthy is the fundamental difference between curves *1–3*. At small L, the $I(P)$ dependence levels off at $P \gtrsim 2$ kbar (curve *1*), whereas under maximal excitation, a superlinear function is observed (curve *3*), with I increasing severalfold as compared with its initial value. It should be noted that the general run of the $I(P)$ curves at a high excitation level (curve *3*) is absolutely identical for all of the InSb samples studied. This means that the decisive influence is exerted

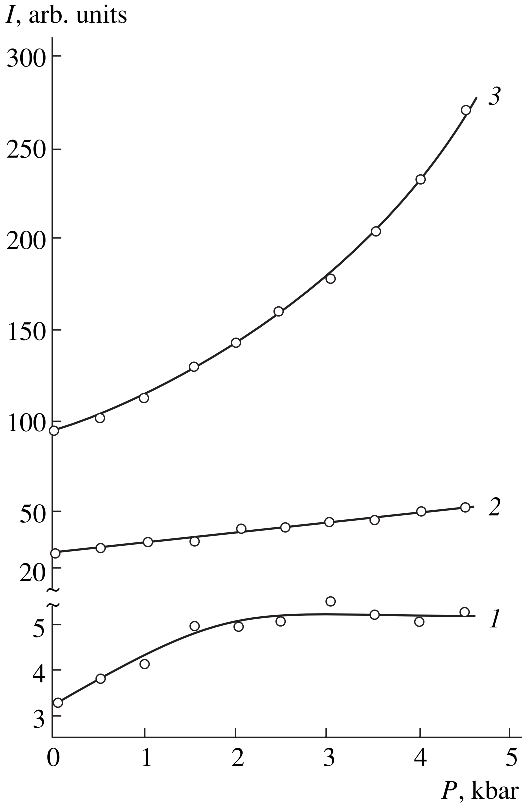

Fig. 4. Deformation dependences of band-to-band emission intensity in n-InSb at different excitation levels, L: (*1*) 5.0×10^{21}, (*2*) 3.0×10^{22}, and (*3*) 2.8×10^{23} photons $\mathrm{cm}^{-2}\ \mathrm{s}^{-1}$.

here by the high density of nonequilibrium current carriers, which ensures domination of the Auger transitions in the recombination processes, rather than by the initial parameters of a crystal. On the other hand, the run of curve *1* (curves *1* also appeared to be qualitatively similar for different samples) indicates the insignificant contribution of the Auger transitions to total recombination in the initial crystal ($P = 0$) at low excitation levels. In this case, the rise in I with increasing P is due only to the growing rate of radiative band-to-band transitions. Curve *2* should be referred to as an intermediate case. The run of curve *3* also suggests that the value $P = 4.5$ kbar, achieved in our experiments, is insufficient and fails to exhaust the potentialities of the elastically strained state with regard to raising the quantum efficiency of IR recombination emission in narrow-gap semiconductors. To our knowledge, the reported nondestructive elastic stresses are at least 5–5.5 kbar for InSb [6, 14] and 3.5–4.2 kbar for $Cd_xHg_{1-x}Te$ [6, 15].

It is noteworthy that a semiconductor structure elastically strained to a required extent can be easily obtained technologically. This can be done, e.g., by using the lattice mismatch between the substrate and the deposited active epitaxial layer of the main material. Another possibility is based on the difference between the linear expansion coefficients of the materials.

Thus, the theoretical estimations and experimental data presented above demonstrate that the nonradiative band-to-band recombination is suppressed in the elastically strained state, and the quantum efficiency of IR emission markedly increases owing precisely to this mechanism. This effect allows substantial modification of the parameters of narrow-gap semiconductors, thus widening the applicability limits of these materials as IR emitters.

ACKNOWLEDGMENTS

We are grateful to F.T. Vas’ko for helpful discussions.

REFERENCES

1. R. N. Zitter, A. S. Strauss, and A. E. Attard, Phys. Rev. **115**, 266 (1959).
2. N. S. Baryshev, V. L. Gel’mont, and M. I. Ibragimova, Fiz. Tekh. Poluprovodn. (Leningrad) **24**, 209 (1990) [Sov. Phys. Semicond. **24**, 127 (1990)].
3. A. V. Germanenko, G. M. Min’kov, and O. É. Rut, Fiz. Tekh. Poluprovodn. (Leningrad) **21**, 2006 (1987) [Sov. Phys. Semicond. **21**, 1216 (1987)].
4. F. T. Vas’ko, S. G. Gasan-zade, M. V. Strikha, and G. A. Shepel’skiĭ, Pis’ma Zh. Éksp. Teor. Fiz. **50**, 287 (1989) [JETP Lett. **50**, 318 (1989)].
5. S. G. Gasan-zade and G. A. Shepel’skiĭ, Fiz. Tekh. Poluprovodn. (St. Petersburg) **27**, 1326 (1993) [Semiconductors **27**, 733 (1993)].
6. A. V. Germanenko and G. M. Minkov, Phys. Status Solidi B **184**, 9 (1994).
7. G. L. Bir and G. E. Pikus, *Symmetry and Strain-Induced Effects in Semiconductors* (Nauka, Moscow, 1972; Wiley, New York, 1974).
8. F. T. Vas’ko, S. G. Gasan-zade, M. V. Strikha, and G. A. Shepel’skiĭ, Fiz. Tekh. Poluprovodn. (St. Petersburg) **29**, 708 (1995) [Semiconductors **29**, 368 (1995)].
9. B. L. Gel’mont, Z. I. Sokolova, and I. N. Yassievich, Fiz. Tekh. Poluprovodn. (Leningrad) **16**, 592 (1982) [Sov. Phys. Semicond. **16**, 1067 (1982)].
10. F. T. Vas’ko and M. V. Strikha, Fiz. Tekh. Poluprovodn. (Leningrad) **24**, 1227 (1990) [Sov. Phys. Semicond. **24**, 773 (1990)].
11. E. V. Bahanova, M. V. Strikha, and F. T. Vas’ko, Phys. Status Solidi B **164**, 157 (1991).
12. V. K. Malyutenko, S. S. Bolgov, V. I. Pipa, and V. I. Chaĭkin, Fiz. Tekh. Poluprovodn. (Leningrad) **14**, 781 (1980) [Sov. Phys. Semicond. **14**, 457 (1980)].
13. S. S. Bolgov and L. L. Fedorenko, Fiz. Tekh. Poluprovodn. (Leningrad) **21**, 1188 (1987) [Sov. Phys. Semicond. **21**, 722 (1987)].
14. R. Bishof, I. Maran, and W. Seidenbusch, Infrared Phys. **34**, 345 (1993).
15. F. T. Vas’ko, S. G. Gasan-zade, V. A. Romaka, and G. A. Shepel’skiĭ, Pis’ma Zh. Éksp. Teor. Fiz. **41**, 100 (1985) [JETP Lett. **41**, 120 (1985)].

Translated by D. Mashovets

Semiconductors, Vol. 36, No. 4, 2002, pp. 410–413. Translated from Fizika i Tekhnika Poluprovodnikov, Vol. 36, No. 4, 2002, pp. 433–436.
Original Russian Text Copyright © 2002 by Vikhrov, Vishnyakov, Maslov, Mishustin.

ELECTRONIC AND OPTICAL PROPERTIES OF SEMICONDUCTORS

Analysis and Refinement of Mathematical Tools for Modified Time-of-Flight Method

S. P. Vikhrov*, N. V. Vishnyakov, A. A. Maslov, and V. G. Mishustin
Department of Microelectronics, Ryazan State Academy of Radio Engineering, Ryazan, 391000 Russia
**e-mail: mel@rgrta.ryazan.ru*

Submitted August 29, 2001; accepted for publication October 18, 2001

Abstract—The modified time-of-flight method for direct measuring of the electric field profile in the space-charge region of the Schottky-type contacts is theoretically substantiated. A technique is developed for disordered semiconductors, such as hydrogenated amorphous silicon. The mathematical tools for calculation of the field profile are refined, the obtained results are analyzed, and applicability limits of the modified time-of-flight technique are demonstrated. © *2002 MAIK "Nauka/Interperiodica".*

1. INTRODUCTION

Experiments with the use of the time-of-flight (TOF) technique are widely discussed in the literature [1–6]. The aim of this experiment is to measure the time necessary for a photoinjected packet of charge carriers to move from one boundary of the sample to another.

The basic TOF experiment feasibility condition is smallness of the transit time in comparison with that necessary for screening of the photoinduced space charge. The dielectric relaxation time $t_{\rm rel} = \varepsilon_s\varepsilon_0/\sigma$ exceeds $t_{\rm tr}$ significantly due to the low conductivity of disordered semiconductors, which provides the opportunity to measure the drift mobility $\mu_{\rm dr}$ and the mobility–lifetime product $\mu\tau$ for both types of carriers by changing the polarity of the applied voltage.

The Gecht TOF technique consists in measuring a charge Q collected on electrodes during the drift of a small charge Q_0 photoexcited by a short light pulse. The smallness of the charge is determined relative to the charge inducing the external field. Then, the charge collection coefficient is defined by

$$G = \frac{Q}{Q_0} = \frac{\mu\tau E}{d}\left(1 - \exp\left(-\frac{d}{\mu\tau E}\right)\right), \tag{1}$$

where d is the interelectrode spacing, and E is the mean electric field in the sample, and $\mu\tau E$ is the drift length.

This technique enables measurement of $\mu\tau$ for electrons and holes separately by changing the voltage polarity, in the case of strongly absorbed light, and the sandwich configuration of the electrodes. Exact knowledge of the number of absorbed photons and the quantum yield of internal photoeffect is not necessary. Ohmic contacts are not necessary for the experiment: the sample can be placed between insulators. It is also important to note that $\mu\tau_{\rm TOF}$ is determined in the Gecht technique not only by mutual recombination of the photoexcited pairs, but also by the capture of carriers by deep traps.

The dependence of the charge collected at electrodes on the applied field should be measured in order to determine $\mu\tau_{\rm TOF}$. When the drift length becomes equal to the interelectrode spacing, the collected charge is equal to that photogenerated in the sample. The $\mu\tau$ value is determined by the field at which the entire amount of charge is collected (Fig. 1):

$$\mu\tau_{\rm TOF} = \frac{d}{E}. \tag{2}$$

However, the experimentally measured dependences and the results of calculation with the use of (2) disagree. This discrepancy is due to the closeness of the following values: exciting light wavelength, field penetration depth, drift and diffusion lengths, and layer thickness. This circumstance complicates the interpretation of the measured dependences.

A modification of the technique proposed by Juska [1] consists in that the coefficient G of the photogenerated charge collection and the electric field profile in

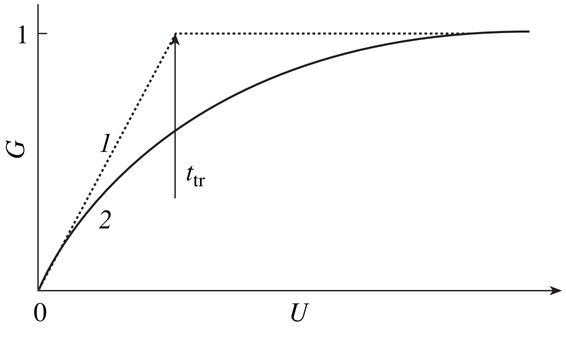

Fig. 1. Charge collection coefficient vs. the applied voltage. (*1*, *2*) Calculation without and with account of carrier capture by deep levels, respectively [2].

the space charge region (SCR) of a disordered semiconductor are measured instead of the carrier transit time between the electrodes, as is done in traditional time-of-flight experiments. This enables the measuring of the mobility lifetime product $\mu\tau$ for electrons and calculating the density of states $g(E)$ in the energy gap of disordered semiconductors with higher precision in comparison with the traditional TOF method. The sensitivity of the method is higher, since the kinetics of the drift current of the photogenerated carriers is measured in the integral regime. The method excludes the influence of the shallow traps, which lead to dispersive transport and complicate the interpretation of results when the kinetics of current are observed directly.

2. METHOD FOR MEASUREMENT OF THE ELECTRIC FIELD DISTRIBUTION

The method for measuring the electric field, when the external voltage pulse is applied in the opposite direction to the internal field, is described in [1, 4, 5]. Theoretical analysis [1] has shown that further study of the offered method is necessary. The aim of the present work is to substantiate mathematically the modified TOF technique, to make more exact the mathematical tools for calculation of the electric field, and to compare the results obtained with those reported in [1].

The general problem is solved theoretically in [1] for the case when the external field is combined additively with the internal field; also, the possible diffusion in the direction opposite to the internal field toward the illuminated electrode with subsequent unlimited recombination is taken into account.

Let us describe the conditions of the experiment and analyze the modified TOF technique offered in [1].

1. The monochromatic light pulse excites a small charge Q_0, which does not essentially change the internal field $E_i(x)$ distribution, i.e., $Q_0 \ll \frac{\varepsilon\varepsilon_0}{d}\int_0^d E_i(x)dx$. The validity of this condition can be verified experimentally by the independence of the charge collection coefficient G on the magnitude of the photogenerated charge.

2. The external electric field is subtracted from the internal one; i.e., the structure is illuminated by the light pulse after the external voltage is switched on, but before any redistribution of the field in the structure. The delay time t_{del} between the voltage switching-on and the light pulse is within the range $RC < t_{\text{del}} < t_{\text{rel}}$, where RC is the time constant of the integrating circuit. The validity of this condition is verified by the independence of the signal from t_{del}.

3. The effect of the surface states is disregarded in the calculations.

4. Charge carriers of only one sign (electrons) are taken into consideration; we neglect the influence of holes.

Let us carry out a mathematical analysis of the technique in order to refine the mathematical tools for the calculation of the photogenerated charge collection coefficient and the electric field profile in the SCR of a disordered semiconductor, which was proposed in [1].

According to the Bouguer–Lambert law of light absorption, the light flux intensity $I(x)$ at the distance x from the illuminated surface of the semiinfinite sample is expressed as a function of the absorption coefficient $\alpha(h\nu)$ in the form

$$I(x) = I_0(1-R)\exp(-\alpha x), \tag{3}$$

where $I(x)$ is the incident light intensity at the depth x, and I_0 is the intensity at the sample surface. Then, for the photogenerated carrier density (we consider only electrons), we can write

$$n(x) = N_0\exp(-\alpha x), \tag{4}$$

where N_0 is the photogenerated electron density in the surface region.

Let us consider the charge collection coefficient G_i for a single electron. It is assumed in [1] that the inequality $\mu\tau E \gg d$ holds for high-quality layers of a-Si:H, where E is the mean electric field in the SCR. If the condition $G_i \longrightarrow 0$ is satisfied, then it is more appropriate to consider that $\mu\tau E \ll d$, where E is a superposition of the oppositely directed internal and external fields. Then, we can neglect the second term in (1):

$$G_i = \mu\tau d^{-1}(x_c - x_g)^{-1}\int_{x_g}^{x_c}\left(E_i(x) + \frac{U}{d}\right)dx, \tag{5}$$

where x_g is the place of generation of an electron ($0 \le x_g \le d$), and x_c is the point where the drift ends (in the section x, the external field exactly compensates the internal field, so that the resulting field $E_i(x_c) + \frac{U}{d} = 0$ (Fig. 2)). The total charge collection coefficient for all electrons then reads

$$G(U,\alpha) = \frac{\sum_{i=1}^{Q_0/e} G_i}{Q_0/e} = \frac{\int_0^d n(x)G_i(x)dx}{\int_0^d n(x)dx} = \frac{(1-R(U,\alpha))\alpha\mu\tau}{(1-\exp(-\alpha d))d} \tag{6}$$

$$= \int_0^d \frac{\exp(-\alpha x_g)}{x_c - x_g}\int_{x_g}^{x_c}\left(E_i(x) + \frac{U}{d}\right)dx\,dx_g,$$

where $R(U, \alpha)$ is a coefficient taking account of the portion of electrons that avoided recombination because of the diffusion against the field:

$$R(U,\alpha) \ge \left(1 + \frac{\alpha\varphi_T}{E_i(0) + U/d}\right)^{-1}, \tag{7}$$

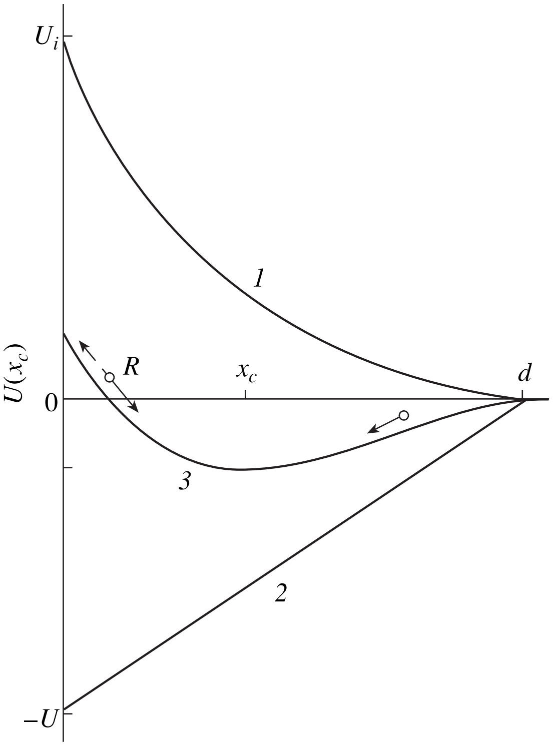

Fig. 2. Potential distribution across the sample thickness. (*1*) Internal potential, (*2*) external potential, and (*3*) total potential.

where $\varphi_T = kT/e$ is the thermal potential [1].

The formula (6) is distinct from the similar expression in [1]. This is due to the use of the condition $\mu\tau E \ll d$, which, in our opinion, is more correct for a mathematical description of the Gecht technique.

It is noteworthy that the distribution of the electric field $E_i(x)$ or the built-in potential U_i and the structure thickness d must be known in order to determine $\mu\tau$.

The presence of the contact field near the illuminated surface enhances separation of photogenerated carriers. However, the field penetration depth is determined by the density of localized states at the Fermi level, i.e., by the states that govern the carrier lifetime. The localized states essentially influence the formation of potential barriers in disordered semiconductors. The space charge and the potential $\varphi(x)$ and field $E_i(x)$ profiles in the SCR are determined not only by the ionized impurities, as in the case of crystalline semiconductors, but also by the density-of-states distribution within the mobility gap. That is why measuring the electric field distribution $E_i(x)$ in the SCR furnishes an opportunity to obtain the distribution law of the localized states, which determine basic electrical properties of disordered semiconductors [7–10].

The calculation of $G(U, \alpha)$ allowed us to propose a method for measuring the field distribution in the structure. A relation between the absorption coefficient $\alpha(h\nu)$ and the place of drift termination x_c must be established to this end:

$$L_{dr} = \mu\tau\bar{E} = \frac{\mu\tau}{L_{dr}}\int_0^{L_{dr}}\left(E_i(x) + \frac{U}{d}\right)dx = \frac{\mu\tau}{x_c - x_g}\int_{x_g}^{x_c}\left(E_i(x) + \frac{U}{d}\right)dx. \tag{8}$$

Hence, it follows that

$$\int_{x_g}^{x_c}\left(E_i(x) + \frac{U}{d}\right)dx = \frac{(x_c - x_g)^2}{\mu\tau}. \tag{9}$$

Then, (6) can be rewritten as

$$G(U, \alpha) = \frac{(1 - R(U, \alpha))\alpha}{(1 - \exp(-\alpha d))d} \times \int_0^d \exp(-\alpha x_g)(x_c - x_g)dx_g. \tag{10}$$

If $G(U, \alpha) = 0$, then

$$x_c = \frac{1}{\alpha} - \frac{d\exp(-\alpha d)}{1 - \exp(-\alpha d)}. \tag{11}$$

The formula (11) exactly reproduces the result obtained in [1], notwithstanding the fact that the boundary conditions and intermediate calculations are not the same (see (5) and (6)). The obtained results confirm the validity of (11) for the calculation of the electric field distribution across the sample thickness.

This dependence allows us to calculate the coordinate of the point at which the resulting field vanishes at a given exciting light wavelength and $G(U, \alpha) = 0$.

The internal electric field at the point x_c is given by

$$E_i(x_c) = \frac{U_{G(U,\alpha) = 0}}{d}. \tag{12}$$

Analysis of (11) shows that the possibility of measuring the field across the sample thickness is limited. At small wavelengths of the exciting light, x_c is determined mainly by the first term $1/\alpha$ and has a value of about 0.1 μm (α reaches values on the order of 10^5 cm^{-1}). At long wavelengths, x_c is limited to half the sample thickness:

$$\lim_{\alpha \to 0} x_c = \lim_{\alpha \to 0}\left(\frac{1}{\alpha} - \frac{d\exp(-\alpha d)}{1 - \exp(-\alpha d)}\right) = \frac{d}{2}. \tag{13}$$

Thus, in contrast to [1], the applicability range of (11) is not only limited by the middle of the sample, but also does not include a region near the surface. This follows from the presence of surface states, whose effect is disregarded in our calculations [4].

The electric field distribution in the structure is calculated using (12) by substituting $U_{G(U,\alpha)=0}$ values obtained at various wavelengths of exciting light. The coordinate x_c, reckoned from the illuminated surface of the structure, is calculated using (11). It is necessary to know $\alpha(h\nu)$ for a concrete structure in order to obtain the distribution $E_i(x)$.

Thus, independent calculation confirmed the validity of formula (11), obtained in [1], for measuring the electric field distribution in SCR of the contact between the metal and the disordered semiconductor. It is shown that application of the condition $\mu\tau E \ll d$ more accurately characterizes the modified TOF technique. The detailed analysis of the mathematical tools revealed coordinate limitations in using (11): the coordinate x_c of the drift termination is determined by the absorption coefficient α at short wavelengths and is limited to half the sample thickness at longer wavelengths. Further experimental studies using the TOF technique should be carried out taking into account the results of this work.

ACKNOWLEDGMENT

This study was supported by grant for scientific research 18-01G of the Ministry of Education of the Russian Federation.

REFERENCES

1. G. B. Yushka and É. A. Montrimas, Litov. Fiz. Sb. **32**, 612 (1992).
2. A. Madan and M. Shaw, *The Physics and Applications of Amorphous Semiconductors* (Academic, Boston, 1988; Mir, Moscow, 1991).
3. T. Tiedje, in *The Physics of Hydrogenated Amorphous Silicon*, Vol. 2: *Electronic and Vibrational Properties*, Ed. by J. D. Joannopoulos and G. Lucovsky (Springer-Verlag, New York, 1984; Mir, Moscow, 1988).
4. R. A. Street, Phys. Rev. B **27**, 4924 (1983).
5. R. A. Street, M. J. Thompson, and N. M. Johnson, Philos. Mag. B **51**, 1 (1985).
6. L. P. Pavlov, *Methods for Measuring the Parameters of Semiconducting Materials* (Vysshaya Shkola, Moscow, 1987).
7. S. P. Vikhrov, N. V. Vishnyakov, and A. A. Maslov, Izv. Vyssh. Uchebn. Zaved., Élektron. **3**, 48 (2000).
8. O. A. Golikova and M. M. Kazanin, Fiz. Tekh. Poluprovodn. (St. Petersburg) **33**, 110 (1999) [Semiconductors **33**, 97 (1999)].
9. O. A. Golikova and M. M. Kazanin, Fiz. Tekh. Poluprovodn. (St. Petersburg) **33**, 336 (1999) [Semiconductors **33**, 335 (1999)].
10. V. P. Afanas’ev, A. S. Gudovskikh, O. I. Kon’kov, *et al.*, Fiz. Tekh. Poluprovodn. (St. Petersburg) **34**, 492 (2000) [Semiconductors **34**, 477 (2000)].

Translated by S. Ktitorov

Semiconductors, Vol. 36, No. 4, 2002, pp. 414–419. Translated from Fizika i Tekhnika Poluprovodnikov, Vol. 36, No. 4, 2002, pp. 437–442.
Original Russian Text Copyright © 2002 by Torkhov.

SEMICONDUCTOR STRUCTURES, INTERFACES, AND SURFACES

Causes of Variation in the Static Current–Voltage Characteristics of the Structures with the Me/*n*–n^+-GaAs Schottky Barrier on Hydrogenation

N. A. Torkhov

Research Institute of Semiconductor Devices, Tomsk, 634045 Russia

e-mail: tna@ic.tsu.ru

Submitted June 19, 2001; accepted for publication September 9, 2001

Abstract—Causes of a decrease in the ideality factor n and an increase in the reverse voltage U_r for the structures with the Schottky barrier (SB) Au/n–n^+-GaAs due to treatment in atomic H were investigated. It was found that the treatment of n–n^+-GaAs in atomic hydrogen induces two processes, which lead to an increase in the reverse voltage U_r and a decrease in the ideality factor n for SB structures. On the one hand, U_r increases and n decreases due to lowering the concentration profile and formation of the inverse concentration gradient of an ionized shallow-level donor impurity in the n layer. This is caused by the passivation of the impurity with H. On the other hand, U_r increases and n decreases due to the formation of a thin (~8 nm) semi-insulating surface layer. In both cases, U_r increases and n decreases owing to an increase in the effective width of the potential barrier at the metal–semiconductor contact as a result of variation in the shape of the concentration profile for the ionized shallow-level donor impurity. *© 2002 MAIK "Nauka/Interperiodica".*

1. INTRODUCTION

It has been reported repeatedly that atomic H can substantially affect the electric properties of n-GaAs epilayers [1–3]. In this case, the variation of static device characteristics of the structures with the Me/n–n^+-GaAs Schottky barrier (SB) was observed [4–6]. Treatment of n–n^+-GaAs epitaxial structures in various H plasmas (RF plasma, power density $P = 0.02$ W/cm^2 [7]; low-frequency plasma, 30 kHz, $P = 0.08$ W/cm^2 [8]) and in the atomic H flow (AH treatment) [9, 10] can decrease the ideality factor n and increase the reverse voltage U_r of Me/n–n^+-GaAs SB diode structures. It was assumed that a decrease in n can be caused by formation of the region depleted of electrons in the vicinity of the n-layer surface [7]. Another assumption concerning the possibility of formation of a thin semi-insulating surface layer due to AH treatment (hydrogenation) of GaAs, which leads to the unusual behavior of capacitance–voltage (C–V) characteristics of SB diode structures, was suggested in [11]. According to [12], an increase in the reverse voltage of hydrogenated diode structures can also be related to a decrease in the conductance of the thin surface layer as a result of variation in its physicochemical properties under the effect of atomic H. This leads to the distortion of the potential of the metal–semiconductor contact. In addition to the aforesaid, other assumptions concerning the cause of variations in the static current–voltage (I–V) characteristics of SB diodes exist. Thus, is has been supposed that a decrease in n and an increase in U_r can be associated with suppressing the electrical activity of surface defects, which introduce deep levels in the band gap [7, 9]. It is the opinion of the authors of these publications that this should lead to the improvement of the characteristic of the diode structure. It was reported that the n-GaAs surface is efficiently passivated in atomic H [3, 10, 11]. More recent data indicated that the effect of atomic H on the surface and a surface region of n-GaAs epilayers could be profound enough to affect not only electrochemical properties of the material [10] but also its structure [11]. Most likely, this should cause variations in static I–V characteristics. It was demonstrated later that the n-GaAs surface layer [13], similarly to Si [14], is amorphized under the effect of atomic H. Thus, in spite of a multitude of assumptions suggested, no sufficiently complete notion exists of processes during AH treatment that lead to an increase in U_r for a certain current and to a decrease in n in SB structures. In this context, interest has emerged in further investigations in this direction.

In this study, forward and reverse static I–V characteristics for SB diodes with a thin semi-insulating surface layer between the barrier contact and n-GaAs are calculated. Variation in the shape of the concentration profile of the ionized shallow-level donor impurity in the n layer is taken into account. For this purpose, the recently developed theory of charge transport of hot carriers was used [15, 16]. The mechanisms of carrier transport in these structures, which lead to the emergence of bending (knee) in the reverse portion of the static I–V characteristic, are described. These mechanisms are related to the formation of a thin semi-insulating surface layer under the effect of atomic H. It is also demonstrated in the study that a thin semi-insulating surface layer apparently consists of amorphized *n*-GaAs.

2. CALCULATION PROCEDURE AND EXPERIMENT

In order to calculate the forward and reverse *I–V* characteristics for the Au/*n*–n^+-GaAs structures, the model of charge transport in SB metal–semiconductor contacts suggested previously was used [15]. The contact potential was determined from the Poisson equation with allowance made for image forces. In order to determine the tunneling probability for electrons $\tilde{T}(E)$, the transfer-matrix method was used. The special feature of the model is the fact that not only electron tunneling through the potential barrier but also the motion in the above-barrier region is taken into account when calculating $\tilde{T}(E)$. The allowance made for above-barrier electron motion permits one to achieve good agreement between theoretical and experimental *I–V* characteristics, especially in the region of large reverse currents for voltages close to those corresponding to breakdown [15]. This is not the case with the use of conventional techniques. The following expression was used for the calculation of the current density:

$$I(E) = \frac{4\pi q m^* kT}{\hbar^3} \times \int_0^\infty \tilde{T}(E)\ln\left[\frac{1+\exp[(E_F-E)/kT]}{1+\exp[(E_F-E-qU)/kT]}\right]dE. \qquad (1)$$

Here, q is the elementary charge, m^* is the effective electron mass, k is the Boltzmann constant, T is temperature, $\hbar$ is the Plank constant, E is the electron energy, E_F is the Fermi level, and U is the potential drop. For reverse biases U_r ($U < 0$), energy was counted from the Fermi level in the metal, and for forward biases U_f ($U > 0$), energy was counted from the Fermi level in the semiconductor.

Static *I–V* characteristics were measured for Au/*n*–n^+-GaAs structures, which were fabricated according to the procedure reported in detail by Torkhov and Eremeev [10]. The density of ionized shallow-level donor impurities of Sn (N_D^+) and the thickness of the *n* layer (w) for $\tilde{T}(E)$ calculations were determined using the *C–V* technique at a frequency of 1 MHz and were found to be $N_D^+ = 3.5 \times 10^{16}$ cm^{-3} (Figs. 1a, 2a) and $w = 0.5$ μm. The concentration in the n^+ layer was 2×10^{18} cm^{-3}. The samples were treated in an atomic H flow in the installation described previously [9, 10] using an atomic H source for 5 min at temperatures T_{tr} = 50–400°C through a protecting SiO$_2$ film ~5 nm thick. The source was based on the arc reflection discharge with a hollow cathode and a self-incandescence element. The protecting SiO$_2$ film was formed on the *n*-layer side during the technical process of preparing the samples for AH treatment. Barrier Au contacts 325 μm in diameter were formed on the *n*-layer side of the samples subsequent to AH treatment. The samples which were not AH-treated are denoted as starting ones in Figs. 1–3 and in the text. The reverse voltages U_r were measured at the current of 10 μA.

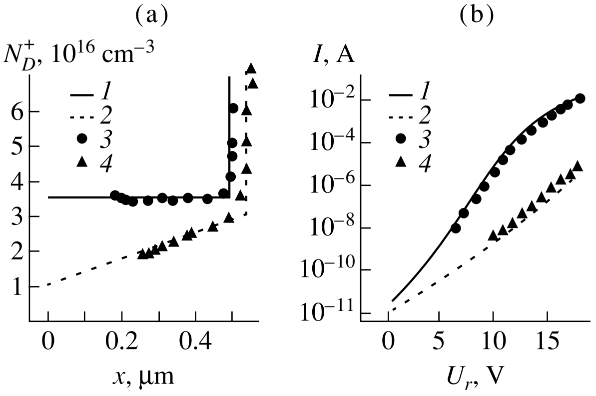

Fig. 1. Concentration profiles of (a) ionized shallow-level donor impurity and (b) reverse portions of current–voltage characteristics of Au/*n*–n^+-GaAs diode structures: (*1*, *2*) calculation and (*3*, *4*) experiment for (*1*, *3*) the starting sample and (*2*, *4*) the sample AH-treated at T_{tr} = 200°C.

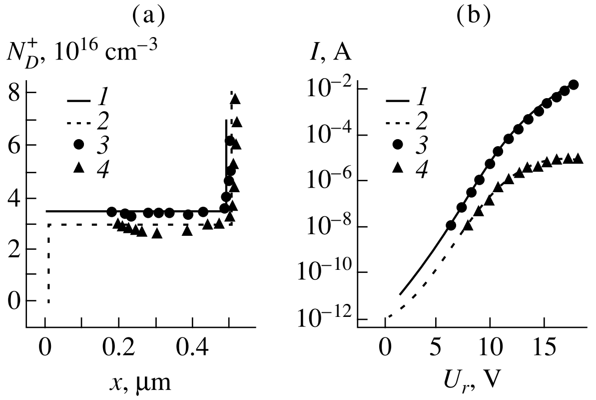

Fig. 2. Concentration profiles of (a) the ionized shallow-level donor impurity and (b) reverse portions of current–voltage characteristics of Au/*n*–n^+-GaAs diode structures: (*1*, 2) calculation and (*3*, *4*) experiment for (*1*, *3*) the starting sample and (*2*, *4*) the sample AH-treated at T_{tr} = 400°C.

The SB height φ was determined using the *C–V* technique at a frequency of 1 MHz. It was equal to φ_{eff} = 0.845 eV for diode structures without hydrogenation. Note that, according to [10], the SB height in almost perfect Au/*n*–n^+-GaAs structures varies only slightly under the effect of atomic H. The calculations were carried out with allowance made for a decrease in the potential barrier height due to the effect of image

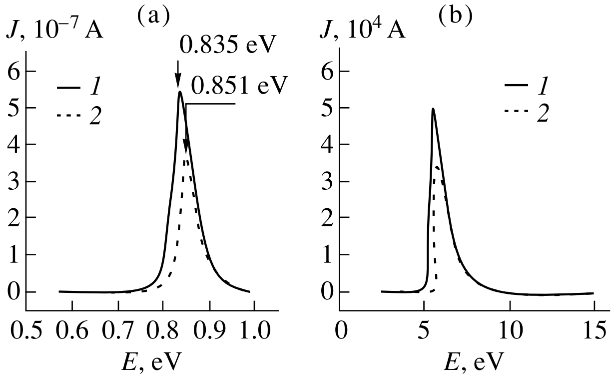

Fig. 3. Dependences of the current density $J(E)$ on electron energy E with the forward bias. (a) U_f = +0.01 V: (*1*) The starting sample, (*2*) the sample treated at $T_{\rm tr}$ = 200°C. (b) U_f = +0.65 V: (*1*) The starting sample and (*2*) the sample treated at $T_{\rm tr}$ = 200°C.

forces ($\Delta\varphi_G$). In this case, the starting value φ_{b0} = 0.87 eV was used: $\varphi_{\rm eff} = \varphi_{b0} - \Delta\varphi_G$. The ideality factor n was determined from the slope of the forward portion of the I–V characteristic on the semilog scale:

$$n = \frac{q}{kT}\frac{\partial U}{\partial(\ln I)}. \quad (2)$$

According to the results of our investigations, the thickness of the low-conductivity surface region (semi-insulating layer) is the determining quantity in calculations of forward and reverse I–V characteristics with the presence of such a region. Thus, according to estimations, a decrease in the N_D^+ density in the narrow surface layer from 10^{15} cm^{-3} by almost an order of magnitude leads to variation in the reverse currents by no more than 20 %. At the same time, variation in the layer thickness by 10 % leads to variation in the reverse currents by several times. For this reason, it is my opinion that the value $N_D^+ = 10^{15}$ cm^{-3}, which was used in calculations for a thin semi-insulating surface layer, is quite realistic.

The thickness of the surface region, which was amorphized under the effect of atomic H, was determined from structure investigations by reflection high-energy electron diffraction using an ÉMR-102 electron diffractometer and was found to be ~8 nm [13].

3. RESULTS AND DISCUSSION

3.1. Increase in the Reverse Voltage

As was reported previously [8, 9, 11], hydrogenation can lead to an increase in the reverse voltage of SB diode structures based on n-GaAs. For unprotected samples, a temperature range of treatment exists, $T_{\rm tr}$ = 150–200°C, for which a maximum is observed in the $U_r(T_{\rm tr})$ dependence. An increase in $T_{\rm tr}$ to 400°C leads to a decrease in U_r. On the one hand, a decrease in U_r is caused by the recovery of the starting concentration N_D^+, and, on the other hand, it is caused by the possible surface damage. With the presence of the protective, 5-nm-thick SiO$_2$ film on the surface of the n-GaAs layer during AH treatment, the increase in $T_{\rm tr}$ to 400°C leads to a further increase in U_r rather than to its decrease. In this case, two portions can be separated in the $U_r(T_{\rm tr})$ dependence. The first portion corresponds to the temperature range of 50–200°C, in which the $U_r(T_{\rm tr})$ dependence nearly coincides with the dependence for the unprotected surface. The coincidence of temperature dependences $U_r(T_{\rm tr})$ for protected and unprotected surfaces apparently points to the common character of the processes, which proceed during hydrogenation. According to the results obtained (Fig. 1b), in both cases U_r increases due to lowering of the profile of electrically active shallow-level donor impurities in the n-GaAs layer (Fig. 1a). The second portion corresponds to the temperature range of 200–400°C and, as was mentioned above, differs from $U_r(T_{\rm tr})$ for the case of an unprotected surface in this range; namely, U_r continues to increase. In this case, a bend emerges in the $I(U_r)$ dependence on the semilog scale (Fig. 2b).

In the region of small currents (for U_r < 10 V), the reverse current I increases with the rise of U_r due to an increase in the extension of the space charge region (SCR) w:

$$I(U_r) = I[w(U_r)]. \quad (3)$$

A further increase in U_r leads to the deviation from dependence (3), i.e., to a decrease in the slope of the $I(U_r)$ curve with increasing voltage. In this case, the behavior of $I(U_r)$ can no longer be explained by a decrease in the free carrier density in the n layer and by the expansion of the SCR. The reason is that, according to [9], the free carrier density increases rather than decreases with increasing $T_{\rm tr}$ above 300°C. At $T_{\rm tr}$ = 400°C, the dopant density for structures hydrogenated virtually coincides with the starting one. In this case, an increase in U_r is probably caused by the formation of a thin surface layer with a low free carrier density under the effect of atomic H (Fig. 2a). Due to specific properties of this layer, the N_D^+ concentration, in contrast with the bulk, does not recover with increasing $T_{\rm tr}$. Conversely, it most likely decreases even more. The specific properties of the surface n-GaAs layer (8 nm) are probably determined by the effect of the neighboring SiO$_2$/n-GaAs interface. The specificity of the effect of the SiO$_2$/n-GaAs interface during AH treatment on the properties of the surface region of the n-GaAs epilayer is reported in detail in [10, 11, 15]. A decrease in N_D^+ in the thin surface layer should lead to an increase in its resistance. This is demonstrated by the data of study [11], in which the requirements for obtaining a clear image using a scanning tunneling microscope with increasing T_{tr} to 400°C are reported. Specifically, it was necessary to increase the potential difference between the surface and the probe from 1.5 V for starting structures to 5 V after AH treatment at $T_{\mathrm{tr}} = 400°\mathrm{C}$ and to 7 V after AH treatment at $T_{\mathrm{tr}} = 200°\mathrm{C}$. In this case, the free carrier density in the bulk of the *n* layer approached the starting value [9, 10].

According to calculations carried out, the thickness of the semi-insulating surface layer Δx, which ensures agreement between experimental and theoretical results, is equal to ~8.3 nm. This virtually coincides with the thickness of the amorphized surface layer (~8 nm) which was determined experimentally (Fig. 2a). As a result, one may conclude that the low-conductivity thin surface layer is composed of the amorphized *n*-GaAs. One of the causes of the decrease in the free carrier concentration in the amorphized layer can be the high content of atomic H, which leads to the passivation of the electrically active shallow-level donor. At the same time, the decrease in N_D^+ can be caused by breaking the covalent bonds of atoms of the main matrix of the crystal during amorphization. This leads to destruction of the periodic structure and formation of more complex atomic bonds. The possibility of the reduction of the Sn valence due to a change in its electron-shell configuration is not excluded. All these factors can lead to the loss in the electrical activity of the Sn donor impurity and to a decrease in the conductivity of the amorphized layer.

According to [15], the current in the Me/n–n^+-GaAs structures with the reverse bias is primarily controlled by electron tunneling through the potential barrier. This is evidenced by the fact that, as U_r increases, the peak in the curve $J(E)$, where J is the current density for electrons with energy E, is shifted to the Fermi level of the metal barrier contact and actually coincides with it for U_r values close to those corresponding to breakdown. For this reason, the presence of a thin semi-insulating layer between the barrier contact and the diode base (*n* layer) can apparently affect the character of electron motion and, as a consequence, the form of the $I(U_r)$ dependence. Note that the thickness of this layer Δx is smaller than the effective potential-barrier width Δh_{eff}. Here, Δh_{eff} is the potential barrier width for energy E, for which the current density $J(E)$ is largest. Thus, the formation of a bend in the reverse portion of the *I–V* characteristic in the presence of the semi-insulating layer Δx thick is probably associated with the fact that the effective barrier width does not always decrease with increasing U_r. A decrease in Δh_{eff} with increasing U_r occurs if $\Delta x < w(U_r)$. In this case, $I(U_r)$ features the known dependence $I \propto \exp(qU_r/kT)$. For a certain U_r, Δx becomes comparable to $w(U_{\mathrm{eff}})$. A further increase in U_r no longer leads to a decrease in w and, consequently, in Δh_{eff}, which is now controlled by the thickness of the semi-insulating layer Δx. As a result, the effective barrier width Δh_{eff} becomes independent of the bias U_r, whereas the dependence $I(U_r)$ changes its character. This leads to the emergence of the bend:

$$I(U_r) = I(\Delta h_{\mathrm{eff}}). \tag{4}$$

In the case of an unprotected surface, the H content in the surface region is lower [17], and a low-conductivity layer is most likely not formed or turns out to be thin. The reason is that the efficient etching of *n*-GaAs is possible at a temperature of ~400°C in the H plasma. Etching of Ga and As on the surface of an *n* layer at such a temperature proceeds at an identical rate. On the one hand, this should prevent the violation of the stoichiometric composition of the surface. On the other hand, processes are possible at such a temperature which lead to the damage of the *n*-GaAs layer surface. One of these processes can be the formation of the As phase. It is known that As adatoms are highly mobile at a temperature of ~400°C, can easily diffuse over the surface, and coalesce into separate drops. As a result of this, as well as other possible damage to the unprotected surface, the $U_r(T_{\mathrm{tr}})$ curve passes through a maximum in the temperature range of 150–200°C with increasing temperature and then decreases, which is accompanied by an increase in *n*. The behavior of $I(U_r)$ for hydrogenated structures does not vary in this situation.

Thus, it is possible to conclude that at least two temperature-dependent processes occur during AH treatment of the structures based on n–n^+-GaAs and lead to an increase in the reverse voltage. The first process is characteristic of the temperature range of 50–200°C. The U_r voltage increases due to a decrease in the density of the ionized shallow-level donor impurity in the *n* layer, which is caused by the passivation of the impurity with H. Changes in the shape of the concentration profile leads to the distortion (broadening) of the potential in the vicinity of the surface and to a decrease in the reverse current, which confirms the inference drawn previously [11]. This process occurs at the surface both protected and unprotected during AH treatment of the *n*-GaAs layer. The second process is characteristic only of the surface of the *n* layer protected by the SiO_2 film and occurs in the temperature range of 200–400°C. In this case, an increase in U_r can be related to the formation of a thin amorphized surface layer with a low conductivity. The mechanism for increasing U_r in this case is the same as at $T_{\mathrm{tr}} = 50$–$200°\mathrm{C}$. Specifically, a decrease in N_D^+ in the subsurface region leads to an increase in the effective potential width. This is accompanied by a decrease in the reverse current and, consequently, an increase in U_r.

3.2. Decrease in the Ideality Factor

The results obtained previously [9, 10] can be indicative of the perfection of the Au/*n*-GaAs interface of starting structures and, as a consequence, the high quality of the diodes fabricated. This is also evidenced by our results of calculating the forward and reverse *I*–*V* characteristics of starting diode structures. These results are consistent with experiment. As was demonstrated previously [9, 15, 17], the ideality factor *n* for the almost perfect SB metal–semiconductor contact with a dopant concentration in the *n* layer of about (2–3.5) × 10^{16} cm^{-3} cannot differ considerably from the value of 1.04. It should be remembered that, in order to obtain a high-quality SB metal–semiconductor contact, the epilayer and barrier metallization must be formed in a single vacuum run using molecular-beam epitaxy [18]. As was mentioned above, AH treatment of the n–n^+-GaAs structures with a preliminarily prepared surface can lead to the amorphization of the surface and subsurface region [13]. A similar effect was also observed for Si [14]. For this reason, a decrease in *n* from 1.04 for starting samples to 1.01 for hydrogenated samples [9, 17] cannot be explained by the perfection of the barrier structure alone. Most likely, as was assumed in [7, 11], the shape of the concentration profile, which changes under the effect of atomic H due to the passivation of the electrically active donor impurity, can control variations in the static device characteristics.

It was mentioned above that there are two processes which determine the behavior of U_r. These processes depend on T_{tr} and on the presence or absence of a protective SiO_2 film on the surface of the *n* layer during the AH treatment. From this point of view, let us consider the effect of AH treatment on the behavior of the ideality factor for the Au/n–n^+-GaAs structures in relation to T_{tr}.

The calculation of the forward-current density *J*(*E*) demonstrated (Fig. 3) that a decrease in *n* for protected and unprotected surfaces at $T_{tr} \leq 200$°C is caused by the same factor, specifically, the bending of the potential $\varphi(x)$, which is caused by the formation of the inverse concentration gradient of N_D^+ in the *n* layer (Fig. 2a). A change in the shape of the concentration profile leads to an increase in the effective potential-barrier width. As a result, the integrated magnitude of the current density decreases, whereas the peak in the *J*(*E*) curve shifts to higher energies, which manifests itself in an increase in the SB effective height (Fig. 3) and a decrease in the current density. With increasing U_f, the distinctions in *J*(*E*) values for hydrogenated and starting samples virtually disappear (Fig. 3b). As a result, the saturation current J_s decreases [19], which manifests itself in increasing φ_{eff} and, ultimately, leads to a decrease in the calculated values of *n* from 1.039 for starting samples to 1.0098 for AH-treated samples. It can be seen that the calculated *n* value for diode structures with an inverse concentration gradient in the *n* layer virtually coincides with the *n* value determined experimentally for hydrogenated diode structures, i.e., 1.01 [7, 10]. Thus, we may assume that a decrease in *n* at $T_{tr} \leq 200$°C is associated with the formation of the inverse concentration gradient of N_D^+ in the *n*-GaAs layer under the effect of atomic H rather than with the passivation of electrically active centers (defects) on the surface as was assumed previously [7, 9].

In the case of the protected surface, a decrease in *n* at $T_{tr} = 200$–400°C is apparently associated with the formation of a thin (~8.3 nm) surface layer with a low density of free charge carriers (electrons) (Fig. 2a). The formation of the low-conductivity surface layer, similarly to the case of $T_{tr} \leq 200$°C, leads to bending of the potential $\varphi(x)$ and a slight increase in the effective potential barrier width. In this case, the peak in the *J*(*E*) curve shifts slightly to higher energies. As a result, the effective barrier height φ_{eff} somewhat increases. In this case, the increase in φ_{eff} is smaller than that at $T_{tr} \leq 200$°C. Consequently, the decrease in the *n* quantity is not appreciable, i.e., $n \approx 1.022$, which is close to the value determined experimentally in study [10] ($n = 1.02$).

An increase in the effective barrier height is given by

$$\Delta\varphi_{eff} = \varphi_{eff(H)} - \varphi_{eff}, \tag{5}$$

where $\varphi_{eff(H)}$ is the effective potential-barrier height for the hydrogenated sample. In practice, such an increase determined from calculations was not observed, since the data spread in determining the φ_{eff} quantity (3 %, which is equivalent to ~0.02 eV) exceeds the value obtained in calculations (~0.016 eV) (Fig. 3a).

Thus, similarly to the case of the reverse bias, it is possible to separate two temperature-dependent processes, which occur during the AH treatment of the n–n^+-GaAs structures and lead to a decrease in the ideality factor. The first process takes place for the surface on the *n*-GaAs layer, both protected and unprotected during the AH treatment, and is characteristic of the temperature range of 50–200°C. A decrease in *n* is due to an increase in the effective potential barrier width, which is caused by the formation of the inverse gradient of the density of ionized shallow-level impurities in the *n* layer as a result of the impurity passivation by atomic H. The second process occurs for the surface of an *n* layer protected by the SiO_2 film. It is most clearly pronounced at the AH treatment temperatures of 200–400°C. In this case, a decrease in *n* is apparently associated with the formation of a thin semi-insulating layer in the surface region.

The calculated thickness of 8.3 nm for the semi-insulating layer coincides with the experimentally determined thickness of ~8 nm for the amorphized region. This may indicate that the amorphized layer which formed during AH treatment has a low conductivity, which is caused by a low free carrier density.

4. CONCLUSION

As a result of the investigations carried out, bending (knee) in the reverse portion of the static *I*–*V* characteristics of Au/n–n^+-GaAs diode structures was observed.

Bending is determined by the formation of a thin semi-insulating layer between the barrier contact and the *n*-GaAs layer under the effect of atomic H. The mechanisms of charge transport, which led to the observed variations in the static *I–V* characteristics of hydrogenated Au/n–n^+-GaAs structures, were investigated. These variations include an increase in the reverse voltage U_r, a decrease in the ideality factor n, and emergence of bending (knee) in the reverse portion of the *I–V* characteristic. It is demonstrated that an increase in the reverse voltage U_r and a decrease in the ideality factor n in the entire temperature range of AH treatment (50–400°C) is governed by the effective potential-barrier width. These phenomena are caused by the distortion of the potential shape due either to the formation of an inverse gradient of density of the ionized shallow-level donor impurity or to the formation of a thin (~8.3 nm) semi-insulating surface layer. In both cases, an increase in U_r and a decrease in n are caused by an increase in the effective potential-barrier width Δh_{eff} at the metal–semiconductor contact due to variation in the shape of the concentration profile of the ionized shallow-level donor impurity.

REFERENCES

1. S. J. Pearton, E. E. Haller, and A. G. Elliot, Appl. Phys. Lett. **44**, 684 (1984).
2. S. J. Pearton, J. Electron. Mater. **14A**, 737 (1985).
3. É. M. Omel’yanovskiĭ, A. V. Pakhomov, and A. Ya. Polyakov, Fiz. Tekh. Poluprovodn. (Leningrad) **21** (5), 842 (1987) [Sov. Phys. Semicond. **21**, 514 (1987)].
4. H.-Y. Nie and Y. Nanichi, J. Appl. Phys. **76** (7), 4205 (1994).
5. S. J. Pearton, W. C. Dautremont-Smith, J. Chevallier, *et al.*, J. Appl. Phys. **59** (8), 2821 (1986).
6. R. L. van Meirhaeghe, W. H. Laflere, and F. Cardon, J. Appl. Phys. **76** (1), 403 (1994).
7. A. Paccagnella, A. Callegari, E. Latta, and M. Gasser, Appl. Phys. Lett. **55**, 259 (1989).
8. U. K. Chakrabarti, S. J. Pearton, W. S. Hobson, *et al.*, Appl. Phys. Lett. **57** (9), 887 (1990).
9. V. G. Bozhkov, V. A. Kagadeĭ, and N. A. Torkhov, Fiz. Tekh. Poluprovodn. (St. Petersburg) **32** (11), 1343 (1998) [Semiconductors **32**, 1196 (1998)].
10. N. A. Torkhov and S. V. Eremeev, Fiz. Tekh. Poluprovodn. (St. Petersburg) **34** (2), 186 (2000) [Semiconductors **34**, 181 (2000)].
11. Y. G. Wang and S. Ashok, J. Appl. Phys. **75** (5), 2447 (1994).
12. N. A. Torkhov and S. V. Eremeev, Fiz. Tekh. Poluprovodn. (St. Petersburg) **33** (10), 1209 (1999) [Semiconductors **33**, 1100 (1999)].
13. N. A. Torkhov, V. G. Bozhkov, V. A. Kagadeĭ, and I. V. Ivonin, in *Proceedings of the 2nd International Conference “Radiation-Thermal Effects and Processes in Inorganic Materials”, Maksimikha, Russia, 2000*, p. 86.
14. A. Watanabe, M. Unno, F. Hojo, and T. Miwa, Jpn. J. Appl. Phys., Part 2 **39** (10A), L961 (2000).
15. N. A. Torkhov and S. V. Eremeev, Fiz. Tekh. Poluprovodn. (St. Petersburg) **34** (1), 106 (2000) [Semiconductors **34**, 108 (2000)].
16. N. A. Torkhov, Fiz. Tekh. Poluprovodn. (St. Petersburg) **35** (7), 823 (2001) [Semiconductors **35**, 788 (2001)].
17. A. V. Panin and N. A. Torkhov, Fiz. Tekh. Poluprovodn. (St. Petersburg) **34** (6), 698 (2000) [Semiconductors **34**, 671 (2000)].
18. D. Mui, S. Strite, and H. Morkoc, Solid-State Electron. **34** (10), 1077 (1991).
19. *Modern Semiconductor Device Physics*, Ed. by S. M. Sze (Wiley, New York, 1997).

Translated by N. Korovin

Semiconductors, Vol. 36, No. 4, 2002, pp. 420–423. Translated from Fizika i Tekhnika Poluprovodnikov, Vol. 36, No. 4, 2002, pp. 443–446.
Original Russian Text Copyright © 2002 by Shevchenko, Yafyasov, Bozhevol'nov, Ivankiv, Perepelkin.

SEMICONDUCTOR STRUCTURES, INTERFACES, AND SURFACES

Field Effect in a System Consisting of Electrolyte and $(\mathrm{TlBiSe_2})_{1-x}$–$(\mathrm{TlBiS_2})_x$ Solid Solution

O. Yu. Shevchenko, A. M. Yafyasov*, V. B. Bozhevol'nov,
I. M. Ivankiv, and A. D. Perepelkin
Institute of Physics, St. Petersburg State University, ul. Ul'yanovskaya 1, Petrodvorets, 198504 Russia
**e-mail: yafyasov@desse.phys.spbu.ru*

Submitted September 12, 2001; accepted for publication September 13, 2001

Abstract—The method of field effect in electrolytes was used to determine the surface electrical properties and band parameters in surface layers of semiconductor solid solutions $(\mathrm{TlBiSe_2})_{1-x}$–$(\mathrm{TlBiS_2})_x$ at room temperature. The dispersion law, the effective mass of electrons in the conduction band, the ionized donor impurity density, and the Fermi level are determined. The experimental and theoretically calculated capacitance–voltage characteristics are compared. *© 2002 MAIK "Nauka/Interperiodica".*

Solid solutions of $\mathrm{TlBiSe_2}$ with $\mathrm{TlBiS_2}$ belong to the group of Tl–V–$\mathrm{VI_2}$ (V: Bi, Sb; VI: S, Se, Te) semiconductors with a layered structure and are the structural analogs to PbSe and PbS [1–4]. The investigation of these materials is of interest because of the possibility of using them to manufacture acoustooptic detectors, IR detectors, thermoelectric generators, and so on [1–4].

The available published data on the band gap E_g, the effective mass of an electron m_e^*, and the dielectric constant ε_{sc} are listed in the table.

The $\mathrm{TlBiS_2}$ crystals grown by the Bridgman–Stockbarger method can have an ordered structure, for instance S–Tl–S–Bi–S [2], obtained by very slow cooling of the crystals, or a disordered structure like S–Tl, Bi–S–Tl, and Bi–S [2]. The electrical and band parameters in $\mathrm{TlBiSe_2}$ thin films for ordered and disordered structures, according to data obtained in [3], are slightly different (see the upper two rows in table).

In this paper, we report the results of studying the ordered structures $(\mathrm{TlBiSe_2})_{1-x}$–$(\mathrm{TlBiS_2})_x$ ($x = 0$, 0.25, 0.50, 0.75, 1.0) grown by the Bridgman–Stockbarger method [1].

The field effect in electrolytes [8–12] was used to determine the electrical properties of the surface and band parameters of surface layers in a semiconductor $(\mathrm{TlBiSe_2})_{1-x}$–$(\mathrm{TlBiS_2})_x$ solid solution. This method is based on the measurement of capacitance–voltage, $C(\varphi)$, and current–voltage, $I(\varphi)$, characteristics of the semiconductor–electrolyte interface [8]. An almost saturated aqueous solution of KCl was used as the electrolyte. The capacitance–voltage and current–voltage characteristics were measured at room temperature in the potentiostatic mode under the cyclic variation of electrode potential φ at a rate of 10–100 mV/s.

The experimental $C(\varphi)$ curves for all $(\mathrm{TlBiSe_2})_{1-x}$–$(\mathrm{TlBiS_2})_x$ compositions are typical of n-type conductivity [13] (Figs. 1–5) and show a hysteresis with a plateau in the cathode range of electrode potentials. The spread in the magnitudes of capacitance (C_p) on the plateau for various compositions of the solid solution is shown in

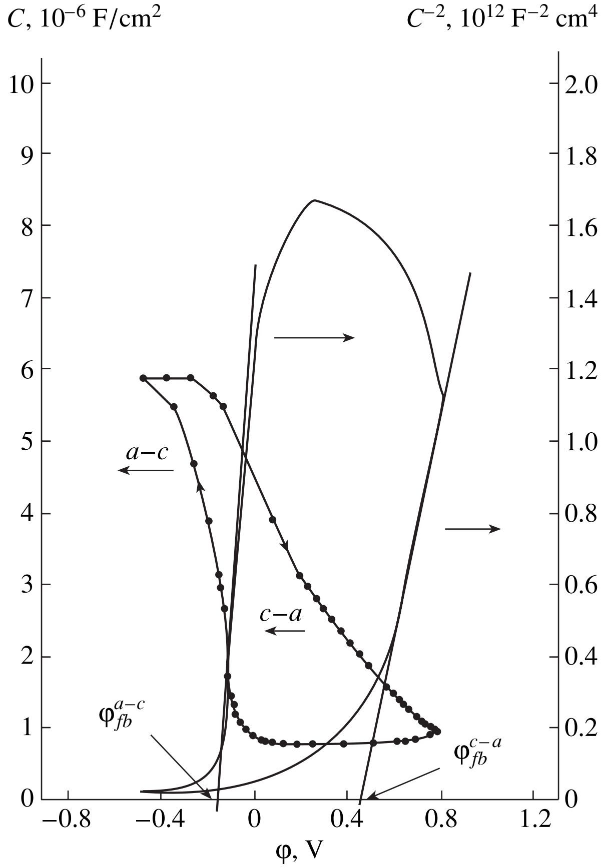

Fig. 1. Experimental $C(\varphi)$ curves for $\mathrm{TlBiSe_2}$ measured using continuous variation in the electrode potential during the anode–cathode–anode cycle and plotted in the $C(\varphi)$ and $C^{-2}(\varphi)$ coordinates.

Literature and experimental parameters of the $(TlBiSe_2)_{1-x}$–$(TlBiS_2)_x$ system

x	E_g, eV	ε_{sc}	m_e^*/m_0	C_p, 10^{-6} F/cm^2	d_i/ε_i, 10^{-8} cm	N_b, 10^{13} cm^{-2}	N_d, 10^{18} cm^{-3}	E_f–E_c, eV	m_e^*/m_0 (experiment)
0	0.45 [3] 0.47 [3] 0.30 [4]	21.50 [3] 20.50 [3] 20.04 [1]	0.085 [3] 0.088 [3] 0.110 [5]	5.0–7.2	1.2–1.8	1.5–3.2	0.70–2.30	(–0.050)–0.030	0.085–0.150
0.25		18.78 [1]		3.8–8.0	1.1–2.3	1.2–2.9	0.50–8.00	0.025–0.070	0.050–0.100
0.50		21.71 [1]		2.2–5.2	1.7–4.0	0.8–1.8	0.17–0.83	(–0.020)–(–0.080)	0.035–0.125
0.75		21.71 [1]		1.4–3.0	3.0–6.3	0.4–0.9	0.27–5.50	0.050–0.200	0.021–0.045
1	0.42 [6]	16.40 [6]	0.250 [7]	1.0–2.1	4.2–8.9	0.06–0.39	0.26–0.35	(–0.150)–(–0.160)	0.015–0.045

the table. The plateau in $C(\varphi)$ curves may be indicative of the existence of an insulator transition layer on the surface; this layer can be characterized by the ratio

$$\frac{d_i}{\varepsilon_i} = \frac{\varepsilon_0}{C_p}, \qquad (1)$$

where d_i is the thickness of the layer, ε_i is its dielectric constant, and $\varepsilon_0 = 8.85418782 \times 10^{-12}$ Φ m^{-1} is the dielectric constant of free space (see table).

The increase in d_i/ε_i (see table) and the reduction of C_p with an increase in x (see table and Fig. 2) can be caused either by an increase of the thickness of the insulator layer d_i or by a reduction of the dielectric constant ε_i of the layer.

The portions of the $C(\varphi)$ curves corresponding to the depletion become rectified in Schottky–Mott coordinates $C^{-2}(\varphi)$ (Figs. 1, 3). This makes it possible to determine the values of the potential of flat bands φ_{fb},

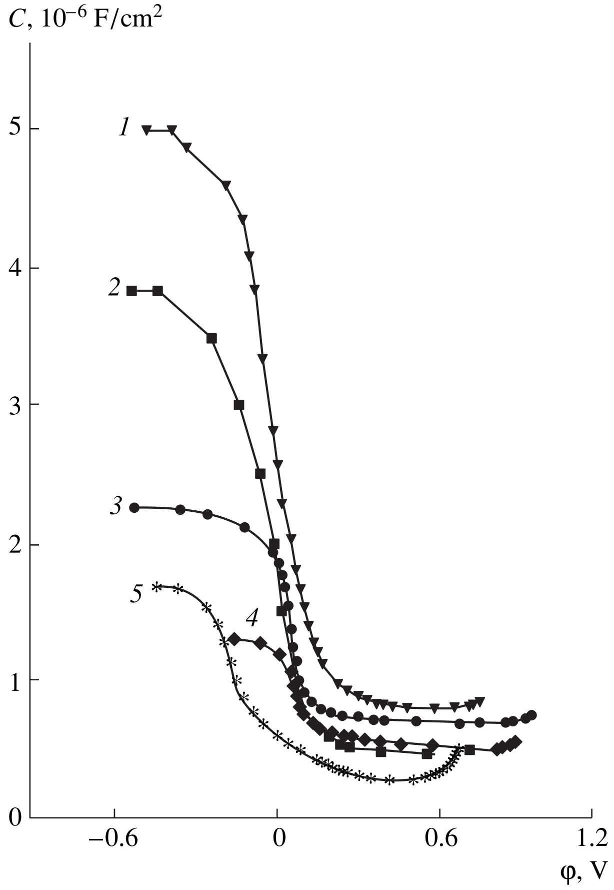

Fig. 2. Experimental $C(\varphi)$ dependences for the $(TlBiSe_2)_{1-x}$–$(TlBiS_2)_x$ system measured using continuous variation in the electrode potential during the anode–cathode cycle for the compositions x = (*1*) 0, (*2*) 0.25, (*3*) 0.5, (*4*) 0.75, and (*5*) 1.0.

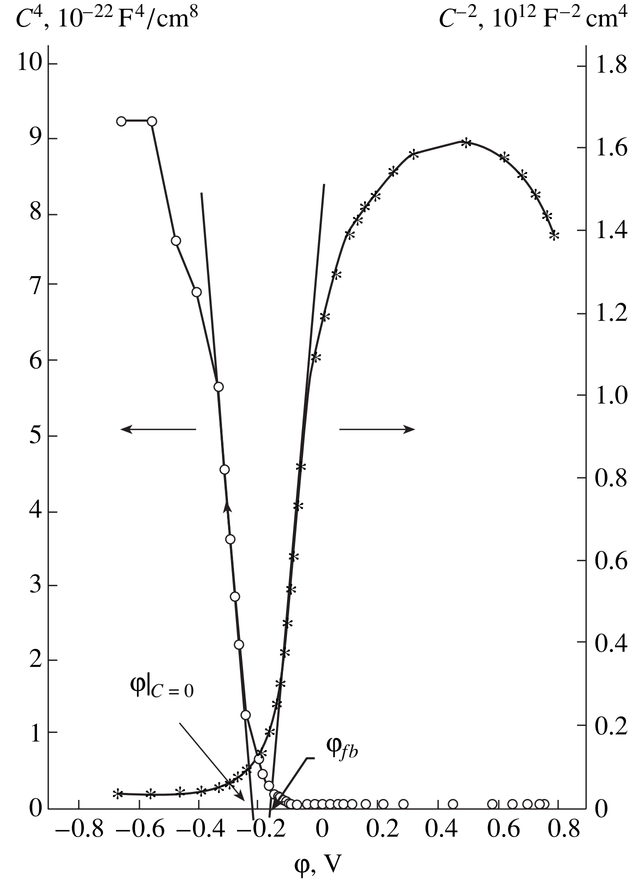

Fig. 3. Experimental $C(\varphi)$ dependence for $TlBiSe_2$ measured using continuous variation in the electrode potential during the anode–cathode cycle and plotted in $C^4(\varphi)$ and $C^{-2}(\varphi)$ coordinates.

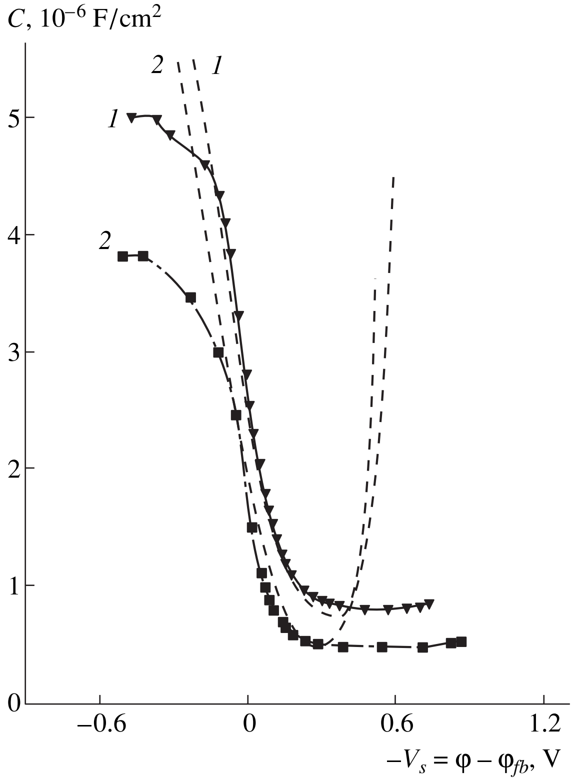

Fig. 4. Experimental $C(\varphi)$ curves (the solid and dot-and-dash lines) measured by continuously varying the electrode potential during the anode–cathode cycle and the theoretical $C_{sc}(V_s)$ dependences (dashed lines) for the $(TlBiSe_2)_{1-x}$–$(TlBiS_2)_x$ compositions with x = (*1*) 0 ($m_e^* = 0.100m_0$, $N_d = 1.2 \times 10^{18}$ cm^{-3}), and (*2*) 0.25 ($m_e^* = 0.100m_0$, $N_d = 4.35 \times 10^{17}$ cm^{-3}).

the density N_b of the charge incorporated into the insulator layer, and the concentration N_d of the ionized donor impurity [13].

The surface density of the charge incorporated into the insulator layer was calculated by the formula

$$N_b = \frac{\Delta\varphi_{fb}C_p}{q}, \qquad (2)$$

where q is the elementary charge; $\Delta\varphi_{fb} = \varphi_{fb}^{a-c} - \varphi_{fb}^{c-a}$; and φ_{fb}^{a-c} and φ_{fb}^{c-a} are the potentials of flat bands for anode–cathode (*a*–*c*) and cathode–anode (*c*–*a*) directions of variations in the electrode potential, respectively (see Fig 1). The values of N_b obtained from the experiment for various compositions of the solid solution are given in the table. As can be seen, an increase in the sulfur content in the solid solution causes a gradual reduction by more than an order of magnitude in the density N_b of the charge incorporated into the insulator layer.

Having determined the flat-band potential φ_{fb} (see Figs. 1, 3), we may pass on from the electrode potentials φ to the surface potentials

$$V_s = -(\varphi - \varphi_{fb}), \qquad (3)$$

and from the measured capacitance to the capacitance of the space-charge region

$$C_{sc}(V_s) = C[-(\varphi - \varphi_{fb})], \qquad (4)$$

and then estimate the concentration of the ionized donor impurity by the formula

$$N_d = \frac{2}{q\varepsilon_0\varepsilon_{sc}}\left[\frac{d(C_{sc}^{-2})}{dV_s}\right]^{-1}. \qquad (5)$$

The values of the concentrations of the ionized donor impurity N_d, calculated from the experimental $C(\varphi)$ curves, are given in the table. It can be seen that the $N_d(x)$ dependence has a minimum at $x = 0.50$. A similar special feature for the electron concentration at $x = 0.5$ was observed previously in [1].

All experimental $C(\varphi)$ dependences in the range of pronounced electron degeneracy are found to be linear in $C^4(\varphi)$ coordinates (Fig. 3). This, according to the formula given in [14]

$$C_{sc} = G(\varepsilon_{sc})^{1/2}\left[\frac{m_e^*}{m_0}\right]^{3/4}|V_s - V_z|^{1/4}, \qquad (6)$$

($G = 8.9738 \times 10^{-6}$ F cm^{-2} V$^{-1/4}$, and $qV_z = E_{c,\,v} - E_f$ is the distance from the edges of the conduction or valence bands to the Fermi level in the bulk) indicates that the dispersion law for the conduction band is parabolic.

The position of the Fermi level with respect to the conduction-band edge, $E_f - E_c$, was determined (see Fig. 3) from the relation

$$\varphi|_{C=0} - \varphi_{fb} = -V_s|_{C_{sc}=0} = \frac{E_f - E_{c,\,v}}{q}, \qquad (7)$$

which readily follows from (3), (4), and (6) after substituting $C = 0$. These data are given in the table.

The effective mass of electrons in the conduction band m_e^*/m_0 was determined from the $C^4(\varphi)$ dependence in the region of pronounced electron degeneracy on the surface (see Fig. 2) by the formula

$$\frac{m_e^*}{m_0} = \frac{G^{-4/3}}{\varepsilon_{sc}^{2/3}}\left(\frac{dC_{sc}^4}{dV_s}\right)^{1/3}, \qquad (8)$$

which was obtained by differentiating (6) with allowance made for (3) and (4).

The corresponding values of m_e^*/m_0 are given in the table. It can be seen that, for $x = 0$, these values are in close agreement with the published data [3, 5], but the value m_e^*/m_0 found for $x = 1$ is considerably smaller

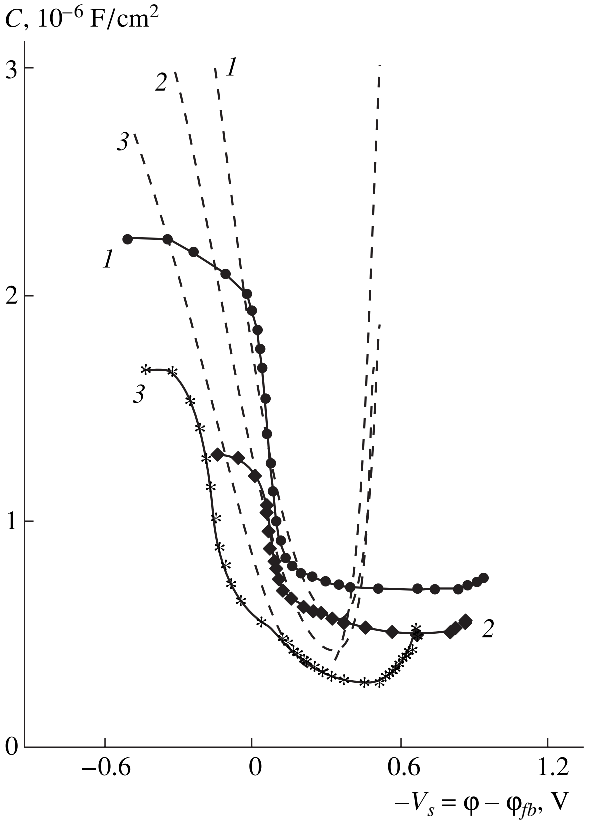

Fig. 5. Experimental $C(\varphi)$ curves (thick solid lines) measured by continuously varying the electrode potential during the anode–cathode cycle and the theoretical $C_{sc}(V_s)$ dependences (dashed lines) for the $(TlBiSe_2)_{1-x}$–$(TlBiS_2)_x$ compositions with x = (thin solid line) (*1*) 0.50 ($m_e^* = 0.050m_0$, $N_d = 6.1 \times 10^{17}$ cm^{-3}), (*2*) 0.75 ($m_e^* = 0.030m_0$, $N_d = 3.35 \times 10^{17}$ cm^{-3}), and (*3*) 1.0 ($m_e^* = 0.025m_0$, $N_d = 2.15 \times 10^{17}$ cm^{-3}).

than that given in the literature [1]. The available data for m_e^*/m_0 for the range $0 < x < 1$ are absent.

The experimental $C(\varphi)$ curves are compared with the calculated $C_{sc}(V_s)$ dependences in Figs. 4 and 5. The $C_{sc}(V_s)$ dependences were obtained by the self-consistent solution of the Schrödinger and Poisson equations using the method described in [15]. The values of m_e^* and N_d (they are given in the captions to Figs. 4 and 5) were taken as parameters from the experiment; the values E_g and ε_{sc} were taken from the literature (see table). It was assumed that the effective mass of a hole $m_h^* = 0.40m_0$ and the spin–orbit splitting energy of the valence band $\Delta = 1.0$ eV.

The comparison of the experimental $C(\varphi)$ curves with the theoretically calculated $C_{sc}(V_s)$ dependences in the region corresponding to accumulation of electrons at the surface shows that theory and experiment agree well for the compositions $x = 0$ and $x = 0.25$ (Fig. 4) and do not agree for $x = 0.50$, 0.75, and 1.0.

REFERENCES

1. M. Ozer, K. M. Paraskevopoulos, A. N. Anagnostopoulos, *et al.*, Semicond. Sci. Technol. **13**, 86 (1998).
2. M. Ozer, K. M. Paraskevopoulos, A. N. Anagnostopoulos, *et al.*, Semicond. Sci. Technol. **11**, 1405 (1996).
3. C. L. Mitsas and D. I. Siapkas, Solid State Commun. **83**, 857 (1992).
4. S. A. Dembrovskii, L. G. Lisovskii, V. M. Bunin, and A. S. Kanischecheva, Izv. Akad. Nauk SSSR, Neorg. Mater. **5**, 2023 (1969).
5. C. L. Mitsas, E. K. Polychroniadis, and D. I. Siapkas, Thin Solid Films **353**, 85 (1999).
6. A. N. Veis, D. D. Koditsa, and N. S. Popovich, Phys. Status Solidi A **107**, K169 (1988).
7. L. I. Vinokurova, Y. Yu. Ivanov, L. S. Klimova, *et al.*, Sov. Phys. Lebedev Inst. Rep., No. 7, 49 (1988).
8. A. M. Yafyasov, V. B. Bozhevol’nov, and A. D. Perepelkin, Fiz. Tekh. Poluprovodn. (Leningrad) **21**, 1144 (1987) [Sov. Phys. Semicond. **21**, 697 (1987)].
9. A. M. Yafyasov, A. D. Perepelkin, Yu. N. Myasoedov, and M. V. Matviiv, Fiz. Tekh. Poluprovodn. (Leningrad) **24**, 875 (1990) [Sov. Phys. Semicond. **24**, 550 (1990)].
10. A. D. Perepelkin, A. M. Yafyasov, and V. B. Bozhevol’nov, Fiz. Tekh. Poluprovodn. (Leningrad) **25**, 156 (1991) [Sov. Phys. Semicond. **25**, 92 (1991)].
11. A. M. Yafyasov, V. G. Savitskiĭ, R. N. Kovtun, *et al.*, Fiz. Tekh. Poluprovodn. (St. Petersburg) **27**, 767 (1993) [Semiconductors **27**, 419 (1993)].
12. A. Yafyasov, V. Bogevolnov, and A. Perepelkin, Phys. Status Solidi B **183**, 419 (1994).
13. S. Sze, *Physics of Semiconductor Devices* (Wiley, New York, 1981; Mir, Moscow, 1984).
14. A. M. Yafyasov, V. V. Monakhov, and O. V. Romanov, Vestn. Leningr. Univ., No. 4, 103 (1986).
15. A. Yafyasov and I. M. Ivankiv, Phys. Status Solidi B **208**, 41 (1998).

Translated by A. Zalesskiĭ

Semiconductors, Vol. 36, No. 4, 2002, pp. 424–429. Translated from Fizika i Tekhnika Poluprovodnikov, Vol. 36, No. 4, 2002, pp. 447–452.
Original Russian Text Copyright © 2002 by Litovchenko, Dmitruk, Korbutyak, Sarikov.

SEMICONDUCTOR STRUCTURES, INTERFACES, AND SURFACES

Effect of Surface on the Excitonic Characteristics of Semiconductors

V. G. Litovchenko*, N. L. Dmitruk, D. V. Korbutyak, and A. V. Sarikov
Institute of Semiconductor Physics, National Academy of Sciences of Ukraine, Kiev, 03028 Ukraine
** e-mail: LVG@isp.kiev.ua*

Submitted July 30, 2001; accepted for publication September 27, 2001

Abstract—The effect of surface treatments on the main characteristics of excitons in the subsurface region of semiconductors (for GaAs), as well as the spatial distribution of main characteristics of excitons (for CdS), was studied. An analysis of experimental data showed that the deposition of insulator layers with a lower dielectric constant on the surface of the semiconductor resulted in an enhancement of the exciton–phonon interaction and an increase in the exciton binding energy. The appearance of the surface layer with a higher defect concentration increasing after some surface treatments results in the lowering of the exciton binding energy in the subsurface region and also in the weakening of the exciton–phonon interaction. *© 2002 MAIK “Nauka/Interperiodica”.*

1. INTRODUCTION

The state of the surface and near-surface environment of a semiconductor substantially affects its excitonic, phonon, and exciton–phonon characteristics. It is known [1–4] that the optical properties of such semiconductors as CdS and GaAs, among others, have a number of special features in the region of excitonic resonances that are directly associated with surface characteristics. These features are as follows: an additional fine structure in the reflection spectrum in the region corresponding to a free exciton, a shift of the overall reflection spectrum to longer wavelengths and broadening of the reflection and absorption lines, a fine structure of the photoluminescence spectrum and a large increase in the intensity of the phonon satellites, and the shape of photoluminescence excitation spectra (the anomalous sharp falloff of the emission intensity in the case of surface excitation). Physically, several mechanisms cause the surface effect on the excitonic characteristics.

(i) The presence of a physical (exciton-free) [5] and a technological “dead” layer, in which the concentration of defects is enhanced due to various reasons; therefore, the lifetime of excitons is significantly decreased and their binding energy E_{ex} and exciton–phonon coupling factor N are likely decreased.

(ii) The effect of image forces on the excitons localized in the subsurface layer:

$$V_{\mathrm{cul}} \approx \frac{e^2}{4\varepsilon_1}\frac{\varepsilon_1-\varepsilon_2}{\varepsilon_1+\varepsilon_2}\left(\frac{1}{Z_e}+\frac{1}{Z_h}\right). \quad (1)$$

Here, $\varepsilon_{1,2}$ is the dielectric constant with index 1 referring to a semiconductor and index 2, to the surrounding medium; Z_e and Z_h are the distances for an electron and hole from the interface between the media, respectively. For a more polarizable medium, $\varepsilon_2 > \varepsilon_1$ and the Coulomb binding energy in the exciton is lowered. The reverse situation (the binding energy E_{ex} increases) is predicted for $\varepsilon_1 > \varepsilon_2$ (this case also includes air surroundings). Theoretically, this mechanism was considered by Hopfield [5], Keldysh and Silin [6], Lozovik and Nishanov [7], Pokatilov *et al.* [8], and others. Recently, calculations indicating a significant increase in the exciton binding energy if a semiconductor is surrounded by a medium with a smaller dielectric constant were carried out in [9]. The influence of the surface microrelief and dielectric properties of the surrounding medium on the characteristics of excitons localized in the subsurface region can be described by the introduction of the effective dielectric constant $\varepsilon_{\mathrm{eff}}$, e.g., according to the effective-medium model [10]:

$$\varepsilon_{\mathrm{eff}} = \varepsilon_1\frac{\varepsilon_2(2-c)+\varepsilon_1 c}{\varepsilon_1(2-c)+\varepsilon_2 c}. \quad (2)$$

Here, ε_1 and ε_2 are the dielectric constants of the semiconductor and surrounding medium, respectively; c is the fraction of the semiconductor phase in the effective medium “semiconductor + environment” under consideration.

(iii) The quantum-mechanical size effect studied previously in a number of papers (see, e.g., [11, 12]). As is known, an increase in the binding energy E_{ex} of a surface exciton, in this case, is caused by the enhancement of the ratio between the kinetic and potential energies of quasi-particles, that is, the vanishing of the kinetic energy of a quasi-particle over one, two, or three coordinates, and, thus, by the increase in the potential energy of a particle with the dimensional confinement of its displacements. In terms of wave mechanics, this means the substitution of the centrally symmetric wave function by that oriented along the layer (rod) or its almost complete localization in a “macroatom” (a zero-dimensional object).

In this paper, we report the results of studying the effect of the surface state and treatment (for CdS and GaAs single crystals) on the main characteristics of excitonic transitions in the subsurface region of a semiconductor; the exciton binding energy E_{ex}, phonon energies, and the exciton–phonon coupling factor are determined. Studies of spatial distributions of the main excitonic characteristic in the subsurface region are also carried out. The excitation spectra of photoluminescence and cathodoluminescence are studied; modulation of the luminescence spectra with a change of the effective depth of free exciton generation due to a change of the energy of quanta exciting electron–hole pairs in a semiconductor (photoluminescence) or of the energy E_0 of the electron beam incident at the surface (cathodoluminescence) was used.

2. THEORETICAL

Measurements of the relative intensities of the zero-phonon emission line and its phonon replicas using the bulk and surface excitation make it possible to determine the electron–phonon coupling strength in various regions of a crystal. At the same time, treatment of the semiconductors results in a change of the characteristics of the surface excitonic transitions. One can determine these characteristics from photoluminescence spectra as a function of the surface state with account of the surface surroundings.

According to [5, 13–15], in terms of an adiabatic approximation, the relative intensity of phonon replicas can be represented by the Poisson law: $I_m = I_0 N^m/m!$ Here, m is the number of the phonon-assisted line ($m = 0$ corresponds to the zero-phonon line); $I_0 \propto |H|^2\exp(-N)$; A is the coupling matrix element; and N is the mean number of phonons emitted, which characterizes the electron–phonon coupling force. In the case of the transition with participation of a local center,

$$N \approx \frac{e^2}{E_{\text{ph}}}\left(\frac{1}{\varepsilon_\infty} - \frac{1}{\varepsilon_0}\right)\frac{5}{16a_B(z)}, \qquad (3)$$

where E_{ph} is the energy of LO-phonons, ε_0 and ε_∞ are the static and high-frequency dielectric constants, and a_B is the Bohr radius of the localized excitation. The generalization of the expression for N to the case of excitonic excitations [15, 16], disregarding the center-of-mass motion, yields the following result:

$$N' = \gamma N,$$

where

$$\gamma = \frac{(\alpha-1)^2(19/5-\alpha+\alpha^2)}{\alpha(1+\alpha)^3} \le 1,$$

and $\alpha = m_h^*/m_e^*$ is the ratio of the hole and electron effective masses. One should note that the Poisson law for the subsequent lines $m \gg 1$ begins to be violated more and more, which is apparently associated with the adiabaticity violation.

The exciton binding energy with the quantum number $n = 1$ is expressed as

$$E_{\text{ex}} = \frac{\mu e^4}{2\hbar^2\varepsilon_0} = \frac{e^2}{2\varepsilon_0 a_B},$$

where $\mu^{-1} = 1/m_e^* + 1/m_h^*$, and $a_B = \hbar^2\varepsilon_0/\mu e^2$. On this basis, the following formula relating E and E_{ex} can be easily obtained:

$$E_{\text{ex}} = N\beta E_{\text{ph}}\frac{8\varepsilon_\infty}{5(\varepsilon_0-\varepsilon_\infty)}. \qquad (4)$$

Thus, the exciton binding energy and its Bohr radius as a function of the semiconductor surface treatment or as a function of the distance to the crystal surface can be determined from the values of E_{ph} and N obtained from the photoluminescence and cathodoluminescence spectra. The meaning of parameter β will be explained below.

3. EXPERIMENTAL

Studies of surface luminescence effects were carried out using both III–V samples (GaAs) and II–VI samples (CdS) [4, 17–21]. Photoluminescence (PL) spectra were measured at the temperature $T = 4.2$ K with the laser radiation excitation in a continuous-wave (helium–neon laser, wavelength $\lambda = 632.8$ nm, peak intensity $L_{\max} = 10^{18}$ photon/(cm^2 s)) and pulsed (ruby laser, wavelength $\lambda = 694.3$ nm, pulse duration $t = 20$–40 ns, $L_{\max} = 10^{25}$ photon/(cm^2 s)) modes. These intensities of laser radiation allowed us to study the subsurface region under the flat-band conditions. Excitation radiation was absorbed at the depth $\lesssim 0.5$ μm, and, thus, the bulk effect was minimized. The PL spectra were measured using an IKS-12 monochromator with a subsequent recording of the sample emission using a FEU-62 photomultiplier.

The surface PL spectra of GaAs were studied in relation to the following treatments [17–21]:

1) chemical polishing etching in $H_2O_2 : H_2SO_4 : H_2O = 1 : 3 : 1$ solutions;

2) doping of the surface with gold, silver, and palladium from solutions; i.e., deposition of metal nanoclusters on the surface;

3) treatment of the surface by intense ruby laser radiation (intensity $L = 10^{26}$ photon/(cm^2 s));

4) irradiation of the surface with an electron beam (400 keV, $2 \cdot 10^6$ rad);

5) irradiation with penetrating ^{60}Co gamma-ray photons (10^6–10^8 rad);

6) pyrolitic deposition of insulating layers of Si_3N_4 and Ge_3N_4 with thickness $d \approx 1000$ Å; and

7) bombardment of the surface with argon ions (1 keV, 10^{15}–10^{19} cm^{-2}).

Table

System	Band, eV	E_{ph}, meV	N	$c = 0.5$	
				$E_{ex}(E_{centre})$, meV	a_B, Å
GaAs coated with Si_3N_4 film; surface exciton	1.5144	~30	0.066	9.45	162
GaAs coated with Ge_3N_4 film; surface exciton	1.5144	~30	0.077	11.02	139
GaAs coated with Si_3N_4 film after γ irradiation; surface exciton	1.5144	~30	0.054	7.73	198
GaAs coated with Ge_3N_4 film after γ irradiation; surface exciton	1.5144	~30	0.069	9.88	155
GaAs coated with Si_3N_4 film; shallow surface center	1.477 1.444	33	0.079	12.44	123
GaAs coated with Ge_3N_4 film; shallow surface center	1.4769 1.4439	33	0.073	11.5	133
GaAs coated with Si_3N_4 film after γ irradiation; shallow surface center	1.477 1.444	33	0.072	11.33	135
GaAs coated with Ge_3N_4 film after γ irradiation; shallow surface center	1.4769 1.4439	33	0.063	9.92	154

Note: E_{centre} denotes the energy of surface center.

The measurements of cathodoluminescence spectra were performed at 77 K for various CdS crystals (block and platelike) as a function of the electron energy, which defined the excitation depth; thus, the distribution of cathodoluminescence properties were studied throughout the depth [4].

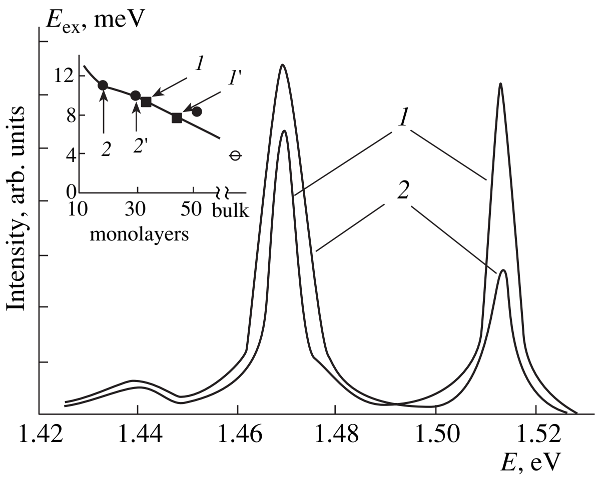

Fig. 1. Photoluminescence spectra of *n*-GaAs samples (electron concentration $n_0 \approx 10^{18}$ cm^{-3}) coated with a Si_3N_4 layer 1000 Å thick: (*1*) prior to irradiation, (*2*) after γ irradiation with the dose 5×10^6 rad; $T = 4.2$ K. In the inset, we show the dependence of the binding energy of the exciton in GaAs on the thickness of the localization region: *1* and *1*' for the binding energy of surface excitons in the case of the Si_3N_4 layer at the surface before and after γ irradiation, respectively; *2* and *2*' are the same for the case of Ge_3N_4 coating.

4. RESULTS AND DISCUSSION

It has been shown [17–21] that, under certain conditions, the manifestation of surface excitons is possible in the PL spectra. This occurs as a result of specific treatments of the surface:

(i) removal of impurities such as silicon from the surface layer; the silicon impurity significantly reduces the lifetime of nonequilibrium electron–hole pairs in GaAs;

(ii) deposition of Ga_3N_4 or Si_3N_4 insulator films onto the surface; this film prevents rapid oxidation of the surface.

After the etching of the surface of the initial GaAs samples in an $H_2O_2 : H_2SO_4 : H_2O = 1 : 3 : 1$ solution, a band at the energy E ≈ 1.515 eV, attributed to the surface excitons, was present in the PL spectra. The intensity of this band decreased after the following surface treatments: doping of the surface with Ag and Pd from the aqueous solutions of salts [21], low-dose bombardment with argon ions with a subsequent doping by Ag and Au atoms [20], irradiation with fast electrons, and exposure to an intense beam of pulsed ruby laser and to γ radiation [21]. This can be explained by the increase in the number of surface nonradiative recombination centers after the surface treatment. Since, under high doses of γ radiation, the intensity of this peak begins to increase, this means that, in addition to the increase in the surface concentration of nonradiative recombination centers, the appearance of new centers of radiative recombination occurs. The resulting intensity is defined by the competition of these two processes.

The first phonon replica of this peak was resolved in PL spectra of the samples coated with Si_3N_4 and Ge_3N_4

films (Figs. 1, 2). The energy of phonons involved in the transitions was determined from the spectra measured and was equal to ~30 meV, and the exciton–phonon coupling factor decreased from 0.066 and 0.077 to 0.054 and 0.069, respectively, as a result of γ irradiation. Simultaneously, the intensities of the peak and its phonon replica decreased. The results obtained are indicative of the change in exciton binding energy at the surface (see formula (4)). The values of the exciton–phonon coupling factor prior to and after the γ irradiation, as well as the values of exciton binding energies at the surface calculated according to (4) together with those of exciton Bohr radii, are listed in the table. The magnitude of the dielectric constant was calculated according to the effective-medium model formula (2) for a semiconductor surface with an insulator film ($\varepsilon_0 = 7$, $\varepsilon_\infty = 4$ [22]). For estimates, the fraction of the semiconductor phase in the effective medium was assumed to be equal to $c = 0.5$. For comparison, one should note that the values of the exciton binding energy and Bohr radius for the semiconductor bulk ($c = 1$) are equal to $E_{\rm ex} = 3.8$ meV and $a_B = 294$ Å. It can be seen that the insulator environment of the semiconductor results in the increase in the exciton binding energy and in the decrease in its Bohr radius (localization enhancement) as compared to the bulk. The destructive effect of the penetrating γ radiation on the surface gives rise to partial exciton delocalization. The dependence of the exciton binding energy in GaAs on the thickness of its localization layer is illustrated in the inset in Fig. 1. Fitting of the calculated values of the exciton binding energy to those obtained experimentally allows us to estimate the thickness of the surface-exciton localization region prior to and after the γ irradiation at 35 and 45 monolayers when there is a Ge_3N_4 layer at the surface.

After deposition of the Si_3N_4 layer at the surface of the GaAs samples, a well-resolved structure associated with phonon replicas of the band with $E \approx 1.477$ eV (emission peaks at 1.477 and 1.444 eV) [17, 18] was observed in the low-temperature PL spectra in addition to the band with $E \approx 1.515$ eV. Thus, the energy of phonons involved in these transitions was equal to 33 meV. This value is consistent with theoretical predictions [23–25], according to which the energy of surface phonon polaritons should be higher than that of the bulk TO-phonon (32 meV) and lower than the LO-phonon energy (36 meV). The calculated value of the electron–phonon coupling factor N was 0.079. Similarly, in GaAs samples coated with Ge_3N_4 films, the bands with energies 1.4769 and 1.4439 eV were observed and corresponded to the phonon energy values found previously [19]. The electron–phonon coupling factor was equal to 0.073 in this case. These bands are apparently associated with radiative recombination via a shallow surface center of structural origin (of the "surface vacancy + N" type). Etching-off of the Si_3N_4 (Ge_3N_4) layer, along with a thin GaAs layer (~100 Å), resulted in the band quenching, which confirmed their surface origin.

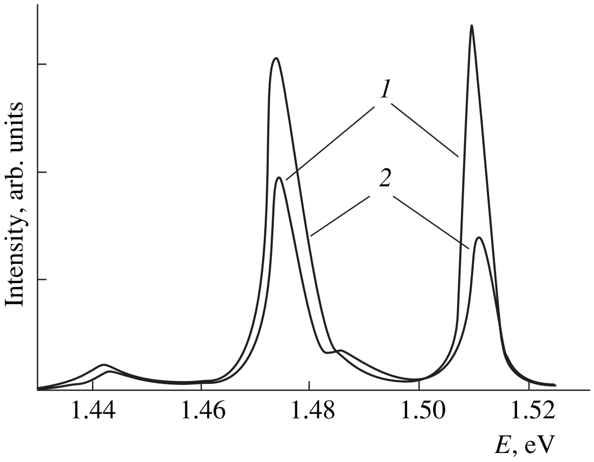

Fig. 2. Photoluminescence spectra of *n*-GaAs samples (electron concentration $n_0 \approx 10^{18}$ cm^{-3}) coated with a Ge_3N_4 layer 1000 Å thick: (*1*) prior to irradiation, (*2*) after γ irradiation at a dose of 10^7 rad; $T = 4.2$ K.

The increase in the intensity of band phonon-replica series and of the band itself associated with emission from a shallow surface center was observed after γ radiation at a dose of $\sim 5 \times 10^6$ rad. In this case, the exciton–phonon interaction factor decreased to 0.072 and 0.063 for the samples coated by Si_3N_4 and Ge_3N_4 layers, respectively; this is apparently associated with the increase in the concentration of the surface vacancies responsible for the appearance of bands.

We now consider dependences of the zero-phonon line (I_0) and phonon replica (I_1, I_2) intensities for CdS single crystals on the electron energy E_0 in the beam. Corresponding data are shown in Fig. 3 [4]. Based on these data, the dependences of the exciton–phonon coupling factor on the penetration depth $z_0(E_0)$ of the excitation electron beam were obtained (Fig. 4). It turns out that the exciton–phonon coupling force in the bulk of CdS crystals was rather large and close to 1, and near the surface itself (at a distance on the order of hundreds of angstroms) it decreased markedly, especially in the case of platetype crystals. Such a behavior can be caused by the fact that, in the case of platelike crystals, the "dead" layer has a minimal thickness on the order of the exciton diameter; i.e., the exciton can closely approach the surface. At the same time, in the bulk CdS crystals, at the surfaces of which a distorted macrolayer exists, the dependence $N[z_0(E_0)]$ is significantly weaker. One should note that the dependence of the effective depth of the electron–hole pair generation by an electron beam (ionization losses of electrons) on electron energy is determined using the approximate Klein expression [26] with the length of the total path $R_B = bE_0^n$ ($n = 1.75$ for CdS, and the magnitude of parameter b is adjusted empirically from the best agree-

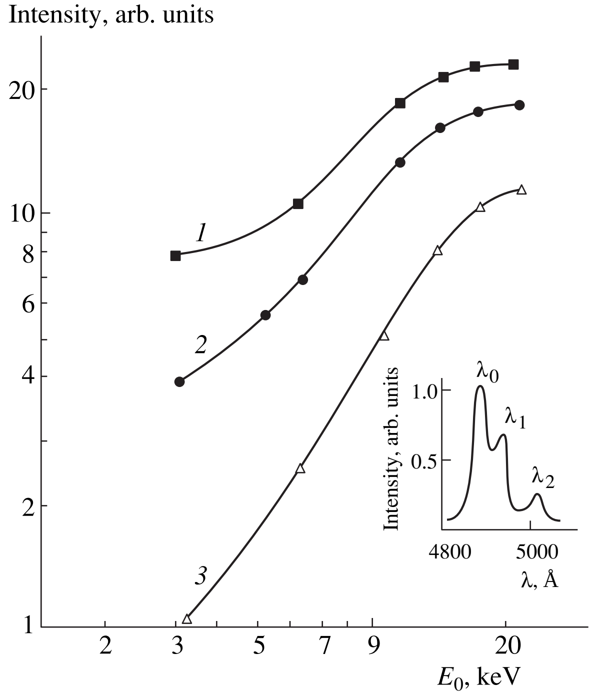

Fig. 3. Dependence of zero-phonon line (*1*) and phonon replica (*2* and *3*) intensities on the electron energy E_0 in the beam for CdS sample 3. In the inset, we show the exciton cathodoluminescence spectrum of a platelike CdS crystal at $T = 77$ K; wavelength: $\lambda_0 = 4880$ Å, $\lambda_1 = 4930$ Å, and $\lambda_2 = 5000$ Å.

ment between calculated and experimental dependences of the no-phonon line intensity $I_0(E_0)$. Thus, the spatial distributions of energy $E_{ex}(z)$ and of the exciton radius $a_B(z)$ were obtained (Fig. 5). When plotting the curves in Fig. 5, the value of parameter β was chosen in such a way as to ensure that the values of E_{ex} and a_B coincided with the known bulk exciton parameters—28.9 meV and 28 Å, respectively [1]. Averaged over both samples and two methods of determination of exciton–phonon coupling, the value of parameter $\beta = 0.37$ differs from the theoretical value of parameter $\gamma = 0.65$ by nearly two times. Consideration of exciton–phonon coupling in [15, 16] apparently did not account for all the features of this phenomenon. It can be seen that, similarly to $N(z)$, the exciton binding energy decreases near the surface by two times or more. This confirms the known statement that there exists a region near the surface of a semiconductor where the excitonic state $n = 1$ is strongly disturbed [1]. The closest-to-surface fraction of this region is referred to as an intrinsic exciton-free "dead" layer, whose thickness is equal to the exciton size by an order of magnitude. The presence of such a layer is caused by the confinement of the electron and hole motion by the surface and by the action of image forces. A more extended layer with a reduced binding energy is apparently caused by the interaction of excitons with the field of charged centers [1]. This

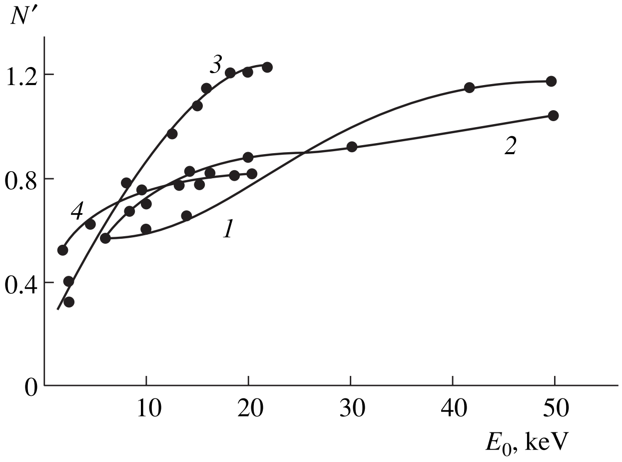

Fig. 4. Dependence of relative intensities of zero-phonon line (I_0) and phonon replicas (I_1, I_2) in CdS on the electron energy: *1* and *2* for sample 1; *3* and *4* for sample 3; *1* and *3* correspond to $2I_2/I_1$; and *2* and *4* correspond to I_1/I_0.

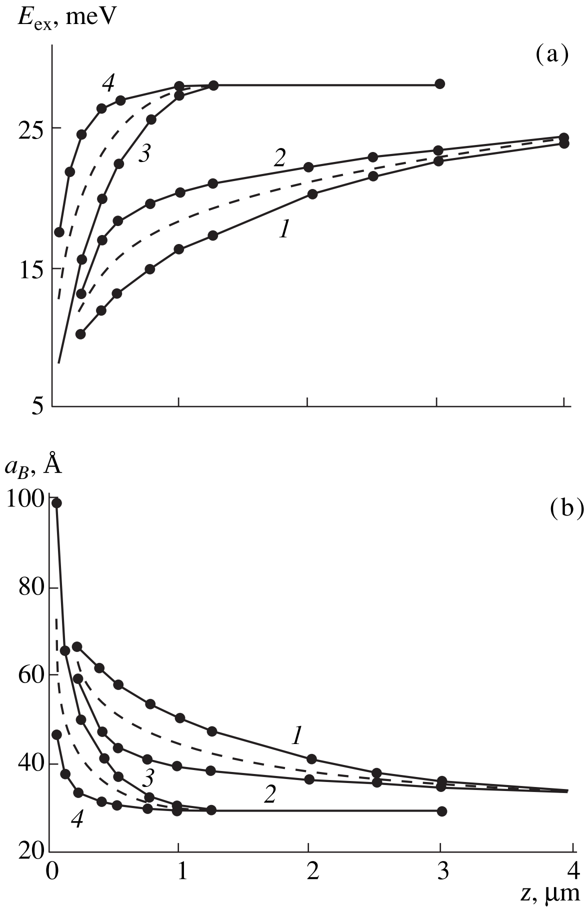

Fig. 5. Dependence of the exciton binding energy E_{ex} (a) and radius a_B (b) for samples 1 (*1*, *2*) and 3 (*3*, *4*) determined from the ratios $2I_2/I_1$ (*1*, *3*) and I_1/I_0 (*2*, *4*). Dashed line represents the averaged data.

can be described in the adiabatic approximation; i.e., here, the description of exciton–phonon coupling by expression (3) is justified. The subsurface nonadiabatic layer itself requires more rigorous consideration.

The binding energy decrease and an increase in the exciton radius in the subsurface submicrometer layer reflect a gradual transition to the "dead" layer caused by the attenuation of excited quasi-particles, with this attenuation being enhanced by the surface (as follows from the broadening of the excitonic lines near the surface from 5 to 10 up to ~15 meV) due to the effect of electric forces of the space charge region (contracted owing to the intense illumination of the crystal [27]), the nonstoichiometric composition of the surface layer (e.g., cadmium enrichment in the case of CdS), or the presence of a large number of surface centers for exciton annihilation. These factors can affect the dielectric parameters of the material and, consequently, the resonance frequency of an exciton. For the elucidation of the specific mechanism of the extended "dead" layer manifestation, the study of the composition of the subsurface region and its structural parameters is required.

5. CONCLUSION

In this study, the effect of surface treatments on the excitonic characteristics of the subsurface region of semiconductors was investigated. By the example of GaAs, it is shown that surface treatment results, as a rule, in a decrease of the electron–phonon interaction factor and in the lowering of the binding energy of surface excitons. Both the increase and decrease of emission intensity can be observed for various bands. This is associated with the competing effect of formation of both radiative and nonradiative recombination centers in the course of treatment. In the GaAs–Si_3N_4 (Ge_3N_4) structure, the effect of the insulator also results in an increase in the surface-exciton binding energy.

The characteristics of bulk excitons on the cathodoluminescence excitation depth was also studied in this work. It is shown that the exciton binding energy decreases as it approaches the surface and causes the presence of subsurface "dead" layers.

ACKNOWLEDGMENTS

This study was supported in part by the International Science & Technology Center, project no. U-31.

REFERENCES

1. V. A. Kiselev, B. V. Novikov, and A. E. Cherednichenko, *Excitonic Spectroscopy of Subsurface Region of Semiconductors* (Leningr. Gos. Univ., Leningrad, 1987).
2. Yu. V. Kryuchenko, D. V. Korbutyak, V. G. Litovchenko, *Excitonic Reflection Spectra of Semiconductor Crystals with Inhomogeneous Subsurface Region* (Inst. of Semicond., Acad. of Sci. of Ukraine, Kiev, 1990).
3. A. S. Batyrev, N. V. Karasenko, B. V. Novikov, *et al.*, Pis'ma Zh. Éksp. Teor. Fiz. **62** (5), 397 (1995) [JETP Lett. **62**, 408 (1995)].
4. N. L. Dmitruk, V. M. Leonov, V. G. Litovchenko, and G. Kh. Talat, Fiz. Tverd. Tela (Leningrad) **20** (2), 518 (1978) [Sov. Phys. Solid State **20**, 300 (1978)].
5. J. J. Hopfield, J. Phys. Chem. Solids **10** (1), 110 (1959).
6. L. V. Keldysh and A. P. Silin, Zh. Éksp. Teor. Fiz. **69** (3), 1053 (1975) [Sov. Phys. JETP **42**, 535 (1975)].
7. Yu. E. Lozovik and V. N. Nishanov, Fiz. Tverd. Tela (Leningrad) **18** (11), 3267 (1976) [Sov. Phys. Solid State **18**, 1905 (1976)].
8. E. P. Pokatilov, S. I. Beril, V. M. Fomin, *et al.*, Phys. Status Solidi B **145**, 535 (1988).
9. M. G. Lisachenko, E. A. Konstantinova, P. K. Kashkarov, and V. Yu. Timoshenko, Phys. Status Solidi A **182**, 297 (2000).
10. A. Sarua, G. Gärtner, G. Irmer, *et al.*, Phys. Status Solidi A **182**, 207 (2000).
11. M. Shinada and S. Sugano, J. Phys. Soc. Jpn. **21** (10), 1936 (1966).
12. R. Del Sole and E. Tosatti, Solid State Commun. **22** (5), 307 (1977).
13. S. I. Pekar, Usp. Fiz. Nauk **1**, 17 (1953).
14. A. S. Davydov and É. N. Myasnikov, *Excitons in Molecular Crystals* (Naukova Dumka, Kiev, 1973).
15. Y. Toyozawa, J. Lumin. **1**, 732 (1970).
16. H. L. Malm and R. R. Hearing, Can. J. Phys. **49**, 2970 (1971).
17. V. A. Zuev, D. V. Korbutyak, and V. G. Litovchenko, Pis'ma Zh. Éksp. Teor. Fiz. **20** (1), 3 (1974).
18. V. G. Litovchenko, V. A. Zuev, D. V. Korbutyak, and G. A. Sukach, in *Proceedings of the 2nd International Conference on Solid Surface, Kyoto, Japan*; Jpn. J. Appl. Phys., Suppl. **32**, 421 (1974).
19. V. A. Zuev, D. V. Korbutyak, V. G. Litovchenko, and G. A. Sukach, Izv. Akad. Nauk SSSR, Ser. Fiz. **38** (6), 1291 (1974).
20. A. V. Drazhan, V. A. Zuev, D. V. Korbutyak, *et al.*, Fiz. Tekh. Poluprovodn. (Leningrad) **11** (7), 1260 (1977) [Sov. Phys. Semicond. **11**, 742 (1977)].
21. V. A. Zuev, D. V. Korbutyak, and V. G. Litovchenko, Fiz. Tekh. Poluprovodn. (Leningrad) **8** (9), 1651 (1974) [Sov. Phys. Semicond. **8**, 1071 (1974)].
22. A. A. Evtukh and V. G. Litovchenko, Optoélektron. Poluprovodn. Tekh. **5**, 3 (1984).
23. R. Fuchs and K. L. Kliewer, Phys. Rev. **140**, A2076 (1965).
24. R. Englman and R. Ruppin, J. Phys. Chem. Solids **1**, 630 (1968).
25. V. V. Bryksin and Yu. A. Firsov, Fiz. Tverd. Tela (Leningrad) **11**, 2167 (1969) [Sov. Phys. Solid State **11**, 1751 (1970)]; Fiz. Tverd. Tela (Leningrad) **14**, 1148 (1972) [Sov. Phys. Solid State **14**, 981 (1972)].
26. C. A. Klein, Appl. Opt. **5**, 1922 (1966).
27. N. L. Dmitruk, V. I. Lyashenko, and A. K. Tereshchenko, Ukr. Fiz. Zh. **17** (8), 1356 (1972).

Translated by T. Galkina

Semiconductors, Vol. 36, No. 4, 2002, pp. 430–433. Translated from Fizika i Tekhnika Poluprovodnikov, Vol. 36, No. 4, 2002, pp. 453–456.

Nature of the Edge Electroluminescence Peak in the Si:(Er,O) Diode Breakdown Mode

A. M. Emel'yanov, Yu. A. Nikolaev, and N. A. Sobolev

Ioffe Physicotechnical Institute, Russian Academy of Sciences, St. Petersburg, 194021 Russia

Submitted October 16, 2001; accepted for publication October 17, 2001

Abstract—Electroluminescence (EL) of erbium- and oxygen-doped Si:(Er,O) diodes at $\lambda = 1.00$–1.65 μm has been studied in the *p*–*n* junction breakdown and forward current modes. The EL was measured at room temperature from the front and back surfaces of the diodes. A peak corresponding to the absorption band edge of silicon was observed in the EL spectra of some diodes in the *p*–*n* junction breakdown mode. The peak is associated with the injection of minority carriers from the metal contact into silicon, with subsequent band-to-band radiative recombination. The band-to-band recombination intensity increases sharply on reaching a certain current density that depends on the fabrication technology. This threshold current density decreases with the temperature of post-implantation annealing of Si:(Er,O) diodes increasing in the range 900–1100°C. © *2002 MAIK "Nauka/Interperiodica".*

1. INTRODUCTION

The breakdown mode of a silicon diode is used to excite the electroluminescence (EL) of rare-earth (Er,Ho) ions in the space charge region of the *p*–*n* junction [1–6]. In erbium- and oxygen-doped Si:(Er,O) diodes [1–5] fabricated by certain technologies, we observed in the *p*–*n* junction breakdown mode an EL band in the range of the band-to-band recombination in silicon, along with a peak at $\lambda \approx 1.54$ μm, associated with radiative transitions of electrons between the ⟨crystal field⟩–split $^4I_{13/2}$ and $^4I_{15/2}$ levels of Er^{3+} ions, and relatively weak and, commonly, nearly λ-independent (at $\lambda \approx 1.2$–1.6 μm) emission due to transitions of "hot" electrons within the conduction band of silicon. Revealing the origin of this band is important for a better understanding of the rare-earth ion excitation and deexcitation mechanisms in semiconductor diodes and of the physical processes occurring in the diodes in the breakdown mode.

Previously, the appearance of an EL band in the range of the silicon band-to-band recombination was also observed in the breakdown mode in some silicon diodes [7, 8]. In [7], the origin of this band was attributed to the impact ionization of atoms.

Based on studies of EL in Si:(Er,O) diodes in the breakdown and forward-current modes, we present the first experimental evidence that the reason for the appearance of the EL band in the band-to-band recombination range in silicon can be related to injection of minority carriers from a metal contact into silicon, which occurs in the breakdown. Some of the technological aspects in the fabrication of silicon diodes exhibiting effective room-temperature EL in the band-to-band recombination range are considered.

2. EXPERIMENTAL PROCEDURE

Implantation of 2.0 and 1.6 MeV erbium ions and 0.28 and 0.22 MeV oxygen ions with doses of, respectively, 3×10^{14} and 3×10^{15} cm^{-2} was done into the front face of polished *n*-type Czochralski-grown 0.3-mm-thick (100) Si wafers with a resistivity of 0.5 Ω cm. The implantation was accompanied by amorphization of the surface layer. Boron (40 keV, 5×10^{15} cm^{-2}) and phosphorus (80 keV, 1×10^{15} cm^{-2}) ions were implanted into the front and back faces of the wafers, respectively, to produce heavily doped p^+ and n^+ layers. Two-stage annealing in a chlorine-containing atmosphere [2], first at $T_1 = 620$°C (1 h) and then at $T_2 = 700$–1100°C (0.5 h), led to recrystallization of the amorphized layer and to the formation of optically and electrically active erbium-related centers. The working area of the mesa diodes was $S \approx 2 \times 2$ mm^2. The breakdown voltage at room temperature was ~6.5 V for diodes annealed at $T_2 = 1000$°C. Aluminum contacts 1 mm in diameter were deposited onto the front and back sides of the diodes by thermal evaporation in vacuum. The EL was excited at room temperature by 5-ms square pulses with a repetition frequency of 32 Hz. The emission from the Al-free surface of the diode structure was focused, using a system of lenses, onto the entrance slit of an MDR-23 monochromator and detected at its output with an uncooled InGaAs diode (with 7-nm resolution in the range $\lambda = 1.0$–1.65 μm).

3. EXPERIMENTAL RESULTS AND DISCUSSION

Let us first discuss the results obtained for a sample annealed at $T_2 = 1000$°C. Figure 1 shows the EL spectra of this Si:(Er,O) diode, which were measured at the same currents in the breakdown (curve *1*) and forward bias modes (curve *2*). In the breakdown mode, a peak at

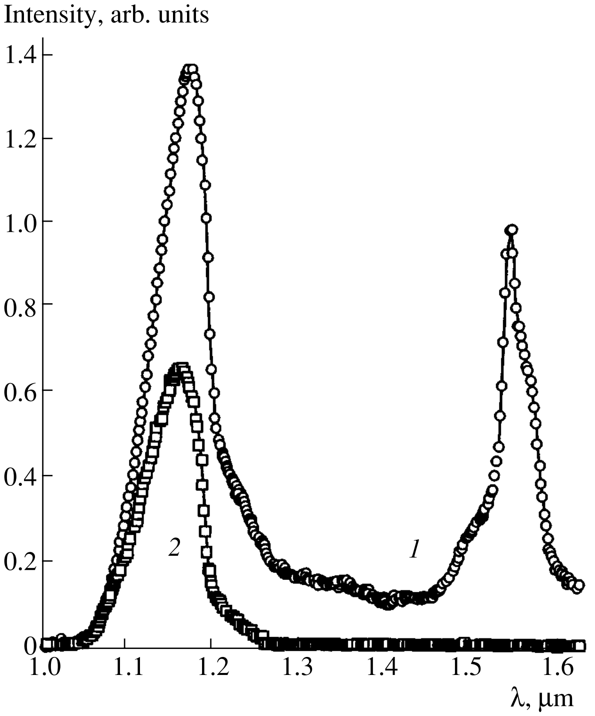

Fig. 1. EL spectra recorded at equal currents through the diode: (*1*) breakdown mode and (*2*) forward current mode.

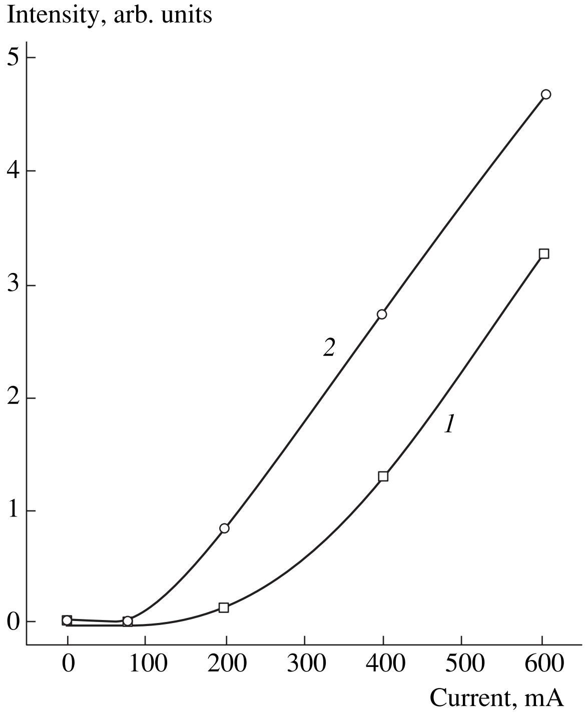

Fig. 2. EL intensity at λ = 1.16 μm vs. the current through the diode: (*1*) forward bias and (*2*) breakdown mode.

$\lambda \approx 1.16$ μm is observed along with the Er-ion EL peak at $\lambda \approx 1.54$ μm and the band of hot-carrier EL. A similar EL peak is observed in the forward current mode (see Fig. 1, curve *2*) and is commonly attributed to band-to-band (indirect) radiative recombination. It is noteworthy that, in the sample under study, the intensity of this peak is lower under forward bias, compared with the case of reverse bias, although this relation may be reversed for diodes fabricated by other technologies. The intensity of the $\lambda \approx 1.16$ μm EL as a function of forward and reverse current is represented in Fig. 2 by curves *1* and *2*, respectively. The EL increases steeply after the threshold current is reached, which differs depending on the direction of the current. The existence of a current threshold can be attributed to the presence of nonradiative recombination channels through which recombination occurs almost entirely at currents below the threshold one.

A specific feature of the band-to-band recombination emission is that it is quite strongly absorbed in the silicon wafer. Therefore, if this emission is mainly generated at one of the wafer surfaces, a significant difference would be expected to appear at one and the same current between the EL spectra recorded from the front and back sides of the wafer. Not only the EL peak intensity, but also other characteristics of the spectra may differ, since the absorption coefficient of silicon in this spectral range is not constant but increases steeply toward shorter wavelengths.

Figure 3 presents the EL spectra measured in the breakdown mode at one and the same current, with emission collected from the front (curve *1*) and back (curve *2*) sides of a wafer. Since the absorption of the Er-ion emission ($\lambda \approx 1.54$ μm) across the wafer thickness is small, curve *2* was recorded with the sample arranged so that the intensity of the Er-related EL peak exactly coincided with that for curve *1*. This alignment also led to virtually coinciding intensities of the “hot” EL in the range $\lambda \approx 1.25$–1.45 μm, which is also manifested in the high transparency range of Si. As seen from Fig. 3, under the experimental conditions, the EL intensity recorded in the breakdown mode in the band-to-band recombination range from the backside of a wafer exceeds that observed from its front. It is necessary to note also that, under the same experimental conditions, the EL intensity measured in the band-to-band recombination range in the forward current mode was, by contrast, higher when recorded from the front side of a wafer. These results show that the intensity of the emission peak of minority carrier recombination is significantly shifted to the front side of the wafer in the forward current mode and to its backside in the breakdown mode. This conclusion is also supported by a comparison of the EL spectra in the band-to-band recombination range normalized to the peak intensity (Fig. 4). As seen in Fig. 4, the EL spectrum observed from the front side of the wafer is narrower than that collected from the back side, owing to the strong absorption of short-wavelength emission in Si.

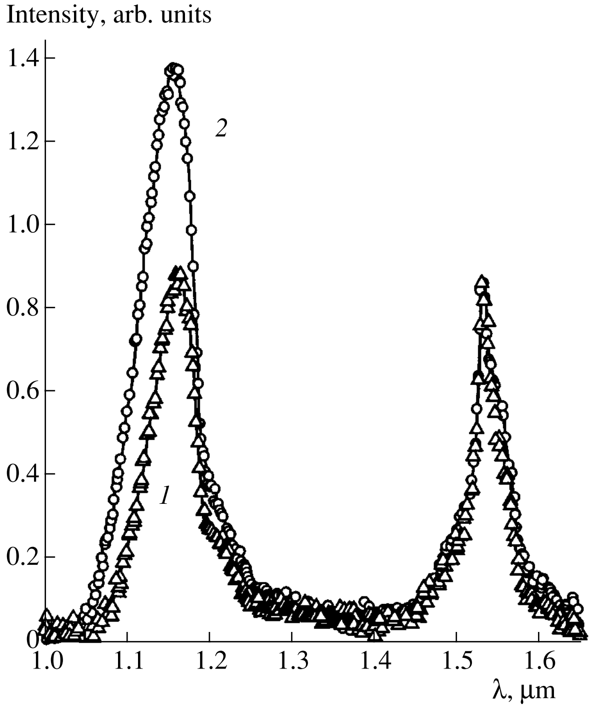

Fig. 3. EL spectra recorded at current of 400 mA in the breakdown mode, with the emission collected from (*1*) front and (2) rear sides of a wafer.

In the breakdown of a *p*–*n* junction, electrons generated in the space charge region arrive at the *n* region, and holes, at the *p* region. Nonequilibrium majority carriers either go to metal contacts or recombine with the minority carriers injected from these contacts. In the latter case, band-to-band recombination emission is generated mainly at the back surface of the sample. It is important that impact ionization is not necessary for emission generation in this case.

In studying the EL from Si:(Er,O) diodes, differing from those described above only in the temperature of the second annealing (in the range $700 \leq T_2 \leq 1100$°C), we found that the peak of the band-to-band recombination EL was observed in the breakdown mode at current densities $j \lesssim 25$ A/cm^2 only at $T_2 \geq 950$°C, and was not observed at $T_2 \leq 900$°C. Also, the technological reproducibility of this peak was very low, in contrast to the Er-related EL peak. This poor reproducibility may be related to the conditions of metal–semiconductor contact fabrication, e.g., to varying parameters of the intrinsic oxide film on the semiconductor surface and varied levels of surface contamination. To elucidate the reasons why the second annealing temperature affects the effect in question, we studied the technologically well-reproducible dependences of the band-to-band EL peak intensity on the forward current density at different T_2. The results we obtained are presented in Fig. 5.

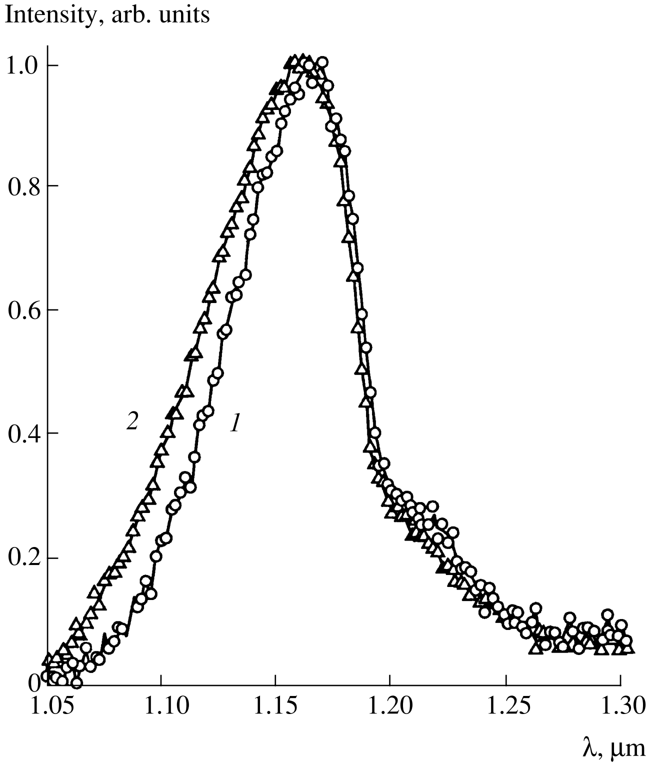

Fig. 4. EL spectra normalized to peak intensity, recorded at a breakdown current of 400 mA, with emission collected from (*1*) front and (*2*) rear sides of a wafer.

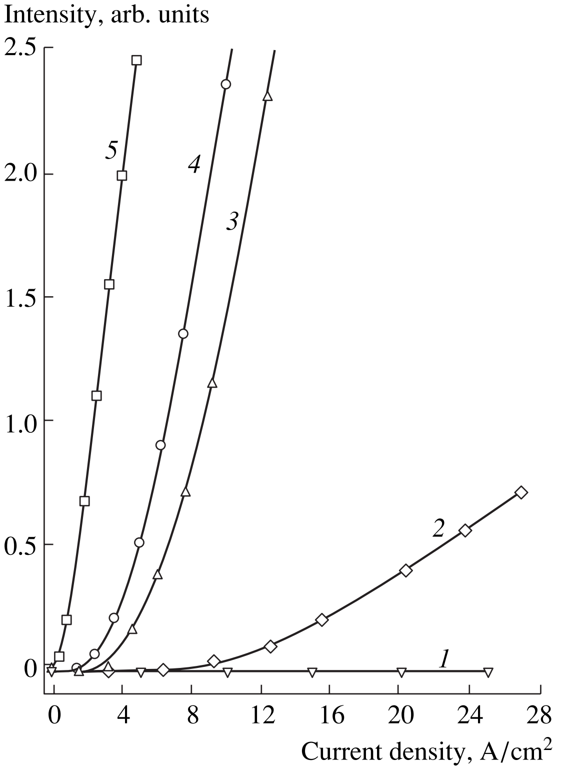

Fig. 5. EL peak intensity in the band-to-band recombination range vs. forward current density for Si:(Er,O) diodes differing in second annealing temperature T_2: (*1*) 700, 800, and 900, (*2*) 975, (*3*) 1000, (*4*) 1025, and (*5*) 1100°C.

As seen, the band-to-band recombination EL is virtually unobservable at $T_2 \leq 900°C$ in the current density range under study. With the second annealing temperature raised to 975°C and above, the threshold current density j_{th}, at which effective emission in the band-to-band recombination range is observed, already falls within the range of current densities we studied and which are shown in Fig. 5. Upon increasing the second annealing temperature, j_{th} decreases. By analogy with the EL in the forward current mode, it may be assumed that the influence of the annealing temperature T_2 on the radiative band-to-band recombination EL in the case of breakdown can be attributed to the effect of the annealing temperature on the threshold (current density) for the appearance of EL from the backside of a silicon wafer.

4. CONCLUSION

We have shown that the band observed in the range of indirect band-to-band recombination in the EL spectrum of a silicon diode in the breakdown mode can be related to the injection of minority carriers into silicon from a metal contact. Therefore, impact ionization processes are not necessary for this EL band to appear. Effective emission in the band-to-band recombination range appears when a certain, technology-dependent current density is reached. This threshold current density decreases with the temperature of the post-implantation annealing of Si: (Er,O) diodes increasing in the range 900–1100°C.

ACKNOWLEDGMENTS

We are grateful to R.V. Tarakanova for assistance in sample preparation.

The study was supported in part by INTAS (grant no. 99-01872) and the Russian Foundation for Basic Research and Office for Scientific and Technical Cooperation, Austria (grant no. 01-02-02000 OSTC).

REFERENCES

1. G. Franzo, S. Coffa, F. Priolo, and C. Spinella, J. Appl. Phys. **81**, 2784 (1997).
2. N. A. Sobolev, A. M. Emel’yanov, and K. F. Shtel’makh, Appl. Phys. Lett. **71**, 1930 (1997).
3. A. M. Emel’yanov, N. A. Sobolev, and A. N. Yakimenko, Appl. Phys. Lett. **72**, 1223 (1998).
4. N. A. Sobolev, A. M. Emel’yanov, and Yu. A. Nikolaev, Fiz. Tekh. Poluprovodn. (St. Petersburg) **34**, 1069 (2000) [Semiconductors **34**, 1027 (2000)].
5. A. M. Emel’yanov, N. A. Sobolev, M. A. Trishenkov, and P. E. Khakuashev, Fiz. Tekh. Poluprovodn. (St. Petersburg) **34**, 965 (2000) [Semiconductors **34**, 927 (2000)].
6. N. A. Sobolev, A. M. Emel’yanov, and Yu. A. Nikolaev, Fiz. Tekh. Poluprovodn. (St. Petersburg) **33**, 931 (1999) [Semiconductors **33**, 850 (1999)].
7. L. A. Kosyachenko and M. P. Mazur, Fiz. Tekh. Poluprovodn. (St. Petersburg) **33**, 170 (1999) [Semiconductors **33**, 143 (1999)].
8. L. A. Kosyachenko, E. F. Kukhto, and V. M. Sklyachuk, Fiz. Tekh. Poluprovodn. (Leningrad) **18**, 426 (1984) [Sov. Phys. Semicond. **18**, 266 (1984)].

Translated by D. Mashovets

Semiconductors, Vol. 36, No. 4, 2002, pp. 434–438. Translated from Fizika i Tekhnika Poluprovodnikov, Vol. 36, No. 4, 2002, pp. 457–461.

Control of the Interband and Intersubband Transition Energy in Quantum Wells Using Localized Isoelectronic Perturbations

K. Durinyan, A. Zatikyan, and S. Petrosyan*

Yerevan State University, Yerevan, 375049 Armenia

** e-mail: stpetros@www.physdep.r.am*

Submitted July 5, 2001; accepted for publication August 28, 2001

Abstract—Within the scope of the simple one-band approximation, the effect of built-in attractive and repulsive δ-shaped potentials on the energy spectra of carriers and oscillator strength was studied for optical transitions in quantum wells. The effect of δ-shaped perturbation on the magnitude and sign of the energy level shift was shown to depend heavily on the isoelectronic probe position and the effective mass inhomogeneity. Calculation of the oscillator strength for intersubband transitions confirms the possibility of developing coupled quantum-well structures with interesting nonlinear properties. *© 2002 MAIK "Nauka/Interperiodica".*

INTRODUCTION

Interband and intersubband optical transitions in heterostructures with quantum wells (QWs) are attracting considerable attention due to ample opportunities for their application in semiconductor lasers and photodetectors of infrared radiation [1, 2]. In this case, it is often required to control the energy position of two-dimensional subbands, as well as the degree of electron and hole wave-function localization in QWs. For given materials of QWs and surrounding barrier layers, such control is conventionally accomplished by selecting the well width or (and) solid solution composition (i.e., the well depth). As a result, the parameters of the electron states belonging to all the subbands of size quantization are simultaneously changed. Obviously, this method is not always convenient, since the requirements for the necessary electron spectrum and minimization of the photodetector dark current can contradict one another [2]. To overcome this problem, more intricate heterostructures are sometimes employed instead of ordinary QWs. In [3], the method of planar isoelectronic perturbation implemented by inducing δ-shaped repulsive or attractive potentials at the QW center was first suggested for the separate control of the QW electron and optical properties. The basic idea of this approach consists in that such a localized perturbation has a significant effect on the energy position of even-numbered subbands of size quantization, leaving virtually unchanged the states belonging to odd-numbered subbands, whose wave function at the point of δ-perturbation has a node.

Experimental study [4, 5] of optical absorption and photoluminescence (PL) of such QWs has shown that such a perturbation indeed makes it possible to affect significantly the energy distance between subbands in comparison with the ordinary QW. If the δ perturbation is not at the QW center, it begins to also affect the states of odd-numbered subbands of electrons and holes. Apart from the level shift, the δ-perturbation affects the wave-function symmetry. Therefore, the selection rules and oscillator strengths for intraband and interband optical transitions are changed. Recently, an isoelectronic perturbation was shown to significantly improve the radiative parameters of indirect-gap GaAsP/GaP-based QWs [6].

In this study, we theoretically investigate the QW energy spectrum with the built-in repulsive or attractive potentials, taking into account the effective mass nonuniformity. The calculations were carried out for built-in barriers of finite width and height and δ-shaped barriers. When built-in potentials are shifted from the QW center, their effect on the energy spectrum can be described with sufficient accuracy in the approximation of the perturbation theory, considering these potentials as δ perturbations. Notwithstanding the fact that all calculations were carried out neglecting the energy spectrum nonparabolicity and electron state mixing, a rather good agreement with the experiment [4, 5] was achieved.

CALCULATION OF THE BOUND STATE ENERGY

First, we consider the case when an isoelectronic perturbation is at the QW center. The structure experimentally studied in [5] was a GaAs/AlAs QW with the confining potential U_0. A thin-layer of wide-gap (AlAs) or narrow-gap (InAs) material was introduced at the QW center. These layers, typically having a thickness of a few monolayers, produce highly localized rectangular attractive and repulsive potentials with a height of V_0 and a thickness of $2\varepsilon \ll 2a$. The electron wave function in the conduction band can be written (as is usual) as the product of the Bloch function $u_c(\mathbf{r})$ at the Brillouin zone center and the smooth envelope function $\varphi(z)$ describing the electron motion along the z-axis,

$$\psi(\mathbf{r}) = \frac{1}{\sqrt{S}} u_c(\mathbf{r}) e^{i\mathbf{k}_\parallel \boldsymbol{\rho}} \varphi(z), \tag{1}$$

where S is the structure cross section and $\mathbf{k}_\parallel$ and $\boldsymbol{\rho}(x, y)$ are the two-dimensional wave vector and radius vector in the plane xy, respectively. In the effective-mass approximation, the envelope function $\varphi(z)$ is determined from the following Schrödinger equation (see [7]):

$$\begin{aligned} &-\frac{\hbar^2}{2}\frac{d}{dz}\left[\frac{1}{m^*(z)}\frac{d}{dz}\right]\varphi(z) \\ &+\left[V(z) + \frac{\hbar^2 k_\parallel^2}{2m^*(z)}\right]\varphi(z) = E\varphi(z). \end{aligned} \tag{2}$$

Here, $V(z)$ is the heterostructure potential pattern and $m^*(z)$ is the effective electron mass. A solution to Eq. (2) for bound states $E < U_0$ in separate regions can be represented (as is usual) as a linear combination of exponential functions of an imaginary or real argument. Using the conventional continuity conditions for $\varphi(z)$ and $\varphi'(z)/m^*$ at each heteroboundary, we can readily derive the equations to determine the bound state energies,

$$-\frac{m_3 k_0}{m_1 \chi}\frac{1 - \dfrac{m_1}{m_2}\dfrac{k}{k_0}\tan k(a-\varepsilon)}{1 + \dfrac{m_2}{m_1}\dfrac{k_0}{k}\tan k(a-\varepsilon)} = \begin{cases} \tanh\chi\varepsilon \text{ for even-numbered states,} \\ \cosh\chi\varepsilon \text{ for odd-numbered states,} \end{cases} \tag{3}$$

where the wave vectors are given by

$$k = \sqrt{\frac{2m_2}{\hbar^2}E - k_\parallel^2}, \quad k_0 = \sqrt{\frac{2m_1}{\hbar^2}(U_0 - E) + k_\parallel^2},$$

$$\chi = \begin{cases} \sqrt{\dfrac{2m_3}{\hbar^2}(V_0 - E) + k_\parallel^2} \text{ repulsive potential,} \\ i\sqrt{\dfrac{2m_3}{\hbar^2}(V_0 + E) + k_\parallel^2} \text{ attractive potential.} \end{cases}$$

The derived transcendent equation can be simplified by performing a passage to the limit ($V_0 \longrightarrow \infty$, $\varepsilon \longrightarrow 0$, $V_0\varepsilon = \text{const}$); i.e., we replace a barrier of finite thickness at the QW center by the δ-shaped barrier. Designating the barrier penetrability as

$$C_0 = \frac{2m_3}{\hbar^2}V_0\varepsilon,$$

the energies of even-numbered states can be described by the simpler equation

$$-\frac{m_3 k_0}{m_1 \chi}\frac{1 - \dfrac{m_1}{m_2}\dfrac{k}{k_0}\tan ka}{1 + \dfrac{m_2}{m_1}\dfrac{k_0}{k}\tan ka} = \pm C_0 a, \tag{4}$$

where the minus and plus signs correspond to the repulsive and attractive potentials, respectively. For odd-numbered states, we obtain an equation coinciding with the analogous one for the simple QW. As expected, the δ-shaped barrier at the QW center has no effect on the energy position of odd-numbered subbands. When a δ-shaped perturbation is not at the structure center, but is shifted to the left or right to the point z_0 it is impossible to obtain simple analytical results. In this case, the energy level shift can be readily estimated using the perturbation theory. Comparing the results of such an approach to the results of an exact solution in the specific case when a perturbation is at the QW center ($z_0 = 0$), it can be concluded that, restricting ourselves to the second order of the perturbation theory, the level shift can be described to within about 5%. Representing the perturbing potential as

$$H' = \frac{\hbar^2}{m_3}C_0\delta(z - z_0) \tag{5}$$

and knowing the energy spectrum $E_n^{(0)}$ and the wave functions $\varphi_n^{(0)}(z)$ of bound states in the ordinary QW without built-in barriers, the energy levels of a QW with a built-in δ-shaped barrier can be written as

$$\begin{aligned} E_n &= E_n^{(0)} + \frac{\hbar^2}{m_3}C_0\left|\varphi_n^{(0)}(z_0)\right|^2 \\ &+ \frac{\hbar^4}{m_3^2}C_0^2\sum_{n \neq m}\frac{\left|\varphi_n^{(0)*}(z_0)\varphi_m^{(0)}(z_0)\right|^2}{E_n^{(0)} - E_m^{(0)}}. \end{aligned} \tag{6}$$

If the point $z = z_0$ is a node for this state, we have $\varphi_n^{(0)}(z_0) = 0$ and $E_n = E_n^{(0)}$. In general, one can see from (6) that the coordinate dependence of electron wave functions in the QW can be determined, in principle, by measuring the energy level shift at various δ-perturbation positions.

In [5], intrasubband absorption spectra in a GaAs/AlAs QW with a width of 33 monolayers were studied. To induce repulsive or attractive potential at the

Table 1. Energy levels in quantum wells (calculation)*

	a	b	c	d	e	f	g
QW profiles		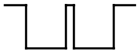	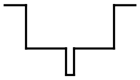	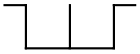	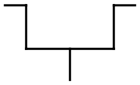	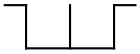	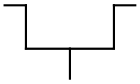
E_1, meV	44.58	88.53	3.63	88.21	2.61	91.29	5.7
E_2, meV	180.2	168.97	186.04	180.2	180.2	180.2	180.2
E_3, meV	410.7	468.29	376.15	467.52	375.06	477.2	377
$E_2 - E_1$	135.62	80.44	182.41	91.99	177.59	88.91	174.5

* The QW wall height at $T = 300$ K is taken as 1.2 eV [5]. Notation: (a) simple QW; (b–g) QWs with (b) AlAs, (c) InAs, (d) AlAs, and (e) InAs δ-shaped barriers; (f, g) calculation in the approximation of the perturbation theory for the cases (d) and (e), respectively.

Table 2. Calculation parameters

Parameters	Units	Values	References
Band gap E_g(GaAs)	eV	1.519	[7]
Electron mass $m_e(\mathrm{Ga}_{1-x}\mathrm{Al}_x\mathrm{As})$	m_0	$0.067 + 0.083x$	[8]
Electron mass m_e(InAs)	m_0	0.023	[7]
Electron mass m_e(AlAs)	m_0	0.15	[9, 10]
Heavy hole mass $m_{hh}(\mathrm{Ga}_{1-x}\mathrm{Al}_x\mathrm{As})$	m_0	$0.62 + 0.14x$	[8]
Light hole mass $m_{lh}(\mathrm{Ga}_{1-x}\mathrm{Al}_x\mathrm{As})$	m_0	$0.087 + 0.063x$	[8]
Attractive potential V_{0e}	eV	0.64	
Attractive potential V_{0h}	eV	0.35	
Repulsive potential V_{0e}	eV	1	
Repulsive potential V_{0h}	eV	0.15	
Exciton binding energy $E^{ex}[e_i - hh_j(lh_j)]$	meV	6.5(9)	[4]

QW center, AlAs or InAs monolayers were introduced, respectively. These additional layers appreciably shift the intraband absorption spectrum caused by transitions between the ground and first excited subbands of size quantization in the QW. For example, the absorption maximum in the QW without built-in potentials corresponds to the photon energy of 138 meV. The introduction of only one AlAs (repulsive potential) or InAs (attractive potential) monolayer into the QW center shifts the absorption peak to 88 and 181 meV, respectively. The calculated electron level positions with respect to the QW bottom are listed in Table 1. The calculation parameters typical of the GaAs/AlAs and GaAs/InAs heterostructures were used (see Table 2). The calculations show that the GaAs/AlAs QWs with a width of 33 monolayers (about 94 Å), containing single AlAs or InAs monolayers, always have five bound levels. One can see from the data of Table 1 that introduction of only one AlAs or InAs monolayer has a marked effect on the arrangement of even-numbered subbands and almost no effect on odd-numbered subbands. For example, if the first level in the QW without built-in potentials is at a height of 44.6 meV, introduction of a repulsive potential drastically shifts the ground level upward; its energy grows approximately twofold and becomes equal to 88.5 meV. The second level shifts downward insignificantly, from 180.2 to 169 meV. As a result, the interband energy distance is reduced from 135.6 to 80.4 meV, which conforms well to the experimentally observed shift of the intraband absorption maximum. The levels are similarly shifted by the attractive potential introduced into the QW center. The ground level descends and approaches the height of 3.6 meV from the QW bottom. The second level is slightly raised to 186 meV. Thus, if the difference $E_2 - E_1$ was 135.6 meV without perturbation, introduction of the attractive potential increases it to 182.4 meV, which also conforms well to the intraband absorption maximum. We note that the higher the level with respect to the QW bottom, the shorter is the shift caused by perturbation. The repulsive potential raises the energy levels of all the even-numbered subbands, but lowers those of odd-numbered ones. In the case of attractive potential, the pattern is opposite. It is noteworthy that this effect is caused by the significant difference of the effective electron mass in different heterostructure regions. In the approximation of uniform effective mass, all the levels are simultaneously shifted upward or downward.

Table 1 lists the data calculated in the approximation of the δ-shaped barrier for built-in potentials [columns (d) and (e)], as well as in the perturbation theory approximation [columns (f) and (g)]. One can see that the bound state energies at $z_0 = 0$, calculated in the second order of the perturbation theory, coincide with the results of exact calculation within an error smaller than 10% and adequately describe the level shift caused by a localized perturbation. We believe that the perturbation theory can also describe the level shift at arbitrary z_0 with the same accuracy.

In [4], the electron and hole states were experimentally probed when studying the interband PL spectra of GaAs/Ga$_{0.71}$Al$_{0.29}$As QWs ($2a$ = 160 Å) at various locations of attractive (InAs) and repulsive (AlAs) perturbations. Some pronounced peaks caused by transitions between electron subbands (e_i) and subbands of light (lh_j) and heavy (hh_j) holes were observed in the spectra measured at low temperatures (10 K). As a perturbation point was shifted from the QW center, the characteristic structure of the interband PL spectra was preserved; however, the peaks were continuously shifted upward or downward on the energy scale.

Taking into account the probability of exciton generation, the interband transition energy can be written as

$$\begin{aligned} &E[e_i - hh_j(lh_j)] \\ &= E_g + E(e_i) + E[hh_j(lh_j)] - E^{ex}[e_i - hh_j(lh_j)], \end{aligned} \tag{7}$$

where E_g is the GaAs band gap and $E^{ex}[e_i - hh_j(lh_j)]$ is the binding energy of an exciton formed by an electron from the ith subband and by heavy or light holes from the jth subband (the subband energies are measured from the top or bottom of corresponding bands). Figure 1 shows the calculated energies of interband optical transitions versus the location of the attractive (Fig. 1a) and repulsive (Fig. 1b) potentials. The numerical parameters used in the calculations are listed in Table 2. As expected [see (6)], the oscillating property of wave functions distinctly manifests itself in the interband transition energy, when electron and hole states are continuously probed by local isoelectronic perturbations. The potential barrier height for electrons at the GaAs/GaAlAs heteroboundary is calculated using the empirical formula $U_{0e} = 1.1x$ (x = 0.29) [8]. For heavy and light holes, the potential well depth is determined from the ratio U_{0e}/U_{0h} = 0.6/0.4 [8]. The heteropotentials V_{0e} and V_{0h}, induced by layers of thickness on the order of one monolayer, are the adjustable parameters. Values of these that yield the best fit to the experiment are listed in Table 2.

OSCILLATOR STRENGTH FOR INTERSUBBAND TRANSITIONS IN THE QUANTUM WELL

As was mentioned above, as the perturbing potential is shifted along the QW, not only the mutual arrangement of energy levels, but also the wave-function symmetry is changed. This, in turn, can affect the conventional selection rules. As is known [2], transitions between subbands with different parity are allowed in ordinary QWs exposed to z-polarized light. The built-in potential violates the QW inversion symmetry; hence, generally speaking, optical transitions between all the subbands become possible. To demonstrate this possibility, we calculate the oscillator strength, which, in the dipole approximation for transitions between subbands n and m, is defined by the matrix element of coordinate z (see [3]),

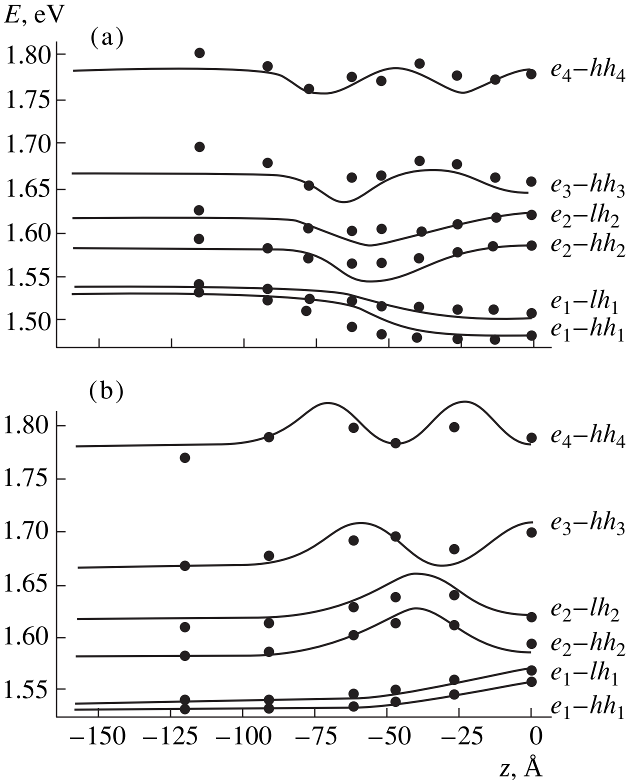

Fig. 1. Dependences of the interband transition energy on the built-in δ-barrier position in the quantum well for the (a) InAs and (b) AlAs barriers; the data were calculated at $k_\parallel = 0$ (solid curves) and experimental points were taken from [4].

$$f_{mn} = \frac{2m_0\omega_{mn}}{\hbar}|\langle\varphi_m(z, z_0)|\mathbf{z}|\varphi(n)(z, z_0)\rangle|^2, \tag{8}$$

where $\omega_{mn} = (E_m - E_n)/\hbar$ and m_0 is the free electron mass. The wave functions $\varphi_n(z, z_0)$ of bound states at a given z_0, to a first approximation of the perturbation theories, are written as

$$\begin{aligned} &\varphi_n(z, z_0) \\ &= \varphi_n^{(0)}(z) + \frac{\hbar^2}{m_3}C_0\sum_{m \neq n}\frac{\varphi_m^{(0)*}(z_0)\varphi_n^{(0)}(z_0)}{E_n^{(0)} - E_m^{(0)}}\varphi_m^{(0)}(z), \end{aligned} \tag{9}$$

where the summation is performed over all the QW bound states. Using formulas (8) and (9), the values of f_{mn} can be readily calculated in relation to the δ-shaped

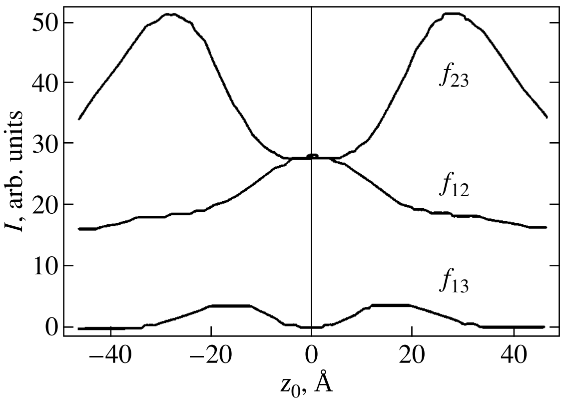

Fig. 2. Dependence of the oscillator strengths f_{13}, f_{12}, and f_{23} on the δ-barrier position in the quantum well.

potential position. The dependences of the oscillator strengths on z_0r optical transitions between three lower subbands in the case of repulsive δ-shaped potential are shown in Fig. 2. One can see that the probability of optical transitions between subbands 1 and 3 also becomes nonzero ($f_{13} \neq 0$, $z_0 \neq 0$) when the δ perturbation is shifted from the QW center. In this case, not only the oscillator strength, but also the intersubband energy distances ($E_2 - E_1$) and ($E_3 - E_2$) are changed. Since, as a rule, the perturbation shifts neighboring subbands oppositely (see Table 1), the first three levels can become equidistant at some z_0. For the considered QW with a width of about 94 Å, such a situation arises at four positions of the δ perturbation within the QW: $z_{01} = \pm 21$ Å and $z_{02} = \pm 25.7$ Å with the corresponding resonance frequencies $\omega_1 = 2.8 \times 10^{14}$ Hz and $\omega_2 = 2.6 \times 10^{14}$ Hz. We note that the oscillator strengths f_{13}, f_{12}, and f_{23} are comparable. Therefore, it can be expected that the condition for the double resonance characterized by high nonlinear susceptibility of the second order can be met in the QW with built-in short-range potentials, which can be used to generate the second harmonic [11]. The QW with the built-in δ-shaped potential is conceptually a system of two coupled QWs. Due to high optical nonlinearity, heterostructures with such coupled QWs have long been studied to generate the difference frequency, as well as the second and third harmonics at the wavelengths $\lambda \approx 10$ μm [12].

CONCLUSION

Thus, we showed that δ-shaped isoelectronic perturbations have a profound effect on the QW energy spectrum. Consideration of the difference between effective masses in different QW regions leads to different behavior of even- and odd-numbered subbands. A change of the δ-shaped barrier position in the QW leads not only to a change in the energy position of subbands, but also to a change of the wave-function symmetry. This in turn affects the selection rules for interband and intersubband transitions. Due to such a dual effect of the δ-shaped barrier, an interesting resonance situation becomes probable when three lower energy levels are arranged equidistantly, which may be employed to generate the second harmonic. Summarizing the above, it can be concluded that the built-in δ-shaped barrier allows for more simple and efficient control of the energy subbands in the QW, which may find new practical applications.

ACKNOWLEDGMENTS

This study was supported by INTAS (grant no. 99-00928) and ISTC (grant no. A-322).

REFERENCES

1. Bin Zhao and A. Yariv, in *Semiconductor Lasers I,* Vol. 1: *Fundamentals,* Ed. by Eli Kapon (Academic, San Diego, 1999).
2. *Intersubband Transitions in QWs: Physics and Applications*, Ed. by H. C. Liu and F. Capasso (Academic, San Diego, 1999).
3. W. Trzeciakowski and B. D. McCombe, Appl. Phys. Lett. **55**, 891 (1989).
4. J.-Y. Marzin and J.-M. Gerard, Phys. Rev. Lett. **62**, 2172 (1989).
5. H. Sakaki, H. Sugawara, J. Motohisa, and T. Nonda, in *Intersubband Transitions in Quantum Wells*, Ed. by E. Rosencher, B. Vinter, and B. Levine (Plenum, New York, 1992), p. 65.
6. K. Arimoto, N. Usami, and Y. Shiraki, Physica E (Amsterdam) **8**, 323 (2000).
7. G. Bastard, *Wave Mechanics Applied to Semiconductor Heterostructures* (Les Editions de Physique, Les Ulis Cedex, 1989).
8. S. Adachi, J. Appl. Phys. **58**, R1 (1985).
9. E. Hess, I. Topol, K. R. Schulze, *et al.*, Phys. Status Solidi B **55**, 187 (1973).
10. *Landolt-Börnstein: Numerical Data and Functional Relationships in Science and Technology, New Series* (Springer-Verlag, Berlin, 1982, 1987), Group III, Vols. 17a and 22a.
11. J. B. Khurgin, *Semiconductor and Semimetals*, Vol. 59: *Nonlinear Optics of Semiconductors II* (Academic, San Diego, 1998), p. 1.
12. C. Sirtori, F. Capasso, D. Sivco, and A. Cho, in *Intersubband Transitions in Quantum Wells: Physics and Device Applications II*, Ed. by H. C. Liu and F. Capasso (Academic, London, 2000), Chap. 2, p. 85.

Translated by A. Kazantsev

Semiconductors, Vol. 36, No. 4, 2002, pp. 439–460. Translated from Fizika i Tekhnika Poluprovodnikov, Vol. 36, No. 4, 2002, pp. 462–483.
Original Russian Text Copyright © 2002 by Bagraev, Buravlev, Klyachkin, Malyarenko, Gehlhoff, Ivanov, Shelykh.

LOW-DIMENSIONAL SYSTEMS

Quantized Conductance in Silicon Quantum Wires

N. T. Bagraev*, A. D. Buravlev*, L. E. Klyachkin*, A. M. Malyarenko*,
W. Gehlhoff, V. K. Ivanov***, and I. A. Shelykh*****
** Ioffe Physicotechnical Institute, Russian Academy of Sciences,*
Politekhnicheskaya ul. 26, St. Petersburg, 194021 Russia
e-mail: impurity.dipole@pop.ioffe.rssi.ru
*** Institut für Festkörperphysik, Technische Universität Berlin, D-10623 Berlin, Germany*
**** St. Petersburg State Technical University, ul. Politekhnicheskaya 29, St. Petersburg, 195251 Russia*
Submitted June 4, 2001; accepted for publication August 29, 2001

Abstract—The results of studying the quantum-mechanical staircase for the electron and hole conductance of one-dimensional channels obtained by the split-gate method inside self-assembled silicon quantum wells are reported. The characteristics of quantum wells formed spontaneously between the heavily doped δ-shaped barriers at the Si(100) surface as a result of nonequilibrium boron diffusion are analyzed first. To this end, secondary-ion mass spectrometry, and also the detection of angular dependences of the cyclotron resonance and ESR, is used; these methods make it possible to identify both the crystallographic orientation of the self-assembled quantum wells and the ferroelectric properties of heavily doped δ-shaped barriers. Since the obtained silicon quantum wells are ultrathin (~2 nm) and the confining δ-shaped barriers feature ferroelectric properties, the quantized conductance of one-dimensional channels is first observed at relatively high temperatures ($T \geq 77$ K). Further, the current–voltage characteristic of the quantum-mechanical conductance staircase is studied in relation to the kinetic energy of electrons and holes, their concentration in the quantum wells, and the crystallographic orientation and modulation depth of electrostatically induced quantum wires. The results show that the magnitude of quantum steps in electron conductance of crystallographically oriented *n*-type wires is governed by anisotropy of the Si conduction band and is completely consistent with the valence-valley factor for the [001] ($G_0 = 4e^2/h$ and $g_v = 2$) and [011] ($G_0 = 8e^2/h$ and $g_v = 4$) axes in the Si(100) plane. In turn, the quantum staircase of the hole conductance of *p*-Si quantum wires is caused by independent contributions of the one-dimensional (1D) subbands of the heavy and light holes; these contributions manifest themselves in the study of square-section quantum wires in the doubling of the quantum-step height ($G_0 = 4e^2/h$), except for the first step ($G_0 = 2e^2/h$) due to the absence of degeneracy of the lower 1D subband. An analysis of the heights of the first and second quantum steps indicates that there is a spontaneous spin polarization of the heavy and light holes, which emphasizes the very important role of exchange interaction in the processes of 1D transport of individual charge carriers. In addition, the temperature- and field-related inhibition of the quantum conductance staircase is demonstrated in the situation when kT and the energy of the field-induced heating of the carriers become comparable to the energy gap between the 1D subbands. The use of the split-gate method made it possible to detect the effect of a drastic increase in the height of the quantum conductance steps when the kinetic energy of electrons is increased; this effect is most profound for quantum wires of finite length, which are not described under conditions of a quantum point contact. It is shown in the concluding section of this paper that detection of the quantum-mechanical conductance under the conditions of sweeping the kinetic energy of the charge carriers can act as an experimental test aiding in separating the effects of quantum interference in modulated quantum wires against the background of Coulomb oscillations as a result of the formation of QDs between the delta-shaped barriers. © *2002 MAIK "Nauka/Interperiodica".*

1. INTRODUCTION

The main characteristic of charge-carrier transport in semiconductor structures is conductance, which is controlled primarily by the processes of inelastic scattering of charge carriers. However, this statement is most important in designing semiconductor devices with characteristic sizes that are larger than the free-path length of charge carriers; at the same time, when describing the characteristics of devices based on quantum wires and quantum dots (QDs), it is important to take into account the effects related to the wave nature of electrons [1]. The charge transport in such devices having a single or several one-dimensional (1D) channels, whose length is smaller than the free path length, is not accompanied with the Joule losses as a result of suppression of the inelastic-scattering processes [1–3]. Therefore, the charge carriers can exhibit ballistic properties under conditions of quasi-1D transport.

In the first approximation, the conductance of a ballistic quantum wire depends only on the transmission coefficient $\mathcal{T}$ [4, 5]; i.e.,

$$G = G_0\mathcal{T}. \tag{1}$$

1063-7826/02/3604-0439$22.00 © 2002 MAIK "Nauka/Interperiodica"

Here,

$$G_0 = g_s g_v \frac{e^2}{h} N, \qquad (2)$$

where g_s and g_v are the spin and valley factors, respectively; N is the number of occupied 1D subbands, which corresponds to the number of the upper occupied 1D subband and may vary in relation to the gate voltage U_g; this voltage controls the number of charge carriers in a quantum wire [6, 7]. Furthermore, the dependence $G(U_g)$ is evidently steplike because the conductance of a quantum wire changes jumplike each time by the value of $g_s g_v e^2/h$ when the Fermi level coincides with one of the 1D subbands.

The level of nanotechnology attained in recent years made it possible to use the split-gate method [6–8], the overgrowth of the edge cleavage [9], the metal point contacts [10], and electrostatic ordering of impurity dipoles [11] to obtain quantum wires that have a single or several 1D ballistic channels within the GaAs–AlGaAs heterostructures [6–10], Si superlattices [11, 12], and individual quantum wells (QWs) at the surface of the PbTe [13] and 6H-SiC [14] single crystals. All these electrostatically induced quantum wires were identified as a result of discovering the quantized conductance in relation to the gate voltage $G(U_g)$; this voltage controlled the Fermi level position in reference to the 1D subbands. Notably, the height of the quantum-staircase steps for the conductance of 1D channels based on the classical GaAs–AlGaAs heterostructures corresponds to $2e^2/h$ ($g_s = 2$ and $g_v = 1$) [6, 7], whereas the step heights in the conductance of quantum wires in many-valley semiconductors (e.g., Si) are equal to $4e^2/h$ ($g_s = 2$, $g_v = 2$) and $8e^2/h$ ($g_s = 2$, $g_v = 4$) [15]. Therefore, study of the electron quantized conductance of an *n*-Si(100) QW can be conducive to the identification of its crystallographic dependence in view of the conduction-band anisotropy, because the valley factor would be different for the quantum wires oriented along the [001] ($g_v = 2$) and [011] ($g_v = 4$) axes. In turn, the quantum wires within a *p*-type (100) QW can be expediently used to determine the relative contribution of heavy and light holes to the height of the quantized-conductance steps. In both cases, we should expect the effects of doubling of the quantum steps when observing the quantum-staircase conductance (1) variation with the gate voltage $G(U_g)$, the demonstration of which was one of the objectives of this study.

In addition, it is of interest to study the processes of quenching the quantized conductance as the voltage applied along the quantum wire increases up to the value for which the transitions of charge carriers between the 1D subbands are induced [16]. Such transitions are most likely to occur at the gate voltages U_g that correspond to the steps of the quantum conductance staircase, which disturbs the linearity of the current–voltage (*I*–*V*) characteristic; expression (1) was obtained under the assumption that this linearity is strictly obeyed [4, 5]. Similar smoothing of the steplike dependence $G(U_g)$ should occur at a finite temperature of a quantum wire, because in this case the number of filled subbands of size quantization becomes indeterminate, whereas expression (1) describes the behavior of quantized conductance only at zero temperature. It is noteworthy that, for low longitudinal voltages, in which case the transitions between the 1D subbands are unlikely, one can observe an enhancement (rather than suppression) of quantum steps due to heating of the ballistic charge carriers. Such an effect of heating should manifest itself, first of all, when studying quantum wires with finite length, whose characteristics are not described in the conditions of a quantum point contact. In this case, important data can be obtained using the split-gate method as this makes it possible to record the dependences of the quantized conductance $G(U_g)$ under the conditions of the sweep of the longitudinal source–drain voltage. Therefore, in order to study the mechanisms of enhancement and suppression of quantum steps, we use quantum wires of various lengths; these wires were obtained in the split-gate mode within a Si QW (100) formed between ferroelectric barriers, which makes it possible to stabilize the conditions of size quantization when a longitudinal electric field varies linearly.

In addition to the quantum step, the plateau of the quantized conductance is an important characteristic of this conductance; the extent and shape of this plateau is controlled by the spin and charge correlations within the ballistic quantum wires. As a rule, the extent of the plateau following the first step in the quantized conductance is somewhat smaller than $g_s g_v e^2/h$, which may result from the effect of the charge-carrier polarization in the zero magnetic field [17–26] or from the disturbance of coherency due to both the electron–electron interaction and the scattering by impurity centers [27–29]. In addition, the residual-impurity atoms distributed over the boundaries of the quantum wire form the basis for the formation of internal barriers, which modulate the characteristics of coherent transport of individual charge carriers. This modulation can give rise to oscillations in the plateau region of quantized conductance, which results from the interference effects induced by the elastic backscattering between the modulating barriers [30]. It is noteworthy that the interference of ballistic charge carriers should manifest itself most pronouncedly if the detection of the conductance $G(U_g)$ quantum staircase is accompanied with a corresponding variation in the charge-carrier kinetic energy, which is accomplished by performing a precision linear increase in the electric field along the modulated quantum wire (100) under conditions of sweeping the longitudinal voltage.

In what follows, we first analyze the characteristics of the self-assembled *n*- and *p*-type QWs formed at the Si(100) surface in the course of nonequilibrium boron diffusion. Further, we report the results of studying the quantized conductance in relation to temperature, charge-carrier concentration, and the modulation depth of silicon quantum wires formed using the split-gate structure built into the plane of the self-assembled QW. Since the obtained self-assembled QWs were extremely narrow (≈2 nm) and the confining barriers had ferroelectric properties, the quantum steps were observed for the first time at a comparatively high temperature ($T \geq 77$ K).

2. EXPERIMENTAL

2.1. Ultrashallow Boron Diffusion Profiles on the Silicon (100) Surface

Individual QWs, on the basis of which the split-gate configuration is accomplished in this study, are formed spontaneously within the ultrashallow p^+ diffusion profiles at the (100) surface of single-crystal silicon. These impurity profiles were obtained as a result of nonequilibrium boron diffusion using precision control over the fluxes of self-interstitials and vacancies, which are generated by the Si–SiO_2 interface (Fig. 1a) and enhance the dopant diffusion according to the "kick-out" (KO) vacancy-related diffusion mechanisms, respectively [31, 32].

The ultrashallow boron diffusion profiles were obtained in single-crystal *n*-Si(100) wafers 350-μm thick with various concentrations of shallow-level P donors. Preliminarily, both surfaces of the wafer were oxidized in the atmosphere of dry oxygen at a temperature of 1150°C. The oxide thickness depended on the oxidation duration. It is noteworthy that the preliminary oxidation of both wafer surfaces was used primarily to accumulate both self-interstitials and vacancies in the substrate, which is attained if there is a thin or thick oxide layer at the surface, respectively [32, 33]. Such an effect cannot be realized if only the operating surface is oxidized, which corresponds to gettering of residual impurities; in this case, the self-interstitials and vacancies form microdefects near the rear substrate surface. After completion of oxidation, photolithography was employed to form openings at the operating side of the wafer; these openings were consistent with the Hall measurement configuration and were used for short-term boron diffusion from the gaseous phase (Fig. 1a).

By varying the diffusion temperature (T_{dif} = 800, 900, and 1100°C) and the thickness of the preliminarily deposited oxide layer, we managed to determine the optimal conditions for the prevalence of the KO or substitutional mechanisms of boron diffusion and ascertain the criteria for their equality. A high level of primary-defect generation, which ensures enhanced or retarded diffusion of impurity atoms, was attained not only owing to the preliminary accumulation of these defects in the substrate but also by feeding the boron-containing gaseous phase with dry oxygen and chlorine compounds.

An analysis of the obtained B concentration profiles in Si(100) using secondary-ion mass spectrometry (Fig. 2) shows that parity between the KO and substitutional diffusion mechanisms, which results in a drastic deceleration of the impurity diffusion, is attained at T_{dif} = 900°C. In this case, the intense annihilation of self-interstitials and vacancies, which forms the basis for the parity between the diffusion mechanisms, stimulates the suppression of the surface deformation potential (SDP) over the diffusion-profile plane [12, 33]. In addition, we should expect that retardation of the fluxes of the impurity atoms, which are dragged by both the self-interstitials and vacancies, can be conducive to an increase in the SDP across the diffusion-profile plane. Apparently, such an anisotropy of SDP causes fluctuations in the dopant concentration, depending on the profile depth (Fig. 3a); these fluctuations were observed using the four-point probe method under conditions of layer-by-layer etching. It is worth noting that difficulties in detecting nonmonotonic variations in concentrations within the profile measured using secondary-ion mass spectrometry (Fig. 3a) are related, on the one hand, to limitations of the resolution of this method and, on the other hand, to smoothing of the ultrashallow diffusion profile as a result of impurity-atom diffusion under exposure to the ion beam.

In turn, if both KO and vacancy-related mechanisms responsible for the enhancement of boron diffusion in silicon (Fig. 2) are dominant, spatial separation of the self-interstitial and vacancy fluxes give rise to the opposite situation; i.e., we have the suppression of the transverse SDP and the crystallography-dependent enhancement of SDP over the diffusion-profile plane [12, 33]. This assumption is supported by the absence of any appreciable fluctuations in the boron concentration under conditions of the layer-by-layer etching off of the corresponding ultrashallow diffusion profile (Fig. 3b) and also by experimental data obtained using scanning tunneling microscopy (STM); these experimental data made it possible to determine SDP with various crystallographic orientations over the diffusion-profile plane, depending on the prevalence of the KO and substitutional mechanisms of the impurity diffusion [33].

2.2. Self-Organized Silicon Quantum Wells

It is important to note that fluctuations in the boron concentration, which arise owing to the SDP anisotropy, are indicative of the possibility of forming self-assembled silicon QWs within the ultrashallow diffusion profiles. Such QWs were identified from the data on the angular dependences of conductivity [34] and the cyclotron resonance of electrons and holes when a magnetic field was rotated in the {110} plane perpendicular to the plane of the boron diffusion profile at the silicon (100) surface [32, 34, 35]. The quenching and shift of the cyclotron-resonance lines detected using an ESR spectrometer (the *X* band, 9.1–9.5 GHz) demonstrated that there was 180° symmetry for the magnetic-

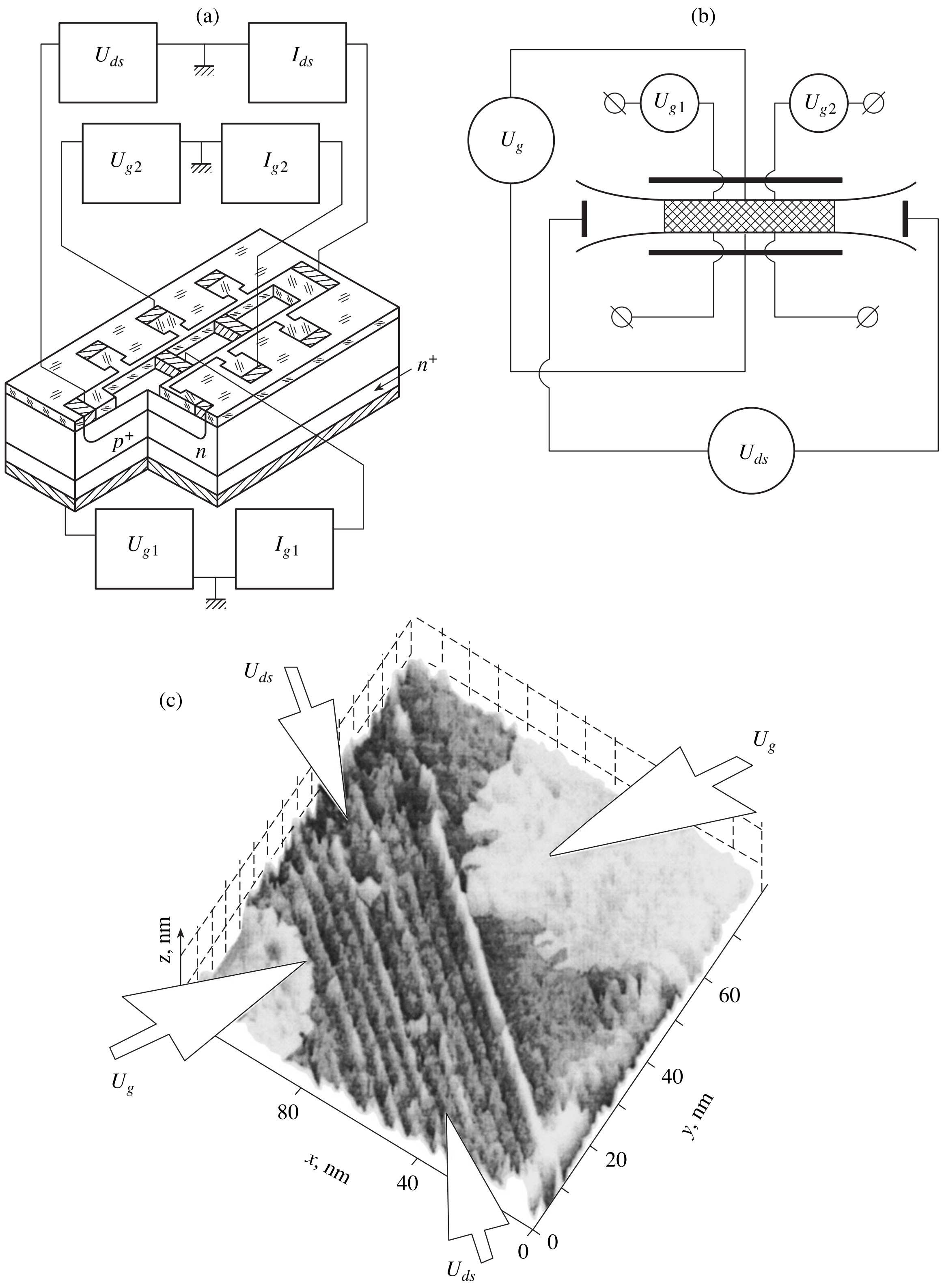

Fig. 1. (a) A planar p^+–n structure fabricated in the Hall configuration for studying the quantum staircase of the electron and hole conductance in relation to the drain–source voltage U_{ds}. (b) Schematic representation of split gate U_g used to form the modulated quantum wires within the quantum wells; the voltages U_{g1} and U_{g2} are applied to the "digit" gates intended for implementation of the quantum dots. (c) A 3D STM image of the split-gate configuration formed within a self-assembled quantum well at the Si(100) surface.

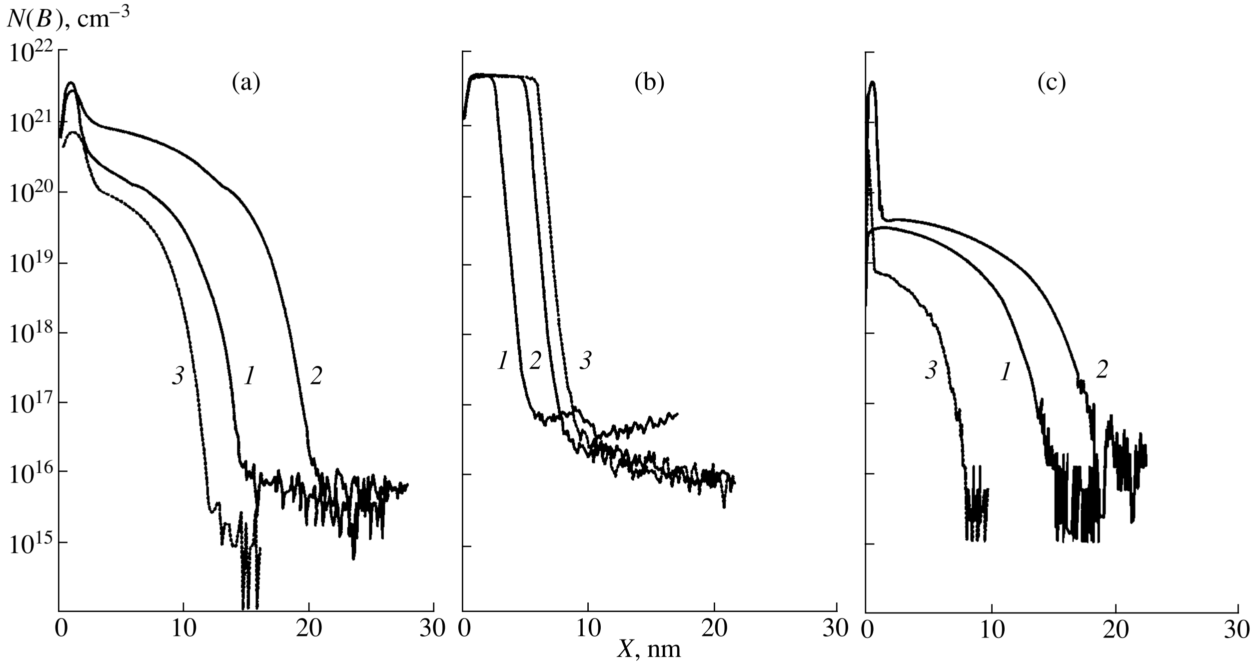

Fig. 2. Ultrashallow B concentration profiles $N(B)$ in n-Si; the profiles were obtained as a result of diffusion at several temperatures T_{dif} after preliminary deposition of an oxide layer with thickness d_{SiO_2} onto both surfaces of the Si(100) wafer. The quantity d_0 is the average oxide-layer thickness corresponding to the situation when the roles of the kick-out and vacancy-related mechanisms of impurity diffusion are comparable. d_{SiO_2}/d_0 = (*1*) 0.17, (*2*) 1.0, and (*3*) 1.28; T_{dif} = (a) 800, (b) 900, and (c) 1100°C.

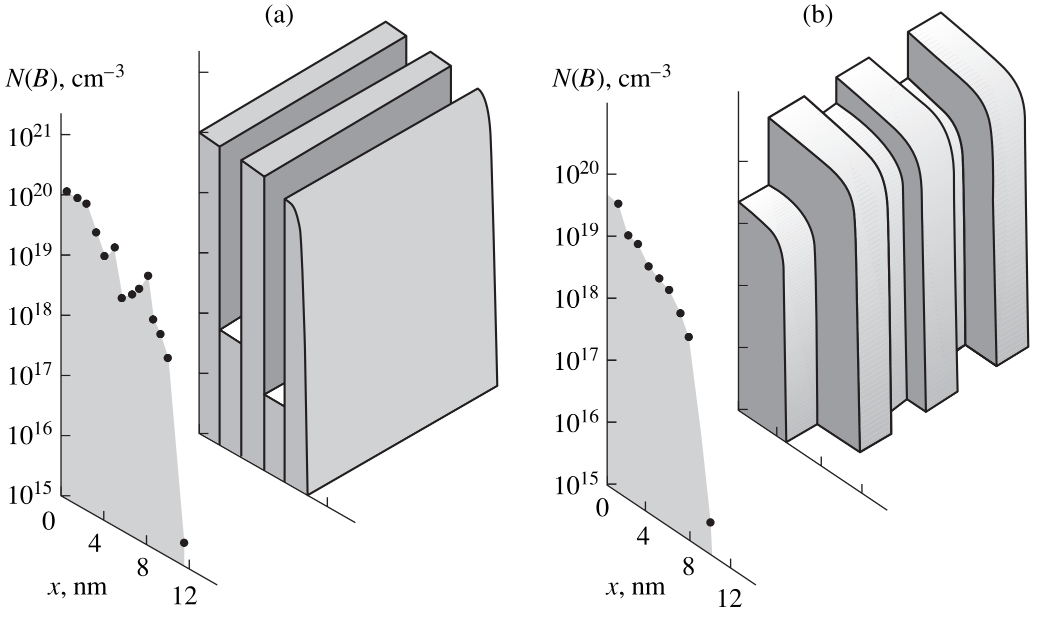

Fig. 3. Ultrashallow boron profiles in n-type silicon with (100) orientation. The profiles were formed as a result of diffusion at temperatures T_{dif} = (a) 900 and (b) 800°C and were obtained using precise layer-by-layer etching off with subsequent measurements of the sheet resistance of the doped layer by the four-point probe method. The insets illustrate the models of obtained profiles; the latter are composed of (a) longitudinal and (b) transverse quantum wells, which are parallel and perpendicular to the p^+–n-junction plane, respectively.

field orientation parallel to the plane of the ultrashallow profile (Fig. 4a) obtained at T_{dif} = 900°C. This made it possible to identify the presence of individual self-assembled longitudinal QWs localized between the heavily doped δ-shaped barriers within the ultrashallow profile obtained under conditions of parity between the KO and substitutional impurity-diffusion mechanisms (see the inset in Fig. 3a) [12, 33, 35, 36]. In turn, the self-

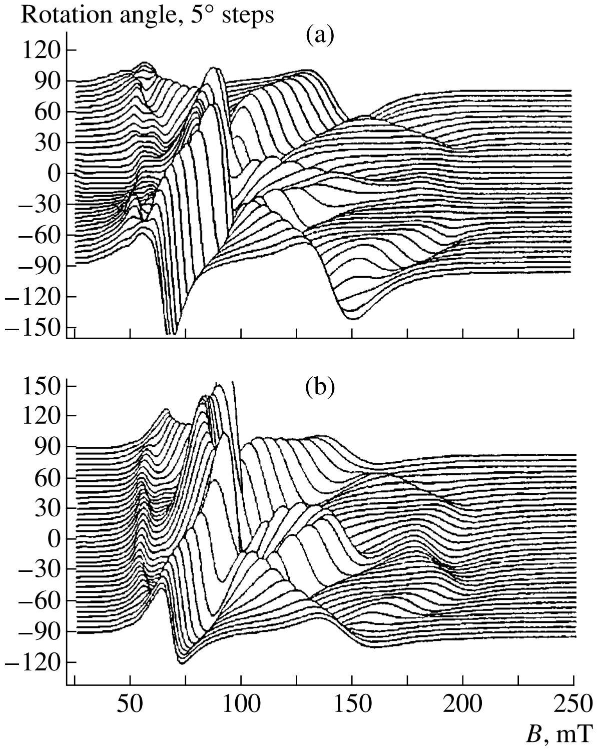

Fig. 4. Angular dependences of cyclotron resonance of the charge carriers in ultrashallow diffusion profiles obtained near the Si(100) surface at $T_{\rm dif}$ = (a) 900 and (b) 1100°C. T = 3.9 K; ν = 9.45 GHz. The external magnetic field is applied in the (110) plane, which is perpendicular to the (100) surface of the sample. The orientations of 0° and ±90° correspond to the directions of the magnetic field parallel and perpendicular to the sample surface.

assembled transverse QWs (see the inset in Fig. 3b) were detected on the basis of the quenching and shift of the cyclotron-resonance lines, which featured 180° symmetry if the magnetic field was oriented perpendicularly to the plane of ultrashallow profiles obtained when either the KO ($T_{\rm dif}$ = 1100°C) or the substitutional ($T_{\rm dif}$ = 800°C) (Fig. 4b) diffusion mechanisms were in effect [12, 32, 35, 36]. In this study, in order to form electrostatic quantum wires in the context of the split-gate scheme (Fig. 1b), we used individual longitudinal QWs of both the *n* and *p* types at the *n*-Si(100) surface (Fig. 5). A change in the conductivity type of QWs formed on identical substrates and under the same technological conditions at $T_{\rm dif}$ = 900°C was accomplished by varying the steepness of the δ-shaped barriers under conditions of changing the composition of the chlorine-containing component in the gaseous mixture. The conduction-electron concentration in the *n*-Si QWs corresponded to the bulk concentration of shallow-level donors, whereas the B concentration in the *p*-type QWs exceeded the concentration of the initial donor impurity.

2.3. Heavily Doped δ-Shaped Barriers

The measured cyclotron-resonance spectra consist of unusually narrow lines, which indicates that the time of the spin–lattice relaxation for nonequilibrium electrons and holes in self-organized silicon QWs is much longer than the corresponding time in the bulk silicon samples [12, 32, 35]. This result is quite surprising, when one takes into account the level of boron doping of the δ-shaped barriers between which the QW is formed. Initially, the temperature dependences of the conductivity and the Seebeck coefficient, and also the local tunneling *I–V* characteristics [34, 37], were used to explain this result; these data made it possible to identify the origination of the correlation energy gap in the density of states of two-dimensional (2D) degenerate hole gas. In the context of the model suggested [34], the main role in the formation of the above correlation gap is played by the reconstruction of the shallow-level

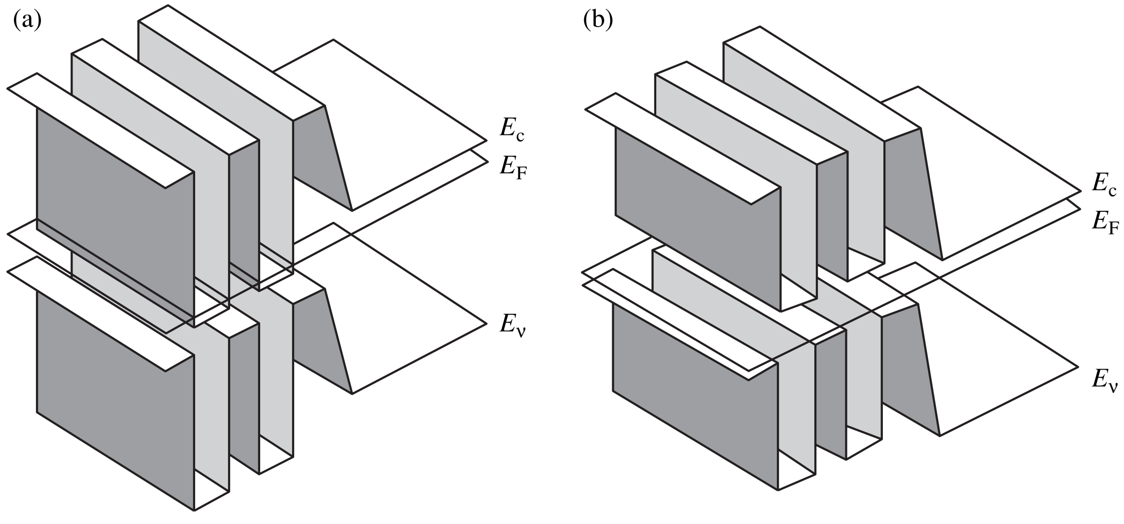

Fig. 5. Schematic representation of the energy-band structure for ultrashallow p^+–n junctions composed of (a) *n*- and (b) *p*-type quantum wells.

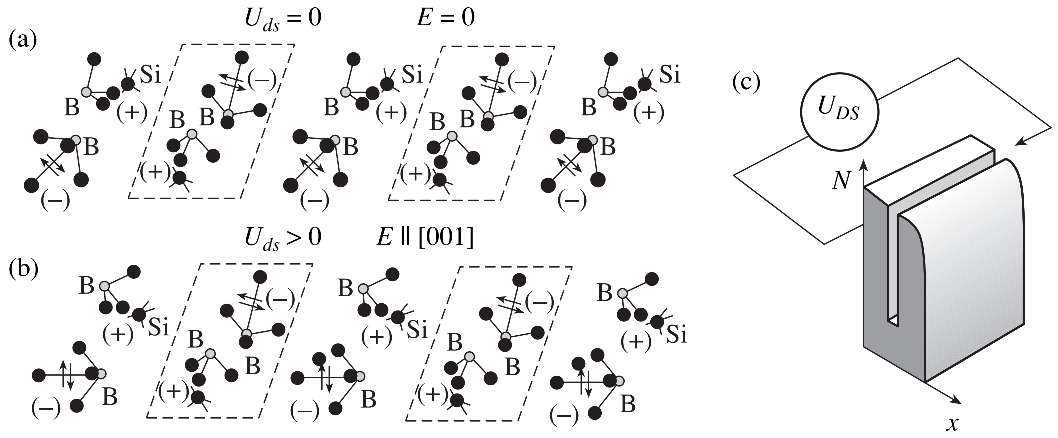

Fig. 6. (a) A system of reconstructed B^+–B^- trigonal dipoles within the heavily doped δ-shaped barriers, which (b), if an external electric field is applied, give rise to the conditions for transverse confinement for the charge-carrier transport in the self-assembled quantum well. (c) A 3D schematic representation of an ultrashallow impurity profile incorporating an individual quantum well between the heavily doped δ-shaped barriers.

boron acceptors, which gives rise to impurity dipole centers with the C_{3v} symmetry: $2B^0 \longrightarrow B^- + B^+$ (Fig. 6a).

In this study, the above model of trigonal impurity dipoles was further confirmed by measurements of the angular dependences of the corresponding ESR spectra (in the X band), which demonstrate that the heavily doped δ-shaped barriers feature ferroelectric properties (Fig. 7). The intensities and positions of the lines in this ESR spectrum depend primarily on the conditions of cooling of the samples. This is an important factor indicative of the dynamic character of magnetic moments induced by the spin–orbit splitting of the valence band in the course of electrostatic ordering of the impurity dipoles in the field of ultrashallow p^+–n or n^+–n junctions. The ESR spectrum under consideration cannot be observed if the sample is cooled in a weak magnetic field. In addition, the amplitudes and positions of the ESR lines recorded after cooling in a magnetic field ($B_c \geq 0.22$ T) depend on the initial crystallographic orientation of the sample (Fig. 7). As the temperature increases, a change in the position of the ESR line is observed; ultimately, this line vanishes at $T \geq 27$ K, which corresponds to the temperature of thermal ionization for the initial phosphorus donor impurity. Thus, the observed trigonal ESR spectrum can transform in the temperature range of 3.8–27 K depending on the strength of the magnetic field used in the course of cooling the sample with ultrashallow diffusion profiles, which include the heavily doped δ-shaped barriers.

Such behavior of dynamic magnetic moments indicates that these moments are formed as a result of magnetic ordering of the B^+–B^- trigonal impurity dipoles by way of the exchange interaction via the shallow-level phosphorus donors, which reside near the plane of the B ultrashallow diffusion profile in n-Si(100). An external magnetic field is the main stimulator of the exchange interaction; this field not only specifies the crystallographic orientation of dynamic magnetic moments along the equivalent $\langle 111 \rangle$ directions (Fig. 7) but also stabilizes the impurity dipoles in the excited triplet state, which is directly involved in the formation of these dipoles. It is the latter circumstance that gives rise to the critical magnetic field $B_c \geq 0.22$ T, which is conducive to magnetic ordering of the magnetic dipoles via the shallow-level phosphorus donors. In turn, a system of impurity dipoles in weak magnetic fields and at low temperatures is apparently in the state of the Van Vleck paramagnet induced by the direct exchange interaction, as a result of which an ESR signal is not observed at all. It is noteworthy that dynamic magnetic moments emerging as a result of local magnetic ordering of the impurity dipoles are formed only in the vicinity of shallow-level donors (see also [38]); this accounts for their paramagnetic properties, which manifest themselves in the metastable behavior of the ESR trigonal spectrum.

Thus, the studies using the ESR and thermoelectric-power measurements have shown that the heavily doped δ-shaped barriers possess ferroelectric properties, because these barriers consist of trigonal B^+–B^- impurity dipoles. As electrostatic ordering within the δ-shaped barriers proceeds (Figs. 6b, 6c), the reconstructed impurity dipoles give rise to transverse constraints on the motion of charge carriers in the plane of a narrow longitudinal QW (Figs. 3a, 5a, 5b), thus stimulating the formation of both smooth and modulated quantum wires (see also [34, 37]). Similar phenomena have recently been observed in low-dimensional superconductors in ferroelectric shells [39]. In other words, the presence of δ-shaped barriers with ferroelectric properties makes it possible to obtain quantum wires under the conditions of the external electric field $U_{DS} = U_g + U_{ds}$ applied parallel to the QW plane (see Fig. 6c); this field, on the one hand, introduces a transverse constraint owing to ordering of the impurity dipoles (U_g) and, on the other hand, induces the transport of individ-

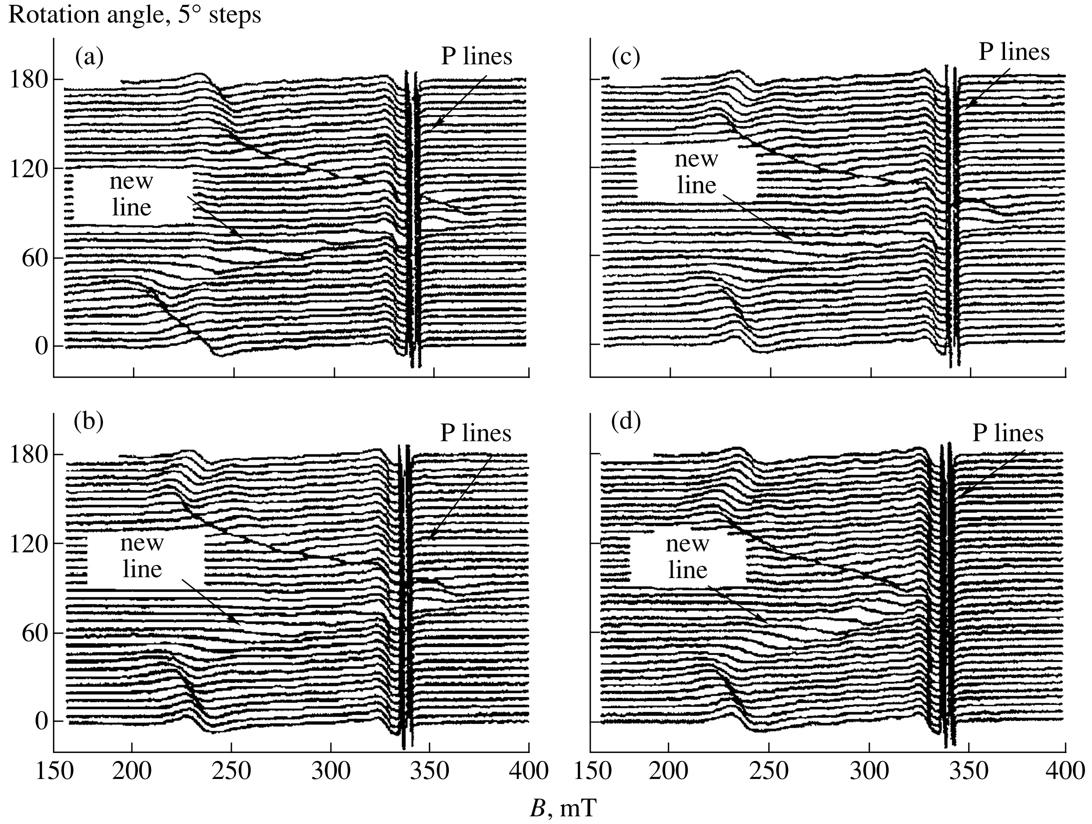

Fig. 7. Angular dependence of the ESR spectrum for a trigonal center within the ultrashallow boron diffusion profile containing self-assembled quantum wells after cooling in an external magnetic field $B_c \geq 0.22$ T. The ultrashallow boron diffusion profile was formed in the *n*-Si substrate with the (100) orientation of the operating surface; the diffusion temperature was $T_{\text{dif}} = 1100°\text{C}$. (a) $B_c \parallel \langle 110\rangle$, (b) $B_c \parallel \langle 112\rangle$, and (c, d) $B_c \parallel \langle 111\rangle$. The magnetic was rotated in the {110} plane perpendicular to the {100} surface of the substrate (orientations 0° and 180°: $B_c \parallel$ is parallel to the substrate surface; orientation 90°: $B_c \perp$ is perpendicular to the substrate surface). $\nu = 9.45$ GHz; T = (a, b, c) 14 and (d) 21 K.

ual charge carriers (U_{ds}). Therefore, in the context of the split-gate structure formed at the surface of a δ-shaped barrier with ferroelectric properties (Figs. 1b, 1c), the quantum wire within a self-assembled QW can be observed even at zero gate voltage. In this case, the quantum-wire width increases as the electrostatic ordering of the impurity dipoles in the longitudinal electric field proceeds; at the same time, the degree of quantum-wire modulation is controlled by the number of unreconstructed dipoles, which may be treated as the [delta]-shaped barriers. It is worth noting that the number of unreconstructed dipoles can be controlled by varying the concentration of the chlorine-containing compounds, which are responsible for the uniform distribution of dopants within the δ-shaped barriers. These characteristics of self-assembled silicon QWs confined by ferroelectric δ-shaped barriers made it possible for the first time to use the split-gate structure (Figs. 1b, 1c) to study quantized conductivity both under zero and nonzero gate voltages. In the latter case, electrostatic ordering of ferroelectric δ-shaped barriers was a stabilizing factor in the size quantization when studying the mechanisms for the enhancement and quenching of quantum-mechanical steps under the effect of a longitudinal electric field.

3. RESULTS AND DISCUSSION

3.1. Quantized Conductance in the n-Type Silicon Quantum Wires

Electron quantized conductance was observed at T = 77 K in the plane of a *n*-Si(100) QW under the effect of an external electric field $U_{DS} = U_g + U_{ds}$. In order to obtain the quantum wires, we used two identical split-gate structures oriented along either the [001] or [011] crystallographic directions. The longitudinal voltage (U_{ds}) was maintained at a level of 0.01 eV during measurements.

The cross-sectional area of the quantum wires under investigation (2×2 nm^2) was governed by the width of the self-assembled QW and by the transverse size constriction induced electrostatically by the gate voltage (U_g): both size constraints are close to the distance between the impurity dipoles (2 nm); this distance is specified by the boron concentration within the δ-shaped barriers. These parameters, along with the 2D

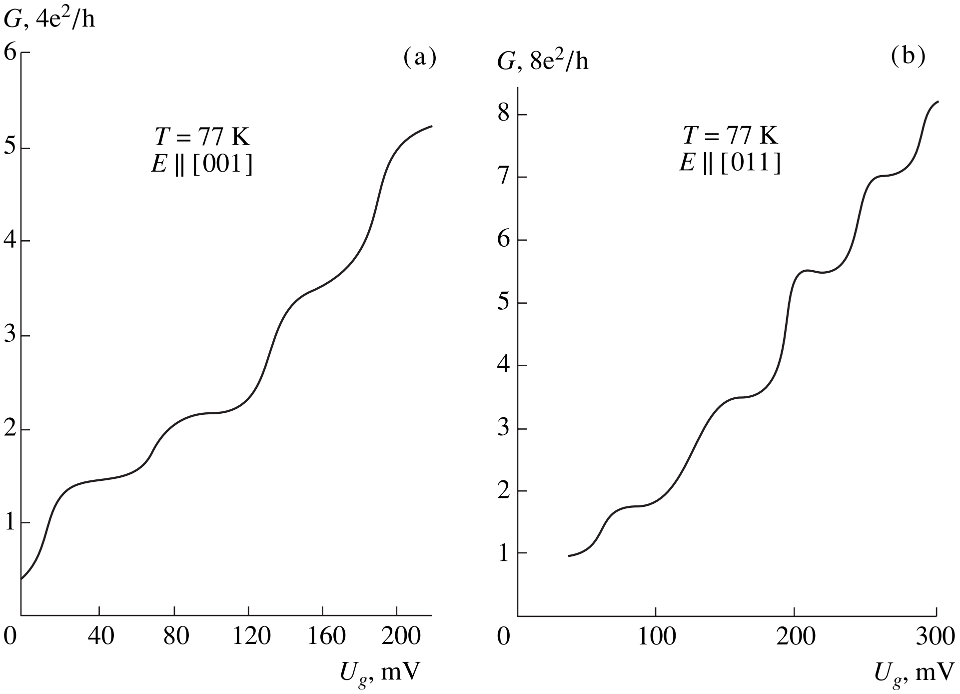

Fig. 8. The *I–V* characteristic of electron conductance in a 1D channel oriented crystallographically along the (a) [001] and (b) [011] axes within a self-assembled *n*-Si quantum well in the Si(100) plane.

electron concentration (8.6×10^{13} m^{-2}) and the effective length of the 1D channels (1.5 μm), which is much smaller than the inelastic-scattering length, made it possible to evaluate the contribution of the various conduction-band valleys in silicon to the *I–V* characteristics of quasi-1D conductance (Fig. 8). The height of the steps in the quantized conductance $G(V_g)$, which are equal to $4e^2/h$ ($g_s = 2$ and $g_v = 2$) (Fig. 8a) and $8e^2/h$ ($g_s = 2$ and $g_v = 4$) (Fig. 8b), and which were observed in studying the crystallographically oriented quantum wires, are quite consistent with the value of the valley factor for the [001] and [011] axes in the Si(100) plane.

Thus, the height of steps in the quantum conductance staircase of 1D channels in *n*-Si is governed primarily by the anisotropy of the conduction band, which is in contrast to the results of studying the quantum wires based on GaAs–AlGaAs heterostructures, for which $G_0 = 2(e^2/h)N$ as a result of $g_s = 2$ and $g_v = 1$ [6, 7].

3.2. Quantized Conductance of p-Si Quantum Wires

Quantized conductance $G(U_g)$, emerging as a result of quasi-1D heavy-hole transport, was observed at 77 K in the course of studying the quantum wire formed within a self-assembled *p*-Si(100) QW using the split-gate method (Figs. 1b, 1c). The cross-sectional area of the 1D channel (2×2 nm^2) is defined, as mentioned above, by the QW width and by the electrostatically induced transverse constraint, which are close to the impurity-dipole spacing (~2 nm) specified by the boron concentration within the δ-shaped barriers. The low concentration of 2D holes (0.8×10^{13} m^{-2}) and the 1D-channel length (0.5 μm) specify the Fermi level position corresponding to the occupation of the 1D heavy-hole subbands, the dominant role of which manifests itself in the height of the steps in the quantum staircase of conductance ($2e^2/h$ for $g_s = 2$ and $g_v = 1$) obtained at $U_{ds} = 0.01$ V (Fig. 9a). The observed special feature of the first quantum step [~$0.7(2e^2/h)$] is apparently caused by the polarization of heavy holes in the zero magnetic field; this polarization is most probable for short and thin quantum wires [17, 22].

It is noteworthy that the very fact of observing quantized conductance for heavy holes is quite surprising considering the large effective mass of these holes, which does not ensure a large energy gap between the coprresponding 1D subbands. In this study, this factor is eliminated to a certain extent owing to the small cross-sectional area of the 1D channel, which makes it possible to detect not only the quantum staircase of conductance but also the spin-related splitting of the first 1D subband. Nevertheless, in spite of the small cross-sectional area of the 1D channel, the thermal energy at $T = 77$ K is quite sufficient to stimulate the transitions between the filled and empty 1D subbands. Such thermally induced transitions bring about quenching of the quantized conductance, which manifests itself primarily in the fact that the quantum-staircase steps become less steep (Fig. 9a). In addition, an increase in the gate voltage U_g is conducive to the enhancement of the noise-related fluctuations of longitudinal voltage U_{ds} as a result of their insufficient

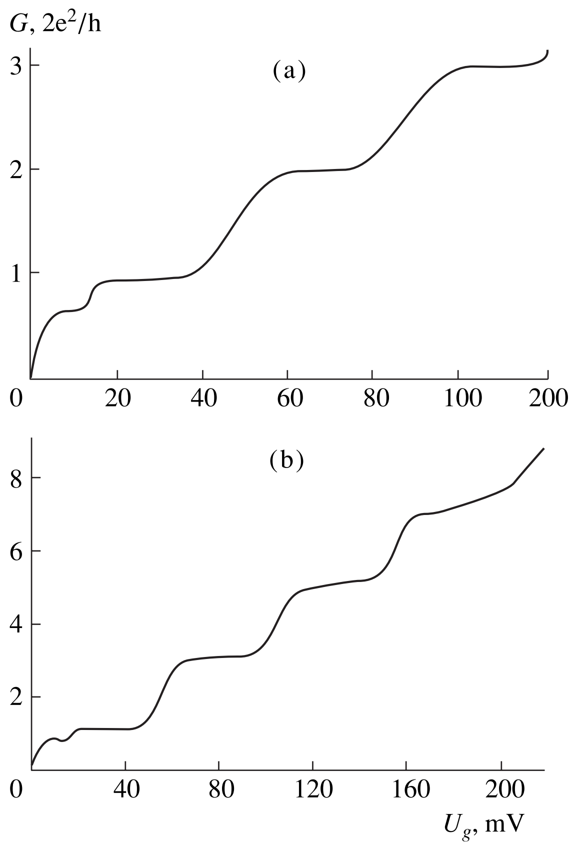

Fig. 9. The *I–V* characteristic for a quantum staircase of hole conductance in 1D channels oriented along the [001] axis within a self-assembled *p*-type quantum well in the Si(100) plane. The Fermi level position corresponds to occupation of the 1D subbands of (a) heavy holes and (b) heavy and light holes. $T = 77$ K.

decoupling, which also manifests itself in the quenching of the quantum conductance staircase as the step number increases. Apparently, the latter circumstance prevented any significant quantum steps from being detected for $N > 3$ in the course of measuring the quantum conductance due to heavy holes. The simultaneous quenching of the conductance quantum staircase and splitting of the first step in the zero magnetic field (Fig. 9a) is quite surprising; this observation indicates that the energy gap between the 1D bands and the energy of spin-induced splitting of the first 1D subband are comparable. In this case, transitions of charge carriers between the empty and occupied 1D subbands stimulate to a much lesser extent the suppression $0.7(2e^2/h)$ of the feature of the first quantum step, because the amount of the spin-induced splitting of the first 1D subband is independent of the 2D carrier concentration. A similar phenomenon has recently been observed in studies of spin-induced splitting of the first 1D electron subband under conditions of varying the longitudinal voltage U_{ds} applied to the quantum wire formed within the GaAs/Al$_x$Ga$_{1-x}$As heterostructure [20].

When considering the quantized conductance $G(U_g)$ caused by the contribution of 1D subbands of both heavy and light holes, we must first of all take into account that size quantization for these holes should be performed independently in view of the significant difference between their effective masses. In this case, the height of steps in the quantum staircase $G_0 = (2e^2/h)g_N N$ is proportional to the factor $g_N = 2$, which accounts for degeneracy of the size-quantization level. However, when studying a quantum wire with a square cross section, we should take into account that the lower 1D subband is nondegenerate ($g_N = 1$); this automatically gives rise to a quantum staircase, the height of the first step of which is equal to $2e^2/h$, whereas the heights of the other steps are equal to $4e^2/h$. Such a dependence was observed at $T = 77$ K in studies of a quantum wire with a square cross section (2×2 nm^2) and a length of 1.5 μm; this wire was obtained by the split-gate method within a self-assembled *p*-Si(100) QW (Fig. 9b). A square cross section of the 1D channel was obtained (as in the case of the above-described quantum wires) owing to the almost complete correspondence between the QW width and the distance between the impurity dipoles with the heavily doped δ-shaped barriers. The 2D density of holes (1.1×10^{13} m^{-2}) specifies the Fermi level position, which corresponds to the occupation of 1D subbands for both heavy and light holes. We should note that the obtained quantum staircase of conductance (Fig. 9b) demonstrates the potential of studying the reciprocal effect of the spin-induced splitting of the first 1D subbands for heavy and light holes in the zero magnetic field. The effects of spin-related splitting of the hole 1D subbands can manifest themselves most markedly in the course of the temperature- and field-induced quenching of the conductance quantum staircase; this effect will be considered below.

3.3. *Quantized Conductance at Finite Temperatures*

As mentioned above, the quantum staircase of conductance $G(U_g)$ may become smoothed as a result of thermal transitions of charge carriers between occupied and unoccupied 1D subbands. Therefore, the issue concerning ballistic conductance at finite temperatures is of interest; at these temperatures, the number of occupied 1D subbands is, in the strict sense, indeterminate because there is a finite temperature-dependent probability of finding charge carriers within any of these subbands.

In this case, occupancy of 1D subbands is governed by the Fermi distribution; i.e.,

$$n(\varepsilon) = \left[\exp\left(\frac{\varepsilon - \mu}{kT}\right) + 1\right]^{-1},$$

where $\varepsilon = E_n + \frac{p^2}{2m}$ (E_n corresponds to the bottom of the nth 1D band), and μ is the chemical potential dependent on both temperature and the charge-carrier concentration; the 1D subbands with various occupancies can contribute to the conductance.

In order to calculate the conductance of a 1D subband, we replace the quantum wire with a point contact, which separates two infinite reservoirs of charge carriers. The difference in chemical potentials to the left and to the right of the point contact is equal to the product of elementary charge by the longitudinal voltage applied to the quantum wire; i.e., $\mu_1 - \mu_2 = eV$. Calculating the current through the point contact as the difference between the current flowing from left to right and that flowing from right to left, we obtain the following expression for the contribution of the jth 1D subband:

$$G_j = \frac{e}{\pi m \hbar V}\int_0^{\infty} p[f(p, \mu_1, T) - f(p, \mu_1 - eV, T)]dp. \quad (3)$$

Here, $f(p, \mu, T)$ denotes the Fermi distribution. Thus,

$$G_j = \frac{e}{\pi m \hbar V}\int_0^{\infty} p\left[\frac{1}{1 + e^{\frac{E_j - \mu_1}{kT}} e^{\frac{p^2}{2mkT}}} - \frac{1}{1 + e^{\frac{E_j - \mu_1 + eV}{kT}} e^{\frac{p^2}{2mkT}}}\right]dp$$
$$= \frac{2ekT}{hV}\ln\left(\frac{1 + e^{\frac{\mu_1 - E_j}{kT}} e^{\frac{eV}{kT}}}{1 + e^{\frac{\mu_1 - E_j}{kT}}}\right). \quad (4)$$

As can be seen, the conductance at a finite temperature depends on both the charge-carrier concentration and the applied longitudinal voltage. For small longitudinal voltages, we have

$$G_j = \frac{2e^2}{h}\frac{e^{\frac{\mu_1 - E_j}{kT}}}{1 + e^{\frac{\mu_1 - E_j}{kT}}}. \quad (5)$$

Let us consider several limiting cases.

(I) Occupied subbands with low-lying bottoms $\frac{\mu_1 - E_j}{kT} \gg 1$. In this case, we may disregard unity in the denominator in formula (5). As a result, the conductance is no different from that at zero temperature [4, 5]; i.e.,

$$G_j = \frac{2e^2}{h}. \quad (6)$$

(II) $\frac{\mu_1 - E_j}{kT} \approx 0$. Such a situation takes place near the regions of jumplike change in the conductance. Expanding the exponential functions into a series, we have

$$G = \frac{e^2}{h}\left(1 + \frac{\mu_1 - E_j}{kT}\right). \quad (7)$$

It follows from (7) that, if the chemical potential coincides with the bottom of a 1D subband, the contribution of this subband to the conductance is smaller by a factor of 2 than the contribution of the occupied 1D subband at $T = 0$.

(III) The higher lying subbands are unoccupied at $T = 0$. For these subbands, $\frac{\mu_1 - E_j}{kT} \ll 0$, so that

$$G_j = \frac{2e^2}{h}e^{\frac{\mu_1 - E_j}{kT}} \ll 1. \quad (8)$$

The contribution of such subbands to the conductance is exponentially small. In addition, if the charge-carrier concentration is fairly low, the condition $\frac{\mu_1 - E_j}{kT} < 0$ is satisfied for all subbands, including that with the lowest energy. In the latter case, the ballistic conductance of a quantum wire

$$G \approx e^2\pi\sqrt{\frac{2\pi}{mkT}}n \quad (9)$$

vanishes as the charge-carrier concentration decreases.

Thus, as a result of the above analysis of the dependence of the conductance on the chemical potential at various temperatures [(5), Fig. 10a], we may conclude that the quantum staircase of conductance is smoothed as the temperature increases and vanishes when kT becomes comparable to the distance between the 1D levels.

Such thermal suppression of the ballistic conductance for partial occupancy of the 1D subbands was observed in studies of a silicon quantum wire (2×2 nm^2) formed electrostatically using the split-gate method within a self-assembled p-Si(100) QW. The Fermi level position controlled by the quantum-wire cross section, the density of 2D holes ($\sim 2.5 \times 10^{13}$ m^{-2}), and the effective length of the 1D channel (~ 4 μm) corresponded to the occupation of the 1D subbands for both the heavy and light holes, which manifests itself in the height of the quantum steps obtained for $U_{ds} = 0.01$ V (Fig. 10b). The observed temperature-induced smoothing of the quantized conductance for the values of U_g corresponding to quantum steps (Fig. 10b) is in good agreement with the dependence calculated using formula (5) (Fig. 10a) and taking into account the energy gap between the 1D subbands for the quantum wires under consideration (~42 meV, see below).

It should be noted that the observed quantum staircase of conductance does not include the first quantum step $G_0 \approx 2e^2/h$ caused by the contribution of heavy holes; in addition, a major portion of the quantum step corresponding to the occupation of the first 1D subband for light holes is smaller than the theoretically predicted value of $G_0 = 4e^2/h$. This suppression of the first steps in the quantum staircase of conductance results from backscattering of charge carriers, which begins to be

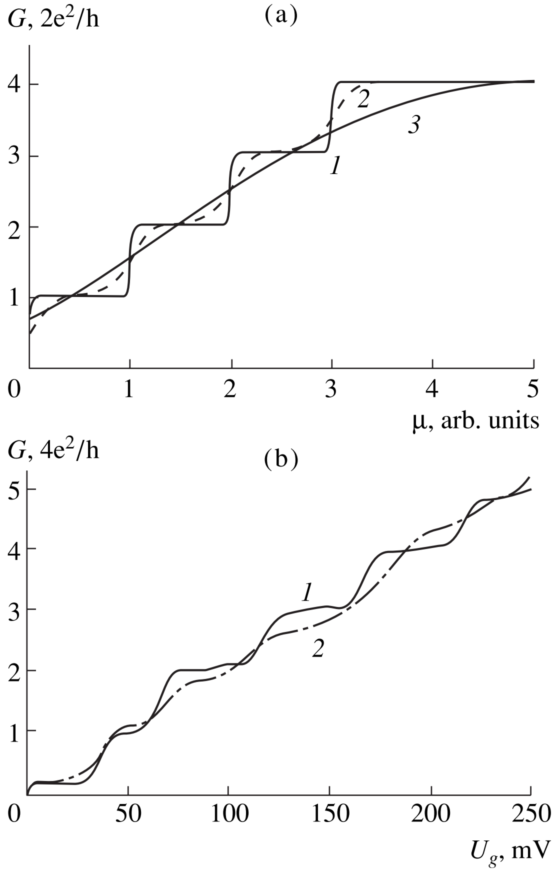

Fig. 10. The temperature-induced quenching of a quantum staircase for hole conductance in a 1D channel oriented along the [001] axis within a self-assembled p-type quantum well in the Si(100) plane. (a) The results of calculation in relation to the chemical-potental position μ for T = (*1*) 0 K, (*2*) $0.1\Delta E/k$, and (*3*) $0.6\Delta E/k$, where ΔE is the energy gap between the 1D subbands. (b) Experimental dependences measured at T = (*1*) 77 and (*2*) 300 K.

dominant within the quantum wires if there are impurity centers at the boundaries of these wires [27, 29].

Thus, the obtained expression for ballistic conductance of a quantum wire at finite temperatures makes it possible to describe the temperature-related quenching of quantum steps, which arise when the Fermi level crosses the size-quantization subbands. It is shown that, in the limiting case of low longitudinal voltages, the contribution of occupied subbands to the ballistic conductance is described by classical formula (2), whereas the conductance becomes halved if these subbands are occupied only partially. This brings about the temperature-related quenching of quantum steps, depending on the Fermi level position when kT approaches the energy gap between the size-quantization levels. In addition, in contrast to the classical behavior of ballistic conductance at $T = 0$ [see (2) and (6)], we should expect that the quantum staircase of conductance is quenched at finite temperatures as a result of a decrease in the charge-carrier concentration. Possibly, this mechanism forms the basis for a sharp decrease in the amplitude ($0.7(2e^2/h)$), which is the special feature of the first quantum step and originates at an ultralow charge-carrier concentration as a result of polarization of quantum wires in the zero magnetic field [19, 40].

3.4. Suppression of the Quantum Steps in a Longitudinal Electric Field

Observation of the quantum staircase of conductance $G(U_g)$ using the split-gate method is almost inevitably accompanied with quenching of this staircase as the step number increases [17, 40–42]. This nonlinear quantized conductance can be a result of an increase in the noise-related fluctuations in the longitudinal voltage U_{ds} as the voltage at the gate U_g increases; these fluctuations induce the transitions of charge carriers between neighboring 1D subbands. Such transitions are most probable for the voltages U_g that correspond to the quantum steps, which gives rise to a nonlinear *I–V* characteristic as the step number increases. Notably, the complete quenching of the conductance quantum staircase is bound to be observed for the values of U_{ds} corresponding to the extent of the plateau between two steps. At first glance, it seems that, by controlling the linearity of the *I–V* drain–source (I_{ds}–U_{ds}) characteristics (expression (2) was derived under the strict requirement of linearity), we can determine the conditions for quenching the conductance quantum staircase [16, 20]. However, this approach is based on the complete independence of U_{ds} from U_g, which is difficult to accomplish in practice because these two voltages are not sufficiently decoupled. Therefore, in order to identify the possible mechanism for nonlinear quenching of quantized conductance, it is expedient to use the sweep of longitudinal voltage U_{ds} within the approach employing the split-gate structure.

The advantages of this method were demonstrated in studies of quenching the quantum staircase for the hole conductance using the split-gate structure oriented along the [001] crystallographic direction in the p-Si(100) QW plane. The concentration of 2D holes (1.6×10^{13} m^{-2}) and the cross-sectional area of the 1D channel (2×2 nm^2) specified the contribution of the light and heavy holes to the quantized conductance, which manifested itself in the staircase step heights measured under the conditions of the longitudinal-voltage U_{ds} sweep at $U_g > 0$ (Fig. 11a). Apparently, the obtained quantum wire was disordered only slightly, which made it possible to see that heavy holes were completely polarized at $T = 77$ K and $U_{ds} = 0.01$ V ($U_g < 0$) in spite of the appreciable length of the 1D channel (5 μm). This inference follows from an analysis of the height of the first step in the quantum staircase of conductunce e^2/h, which is caused by the contribution of heavy holes and corresponds to the conductance of the 1D channel polarized in the zero magnetic field as a result of insignificant disorder, $G = 1/2G_0$ [19, 43]. In this case, the height of the second quantum step, which represents the contribution of light holes to the conductance of square *p*-type quantum wires, is also indicative of the spontaneous spin polarization of these holes in the zero magnetic field, $G = 0.7(4e^2/h)$ (see Fig. 11a). The detected polarization of heavy and light holes emphasizes the extremely important role of exchange interaction when studying the transport of individual charge carriers in short, thin quantum wires [17–26]. Furthermore, in the case under consideration, heavy holes can be polarized as a result of both a transition to an excited triplet state and the exchange interaction with the light holes, which, in turn, gives rise to polarization of the latter holes.

It should be noted that quenching of the conductance quantum staircase as a result of sweeping the longitudinal field was detected not only when the voltages U_g and U_{ds} were completely independent within the split-gate structure (Fig. 11a) but also under the effect of an external electric field $U_{DS} = U_g + U_{ds}$ applied parallel to the plane of the studied QW confined between two ferroelectric δ-shaped barriers [34, 37]. In this case, the sweep of longitudinal voltage $U_{DS} > 0$, on the one hand, stimulated the formation of 1D subbands owing to ordering of the impurity dipoles in the ferroelectric δ-shaped barriers ($U_g > 0$) and, on the other hand, ensured the transport of individual holes ($U_{ds} > 0$). Furthermore, for $U_g > 0$, there was good agreement between the results obtained using both methods under consideration.

The experimental voltage dependence of quenching of the quantum staircase for the hole conductance can be used to determine the energy gap between the 1D hole subbands. It is important to emphasize that the sweep of the longitudinal electric field was absolutely linear in the entire range of detecting the quantum staircase of conductance; the complete quenching of this staircase was attained when eU_{ds} became comparable to the energy gap between the 1D hole subbands. The dependence of the quantum-step width on U_{ds} is obtained using the data represented in Fig. 11a and is shown in Fig. 11b. The energy gap between the 1D hole subbands (42 meV) (see Fig. 11b) is in good agreement with the extent of the plateau between the quantum steps (Fig. 11a). Nevertheless, it is noteworthy that the dependence shown in Fig. 11b was plotted disregarding the possibility that the quenching of the conductance quantum staircase is enhanced as the step number increases, which has been recently observed in studying quantum wire in GaAs–GaAlAs [20]. However, the data reported in [16, 20] demonstrate that the quantum staircase of electron conductance can be suppressed at values of eU_{ds} much less than the extent of the plateau between quantum steps, which was recently observed when studying quantum wire in GaAs–GaAlAs [20]. However, there are data [16, 20] demonstrating that the quantum staircase of electron conductance can be suppressed at values of eU_{ds} much less than the extent of the plateau between the quantum steps, which raises the question as to the actual dependence of U_{ds} on U_g in the context of the used [16, 20] split-gate structure.

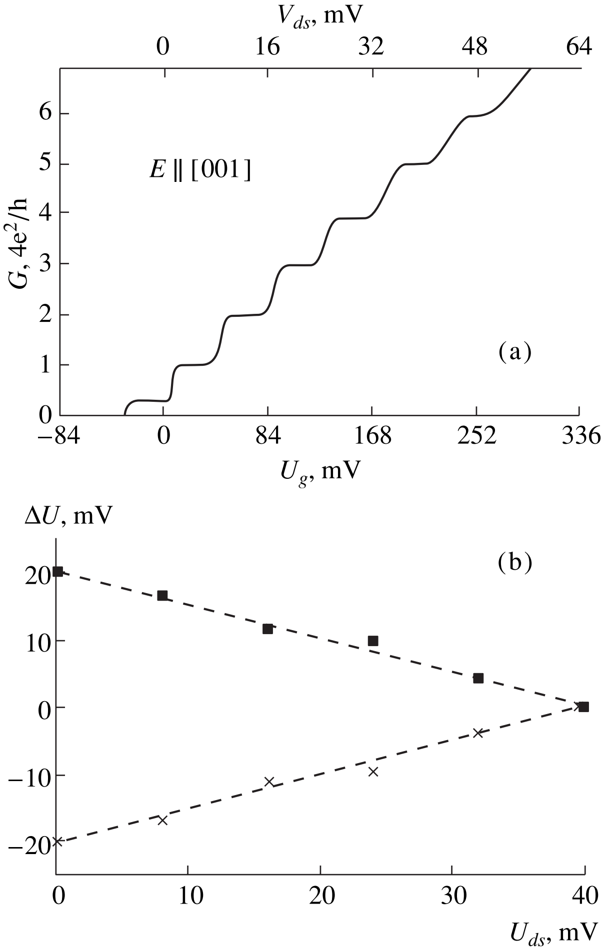

Fig. 11. (a) The field-induced quenching of the quantum staircase for hole conductance in a 1D channel oriented along the [001] axis within a self-assembled *p*-Si quantum well in the Si(100) plane; this quenching was observed at $T = 77$ K when varying the drain–source voltage. The Fermi level position corresponds to occupation of 1D subbands of the heavy and light holes. (b) The corresponding quenching of the plateau in the quantum staircase of the hole conductance; the results were obtained using the data shown in Fig. 11a.

3.5. Quantized Conductance During Heating of the Ballistic Charge Carriers in a Longitudinal Electric Field

When analyzing the shape of steps in the quantum staircase of conductance, it is necessary to take into account the possible enhancement of these steps due to heating of the ballistic charge carriers; the latter are heated even for small values of longitudinal voltage if the induced transitions between the 1D subbands are unlikely. Such effects of heating are bound to manifest themselves primarily in studies of finite-length quantum wires whose characteristics are not described within the mode of the quantum point contact. In this case, not only the height of the quantum steps can vary but also the plateaus in the quantum staircase of conductance may become distorted, which makes it more difficult to use the split-gate configuration to identify the relative contribution of elastic backscattering and electron–electron interaction to the formation of the above staircase [29, 41]. The capabilities of experimental estimation of the effect of charge-carrier heating on the characteristics of quantized conductance are demonstrated below when discussing the results of studying a *n*-Si quantum wire.

We first consider the special features of conductance of the quantum wire, to which a finite longitudinal voltage is applied, compared to the case of a quantum point contact in the limit of infinitely low longitudinal voltages. To this end, we consider a quantum wire whose length is limited by the interval $[0; L]$ and the drop of electric potential along which is described by a smooth, steadily decreasing function $-U(x)$ such that $U(0) = 0$ and $U(L) = V$. We assume that the charge-carrier distribution in this quantum wire is in the locally equilibrium state and coincides with the Fermi distribution at each point, whereas the chemical potential μ depends on the coordinate x as $\mu(x) = \mu_0 - eU(x)$. The only condition for the applicability of such an approximation consists in that the quantum-wire length should be sufficiently large and the potential falloff be gradual. At $T = 0$, the current through the left-hand boundary of the quantum wire is equal to

$$I = \sum_i dI(x_i), \tag{10}$$

where $dI(x_i)$ denotes the contribution of electrons from the quantum-wire segment $[x_i; x_i + dx]$ to the current. This current is not equal to $G_0 dU_i$ as in the case of a quantum point contact ($G_0 = 2e^2/h$). This is caused by the fact that heating of a charge carrier occurs in an extended quantum wire within the interval $[x_i; L]$; as a result, the charge carrier acquires an additional energy $\sqrt{2e[V - U(x_i)]/m}$. Thus, at $T = 0$, we have

$$\begin{aligned} dI(x) &= e \sum_{\varepsilon_F - eV < \varepsilon < \varepsilon_F} v_x = \frac{e}{m} \sum_{\varepsilon_F - edV < \varepsilon < \varepsilon_F} p_x \\ &= \left(G_0 + \frac{e^2}{2\pi\hbar p_F}\sqrt{2me[V-U]}\right)dU, \end{aligned} \tag{11}$$

where v_x is the x component of the charge-carrier velocity and p_F is the initial charge-carrier momentum equal to the Fermi momentum. In order to determine the total current through the left-hand edge of the quantum wire, we should integrate (11) with respect to U; i.e.,

$$\begin{aligned} I &= \int_0^V \left(G_0 + \frac{e^2}{2\pi\hbar p_F}\sqrt{2me[V-U]}\right)dU \\ &= G_0 V\left\{1 + \frac{2\sqrt{2meV}}{3p_F}\right\}. \end{aligned} \tag{12}$$

Thus, the conductunce of the finite-length quantum wire is given by

$$G = \frac{I}{V} = G_0\left\{1 + \frac{2\sqrt{2meV}}{3p_F}\right\}. \tag{13}$$

The value given by (13) is always larger than the conductance of a quantum point contact, because heating of a charge carrier within a quantum wire is accounted for in (13). In addition, in contrast to the case of a quantum point contact, the conductance of a finite-length ballistic quantum wire depends nonlinearly on the applied longitudinal field. The quantum-wire length and the form of the falloff of the potential $U(x)$ do not appear in the formula for conductance; i.e., this formula is universal.

If a quantum wire at a finite temperature is considered, expression (11) can be modified similarly to (5); i.e.,

$$\begin{aligned} dI(x) &= \frac{2e}{2\pi\hbar m}\int_0^\infty (p + \sqrt{2me[V-U]}) \\ &\times [f(p, \mu, T) - f(p, \mu - edU, T)]dp \\ &= \frac{G_0 dU}{1 + e^{\frac{E_i - \mu}{kT}}} + \frac{2e^2 dU}{h}\sqrt{\frac{e[V-U]}{kT}} \\ &\times \int_0^\infty \frac{dx}{1 + \cosh[x^2 + (E_i - \mu)/2mkT]}. \end{aligned} \tag{14}$$

Thus, the conductance is given by

$$\begin{aligned} G &= \frac{I}{V} = \frac{1}{V}\int dI \\ &= G_0\left\{\frac{1}{1 + e^{\frac{E_i - \mu}{kT}}} + \sqrt{\frac{eV}{kT}}g(\mu, E_i, T)\right\}. \end{aligned} \tag{15}$$

It can be seen that the obtained dependence of ballistic conductance on the longitudinal voltage $G = a + \sqrt{bV}$ is not qualitatively different from that at $T = 0$. However, the constants appearing in expression (15) depend on temperature. Thus, both at zero and at finite temperatures, the allowance made for the field-induced charge-carrier heating leads to an increase in the conductance in reference to the conventional value $G_0 = 2e^2/h$. This increase is most pronounced if the chemical potential coincides with the bottom of a 1D subband. As a result of the field-induced charge-carrier heating, the ballistic conductance tends to infinity at these points at $T = 0$, whereas an increase in temperature leads to smoothing of the conductivity jump under consideration (Fig. 12a). In addition, the effect of the field-induced heating on the shape of the quantum staircase of conductance can even out as a result of the staircase quenching stimulated by electrically induced transitions between the 1D subbands (Fig. 12a). The quantum-step quenching starts to be dominant in competition with the processes of the field-induced heating of charge carriers if the longitudinal voltage U_{ds} increases uncontrollably under the conditions of the voltage sweep at the gate U_g, which is often encountered if the above two voltages are not uncoupled sufficiently. In this case, the above-considered quenching of the conductance quantum staircase should be observed with increasing step number; at the same time, the effects of the field-induced heating manifest themselves only if we deal with the small-numbered steps (Fig. 12a).

Such a dependence $G(U_g)$ was observed at $T = 77$ K in the course of studying the [001] 1D channel obtained in the n-Si(100) QW using the split-gate method (Fig. 12b). The longitudinal voltage (U_{ds}) was set at a level of 0.01 V. The heights of the steps in the electron quantized conductance $G(U_g)$, $4e^2/h$ ($g_s = 2$, $g_v = 2$) are in good agreement with the values of the valley factor for the [001] axis in the Si(100) plane. The cross-sectional area of the quantum wires (2×2 nm^2) and the low concentration of 2D electrons (7.0×10^{12} m^{-2}) ensured the detection of both polarization due to the exchange interaction and the field-induced heating of electrons in the 1D channel with an effective length of 2.5 μm. The shape of the first step indicates that there is a $0.7(4e^2/h)$ special feature, which apparently is indicative of the emergence of spontaneous spin polarization in the 1D channels due to the exchange interaction [17, 22]. The obtained $G(U_g)$ dependence shows that the exchange interaction suppresses to a large extent the processes of the field-induced heating of charge carriers in quantum wires with a low electron concentration. However, an increase in the electron concentration under the conditions of sweeping the voltage at the gate leads to a decrease in the efficiency of the exchange interaction and to a corresponding increase in the height of the second step under the conditions of dominant field-induced heating (Fig. 12b). Nevertheless, the detected quantum conductance staircase of conductance demonstrates the effect of the field-induced heating on only the second step, whereas the other quantum steps are rapidly suppressed as their number increases. The observed quenching of the quantum conductance staircase is apparently a result of the above-mentioned uncontrolled increase in the longitudinal voltage U_{ds} under the condition of the sweep in the gate voltage U_g, which is enhanced in thin quantum wires with a low linear concentration of charge carriers.

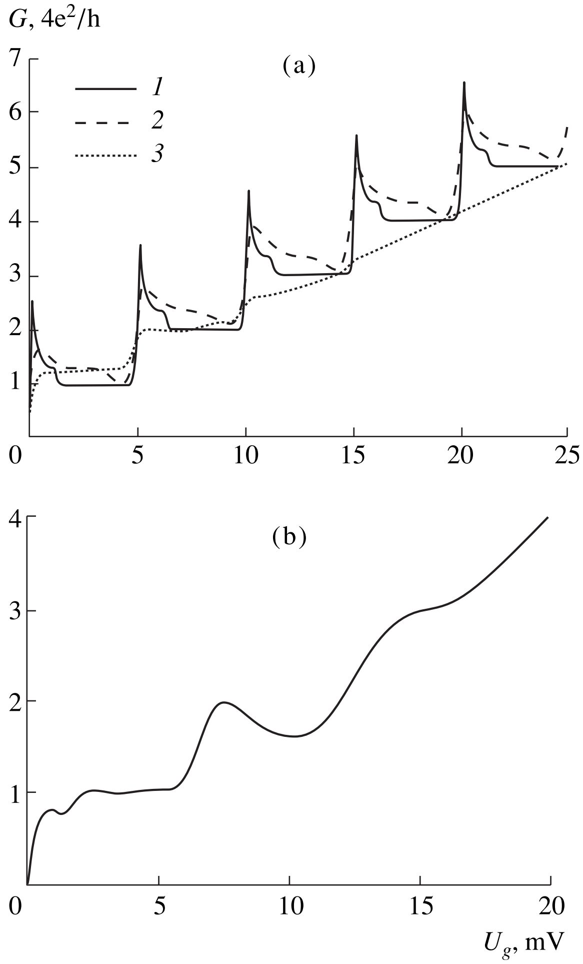

Fig. 12. The field-induced heating of the quantum staircase of electron conductance in a 1D channel oriented along the [001] axis within a self-assembled n-type quantum well in the Si(100) plane; the effect was observed by varying the drain–source voltage. (a) The results of numerical calculation for $kT/\Delta E$ = (*1*) 0.01, (*2*) 0.05, and (*3*) 0.05 taking into account the field-induced quenching illustrated in Fig. 11b. (b) Experimental dependence obtained at $T = 77$ K.

It is noteworthy that the suggested mechanism for an increase in the ballistic conductance as a result of the field-induced heating of the charge carriers makes it possible to account for the increase in the step height [9] and for the distortions in the form of plateaus in the quantum staircase of conductance [29]; these distortions were observed in studies of long quantum wires, which were considered previously in terms of the model of elastic electron–electron and electron–impurity scattering [27]. Therefore, in order to determine the relative contribution of these two mechanisms to the characteristics of the conductance quantum staircase, it seems necessary to perform additional experimental testing using a variation in the initial concentration of 2D charge carriers.

3.6. Quantized Conductance under Conditions of Charge-Carrier Interference in Modulated Quantum Wires

As mentioned above, the step heights in the quantum staircase of conductance are, as a rule, slightly smaller than $G_0 = g_s g_v e^2/h$, which, in particular, can result from the effect of elastic scattering of the charge carriers at the impurity centers located at the quantum-wire boundaries [27, 29]. However, internal barriers formed by the residual impurity centers not only assist the quenching of the quantized conductance but also modulate it in relation to the gate voltage U_g and at additional "finger" gates (Fig. 1b). Experimentally, two types of quantum-conductance oscillations were observed; these oscillations were induced by the passage of individual charge carriers through the QDs formed between the barriers within the modulated quantum wire.

The first type of oscillations include the Coulomb oscillations that arise owing to recharging of the QDs in relation to the potential localized at the barriers using the finger gates U_{g1} and U_{g2} (Fig. 1b) for the specified constant energy of tunneling individual charge carriers (U_{ds} = const) [1, 3, 30, 44, 45]. The Coulomb oscillations have a multielectron origin and are related to the electrostatic repulsion of charge carriers that reside within a QD. Therefore, the Coulomb oscillations can emerge only if there is a weak coupling between the QD incorporated into the quantum wire and the remaining part of the quantum wire. In other words, potential barriers should be sufficiently high and wide in order to ensure the long lifetimes of charge carriers within a QD [45, 46]. In this case, the conductance is always found much lower than $g_s g_v e^2/h$ [3, 44–46]; i.e., we have

$$G = g_s g_v \frac{e^2}{h} \frac{\mathcal{T}_1 \mathcal{T}_2}{\mathcal{T}_1 + \mathcal{T}_2} \frac{4\Gamma_1 \Gamma_2}{E_a^2(U_g) + (\Gamma_1 + \Gamma_2)^2}, \qquad (16)$$

where $\mathcal{T}_1$ and $\mathcal{T}_2$ are the coefficients of transmission through the barriers confining the QD; Γ_1 and Γ_2 are the widths of the quasi-bound states related to the escape of charge carriers through the left- and right-hand barriers, respectively; and $E_a(U_g)$ is equal to the width of the Coulomb gap (e^2/C) (C is the QD capacitance) except for the values of U_g corresponding to the condition for the charge degeneracy $U_g = -(N + 1/2)e/C$; if this condition is satisfied, this gap becomes equal to zero, as a result of which the conductance becomes nonzero.

Thus, the conductance of quantum wire containing a QD, which is loosely connected to the edges, depends in an oscillatory manner on the voltage applied to the QD. The maxima in the conductance are governed by the conditions for degeneracy of the QD. The values of the conductance even at the peak points are much smaller than the conductance quantum $g_s g_v e^2/h$.

The distance between two neighboring peaks in the case of tunneling through a QD with a small number of electrons is given by

$$\Delta U_g = \frac{e}{C} + \frac{\varepsilon_{N+1} - \varepsilon_N}{e} \qquad (17)$$

and, thus, depends on the peak number, in contrast to a multielectron QD for which we have $\Delta U_g = e/C$. In other words, the Coulomb oscillations are periodic in the case of tunneling through the multielectron QDs, whereas in the transport of charge carriers via the small-electron QDs the periodicity is perturbed. It is noteworthy that the positions of the conductance resonances can be determined more accurately using the numerical calculation of the energy eigenvalues for an actual form of QDs [47].

The second type of oscillation in the plateau of the quantized conductunce emerges if the space between the potential barriers is strongly coupled to the remaining part of the quantum wire. In this case, the treatment of 1D transport as single-electron tunneling is apparently inadequate. The approach based on the quantum interference induced by the processes of charge-carrier elastic backscattering between the modulating barriers is apparently preferable. This approach makes it possible to explain the oscillatory dependence of the conductance on the Fermi energy, i.e., on the values of both the transverse (U_g) and longitudinal (U_{ds}) electric field. The conductance oscillations in relation to the applied voltage are a direct consequence of oscillations in the transit coefficient in relation to the energy of the particles incident on the potential barrier $\mathcal{T}(E_F)$.

It is worth noting that the conductance peaks originate at the energy values that correspond to the passage through a system of barriers without reflection ($\mathcal{T} = 0$) as a result of interference of the waves subjected to multiple scattering in the interbarrier region. Furthermore, in contrast to single-electron tunneling through a QD, the conductance at the resonance points coincides with the conductance quantum ($g_s g_v e^2/h$) in the case of quantum interference.

The role of interference in the formation of $\mathcal{T}(E)$ ($k \propto E$) can be illustrated more conveniently using the example of a 1D system composed of two barriers, which are not necessarily identical and not necessarily δ-shaped. Let t_1 and t_2 denote the absolute amplitudes of the waves transmitted through the first and second barriers, and let r_1 and r_2 denote the corresponding amplitudes for the reflected waves. We denote a variation in the phase of the wave passed through the first barrier by φ_{11}, and in the second barrier by φ_{22}; a variation in the phase of the wave propagating from right to left after reflecting from the first barrier is denoted by φ_{12}, and from left to right after reflecting the second barrier, by φ_{21}. The amplitude of the waves transmitted through a two-barrier system is then given by

$$\begin{aligned} A &= t_1 t_2 e^{i(\varphi_{11} + \varphi_{22})} \sum_{j=1}^{\infty} r_1 r_2 e^{i(\varphi_{12} + \varphi_{21})} \\ &= \frac{t_1 t_2 e^{i(\varphi_{11} + \varphi_{22})}}{1 - r_1 r_2 e^{i(\varphi_{12} + \varphi_{21})}}. \end{aligned} \qquad (18)$$

Thus, the transmission coefficient is equal to

$$\mathcal{T} = \frac{\mathcal{T}_1\mathcal{T}_2}{1 + (1 - \mathcal{T}_1)(1 - \mathcal{T}_2) - 2\sqrt{(1 - \mathcal{T}_1)(1 - \mathcal{T}_2)}\cos(\varphi)},$$
$$\varphi = \varphi_{12} + \varphi_{21}. \qquad (19)$$

The difference of formula (19) from its classical analogue consists in the presence of the factor accounting for interference $e^{i(\varphi_{12} + \varphi_{21})}$, which brings about an increase in the coefficient of passage through a two-barrier system for certain energies of the incident particle. The multiple scattering events are especially important for the incident-particle energies so that the transmission coefficient reaches unity. Therefore, for a system consisting of several barriers, the notion of a quasi-level is sometimes introduced; these quasi-levels correspond to the energies for which a particle confined in the interbarrier space experiences multiple-scattering events before leaving this space. In this case, the time of residence of the particle between the barriers is increased; i.e., a “quasi-bound” state emerges. If the particle energy is in resonance with the quasi-level energy, the coefficient of the transmitted wave attains the value of unity. In the vicinity of resonance, the amplitude of the transmitted wave is described by the Breit–Wigner formula; i.e.,

$$A = \frac{i\Gamma/2}{\varepsilon - \varepsilon_n + i\Gamma/2}, \qquad (20)$$

where ε is the particle energy, ε_n is the quasi-level position, and Γ is the quasi-level width.

It can be seen that consideration of interference radically affects the $\mathcal{T}(E)$ dependence. For certain energies of the incident particle, the interference brings about an increase in the transmission probability up to the value of unity; for other energies, the interference leads to an appreciable decrease in this probability. We note that, for small values of E, interference brings about a decrease in the transmission coefficient.

Thus, in contrast to the case of Coulomb oscillations, the conductance of a quantum wire for the resonance energies under the conditions of quantum interference at the modulating barriers corresponds to $g_s g_v e^2/h$. Nevertheless, it is of interest to formulate a more stringent test in order to establish a demarcation line between the contributions of these mechanisms to the formation of the conductance quantum staircase.

First, we note that the Coulomb oscillations can be observed only in relation to the voltage applied to the modulating barriers U_{g1}, U_{g2}, and U_g [1, 3, 44, 45], whereas the interference-related oscillations are observed under conditions of varying both the transverse (U_g) and longitudinal (U_{ds}) voltages [30, 34, 37].

Second, if the conductance is measured in relation to the transverse voltage U_g, the strength of the barriers confining the QD can be used as a test for separating the interference from the Coulomb oscillations. For high barrier strength, a single-electron recharging is observed, whereas the quantum interference is observed for low barrier strength. We now justify this statement and consider in more detail which strengths should be considered as high and which as low. To this end, we take into account that the single-electron recharging of a QD can be described using the tunneling Hamiltonian of the Anderson type; i.e.,

$$\hat{H} = \sum_i \varepsilon_i c_i^+ c_i + \sum_i \varepsilon_k a_i^+ a_k + \sum_i \varepsilon_k b_i^+ b_k$$
$$+ \sum_{i,k} (t_a c_i^+ a_k + t_a^* a_k^+ c_i) \qquad (21)$$
$$+ \sum_{i,k} (t_b c_i^+ b_k + t_b^* b_k^+ c_i) + U \sum_{i<j} c_i^+ c_i c_j^+ c_j,$$

where c_i^+, c_i, a_k^+, a_k, b_k^+, and b_k are the operators of creation and annihilation of an electron in a QD and at the left- and right-hand boundaries. The first term describes the Hamiltonian of an isolated QD; the second term, the Hamiltonian of the left-hand edge; the third term, the Hamiltonian of the right-hand edge; the fourth term, the transitions between the left-hand edge and the QD; the fifth term, the transitions between the right-hand edge and the QD; and the sixth term, the multiparticle interactions in the QD [47].

The possibility of using the above Hamiltonian relies on good definiteness of single-particle energies ε_i in a QD. In other words, the distance between the neighboring energy levels $\Delta\varepsilon$ should be much larger than the level width Γ: $\Delta\varepsilon \gg \Gamma$.

Let us use the semiclassical approximation to calculate the level width of a QD restricted by two barriers, the coefficients of transmission through which are equal to $\mathcal{T}_1$ and $\mathcal{T}_2$. The quantity Γ is related to the possibility of an electron to leaving the QD through the left-hand barrier with permeability $\mathcal{T}_1$ and through the right-hand barrier having the permeability $\mathcal{T}_2$ and can be represented as $\Gamma = \Gamma_1 + \Gamma_2$, where the Γ_1 and Γ_2 widths are governed by the possibility of leaving the QD through the left- and right-hand side barriers, respectively [45, 46]. According to the uncertainty relation, $\Gamma_i\tau_i \approx \hbar$, where τ_i denotes the charge-carrier lifetime in relation to the carrier leaving through the ith barrier. Assuming that the charge carrier arrived at the QD from the left, we obtain the following expressions for τ_1 and τ_2 in the form of a series:

$$\tau_2 = \tau\mathcal{T}_2 + 3\tau\mathcal{R}_2\mathcal{T}_2 + 5\tau\mathcal{R}_2^2\mathcal{T}_2 + \ldots$$
$$= t\mathcal{T}_2(1 + 3\mathcal{R}_2 + 5\mathcal{R}_2^2 + \ldots) = \tau\mathcal{T}_2\sum_{j=1}^{\infty}(2j+1)\mathcal{R}_2^j, \qquad (22)$$
$$\tau_1 = 2\tau\mathcal{T}_1 + 4\tau\mathcal{R}_1\mathcal{T}_1 + 6\tau\mathcal{R}_1^2\mathcal{T}_1 + \ldots$$
$$= 2t\mathcal{T}_1(1 + 2\mathcal{R}_1 + 3\mathcal{R}_1^2 + \ldots) = 2\tau\mathcal{T}_1\sum_{j=0}(j+1)\mathcal{R}_1^j.$$

Here, $\tau = L/v$ is the time of transit of the interbarrier distance L by a charge carrier with the velocity v and $\mathcal{R}_i = 1 - \mathcal{T}_i$. Performing a summation of the above series using the conventional method, we obtain

$$\begin{gathered}\tau_2 = \frac{\tau(1+\mathcal{R}_2)}{\mathcal{T}_2} \approx \frac{2\tau}{\mathcal{T}_2},\\ \tau_1 = \frac{2\tau}{\mathcal{T}_1}.\end{gathered} \tag{23}$$

Thus,

$$\Gamma \approx \frac{\hbar v(\mathcal{T}_1 + \mathcal{T}_2)}{2L}. \tag{24}$$

The distance $\Delta\varepsilon$ between two neighboring levels in a QD can be estimated at

$$\Delta\varepsilon \approx \frac{\hbar^2}{100mL^2} + \frac{e^2}{L}, \tag{25}$$

where the first term corresponds approximately to the distance between the neighboring size-quantization levels in the QD, and the second term accounts for the contribution of the Coulomb electron repulsion (the QD capacitance $C \propto L$). Hence, it follows that the condition for the applicability of the formalism of single-electron tunneling and, correspondingly, the condition for observation of the Coulomb oscillations is given by

$$\frac{vL(\mathcal{T}_1 + \mathcal{T}_2)}{\dfrac{\hbar}{100m} + \dfrac{e^2}{\hbar}L} \ll 1. \tag{26}$$

The above oscillations are observed predominantly in the course of tunneling of charge carriers with low velocities v through the QDs that have a small size L and are confined by slightly transparent barriers ($\mathcal{T}_1 + \mathcal{T}_2 \ll 1$). Otherwise, the passage of charge carriers through a system of modulating barriers occurs according to the quantum-interference mechanism.

Thus, the identification of the Coulomb oscillations against the background of the quantum-interference effects is quite a challenge. This is especially so as, under the conditions of the split-gate method, a variation in the voltage applied to the main and/or "finger" gates is accompanied with a corresponding change in the kinetic energy of the charge carriers. Therefore, the most optimal test for the detection of quantum interference in modulated quantum wires consists in the observation of the conductance quantum staircase under conditions of a precise linear increase in the charge-carrier energy (see, e.g., Fig. 11a).

In this situation, oscillations in the plateaus of the conductance quantum staircase originate owing to the energy dependence of the transmission coefficient $\mathcal{T}(E)$ [see (19), (20)], because a modulated quantum wire can be thought of as a regular 1D quantum structure. Furthermore, the actual profile of each barrier $V(x)$ can be replaced by the δ-shaped profile. In this case, the potential barrier of an individual barrier can be represented as $\alpha\delta(x - R_b)$, where R_b is the barrier location point and the constant factor α is determined from the expression

$$\alpha = \int_{-\infty}^{+\infty} V(x)dx, \tag{27}$$

which is equivalent to the condition for equality between the strengths of actual and δ-shaped barriers. The Hamiltonian of a quantum wire can then be written as

$$U(x) = \alpha\sum_{j=0}^{n-1}\delta(x - Lj), \tag{28}$$

where n is the number of barriers and L is the interbarrier distance. This potential has been used (in the context of the transfer-matrix method [48]) to obtain an analytic expression that describes the energy dependence of the transmission coefficient $\mathcal{T}(E)$. However, in order to correctly consider the oscillations of the plateau in the conductance quantum staircase, we have to take into account the potential drop between the modulating barriers. In this case, we should take into consideration not only potential (28) but also the potential $U_{ext}(x)$, which is induced by external sources and presumably depends linearly on an external electric field applied along the quantum wire; i.e.,

$$U_{ext} = -eEx. \tag{29}$$

Therefore, in what follows, it is expedient to use a simplified model according to which the falloff of potential is steplike; as a result, we have the following expression for scattering potential (see the inset in Fig. 13b):

$$\begin{gathered}U(x) = \sum_{j=0}^{n-1}\delta(x - Lj) + U_{ext}(x),\\ U_{ext}(x) = \begin{cases} 0, & x < 0 \\ -eEjL, & x \in [(n-1)\alpha, n\alpha] \\ -eEL(n-1), & x > (n-1)\alpha. \end{cases}\end{gathered} \tag{30}$$

The wave number of the incident charge carrier is proportional to the electric-field strength $k_0 \propto E$, with the coefficient of proportionality being a free parameter of the model. As the charge carrier moves, its wave number varies. In the region between the jth and $(j + 1)$th barriers, the wave number is given by

$$k_j = \sqrt{k_0^2 + 2meELj}. \tag{31}$$

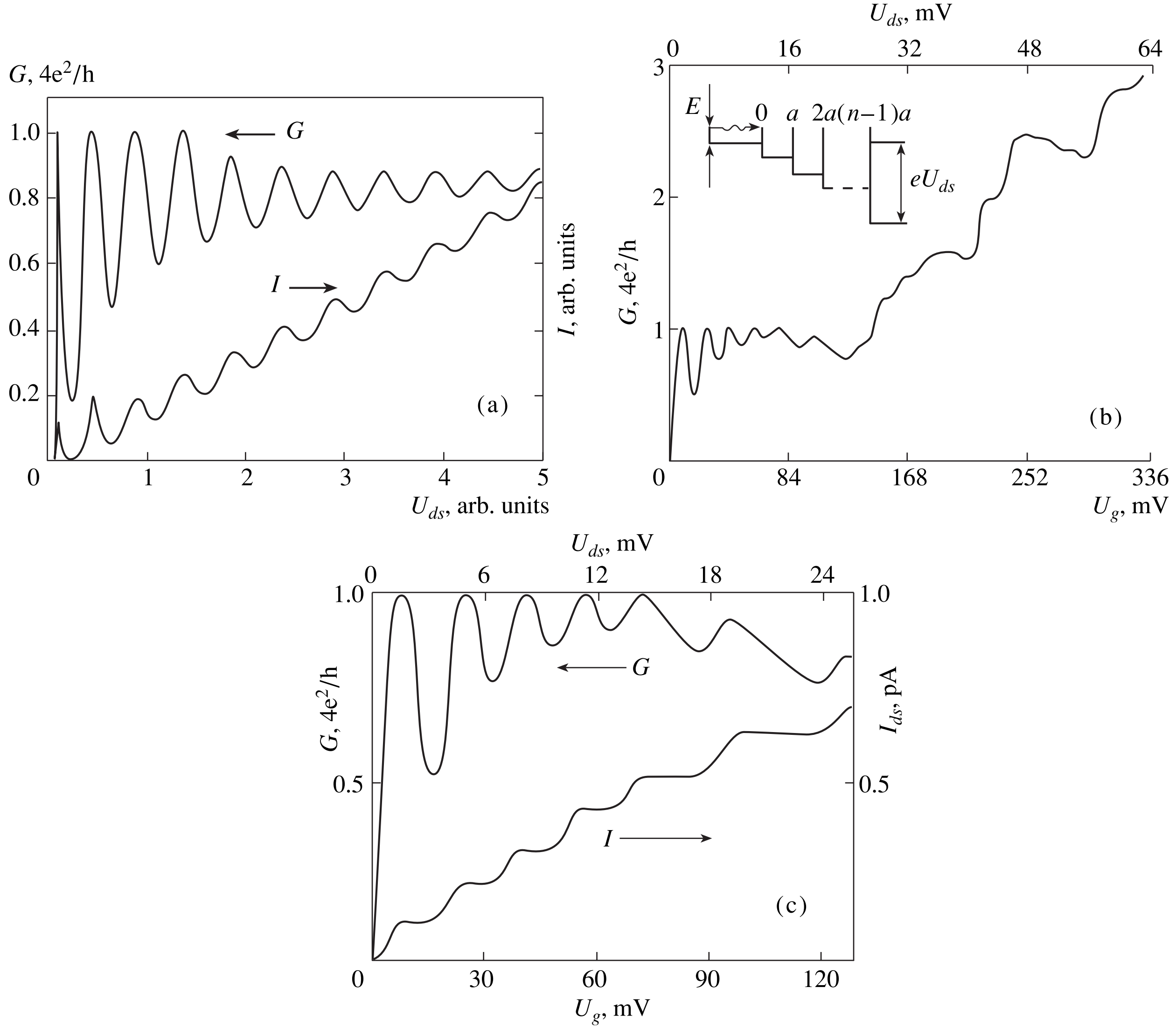

Fig. 13. (a) The results of numerical calculation of periodic oscillations in the region of quantum steps and the plateau in the quantum staircase of conductance; these oscillations are caused by quantum interference of charge carriers at the barriers within a modulated quantum wire. The strength of an individual barrier (α) and the interbarrier distance (L) are expressed in atomic units, with n standing for the number of barriers; $n = 2$, $L = 20$, and $\alpha = 0.2$. (b, c) The I–V characteristics of the quantum staircase for the hole conductance in a modulated 1D channel oriented along the [001] axis within a self-assembled p-type quantum well in the Si(100) plane. Measurements were performed at $T = 77$ K under conditions of variation in the drain–source voltage. The Fermi level position corresponds to occupation of the 1D subbands for the heavy and light holes. A 1D system of individual δ-shaped barriers under the effect of an external electric field is illustrated in the inset in Fig. 13b.

Thus, the wave function in this region can be represented as

$$\psi_j(x) = A_j \exp(ik_j x) + B_j \exp(-ik_j x). \tag{32}$$

Correspondingly, the continuity condition at the boundary between the jth and $(j+1)$th regions is given by

$$A_{j+1}\exp(ik_{j+1}Lj) + B_{j+1}\exp(-ik_{j+1}Lj)$$
$$= A_j\exp(ik_jLj) + B_j\exp(-ik_jLj),$$

$$ik_{j+1}(A_{j+1}\exp(ik_{j+1}Lj) - B_{j+1}\exp(-ik_{j+1}Lj)) \tag{33}$$
$$- ik_j(A_j\exp(ik_jLj) - B_j\exp(-ik_jLj))$$
$$= \frac{2m\alpha}{\hbar^2}(A_j\exp(ik_jLj) + B_j\exp(-ik_jLj)).$$

It is convenient to use the matrix approach in further considerations; to this end, we introduce a column of new vector amplitudes. We then use the vectors $\mathbf{X}_{j+1} = \begin{pmatrix} A_{j+1} \\ B_{j+1} \end{pmatrix}$ and $\mathbf{X}_j = \begin{pmatrix} A_j \\ B_j \end{pmatrix}$ to obtain

$$\mathbf{X}_{j+1} = \mathbf{D}_j\mathbf{X}_j, \tag{34}$$

$$\mathbf{D}_j = \begin{pmatrix} \left(-\frac{im\alpha}{\hbar^2 k_{j+1}} + \frac{1}{2} + \frac{k_j}{2k_{j+1}}\right)\exp[i(k_j - k_{j+1})Lj] & \times\left(-\frac{im\alpha}{\hbar^2 k_{j+1}} + \frac{1}{2} - \frac{k_j}{2k_{j+1}}\right)\exp[-i(k_j + k_{j+1})Lj] \\ \left(\frac{im\alpha}{\hbar^2 k_{j+1}} + \frac{1}{2} - \frac{k_j}{2k_{j+1}}\right)\exp[i(k_j + k_{j+1})Lj] & \times\left(\frac{im\alpha}{\hbar^2 k_{j+1}} + \frac{1}{2} + \frac{k_j}{2k_{j+1}}\right)\exp[-i(k_j - k_{j+1})Lj] \end{pmatrix}. \quad (35)$$

The amplitudes of the transmitted and reflected waves are determined from a system of two linear algebraic equations written in matrix form as

$$\mathbf{X}_n = \mathbf{D}_{n-1}\mathbf{X}_{n-1} = \mathbf{D}_{n-1}\mathbf{D}_{n-2}\ldots\mathbf{D}_0\mathbf{X}_0 = \Re\mathbf{X}_0,$$

$$\Re = \prod_{j=0}^{n-1}\mathbf{D}_j, \quad (36)$$

$$\mathbf{X}_0 = \begin{pmatrix}1\\B\end{pmatrix}, \quad \mathbf{X}_n = \begin{pmatrix}A\\0\end{pmatrix}.$$

A solution to this system of equations has the following form:

$$B = -\frac{\Re_{21}}{\Re_{22}}, \quad A = \Re_{11} - \frac{\Re_{12}\Re_{21}}{\Re_{22}}. \quad (37)$$

The matrix product $\Re = \mathbf{D}_{n-1}\mathbf{D}_{n-2}\ldots\mathbf{D}_0$ can be analytically calculated only for the zero longitudinal electric field, because, when such a field exists, only a numerical analysis is possible if n is an arbitrary number.

The transmission coefficient is calculated as the ratio between the densities of the transmitted and incident particle fluxes; i.e.,

$$\mathcal{T} = \frac{J_{tr}}{J_f} = \frac{k_n}{k_0}|A|^2. \quad (38)$$

The results of numerical calculations of the conductance G and current I, in relation to the parameters of a modulated quantum wire, are shown in Fig. 13a. Periodic oscillations of the conductance and current arise as a result of the quantum interference of charge carriers at the barriers within a modulated quantum wire. It is noteworthy that the values of the parameters of a modulated quantum wire, especially the individual-barrier strength, used in calculations of the dependences shown in Fig. 13a were chosen in the context of the γ-potential model, because the ballistic-carrier interference indicated by the quantized-conductance oscillations disappears instantaneously as soon as the barriers within a modulated quantum wire cease to be abrupt. The cause of this limitation is the suppression of backscattering of ballistic charge carriers in the regions between the barriers and also the enhancement of the scattering of these carriers within the single-electron subbands.

Thus, the suggested model of a modulated quantum wire makes it possible to describe the oscillations of the plateau in the quantized conductance in terms of quantum interference of the charge carriers at extremely abrupt internal barriers. In this paper, these oscillations are demonstrated on the basis of the results of studying 5-μm-long modulated [001] quantum wire obtained using the split-gate method in the plane of a p-Si(100) QW (Figs. 13b, 13c). The concentration of 2D holes (1.6×10^{13} m^{-2}) and the cross-sectional area of the 1D channel (2×2 nm^2) defined the contribution of the light and heavy holes to the quantized conductance; this contribution manifested itself in the corresponding step heights measured under the conditions of the swept voltage $U_{DS} = U_g + U_{ds}$ applied parallel to the QW confined by two ferroelectric δ-shaped barriers. As mentioned above, the 1D subbands are formed in this case owing to the ordering of the impurity dipoles in ferroelectric δ-shaped barriers ($U_g > 0$), whereas the sweep of the longitudinal voltage U_{ds} induces a change in the kinetic energy of ballistic holes. The aforesaid makes it possible to identify the observed oscillations of the plateau in the quantized conductance with induced interference effects as a result of elastic backscattering of holes at the δ-shaped barriers. These effects are suppressed as the number of upper occupied states increases; this is caused by the supersensitivity of the ballistic-hole interference to the quantum-wire width and to the degree of abruptness of modulating barriers (Fig. 13b).

It is worth noting that oscillations in the plateau in the quantized conductance in relation to U_{ds} can apparently be used as an experimental test for distinguishing the effects of quantum interference in modulated quantum wires against the background of Coulomb oscillations emerging as a result of the formation of QDs between the δ-shaped barriers in the case of sweeping the U_g, U_{g1}, and U_{g2} voltages. Such an interrelation between the Coulomb oscillations and interference effects was observed previously [30] in the split-gate structures and was possibly a consequence of uncontrolled spread in U_{ds} in the course of measuring the dependence $G(U_g)$. The amplitude of background oscillations caused by quantum interference at the δ-shaped barriers was comparable to the amplitude of the detected Coulomb oscillations.

Identification of the Coulomb oscillations against the background of several plateaus in the conductance quantum staircase [41, 42] is a much more difficult problem. In this case, the shape of the measured I–V characteristic is similar to that shown in Figs. 13b and 13c; however, in contrast to the quantum interference at the δ-shaped barriers, the Coulomb oscillations have a much smaller amplitude against the background of the conductance quantum staircase, $\Delta G \ll g_s g_v e^2/h$. However, the most important indication that the oscillations can be attributed either to the plateau region in the conductance quantum staircase or to the quantum interference consists in the different reactions of the above effects to changes in the charge-carrier kinetic energy when U_{ds} is varied.

CONCLUSION

Thus, we used the split-gate method to implement and study various versions of the quantum staircase for the electron and hole conductance of 1D channels induced electrostatically within self-assembled silicon QWs. To this end, we used narrow (2 nm) QWs formed spontaneously between highly doped δ-shaped barriers within ultrashallow (10–30 nm) boron diffusion profiles obtained by nonequilibrium diffusion at the Si(100) surface. The characteristics of the self-assembled *n*- and *p*-Si QWs were determined by measuring the angular dependences of the cyclotron resonance and ESR spectra, which made it possible to identify the crystallographic orientation of the QWs and the ferroelectric properties of the δ-shaped barriers. Due to the small width of the QWs and the ferroelectric properties of the δ-shaped barriers confining these QWs, the *I–V* characteristics of the conductance quantum staircase were studied for the first time at relatively high temperatures ($T \geq 77$ K) in relation to the kinetic energy of electrons and holes.

It was ascertained that the step heights in the electron conductance of the *n*-type quantum wires are controlled by the Si conduction-band anisotropy in the [001] ($G_0 = 4e^2/h$, $g_v = 2$) and [011] ($G_0 = 8e^2/h$, $g_v = 4$) orientations.

We detected the quantum staircase of the hole conductance for the first time in *p*-Si quantum wires. In this case, the quantum steps of conductance originated as a result of independent contributions of the 1D subbands of heavy and light holes, which manifested itself (when studying the square quantum wires) in the doubling of the quantum-step heights ($G_0 = 4e^2/h$), with the exception of the first-step height, which was equal to $2e^2/h$ due to nondegeneracy of the lower 1D subband.

It is shown that temperature- and field-related quenching of the conductance quantum staircase arises when kT and the energy of the field-induced heating of charge carriers become comparable to the energy spacing between the 1D subbands.

We observed an enhancement of the quantum-step amplitudes with an increase in the kinetic energy of electrons in the finite-length quantum wires that cannot be described in terms of a point quantum contact.

We detected the spontaneous spin polarization of the heavy and light holes; this polarization is caused by the predominance of the exchange interaction when the lower 1D subbands in silicon quantum wires are occupied only slightly.

We observed oscillations in the plateau of the conductance quantum staircase; these oscillations are caused by quantum interference of holes at the δ-shaped barriers in the *p*-Si modulated quantum wires. We determined the conditions for the applicability of the split-gate method to the detection of quantum interference against the background of Coulomb oscillations under the conditions of transport of individual charge carriers in modulated quantum wires.

ACKNOWLEDGMENTS

We are grateful to V.I. Perel' and V.V. Kveder for their helpful participation in discussions of the results.

This study was supported in the framework of the Programs “Physics of Solid-State Nanostructures” (project no. 97-1040) and “Fullerenes and Atomic Clusters” (project no. 3-1-98).

REFERENCES

1. T. J. Thornton, Rep. Prog. Phys. **58**, 311 (1995).
2. C. W. J. Beenakker and H. van Houten, in *Solid State Physics*, Ed. by H. Ehrenreich and D. Turnbull (Academic, New York, 1991).
3. M. A. Kastner, Phys. Today **46**, 24 (1993).
4. R. Landauer, IBM J. Res. Dev. **1**, 233 (1957).
5. M. Büttiker, Phys. Rev. Lett. **57**, 1761 (1986).
6. D. A. Wharam, T. J. Thornton, R. Newbury, *et al.*, J. Phys. C **21**, L209 (1988).
7. B. J. van Wees, H. van Houten, C. W. J. Beenakker, *et al.*, Phys. Rev. Lett. **60**, 848 (1988).
8. T. J. Thornton, M. Pepper, H. Ahmed, *et al.*, Phys. Rev. Lett. **56**, 1198 (1986).
9. A. Yacoby, H. L. Stormer, S. N. Wingreen, *et al.*, Phys. Rev. Lett. **77**, 4612 (1996).
10. J. I. Pascual, J. Mendez, J. Gomez-Herrero, *et al.*, Phys. Rev. Lett. **71**, 1852 (1993).
11. N. T. Bagraev, W. Gehlhoff, L. E. Klyachkin, *et al.*, Mater. Sci. Forum **258–263**, 1683 (1997).
12. N. T. Bagraev, E. I. Chaikina, W. Gehlhoff, *et al.*, Solid-State Electron. **42**, 1199 (1998).
13. G. Grabeski, J. Wrobel, T. Dietl, *et al.*, Phys. Rev. B **60**, 5133 (1999).
14. N. T. Bagraev, A. D. Buravlev, L. E. Klyachkin, *et al.*, in *Proceedings of the ISSCRM-2000* (Novgor. Gos. Univ., Novgorod, 2000), p. 76.
15. Y. Nakajima, Y. Takahashi, S. Horiguchi, *et al.*, in *Extended Abstracts if the International Conference on Solid State Devices and Materials, IC SSDM, Yokohama, Japan, 1994*, p. 538.
16. I. P. Kouwenhoven, B. J. van Weecs, C. J. P. M. Harmans, *et al.*, Phys. Rev. B **39**, 8040 (1989).
17. K. J. Thomas, J. T. Nicholls, M. Y. Simmons, *et al.*, Phys. Rev. Lett. **77**, 135 (1996).
18. K. J. Thomas, J. T. Nicholls, N. J. Appleyard, *et al.*, Phys. Rev. B **58**, 4846 (1998).
19. K. J. Thomas, J. T. Nicholls, M. Pepper, *et al.*, Phys. Rev. B **61**, 13365 (2000).

20. K. S. Pyshkin, C. J. B. Ford, R. H. Harrell, *et al.*, Phys. Rev. B **62**, 15842 (2000).
21. Chuan-Kui Wang and K.-F. Berggren, Phys. Rev. B **54**, 14257 (1996).
22. Chuan-Kui Wang and K.-F. Berggren, Phys. Rev. B **57**, 4552 (1998).
23. A. M. Bychkov, I. I. Yakymenko, and K.-F. Berggren, in *Proceedings of the 8th International Symposium "Nanostructures: Physics and Technology", St. Petersburg, 2000*, p. 391.
24. Kenji Hirosi, Shu-Shen Li, and N. S. Wingreen, Phys. Rev. B **63**, 33315 (2001).
25. A. Gold and L. Calmels, Philos. Mag. Lett. **74**, 33 (1996).
26. B. Spivak and Fei Zhou, Phys. Rev. B **61**, 16730 (2000).
27. Masao Ogata and Hidetoshi Fukuyama, Phys. Rev. Lett. **73**, 468 (1994).
28. Takashi Kimura, Kazuhito Kuroki, and Hideo Aoki, Phys. Rev. B **53**, 9572 (1996).
29. Siego Tarucha, Tacashi Honda, and Tadashi Saki, Solid State Commun. **94**, 413 (1995).
30. T. Heinzel, S. Manus, D. A. Wharam, *et al.*, Europhys. Lett. **26**, 689 (1994).
31. U. Gösele and T. Y. Tan, Defect Diffus. Forum **59**, 1 (1988).
32. W. Gehlhoff, N. T. Bagraev, and L. E. Klyachkin, Mater. Sci. Forum **196–201**, 467 (1995).
33. N. T. Bagraev, A. D. Buravlev, L. E. Klyachkin, *et al.*, Fiz. Tekh. Poluprovodn. (St. Petersburg) **34**, 726 (2000).
34. N. T. Bagraev, E. I. Chaikina, L. E. Klyachkin, *et al.*, Superlattices Microstruct. **28**, 337 (1998).
35. W. Gehlhoff, N. T. Bagraev, and L. E. Klyachkin, Solid State Phenom. **47–48**, 586 (1996).
36. A. N. Andronov, N. T. Bagraev, L. E. Klyachkin, *et al.*, Fiz. Tekh. Poluprovodn. (St. Petersburg) **33**, 851 (1999) [Semiconductors **33**, 782 (1999)].
37. N. T. Bagraev, L. E. Klyachkin, A. M. Malyarenko, and W. Gehlhoff, Superlattices Microstruct. **23**, 1333 (1998).
38. N. T. Bagraev, L. S. Vlasenko, and A. I. Merkulov, Zh. Éksp. Teor. Fiz. **81**, 2160 (1981) [Sov. Phys. JETP **54**, 1147 (1981)].
39. B. Camarota, F. Parage, and I. Wooldridge, J. Low Temp. Phys. **118**, 589 (2000).
40. C.-T. Liang, M. Pepper, M. Y. Simmons, *et al.*, Phys. Rev. B **61**, 9952 (2000).
41. C.-T. Liang, M. Y. Simmons, C. G. Smith, *et al.*, Phys. Rev. Lett. **81**, 3507 (1998).
42. C.-T. Liang, M. Y. Simmons, C. G. Smith, *et al.*, Physica E (Amsterdam) **6**, 418 (2000).
43. A. V. Andreev and A. Kamenev, Phys. Rev. Lett. **81**, 3199 (1998).
44. U. Meirav, M. A. Kastner, and S. J. Wind, Phys. Rev. Lett. **65**, 771 (1990).
45. J. Göres, D. Goldhaber-Gordon, S. Heemeyer, and M. A. Kastner, Phys. Rev. B **62**, 2188 (2000).
46. L. I. Glazman, J. Low Temp. Phys. **118**, 247 (2000).
47. S. Tarucha, D. G. Asuting, and T. Honda, Phys. Rev. Lett. **77**, 3613 (1996).
48. N. T. Bagraev, W. Gehlhoff, V. K. Ivanov, *et al.*, Phys. Low-Dimens. Semicond. Struct. **1–2**, 37 (2000).

Translated by A. Spitsyn

Semiconductors, Vol. 36, No. 4, 2002, pp. 461–465. Translated from Fizika i Tekhnika Poluprovodnikov, Vol. 36, No. 4, 2002, pp. 484–489.

LOW-DIMENSIONAL SYSTEMS

Exciton Recombination in δ-Doped Type-II GaAs/AlAs Superlattices

K. S. Zhuravlev*, A. K. Sulaĭmanov, A. M. Gilinskiĭ, L. S. Braginskiĭ,
A. I. Toropov, and A. K. Bakarov

Institute of Semiconductor Physics, Siberian Division, Russian Academy of Sciences,
pr. Akademika Lavrent'eva 13, Novosibirsk, 630090 Russia

**e-mail: zhur@thermo.isp.nsc.ru*

Submitted July 16, 2001; accepted for publication September 13, 2001

Abstract—Radiative recombination of excitons in δ-doped type-II GaAs/AlAs superlattices (SLs) is studied experimentally. With an increase in the impurity density in δ-layers from 2×10^{10} to 7.5×10^{11} cm^{-2}, the integrated intensity of SL photoluminescence (PL) decreases by a factor of 4–6; the intensity of excitonic PL drops considerably (up to 70–80 times), which is accompanied by an increase in the exciton radiative decay rate. Uniform doping of the SL does not result in the exciton PL quenching. Analysis of the temperature dependence and the kinetics of the PL indicate that impurity quenching of the excitonic PL in δ-doped structures is not related to a reduction in the exciton localization energy and cannot be explained by an increase in the density of nonradiative recombination centers. We conclude that the PL quenching is mainly caused by the appearance of built-in electric fields originating from ionized impurities, which hinders the formation of the excitons. *© 2002 MAIK "Nauka/Interperiodica".*

1. INTRODUCTION

Mechanisms of recombination of elementary excitations in type-II quantum wells and superlattices (SLs) differ considerably from mechanisms of recombination in direct-gap SLs and bulk materials and have been intensively studied over the years both experimentally and theoretically [1–7]. In recent years, in addition to their significance for fundamental matters, these studies have also gained importance for applications. It was demonstrated that suppression of Auger recombination (the main channel of nonradiative recombination at high temperatures and high excitation densities) is possible in type-II SLs [1], which opens the way to the development of low-threshold injection lasers on the basis of such structures [2]. The most important fact about recombination in type-II GaAs/AlAs SLs is that the large quasi-momentum of an electron in the X valley of the AlAs conduction band is scattered when it recombines with a hole in the Γ valley of the GaAs valence band. Quasi-momentum scattering can take place both at smooth and rough heterointerfaces [3, 4, 8]; in addition, processes involving phonons, impurities, and nonradiative recombination centers are possible [1, 5, 6]. This paper is devoted to the experimental investigation of the influence of impurities on exciton recombination in type-II GaAs/AlAs SLs. Previously, the role of impurities in exciton recombination was examined only in uniformly doped type-II heterostructures. Here, we report on the study of photoluminescence (PL) in δ-doped SLs and discuss the difference between δ-doped and uniformly doped structures.

2. EXPERIMENTAL

The structures under study were δ-doped type-II GaAs/AlAs SLs grown by molecular-beam epitaxy on GaAs(100) substrates at 600°C. The samples contain a 0.5-μm GaAs buffer and an SL formed by 40 pairs of 7 monolayer-thick GaAs and 9 monolayer-thick AlAs layers. GaAs layers were doped with beryllium (an acceptor impurity), and AlAs layers were doped with silicon (predominantly a donor impurity). The impurity δ-layers were located at a distance of two monolayers from the direct interface (AlAs grown on GaAs). The donor and acceptor densities were set equal to each other and varied in different samples from 2×10^{10} to 7.5×10^{11} cm^{-2}. Two series of samples were grown using source materials (Ga, Al, and As) from different suppliers. An Ar-ion laser (λ = 488 nm) was used for steady-state photoluminescence (PL) excitation; the power density on the sample surface was 30 W/cm^2. In the time-resolved measurements of the transient PL kinetics and spectra, we used excitation by the second harmonic of a pulsed YAG:Nd laser (λ = 532 nm) with the following parameters: laser pulse width, 150 ns; repetition rate, 5 kHz; peak power density on the sample surface, 350 W/cm^2. The PL spectra and kinetics were recorded using a spectrometer based on a double-grating monochromator and a photomultiplier with an S-20 photocathode operating in the photon-counting mode.

3. RESULTS

Figure 1 represents the low-temperature (T = 4.2 K) steady-state PL spectra of δ-doped type-II GaAs/AlAs

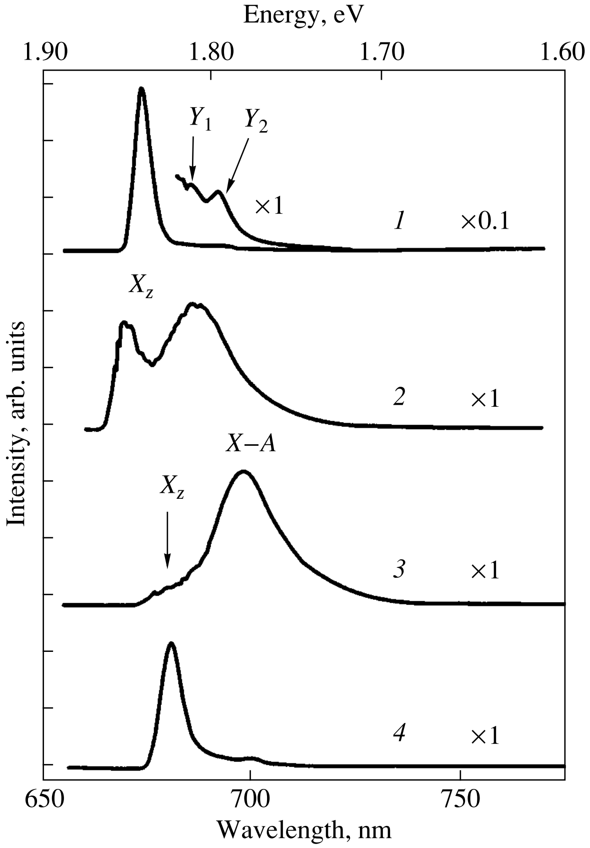

Fig. 1. Steady-state low-temperature (T = 4.2 K) PL spectra of doped type-II SLs: δ-doped SLs with impurity densities of (*1*) 5.5×10^{10}, (2) 2×10^{11}, and (*3*) 7.5×10^{11} cm^{-2}; and (*4*) a uniformly doped SL with the mean distance between the impurity atoms corresponding to that in a δ-doped structure with impurity density of N_D, N_A = 7×10^{11} cm^{-2}.

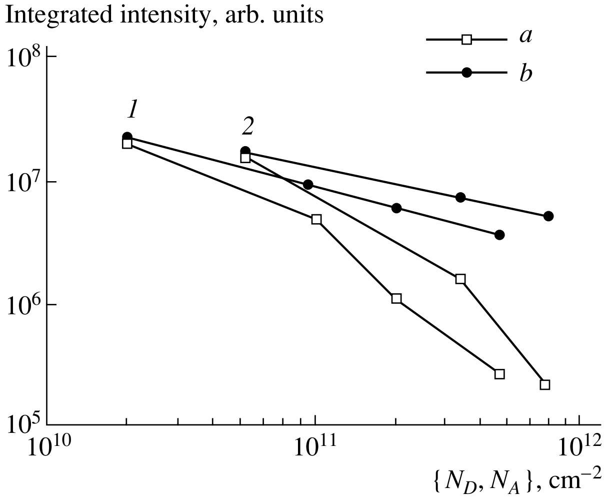

Fig. 2. Dependences of (*a*) exciton zero-phonon PL intensity and (*b*) integrated intensity of the exciton line, its phonon replicas, and the donor–acceptor recombination line in δ-doped SL structures of the growth series *1* and *2* on impurity density. The measurement temperature T = 4.2 K.

SLs with different impurity densities. The spectrum of a GaAs/AlAs SL uniformly doped with Si to a bulk concentration of 5×10^{17} cm^{-3} is also shown. One can see that, at low impurity densities, the spectrum of a δ-doped structure is dominated by the line of the X_z exciton, which is formed by an electron in the X_z valley of the AlAs conduction band and a hole in the Γ valley of the GaAs valence band (cf. curve *1*). The lines Y_1 and Y_2 are phonon replicas of the X_z line and are shifted from it by 27 and 49 meV, respectively; the first value corresponds to the LA phonon energy in GaAs and AlAs, and the second, to the LO phonon energy in AlAs. With an increase in the impurity density, the X_z line intensity decreases. In the samples where the impurity density exceeds 10^{11} cm^{-2}, a long-wavelength line, marked as *D*–*A*, appears in the spectrum; previously, we established that this line originated from impurity transitions between donors in the AlAs layers and acceptors in the GaAs layers [7]. It becomes dominant in the spectra of the samples with the highest impurity densities. In contrast to δ-doped structures, the spectrum of the sample with the uniformly doped SL (see curve *4*) is dominated by the X_z exciton zero-phonon line. Meanwhile, for a bulk impurity density of 5×10^{17} cm^{-3}, the average distance between the impurity atoms is the same as that in the plane of a δ-doped layer with an impurity density of 7×10^{11} cm^{-2}.

In Fig. 2, the X_z zero-phonon line intensity and the integral PL intensity are plotted as a function of the impurity density for the samples of both growth series. The integrated PL intensity denotes the total intensity of the zero-phonon exciton line, its phonon replicas, and the donor–acceptor recombination line. One can see that the X_z line intensity and the integrated PL intensity decrease with an increase in the doping level. Note that the integrated PL intensity is reduced by a factor of 4–6, while the X_z line intensity falls 70–80 times, following the dependence close to the power law with an exponent of ~ 1.2. A steady decrease in the SL integrated PL intensity with an increase in the doping level indicates that the probability of nonradiative recombination of the charge carriers increases as the impurity density in the SL is raised. The choice of source materials (Ga, As, and Al) has no effect on the shape of the dependences observed, the only distinction between the two series of the samples being the 40–60% difference in the absolute values of the PL intensity.

The observed impurity quenching of the excitonic PL in δ-doped SLs may be related either to an increase in the rate of exciton nonradiative recombination with increasing impurity density, or to the effect of built-in electric fields induced by ionized impurities, which hinder exciton formation in heavily doped structures. An increase in the nonradiative recombination rate may be caused by a reduction in the energy of exciton localization at heterointerface irregularities, as well as by an increase in the number of nonradiative recombination centers. To clarify the role of different mechanisms for the impurity quenching of excitonic emission, we stud-

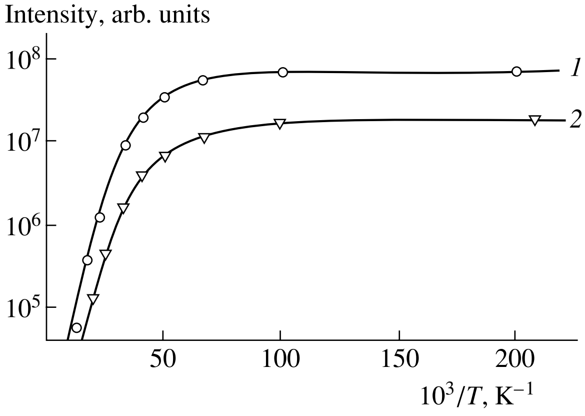

Fig. 3. Temperature dependences of the exciton zero-phonon PL intensity in two δ-doped SL structures with the impurity density of (*1*) 2×10^{10} and (*2*) 2×10^{11} cm^{-2}. Symbols represent experimental points and solid lines represent the results of calculation according to (1).

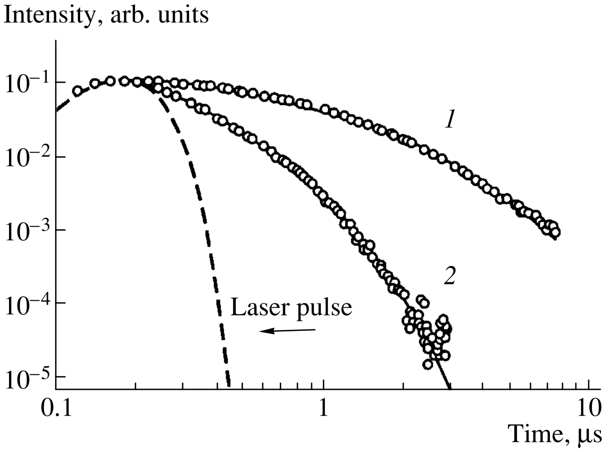

Fig. 4. Decay kinetics of the transient excitonic PL in δ-doped SLs at $T = 4.2$ K. Symbols represent experimental points and solid lines represent the results of calculation according to (2). The doping level in the two samples is (*1*) 5.5×10^{10} and (*2*) 5×10^{11} cm^{-2}. The time profile of the laser pulse is shown by a dashed line.

ied the kinetics and the temperature dependence of the PL in SL structures. The data obtained made it possible to determine whether the exciton localization energy and the density of nonradiative recombination centers depend on the doping level.

To determine the exciton localization energy, we examined the temperature dependence of the steady-state PL spectra of the SLs. In Fig. 3, the temperature dependence of the integrated intensity of the X_z exciton line is shown for the two samples with different impurity densities. The measured dependences were fitted using the following expression [9]:

$$I(T) = I_0/[1 + A\exp(-E_a/kT) + B\exp(-E_b/kT)]. \quad (1)$$

Here, E_a is the energy of the exciton localization at heterointerface irregularities, E_b is the exciton binding energy, I_0 is the low-temperature intensity of the exciton emission line, and A and B are constants. The values of the localization energy obtained from this fit are in the range from 4 to 5.5 meV for the samples with an impurity density as high as 5×10^{11} cm^{-2}. This is somewhat lower than the value $E_a = 6.8$ meV reported in [6]; the discrepancy is due to the difference in the SL parameters. The exciton binding energy in the same samples varies between 19 and 22 meV; this is in agreement with the value $E_b = 15$ meV calculated in [10] for an SL with approximately the same parameters. We did not find any dependence of the energies E_a and E_b on the doping impurity density. Thus, it can be concluded that the exciton diffusion coefficient is independent of the impurity density up to the level of 5×10^{11} cm^{-2}. In the samples with a doping level above this value, the X_z line becomes strongly overlapped with the donor–acceptor recombination line, which makes it impossible to determine E_a and E_b reliably.

The density of nonradiative recombination centers can be determined from the analysis of the exciton PL kinetics. In Fig. 4, the exciton PL decay curves for two samples with different doping levels are shown. It can be seen that the exciton recombination rate increases with increasing impurity density. To evaluate the density of nonradiative recombination centers, the decay curves were fitted by an expression obtained in the context of the model taking into account exciton diffusion between the localized states and their nonradiative recombination in the course of this diffusion [5]; in the two-dimensional case, it can be written as

$$I(t) \propto (1 + 2w_r t)^{-3/2} \times \exp[-4\pi D_E n_d t/\ln(\beta + 4\alpha D_E t/L^2)]. \quad (2)$$

Here, t is the time, w_r is the ensemble-averaged rate of radiative recombination of the excitons, n_d is the density of nonradiative recombination centers, D_E is the exciton diffusion coefficient, L is the average distance between the localized states, and $\alpha = 5.7$ and $\beta = 17.5$ are the constants [5]. It is assumed that the average distance between the nonradiative recombination centers, $(n_d)^{-1/2} \gg L$, and the quasi-momentum relaxation in the process of exciton radiative recombination takes place by scattering at the interface roughness. In the course of their diffusion between localized states, excitons can be trapped by randomly arranged nonradiative recombination centers and recombine there. Since the energy E_a of the exciton localization at the interface irregularities is independent of the doping level, it was assumed in the calculation that the diffusion coefficient D_E is the same for all structures and equal to 0.002 cm^2 s^{-1} [6]. The choice of L is not very important, since this parameter appears in the expression for $I(t)$ under the logarithm

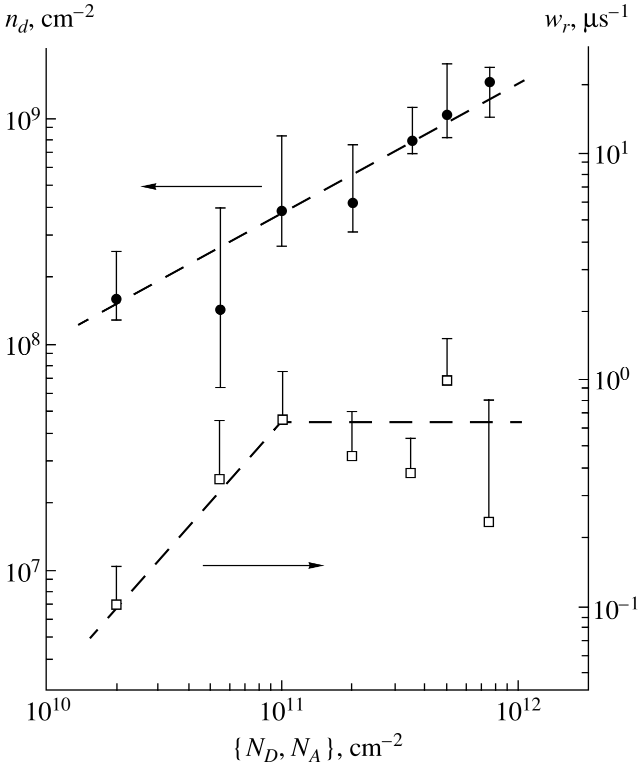

Fig. 5. Dependences of the density of nonradiative recombination centers n_d and the average radiative recombination rate w_r on the doping level. See the text about the determination of the errors shown by the error bars.

sign. We only need to satisfy the condition $(n_d)^{-1/2} \gg L$; thus, it was assumed that $L = 20$ nm [5]. The values of w_r and n_d were varied to get the best agreement between the calculated decay curves (solid lines in Fig. 4) and the experimental data.

In Fig. 5, the density of nonradiative recombination centers n_d and the average exciton radiative recombination rate w_r, determined from the decay curve fits, are plotted as a function of the doping level. With an increase in the impurity density, n_d increases, while w_r first increases and then remains nearly constant. The initial increase in w_r is nearly linear with respect to the impurity density. Note that $I(t)$ depends on n_d exponentially, whereas w_r only appears in the relatively slowly varying prefactor; thus, the error in the values of w_r obtained from the results of fitting is larger than that for n_d. The errors in w_r and n_d are shown in Fig. 5; to determine these, the corresponding parameter was varied until the discrepancy between the fitting curve and the experimental data increased by a factor of three in comparison to the optimum case. The lower limit for w_r appears to be very close to the best-fit value and is not shown in the figure. Since the shape of the calculated decay curves depends on w_r rather weakly, a more simple expression, derived disregarding the exciton diffusion [8], can be used to fit experimental curves. The absolute values of w_r obtained in this way differ by about a factor of two from those represented in Fig. 5; however, the general behavior of the calculated parameters as a function of the doping level remains the same.

4. DISCUSSION

Now, let us consider the variation in the recombination properties of type-II SLs with the density of impurities in the δ-layers. It is known that, in type-II GaAs/AlAs SLs, electrons and holes are separated both in the real space and in the quasi-momentum space: electrons occupy the X valley in AlAs, and holes occupy the Γ valley in GaAs. Because of this, in the process of exciton recombination, an electron has to move to the neighboring layer and its quasi-momentum must change by a large amount, $\sim\pi\hbar/a$ (where $\hbar$ is the Plank constant and a is the lattice constant). In a perfect SL (i.e., in the absence of phonons, impurities, heterointerface roughness, and nonradiative recombination centers), the quasi-momentum of an X_z exciton can be scattered only at the interfaces. In this case, the exciton radiative recombination rate w is constant, and the exciton density $N(t)$ and luminescence intensity $I(t)$ decay exponentially [4]: $N(t) \propto \exp(-wt)$, and $I(t) \propto w\exp(-wt)$. When the quasi-momentum can be scattered by impurities or interface roughness, the exciton recombination rate is a quantity that depends randomly on the location of an impurity (or interface irregularity). Averaging of the emission intensity $I(t) \propto w\exp(-wt)$ over the distribution of the random variable w results in the appearance of a nonexponential factor in the expression describing the exciton luminescence decay. In the case of impurity scattering, the decay follows a power-law dependence $(1 + 2w_rt)^{-3/2}$ [8], and in the case of scattering by interface roughness, it has a more complicated form [4]. When the presence of the nonradiative recombination centers is taken into account, an additional factor appears in the expression for the PL decay kinetics [the second factor in formula (2)], which, to the first approximation, may be considered exponential (neglecting the time dependence of the logarithmic denominator).

With an increase in the density of impurities introduced by δ-doping, the power-law factor changes (the parameter w_r in expression (2) increases up to an impurity density of 1×10^{11} cm^{-2}); this is related to an increase in $w \propto N_D, N_A$. At higher doping levels, when the mean distance between the impurities becomes comparable to the size of the exciton, several impurity centers simultaneously affect the exciton recombination and the relative magnitude of the random potential fluctuations decreases due to averaging over several neighboring impurity atoms. The limiting case of a closely packed δ-doped layer corresponds to exciton scattering by a smooth boundary, which is similar to the case of scattering at an ideal heterointerface; the recombination kinetics becomes exponential and the power-law factor in (2) disappears. This explains the absence of a doping-level dependence of w_r for impurity densities exceeding 1×10^{11} cm^{-2}.

One can see from Fig. 5 that an increase in the impurity density leads to an increase in the density of nonradiative recombination centers; the latter increase follows a power law with an exponent of about 0.6. The decrease in the SL-integrated PL intensity as a function of the doping level follows the same law with the same exponent (see Fig. 2), while the exciton zero-phonon PL intensity shows a decrease following a power law whose exponent is twofold greater. Thus, the dependence of the SL integrated PL intensity on the doping level can be well explained by an increase in the density of the nonradiative recombination centers; at the same time, this cannot explain the considerable drop in the excitonic PL intensity. We conclude that the impurity-related quenching of the excitonic PL, accompanied by an increase in the radiative recombination rate, should be attributed to the effect of the built-in electric fields, induced by ionized impurities. As the impurity density is raised, the magnitude of the built-in fields increases; note that, in the case of δ-doping considered in this study, these fields are much higher than in the case of uniform doping. An enhancement of the built-in field leads to an increase in the number of charge carriers that are involved in the screening of this field and that cannot bind to excitons. It is this effect that explains why an increase in the impurity density results in the strong quenching of the excitonic PL intensity, while quenching of the integrated PL intensity is less pronounced. In addition, the existence of the built-in electric fields leads to a lowering of the crystal symmetry, which makes Γ–X mixing of electron states more effective [11]; thus, the probability of an electron from the X valley of the AlAs conduction band being found in the Γ valley of the GaAs conduction band increases. This also results in a higher rate of radiative recombination.

5. CONCLUSION

Thus, radiative recombination of the excitons in δ-doped type-II SLs was investigated for the first time. It was found that an increase in the density of impurities in δ-doped layers from 2×10^{10} to 7.5×10^{11} cm^{-2} leads to a 70- to 80-fold reduction in the exciton PL intensity, while the integrated PL intensity is reduced by a factor of 4–6. In a uniformly doped SL with a bulk impurity concentration of 5×10^{17} cm^{-3}, where the mean distance between the impurity atoms corresponds to that in the plane of a δ-doped layer with an impurity density of 7×10^{11} cm^{-2}, exciton PL quenching is not observed. It is shown that the exciton radiative recombination rate in δ-doped structures increases with increasing doping level. Studies of the temperature dependence and the kinetics of the PL demonstrated that the quenching of the zero-phonon exciton emission line in the δ-doped SL structures is not related to any reduction in the exciton localization energy and cannot be explained simply by an increase in the density of nonradiative recombination centers. We conclude that the excitonic PL quenching is mainly caused by the appearance of the built-in electric fields (induced by ionized impurities), which hinders the exciton formation.

ACKNOWLEDGMENTS

This study was supported by the Russian Foundation for Basic Research (project no. 00-02-17658) and by the Interdisciplinary Science and Technology Program “Physics of Solid-State Nanostructures” (project nos. 99-1133 and 2000-1F).

REFERENCES

1. G. G. Zegrya and A. D. Andreev, Zh. Éksp. Teor. Fiz. **109** (2), 615 (1996) [JETP **82**, 328 (1996)].
2. V. G. Litovchenko, D. V. Korbutyak, A. L. Bercha, *et al.*, in *Proceedings of the 25th International Conference on Physics of Semiconductors, Japan, 2000,* D092.
3. F. Minami, K. Hirata, K. Era, *et al.*, Phys. Rev. B **36**, 2875 (1987).
4. L. S. Braginsky, M. Yu. Zaharov, A. M. Gilinsky, *et al.*, Phys. Rev. B **63**, 195305 (2001).
5. I. N. Krivorotov, T. Chang, G. D. Gilliland, *et al.*, Phys. Rev. B **58**, 10687 (1998).
6. G. D. Gilliland, A. Antonelli, D. J. Woldford, *et al.*, Phys. Rev. Lett. **71**, 3717 (1993).
7. K. S. Zhuravlev, D. A. Petrakov, A. M. Gilinsky, *et al.*, Superlattices Microstruct. **28** (2), 105 (2000).
8. M. V. Klein, M. D. Sturge, and E. Cohen, Phys. Rev. B **25**, 4331 (1982).
9. K. D. Glinchuk and A. V. Prokhorovich, Phys. Status Solidi A **29**, 339 (1975).
10. M. M. Dignam and J. E. Sipe, Phys. Rev. B **41**, 2865 (1990).
11. J. Feldmann, J. Nunnenkamp, G. Peter, *et al.*, Phys. Rev. B **42**, 5809 (1990).

Translated by M. Skorikov

Semiconductors, Vol. 36, No. 4, 2002, pp. 466–471. Translated from Fizika i Tekhnika Poluprovodnikov, Vol. 36, No. 4, 2002, pp. 490–495.
Original Russian Text Copyright © 2002 by Bilenko, Belobrovaya, Zharkova, Mysenko, Khasina.

AMORPHOUS, VITREOUS, AND POROUS SEMICONDUCTORS

The Effect of Adsorption on the Electrical Properties of Structures Based on Oxidized Porous Silicon

D. I. Bilenko*, O. Ya. Belobrovaya, É. A. Zharkova, I. B. Mysenko, and E. I. Khasina

Research Institute of Mechanics and Physics, Chernyshevskiĭ State University,
ul. Astrakhanskaya 83, Saratov, 410026 Russia
** e-mail: bil@ns.ssu.runnet.ru*

Submitted August 27, 2001; accepted for publication September 11, 2001

Abstract—The effect of adsorption of hydrogen-sulfide and acetone polar molecules on current–voltage characteristics and time dependences of the current was studied for the ⟨Pd–por-Si(O)–p^+-Si–Al⟩ structures based on oxidized porous silicon. Structures of two types were obtained—those with a Schottky barrier and those with space-charge-limited currents. The presence of a positive space charge was found near the palladium electrode; this charge defined the current–voltage characteristics in the region of $V < 0.2$ V and varied appreciably depending on the gas used. The parameters of the layer of oxidized porous Si and the range of operating voltages corresponding to the most marked effect of a gas were determined. A maximum current variation up to 10^3 times under the action of hydrogen sulfide with a concentration of ~10 ppm was obtained for the structures with the Schottky barrier with a reverse voltage close to that of reversible breakdown. The results obtained are explained by the charge exchange of traps, which is corroborated by a Fermi level shift and a Schottky barrier lowering caused by the adsorption of polar molecules. *© 2002 MAIK “Nauka/Interperiodica”.*

INTRODUCTION

The study of the influence of adsorption of various substances on properties of porous silicon (por-Si), which is a material with quantum-mechanical size effects and a well-developed surface, makes it possible to extend the range of investigated properties of semiconductor materials and to enhance the potentialities of using these structures in sensors. In spite of the intense study of por-Si properties before and after the action of various gas media [1–9], the electrical properties of the structures with modified por-Si layers, for example, with partially oxidized por-Si {por-Si(O)} layers, have been insufficiently studied [8–10]. Partial oxidation can serve to stabilize por-Si properties.

The current–voltage (*I*–*V*) characteristics of the structures define a number of functional characteristics and represent a tool for studying physical processes in the structures (the mechanisms of conductivity and contact phenomena).

The studies on the investigation of the *I*–*V* characteristics of structures based on porous silicon without special oxidation and the influence of the adsorption of methanol, acetone, and hydrogen on these characteristics are well known [3, 4, 7]. In these studies, it was pointed out that the *I*–*V* characteristics are diverse and depend on the thickness and porosity of por-Si, properties of the substrate and junctions, temperature, and ambient-medium composition. The investigations that we carried out previously made it possible to establish the high sensitivity of the structures based on por-Si(O) to the action of hydrogen sulfide and acetone [8, 9]. However, the mechanisms of the influence of the ambient medium on properties of the structures and the kinetics of their variation as a result of adsorption remain unknown.

In this paper, we report the results of investigating the effect of adsorption of various gases on the charge transport in ⟨Pd–por-Si(O)–p^+-Si–Al⟩ and the possibilities of developing highly sensitive sensors on their basis.

PRODUCTION OF STRUCTURES AND MEASUREMENT PROCEDURE

The porous-silicon layers were obtained by the electrochemical etching of single crystal *p*-Si with $\rho = 0.03\ \Omega$ cm. The etching was performed in the HF : C_2H_5OH : H_2O solution for various volume ratios of components and at a current density of 2–30 mA/cm^2. The subsequent anode oxidation of por-Si layers was performed in a 0.04N solution of KNO_3 in $C_2H_4(OH)_2$ for 1–5 min with a current density of 10 mA/cm^2. According to the method described in [9], the porous-silicon thickness *d* and its porosity *q* were determined directly during the layer formation from the interference of laser radiation directed to the untreated side of the substrate. In this investigation, we used samples with *d* ranging from 2 to 10 μm and with *q*, from 0.6 to 0.85.

The ⟨Pd–por-Si(O)–p^+-Si–Al⟩ diode structures were formed by vacuum deposition of the palladium electrode on the por-Si(O) layer (the so-called catalytic electrode) and of the aluminum ohmic contact on the

p^+-Si substrate. The Pd layers were monitored during the deposition, and their thicknesses varied from 50 to 60 nm. The reference samples of metal layers on glass obtained by the same method were monitored using an ellipsometer; it was found that the porosity of these layers amounted to 0.2–0.3.

The influence of a gas medium (hydrogen sulfide, acetone, and carbon tetrachloride) on the samples was investigated in a chamber in which the gas medium could be reversibly changed. The diluting gas for hydrogen sulfide was nitrogen. In previous experiments, it was established that nitrogen affects neither the electrical nor optical properties of the structures under study.

CURRENT–VOLTAGE CHARACTERISTICS OF STRUCTURES

The *I–V* characteristics in air and in a gas medium were measured in darkness, which excluded the effect of scattered daylight on the results obtained. The *I–V* characteristics of the ⟨Pd–por-Si(O)–p^+-Si–Al⟩ structures were shown (Fig. 1) to have a number of special features. The forward *I–V* characteristic (negative voltage across the palladium layer) involves a descending portion in the region of small voltages, the negative slope of the *I–V* characteristic being changed for the positive one with a further increase in the voltage. In the reverse portion of the *I–V* characteristic, we observed a negative value of current, which decreased as the applied voltage increased, and the change in the current direction took place for a voltage of ~0.01–0.2 V depending on the por-Si(O) properties. The rectification factor decreases as the applied voltage increases.

For the structures in which the Pd layer is replaced by the Al layer, no such features were observed.

In the region of voltages higher than 0.2 V, the form of the current–voltage dependence varies as V increases. According to *I–V* characteristics, the samples investigated can be divided into two groups. For the group I samples, the current–voltage dependence is described by the power law with a portion caused by the space-charge-limited current (SCLC) ($I \propto V^m$ with $m = 2$–4). For the group II samples, the *I–V* characteristics have exponential dependences $I(V)$ characteristic of the Schottky barriers $\{I \propto \exp(qV/nkT)\}$ with reversible "breakdown" in the reverse portion or of the Pool–Frenkel emission ($I \propto \exp V^{0.5}$). Such dependences were previously observed in the ⟨Pd–por–p^+-Si–Al⟩ structures without the special oxidation of por-Si [6, 7].

Using the portions of the *I–V* characteristics with the space-charge-limited current, we estimated the trap concentration N_n by two methods: from a voltage value for which the ohmic-conductivity current transforms into the SCLC [11, 12] and by the so-called "step-by-step" method for the exponential energy distribution of traps in the band gap [13]. Values of the trap concentration averaged over the energy gap determined by both methods were within 3×10^{17}–10^{18} cm^{-3} eV^{-1}.

We discovered the existence of an incorporated space charge controlled in sign and value by the field applied and the ambient medium. The incorporated charge likely causes the features of the *I–V* characteristics of the investigated structures for low voltages. This fact is corroborated by the measurements of the short-circuit current and the open-circuit voltage V_{oc}. In the initial state, the positive charge at the palladium electrode generates an emf and a current opposite to the current from an external source if the structure is switched on into the reverse direction (positive voltage across Pd). As the applied voltage V increases and approaches V_{oc}, the "negative" current decreases. When applying an external voltage in the conductivity direction (negative voltage across Pd), the positive space charge decreases due to the injection of electrons and their recombination, and the current decreases and attains a minimum value for $V \le V_{oc}$. The asymmetry of the Pd–por-Si(O) & por-Si(O)–p^+-Si barriers is favorable to forming the space charge. For the ⟨Al–por-Si(O)–p^+-Si–Al⟩ structures, the open-circuit voltage is less than 5–10 mV, that is, by a factor of 10–40 less than that for the samples with the upper palladium electrode. The value of V_{oc} depends heavily on structure parameters: the porosity and por-Si-layer thickness, the oxidation degree of this layer, and the material and thickness of the metal layer. A short-circuit current in the initial state is 1–3 nA. In the ⟨Pd–por-Si(O)–p^+-Si–Al⟩ structures, the differential resistivity is on the order of 10^{10} Ω for a por-Si thickness of 6–10 μm and voltage values less than 0.1 V, which exceeds the differential resistivity of an initial unoxidized por-Si layer of the same thickness.

EFFECT OF ADSORPTION ON ELECTRICAL PROPERTIES OF STRUCTURES

The study of the effect of gases on the electrical properties of the obtained ⟨Pd–por-Si(O)–p^+-Si–Al⟩ structures showed that polar and nonpolar molecules of gases (hydrogen sulfide and acetone) change not only the current for the given voltage and the open-circuit voltage, but also the parameters of the current–voltage dependence. The adsorption of nonpolar molecules (nitrogen and carbon tetrachloride) affects the indicated characteristics of the ⟨Pd–por-Si(O)–p^+-Si–Al⟩ structures to a much lesser extent. For example, the introduction of hydrogen sulfide into nitrogen up to the concentration $C \approx 200$ ppm results in a rise in the reverse current under a near-breakdown voltage by more than 2–3 orders of magnitude (Fig. 1), while the current varies by less than a factor of 1.2 for the same carbon tetrachloride concentration. The adsorption exerts no effect on the shape of the current–voltage dependence outside the space-charge region ($V > 0.2$ V), but the parameters of such dependences change appreciably as a result of the adsorption. Such a situation is common

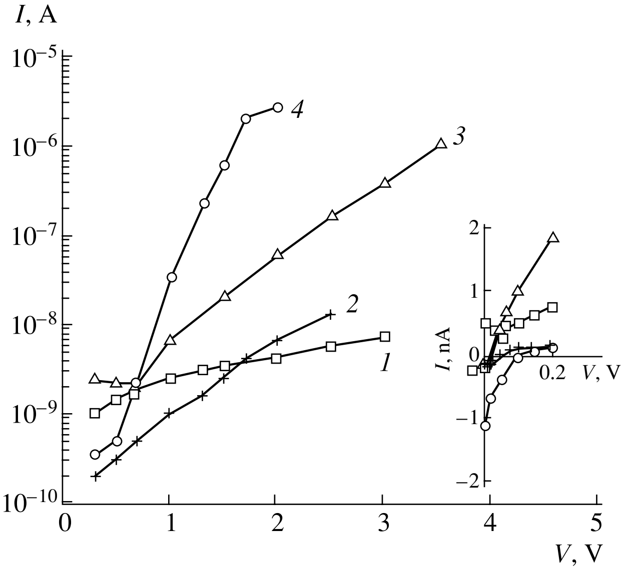

Fig. 1. Reverse portion of the current–voltage characteristic for the ⟨Pd–por–p^+-Si–Al⟩ structure in the initial state and after the adsorption. In air: (*1*) Pd_-; (*2*) Pd_+; (*3*) 1000 ppm acetone, Pd_+; (*4*) 200 ppm hydrogen sulfide, Pd_+. In the inset, *I*(*V*) for $V < 0.2$ V. The designations of curves correspond to the main panel.

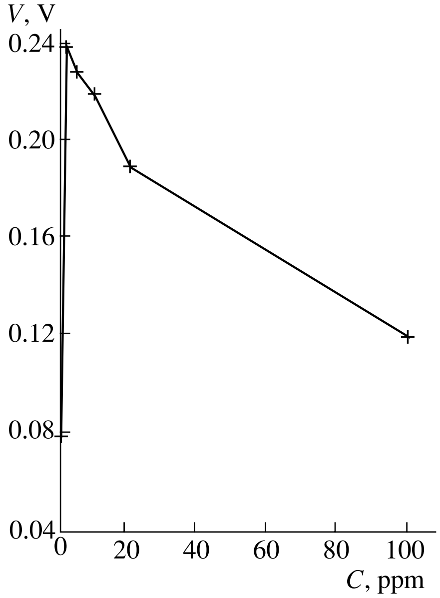

Fig. 2. Open-circuit voltage as a function of a hydrogen-sulfide concentration.

for both groups of samples. In the case of the adsorption of hydrogen sulfide or acetone (Fig. 1) by the samples described by the Schottky-barrier model, the exponent *n* in the exponential region decreases by a factor of 2–5. For the power dependence *I*(*V*), the exponent *m* remains virtually unchanged. The parameters describing the Pool–Frenkel emission also change. As a result of adsorption, the slope of the straight line ln*I* ($V^{0.5}$) and the saturation current vary, which, according to the calculations [14], corresponds to a decrease in the operating thickness of the layer from 10^3–10^4 Å in the initial state to 400–500 Å, which is much less than the por-Si(O)-layer thickness. In this case, the trap-barrier height decreases by a factor of 1.2–1.5.

A decrease in the exponent *n* in the *I*–*V* characteristic of the $I \propto \exp(qV/nkT)$ type during adsorption is apparently associated with an increase in the diffusion length *L* for the injected electrons in long diodes due to the capture of holes by traps and the decrease in the recombination rate [15]. For example, the decrease in *n* from 50 in the initial state to 10 due to adsorption in the region of voltages of 0.5–1.7 V (Fig. 1) corresponds to an increase in *L* by a factor of 1.5 and, thus, to the recombination-center concentration decrease by a factor of ~2.

The change in the current under the action of hydrogen sulfide or acetone in the ⟨Pd–por-Si(O)–p^+-Si–Al⟩ structures is approximately 100 times less than for the same sample with the Pd electrode.

The dependence of the open-circuit voltage V_{oc} on the hydrogen-sulfide concentration is shown in Fig. 2. An abrupt variation in V_{oc} by a factor of three is observed with increasing the hydrogen-sulfide concentration up to 1 ppm. Beyond this concentration, V_{oc} drops. Thus, polar molecules of hydrogen sulfide and acetone induce an additional positive charge on por-Si(O), which leads to a rise in V_{oc} as compared with the initial state.

We discovered instabilities of the current in the ⟨Pd–por-Si(O)–p^+-Si–Al⟩ structures when applying an external voltage $V > 10$ V and under the action of a high hydrogen-sulfide concentration of approximately 10^4 ppm. Similar oscillations, but with smaller amplitudes, were observed in structures with por-Si having a natural oxide and being exposed to the ether atmosphere [16]. After the gas action was terminated, the initial current values were restored within 2–3 min. The current oscillations observed are apparently associated with the charge exchange of the surface and bulk por-Si traps in strong electric fields under the adsorption of polar molecules.

KINETICS OF CURRENT VARIATION

The current-variation kinetics was studied for the structures with por-Si(O) in air and in the case of the adsorption of polar molecules. For every fixed value of *V*, we measured the dependence of current *I* on time *t*. The time interval of current variation amounted to 0–120 s with a step of 2–5 s. From *I*(*t*) obtained for various voltages, we plotted the *I*–*V* characteristics corresponding to given values of *t*. The dependences *I*(*V*, *t*) for a fixed voltage were measured for the samples with two types of *I*–*V* characteristics, i.e., with the Schottky barrier and with the space-charge-limited currents [11]. The features of time dependences of the *I*–*V* characteristics were similar in both cases, but the most abrupt variations of current in time were observed for the samples with the SCLCs for a reverse bias across the palladium electrode (Pd_+). The characteristic dependences $I(V, t)$ for such a sample are shown in Fig. 3. In the initial state (i.e., before gas action) in the SCLC region at the voltages $V > V_{oc}$, the current varies substantially within the time interval of 2–60 s. For the first 15 s, we observed voltage portions with abrupt minima of current, which were gradually smoothed with increasing t, and, for $t \geq 60$ s, the current became steady. The minima in the dependences $I(V)$ take place in the voltage ranges of 0.5–0.6 and 1.0–1.1 V.

The kinetics of the reverse-current decrease for $V > V_{oc}$ outside the special points (the points of the minimum of V in Fig. 3), and for V lower than the breakdown voltage the kinetics can be characterized by the power dependence $I(t) = I_0 t^{-\beta}$ in the interval of 1–45 s with the subsequent slow current leveling off. The exponent β is determined by the applied voltage and amounts to 0.1–0.3. For the structures with a Schottky barrier, the current varies insignificantly with time (by 10–15%) in the region of V close to the breakdown.

The polar molecules adsorbed; that is, the acetone molecules substantially influence the time dependences of the current. It was established that the adsorption leads to the following.

For the structures with SCLCs, the value and the position of the minimum of I and V are changed at the initial stage for $t < 15$ s and additional current minima appear (Fig. 3). The exponent β increases by a factor of 5–10.

The current variation in the Schottky-barrier structures are less abrupt, and β increases no more than by a factor of 1.2–1.3. Near the breakdown, the current is virtually invariable with time.

The current minima discovered in the time dependences of the I–V characteristics can apparently be explained by the distribution of the trap-state density in the band gap and by the variation in the Fermi level position depending on the voltage applied. In the case of adsorption of polar molecules, the density of trap states varies, which leads to the appearance of new current minima.

The energy position of the traps can be estimated from the capture time of injected charge carriers according to the expression $t = t_0 \exp E/kT$, where t_0 is the parameter equal to $\sim 10^{-10}$ s [12]. The energy E corresponding to the capture times of 5 and 45 s amounts to 0.62 and 0.67 eV, respectively.

The current–voltage characteristics in the SCLC region for the initial state and after the action of acetone made it possible to estimate the shift of the Fermi level E_F in the steady mode due to variation in the trap filling. The shift in the E_F position is calculated from the formula [13] as

$$\Delta E_F = kT \ln(I_2 V_1 / I_1 V_2),$$

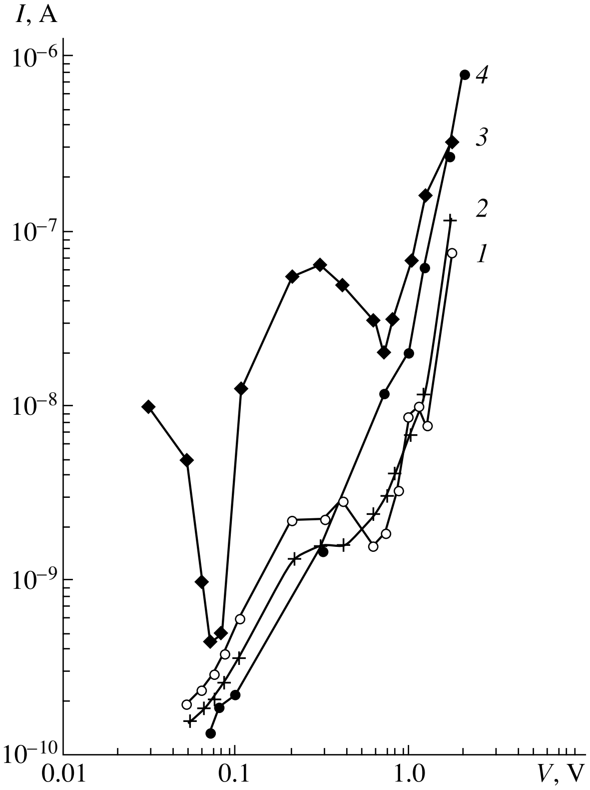

Fig. 3. Current–voltage characteristic of the ⟨Pd–por-Si(O)–p^+-Si–Al⟩ structure in various intervals of time. Pd_+ in air: t = (*1*) 5 and (*2*) 60 s; Pd_+ in acetone: t = (*3*) 5 and (*4*) 60 s.

where I_1, V_1, and I_2, V_2, are the current and voltage values in the $I(V)$ dependence.

The adsorption of polar molecules was found to induce a Fermi-level shift by a value equal to 0.03–0.05 eV. These values agree well with the values of ΔE_F obtained from the measurements of the voltage corresponding to the transition from the ohmic conductivity to the space-charge-limited currents. A certain Fermi level shift is caused by the variation in the concentration of free charge carriers by a factor of ~5, which is close to the experimentally observed current variation by a factor of 4 in the given experiment. Thus, the shifts ΔE_F obtained for the acetone adsorption are evidently associated with the variation in the concentration of the free charge carriers and the carriers captured by the traps located both on the surface and in the bulk of por-Si(O).

The investigation of the current of structures within the air–gas–air time cycle showed that, for concentrations of hydrogen-sulfide lower than 100 ppm, the initial current value is restored in air within 80–100 s. For higher concentrations above 10^4 ppm, we observe a residual current, which returns to the initial value within tens of hours. The presence of a residual current in the por-Si(O) structures was noted [10] in the case of the adsorption of ethanol and ammonia of high concentrations.

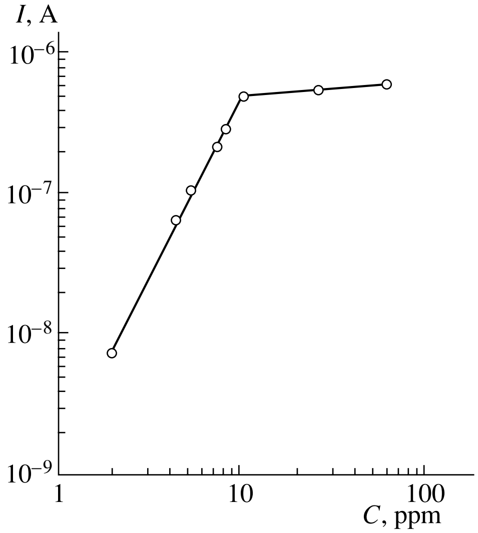

Fig. 4. Current as a function of a hydrogen-sulfide concentration for the structure with the Schottky barrier. Pd_+, $V = 1$ V, $I_i = 0.9$ nA.

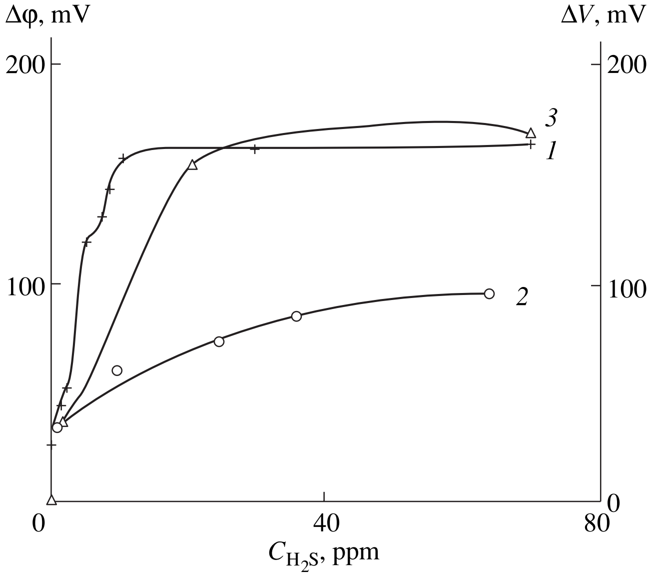

Fig. 5. Concentration dependence of Δφ and ΔV_{oc} for the structure on the basis of por-Si(O). (*1*) Δφ, (*2*) ΔV_{oc}, (*3*) Δφ for a single-crystal silicon.

SENSITIVITY OF POR-Si(O) TO THE ADSORPTION OF POLAR MOLECULES

The sensitivity of the structures in the case of adsorption can be characterized by the dependences of the potential barrier or the open-circuit voltage on the adsorbate concentration. The investigation of the current–voltage characteristics made it possible to find the region of structure parameters measured *in situ* and the mode of operation of the ⟨Pd–por–p^+-Si–Al⟩ structure for which sensitivity to gas action is highest. In this region, the values of the thickness (d), the porosity (q), time (t_0) of oxidation of the por-Si layer, and thicknesses of the palladium electrode (d_1) are within the following ranges: $d = 6–10$ μm, $q = 0.78–0.85$, $t_0 = 2–3$ min, and $d_1 = 50–60$ nm.

The highest sensitivity to the adsorption of polar molecules of hydrogen sulfide and acetone is found for the structures with the $I–V$ characteristics typical of the Schottky barrier. For them, a current variation is observed for both forward and reverse biases across the palladium electrode. However, in the case of the reverse bias for V close to the reversible breakdown, an increase in the current is by an order of magnitude higher than for the forward bias. The variation of current for a hydrogen-sulfide concentration above 10 ppm amounts to $\sim 10^3$. The current dependence on hydrogen-sulfide concentration for such a structure is shown in Fig. 4. In the range of concentrations $C = 1–10$ ppm, the dependence of current on C has the form $I \propto C^\alpha$, where $\alpha \approx 2.4$. When a concentration increases up to $C > 10$ ppm, we observe the current saturation. For the reverse bias, the introduction of hydrogen sulfide at a relative concentration of 10^{-8} into nitrogen induces a variation in the current by a factor of 2–3. The dependence $I(C)$ can be used for determining low concentrations of hydrogen sulfide.

The experimental current dependence on adsorbate concentration make it possible to determine the variation in the potential-barrier height in the ⟨Pd–por-Si(O)–p^+-Si–Al⟩ structure under the action of hydrogen sulfide. For various mechanisms of charge transport in the diode structures, the dependence of the current on the potential-barrier height φ is exponential: $I = I_0 \exp(-\varphi/kT)$ [14]. Determining the dependence of $\ln I_g/I_{\rm init}$ on the hydrogen-sulfide concentration, where $I_{\rm init}$ and I_g are the currents in the initial state and in the gas medium with hydrogen sulfide, respectively, it is possible to find variation in the barrier height Δφ as a function of the H_2S concentration. The obtained dependence $\Delta\varphi(C)$ agrees with the measured variation in the open-circuit voltage that is shown in Fig. 5. For comparison, we display the concentration dependence of $\Delta\varphi(C)$ for similar structures on single-crystal Si [17], which shows that, in the structure with layers of partially oxidized porous silicon, $\Delta\varphi(C)$ amounts to 150 mV for $C > 10$ ppm, which exceeds the same value for the structures based on single-crystal silicon by a factor of 2–3.

The adsorption of polar molecules probably changes the density of surface states in the adsorbate–adsorbent system and their energy distribution, which, in its turn, influences the trap distribution over the band gap of por-Si(O). This fact is corroborated by the experimental data on the Fermi level shift, the variation in the potential-barrier height in the Pd–*por*-Si(O) structures, the appearance of new minima of current, and the shift of extrema in the time dependence of current on voltage.

CONCLUSION

The analysis of the current–voltage characteristics and the kinetics of variation of the current of the ⟨Pd–por-Si(O)–p^+-Si–Al⟩ structures with a specially oxidized layer of porous silicon showed a number of current-flow features in the case of adsorption. An appreciable variation in the *I–V* characteristics and in the time dependence of current is observed only under the action of polar molecules (hydrogen sulfide or acetone).

A positive space charge found on the Pd electrode varies in the case of adsorption and defines special features of the *I–V* characteristics in the region of voltages lower than V_{oc}. The properties of structures based on por-Si(O) can be explained by the Fermi level shift and by the lowering of the height of the Pd–por-Si(O) barrier under the adsorption effect. The structures produced on the basis of partially oxidized porous silicon have exceptionally high sensitivity to the action of hydrogen sulfide and acetone and can form the basis for developing gas-media sensors.

REFERENCES

1. M. Ben-Chorin, F. Moller, and F. Koch, J. Appl. Phys. **77**, 4482 (1995).
2. M. Ben-Chorin, F. Moller, and F. Koch, Phys. Rev. B **49**, 2981 (1994).
3. M. Ben-Chorin, A. Kux, and I. Schecter, Appl. Phys. Lett. **64**, 481 (1994).
4. D. Stivenard and D. Deresmes, Appl. Phys. Lett. **67**, 1570 (1995).
5. S. P. Zimin, Fiz. Tekh. Poluprovodn. (St. Petersburg) **34**, 359 (2000) [Semiconductors **34**, 353 (2000)].
6. S. V. Slobodchikov, Kh. M. Salikhov, and E. V. Russu, Fiz. Tekh. Poluprovodn. (St. Petersburg) **32**, 1073 (1998) [Semiconductors **32**, 960 (1998)].
7. S. V. Slobodchikov, Kh. M. Salikhov, and E. V. Russu, Fiz. Tekh. Poluprovodn. (St. Petersburg) **31**, 15 (1997) [Semiconductors **31**, 11 (1997)].
8. D. I. Bilenko, O. Ya. Belobrovaya, E. A. Jarkova, *et al.*, Sens. Actuators A **62**, 621 (1997).
9. D. I. Bilenko, O. Ya. Belobrovaya, E. A. Jarkova, *et al.*, Sens. Actuators A **79**, 147 (2000).
10. V. M. Demidovich, G. B. Demidovich, S. N. Kozlov, and A. A. Petrov, Pis'ma Zh. Tekh. Fiz. **24** (2), 27 (1998) [Tech. Phys. Lett. **24**, 53 (1998)].
11. M. A. Lampert and P. Mark, *Current Injection in Solids* (Academic, New York, 1970; Mir, Moscow, 1973).
12. S. V. Slobodchikov, Kh. M. Salikhov, E. V. Russu, *et al.*, Fiz. Tekh. Poluprovodn. (St. Petersburg) **29**, 1517 (1995) [Semiconductors **29**, 791 (1995)].
13. K. Mackenzie, P. LeComber, and W. Spear, Philos. Mag. B **46**, 377 (1982).
14. S. Sze, *Physics of Semiconductor Devices* (Wiley, New York, 1981; Mir, Moscow, 1984), Vol. 1.
15. E. I. Adirovich, in *Double-Injection Currents in Semiconductors* (Sov. Radio, Moscow, 1978), p. 200.
16. A. N. Laptev, A. V. Prokaznikov, and N. A. Rud', Pis'ma Zh. Tekh. Fiz. **26** (23), 47 (2000) [Tech. Phys. Lett. **26**, 1049 (2000)].
17. M. S. Shivaraman, J. Appl. Phys. **47**, 3592 (1976).

Translated by V. Bukhanov

Semiconductors, Vol. 36, No. 4, 2002, pp. 472–475. Translated from Fizika i Tekhnika Poluprovodnikov, Vol. 36, No. 4, 2002, pp. 496–499.
Original Russian Text Copyright © 2002 by Gergel', Kul'kova, Mokerov, Timofeev, Khrenov.

PHYSICS OF SEMICONDUCTOR DEVICES

Special Features of Electron Drift in Submicrometer GaAs Structures

V. A. Gergel', E. Yu. Kul'kova, V. G. Mokerov,
M. V. Timofeev, and G. Yu. Khrenov

Institute of Radio Engineering and Electronics, Russian Academy of Sciences,
ul. Mokhovaya 18, Moscow, 101999 Russia

Submitted July 10, 2001; accepted for publication August 28, 2001

Abstract—A quasi-hydrodynamic model of a submicrometer field-effect transistor was used to study the effect of the drift-velocity overshoot on the characteristics of drain-current saturation. It is shown that, in submicrometer transistor structures based on many-valley semiconductors, the current saturation is controlled by levelling off of the electron-drift velocity in the channel, with this levelling off being caused by the effective intervalley scattering. It is also shown that the highest electron-drift velocity in the channel is inversely proportional to the transistor gate length. *© 2002 MAIK “Nauka/Interperiodica”.*

As is well known [1, 2], typical voltages (1–5 V) correspond to fairly high electric fields (E) in submicrometer semiconductor structures; these fields bring about an appreciable heating of the electron subsystem and corresponding suppression of electron mobility μ. However, in actually important situations when the effective heating length $\mu E\tau$ (τ is the energy-relaxation time and μ is the mobility) exceeds the distance between the corresponding n^+-type contacts (L), the electron-subsystem temperature in the sample is found to be lower than the steady-state value $e\mu E^2\tau$ (in energy units); correspondingly, the effective velocity of electron flux exceeds the levelled-off velocity $v_s \approx 10^7$ cm/s, which is referred to as the drift-velocity overshoot [3].

In the previous paper [4], we suggested an illustrative analytical description of this phenomenon by reducing the well-known equation for energy balance in the quasi-hydrodynamic (thermal) model of the electron drift to the following form:

$$-\frac{5}{2}\frac{dT}{dx}j + \frac{ed\varphi}{dx}j - n\frac{T-T_0}{\tau} = 0. \qquad (1)$$

Here, n is the electron concentration, $j = nv$ is the electron-flux density, and $T - T_0$ is the difference between the electron-subsystem temperature T and the steady-state (lattice) temperature T_0. It is clear that, using the assumption that $L \ll \mu E\tau$, we may ignore the thermal-relaxation term in Eq. (1) and obtain a very simple expression ($T = T_0 + (2/5)e\varphi$) for the electron-subsystem temperature equal to T_0 at the n^+ contact to the source where the potential $\varphi(0) = 0$; if this expression is used, the local electron mobility, which is known to be a function of electron-subsystem temperature, becomes a function of the local potential φ.

According to the model we referred to as “ultraquasi-hydrodynamic” in our previous publication [4], the electron-flux velocity becomes local again, i.e.,

$$\mu\left(T_0 + \frac{2}{5}e\varphi\right)\frac{d\varphi}{dx},$$

which greatly facilitates the calculation of the current–voltage characteristics of submicrometer-scale semiconductor-device structures.

Thus, for the field-effect transistors (most important from the practical standpoint), in which case the local surface electron density n_s is defined by the capacitance-related expression $n_s e = C(V - \varphi)$ (C is the specific capacitance, V is the excess of the gate voltage over the threshold voltage, and φ is the local electrostatic potential in the channel), the current can be determined by integrating the expression

$$I = C(V-\varphi)\mu\left(T_0 + \frac{2}{5}e\varphi\right)\frac{d\varphi}{dx} = \text{const} \qquad (2)$$

with respect to the channel length from the source ($\varphi = 0$) to the drain where $\varphi = \min\{V_D, V\}$; here, V_D is the voltage at the transistor drain. In this case, the entire specificity of the temperature dependence can be derived from the form of the dependence $\mu(\varphi)$.

In a previous paper [4], we used the simplest temperature dependence of mobility $\mu(T) \propto T^{-1/2}$, which corresponds to the predominance of scattering by acoustic phonons [5]; therefore, the result obtained in [5] ($I \propto V^{3/2}$) is not exactly realistic. It is clear that, in order to obtain convincing results, we have to introduce a correct dependence $[\mu(T)]$ into formula (2); this dependence should correspond to the electron-transport properties of specific materials in a fairly wide temperature range, which will be exactly performed in application to gallium arsenide.

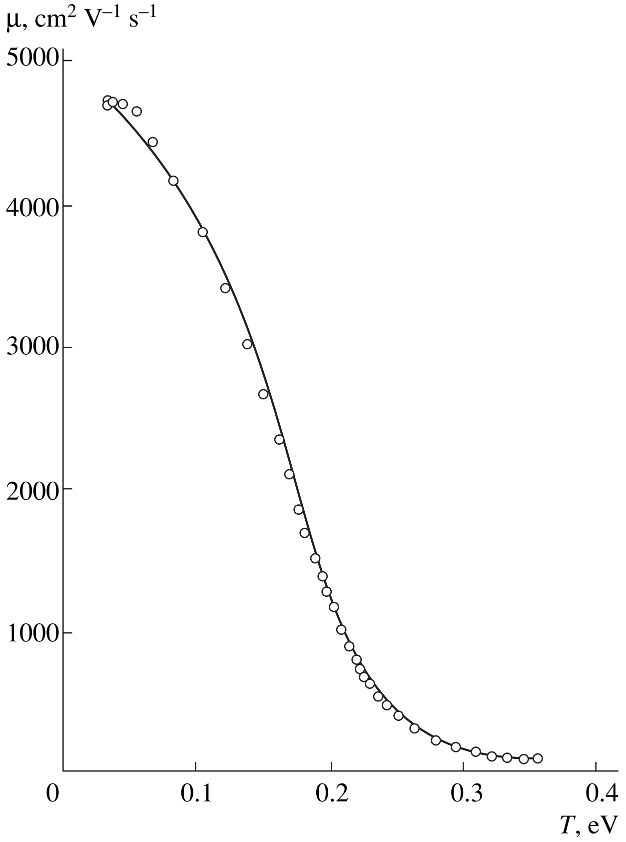

Fig. 1. Electron mobility μ as a function of the effective electron-gas temperature T. The circles correspond to the results of calculations by the Monte-Carlo method, and the solid line represents the results of calculation using formula (3).

As is well known [6], the most consistent and precise method for describing the transport processes in electron–hole plasma in semiconductors consists in the kinetic approach based on solving the Boltzmann equation for a one-particle distribution function for the charge carriers. The use of the Boltzmann kinetic equation makes it possible to take into account both the specificities of a complex, many-valley spectrum of charge carriers in a semiconductor and the fairly wide range of mechanisms for the charge-carrier scattering without using simplifying assumptions about quasi-elasticity of the scattering events. A favorable special feature of the kinetic approach to the description of the electron transport in semiconductors is the high precision and reliability of the obtained results, which makes it possible, in particular, to use these results to verify the lower-level models and also to calculate the phenomenological transport parameters used in these models. As a rule, the Boltzmann equations are solved using the macroparticle method, according to which the carrier-scattering events are described using the Monte Carlo stochastic procedures [6]. The use of the macroparticle method is appreciably simplified if we assume that the electric field and the concentration of the electron–hole plasma are uniform in the semiconductor. In this case, the above method automatically involves the procedure of averaging over the electron path and ensures the calculation of the mean velocity and energy of electrons as the corresponding functions of the electric field.

In this study, the above macroparticle method was applied to GaAs; we simulated the transport process in a constant and spatially uniform electric field taking into account three types of nonequivalent, nonparabolic, and spherically symmetric valleys (Γ, L, and X) in the GaAs electron spectrum and the main mechanisms of electron scattering (by charged impurities and by optical, acoustic, and intervalley phonons) [7]. The dependences of the mean velocity (mobility) and mean energy of electrons on the electric field strength, obtained as a result of simulation, were then recalculated (in order to eliminate the electric field) and converted to the sought-for dependence of mobility on the mean energy W or on the effective electron-gas temperature $T = (2/3)W$. The calculated electron-mobility dependence $\mu(T)$ for $T_0 = 300$ K and the dopant concentration of 10^{17} cm^{-3} is shown in Fig. 1.

The arrangement of points in Fig. 1, with each of the points corresponding to a specific numerical experiment, demonstrates that electron mobility decreases appreciably starting at temperatures of about 0.2 eV, which correspond to the onset of both the occupation of the upper energy valleys with electrons and the predominance of the intervalley-scattering mechanism. By performing a number of similar numerical experiments for several typical charged-impurity concentrations in the range of 10^{15}–10^{18} cm^{-3}, we ascertained that the following analytic expression can be used to adequately describe the above results:

$$\mu(T) = \mu_0(T_0)$$
$$\times\left\{\left(\frac{T}{T_0}\right)^2\left[1+\left(\frac{T}{5T_0}\right)^6+\left(\frac{T}{6T_0}\right)^{16}\right]+12\frac{N_{\mathrm{im}}}{10^{17}}\right\}^{-1/4}. \quad (3)$$

Here, $\mu_0(T_0) \approx 8 \times 10^3$ cm^2 V^{-1} s^{-1} is the low-field electron mobility in undoped GaAs at room temperature and N_{im} is the impurity concentration. The solid line in Fig. 1 represents the results of calculations based on formula (3). We then introduce $T = T_0 + (2/5)e\varphi$ into (3) and substitute this formula for mobility into the integral corresponding to (2). As a result, we obtain

$$I = \frac{C\mu_0}{L}\int_0^{V_D} d\varphi(V-\varphi)$$
$$\times\left\{\left(\frac{T}{T_0}\right)^2\left[1+\left(\frac{T}{5T_0}\right)^8+\left(\frac{T}{6T_0}\right)^{16}\right]+12\frac{N_{\mathrm{im}}}{10^{17}}\right\}^{-1/4}, \quad (4)$$

where $T_0 = 0.026$ eV.

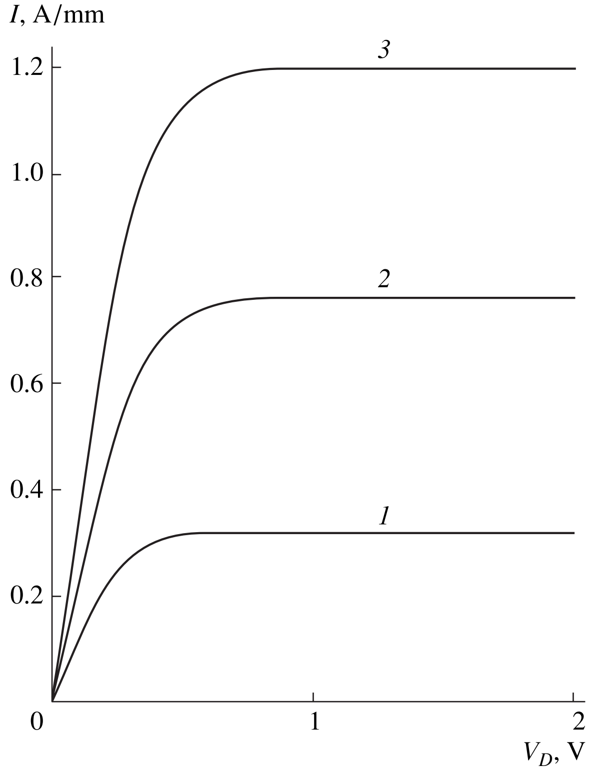

Fig. 2. The drain current *I* as a function of the drain voltage V_D in a field-effect transistor for the voltages V = (*1*) 0.8, (*2*) 1.6, and (*3*) 2.4 V.

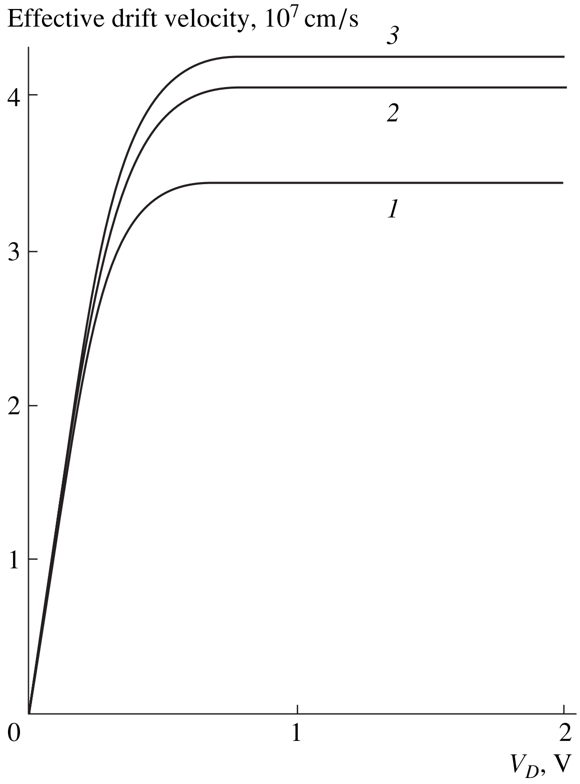

Fig. 3. Effective drift velocity of electrons in the channel of a field-effect transistor as a function of the drain voltage V_D for the voltages V = (*1*) 0.8, (*2*) 1.6, and (*3*) 2.4 V.

An analysis of expression (4) shows that, formally, the abrupt decrease in mobility starting with temperatures of ~200 K and corresponding to the inclusion of the predominant intervalley-scattering mechanism ensures a rapid convergence of the integral for φ in (4), so that its value becomes almost independent of the upper limit. This tendency is illustrated in Fig. 2, where we show the results of numerical integration for the following typical values of the structure parameters: L = 0.3 μm, $C = 10^{-7}$ Φ/cm^2, and $\mu_0 = 8000$ cm^2 V^{-1} s^{-1}.

Figure 2 demonstrates that transistor-current saturation occurs at the drain voltages of ~0.5 V, which are much lower than voltages at the transistor gate. This circumstance unambiguously indicates that the current saturation is precisely caused by the drift-mobility levelling off, rather than by the channel cutoff.

In the situation under consideration, it is reasonable to determine the effective velocity of submicrometer electron drift by dividing the current dependences by the effective charge *CV*. The corresponding dependences are shown in Fig. 3. As might be expected, the effective levelled-off velocity depends only slightly on the gate voltage even at comparatively low voltages.

The dependences represented in Fig. 3 clearly demonstrate the major physical result of this study; this result consists in the fact that, due to a rapid decrease in the electron mobility at electron-gas temperatures corresponding to the prevalence of intervalley scattering, the effective electron velocity ceases to depend on the drain voltage V_D at comparatively small values of V_D related to the onset of occupation of the upper valleys in the energy spectrum. This means that, in the submicrometer structures based on GaAs and related materials, a specific levelling off of the effective drift mobility occurs even under conditions of the overshoot effect; the specificity of the situation under consideration consists in the fact that the levelling off occurs for the voltage (rather than electric-field) dependences. It is noteworthy that, in the case of levelling off under investigation, the inverse proportionality of the drift velocity to the channel length, which is characteristic of the ideal model of a field-effect transistor with a constant charge-carrier mobility, is preserved. We note that, for the channel length of ~0.1 μm (quite reasonable with the modern level of technology), numerical values of the "submicrometer" levelled-off velocity exceed the conventional value $v_s \approx 10^7$ cm/s by an order of magnitude. In addition, it is worth noting that the above result is also of practical importance, because this result justifies further attempts at improving the technology with respect to reduction of the channel length in field-effect transistors.

ACKNOWLEDGMENTS

This study was supported by the Russian Foundation for Basic Research, project no. 01-02-16360.

REFERENCES

1. M. Feng, C. L. Lau, and V. Eu, IEEE Electron Device Lett. **12**, 40 (1991).
2. N. A. Bannov and G. Yu. Khrenov, Tr. Fiz.-Tekhnol. Inst. Akad. Nauk SSSR **1**, 11 (1989).
3. T. Enoki, S. Sugitani, and Y. Yamane, IEEE Trans. Electron Devices **37**, 935 (1990).
4. V. A. Gergel’, V. G. Mokerov, M. V. Timofeev, and Yu. V. Fedorov, Fiz. Tekh. Poluprovodn. (St. Petersburg) **34**, 239 (2000).
5. A. I. Anselm, *Introduction to Semiconductor Theory* (Nauka, Moscow, 1978; Prentice-Hall, Englewood Cliffs, 1981).
6. W. Fawcett, D. A. Boardman, and S. Swain, J. Phys. Chem. Solids **31**, 1963 (1970).
7. V. A. Nikolaeva, V. D. Pishchalko, V. I. Ryzhiĭ, *et al.*, Mikroélektronika **17**, 504 (1988).

Translated by A. Spitsyn

Semiconductors, Vol. 36, No. 4, 2002, pp. 476–479. Translated from Fizika i Tekhnika Poluprovodnikov, Vol. 36, No. 4, 2002, pp. 500–503.
Original Russian Text Copyright © 2002 by Slobodchikov, Salikhov, Russu.

PHYSICS OF SEMICONDUCTOR DEVICES

Long-Term Variation of Electrical and Photoelectric Characteristics of Pd–*p*-InP Diode Structures

S. V. Slobodchikov, Kh. M. Salikhov, and E. V. Russu
Ioffe Physicotechnical Institute, Russian Academy of Sciences, St. Petersburg, 194021 Russia

Submitted August 2, 2001; accepted for publication August 29, 2001

Abstract—Electrical and photoelectric characteristics of Pd–*p*-InP diode structures were studied after their storage in air for many years. An increase in the Schottky barrier height by 0.2–0.3 eV and a rise in photosensitivity were revealed. The current transport mechanism is governed by a generation-recombination current and by tunneling via 0.28 and 0.40 eV levels. An assumption is made that these impurity centers lie in the surface layer of *p*-InP at the heterointerface with Pd. © *2002 MAIK “Nauka/Interperiodica”*.

Our previous studies of Au–*p*-InP diode structures subjected to prolonged exposure to air (for 2–3 years) revealed a fundamental change in their electrical and photoelectric properties [1]. It was found that this change is related to structural changes, i.e., to the formation of Au–*n*-In_2O_3–*p*-InP heterostructures. We analyzed some electrical and photoelectric properties of diode structures based on n(*p*)-InP with a palladium contact in connection with the problem of hydrogen detection in [2, 3]. In this paper, we report the results obtained in studying the mentioned characteristics in a Pd–*p*-InP diode structures kept in air for 10–12 years.

The structures were fabricated using Czochralski-grown *p*-InP crystals with carrier concentration $p_0 = 10^{16}$ cm^{-3}. A palladium layer 400 Å thick was deposited by vacuum evaporation at a residual pressure of 10^{-5} mm Hg. Ohmic contacts to *p*-InP were fabricated by depositing the Ag+Zn alloy. The active surface area of the structure was 6×10^{-2} cm^2. Capacitance–voltage, current–voltage (*I*–*V*), and photoelectric characteristics of the structures were studied, together with the effect of the magnetic field on the photocurrent.

Figure 1 presents the dependence of the capacitance on the reverse bias, $C^{-2} = f(V)$. The Schottky barrier height, estimated from this dependence, is $\varphi \approx 1.1$ eV. This value exceeds, by 0.2–0.3 eV, the barrier heights obtained for freshly prepared samples and for published values [4]. The photosensitivity (photovoltage) increases under the same conditions by a factor of 1.5–2.0. The spectral curves measured at $T = 110$ and 300 K (Fig. 2) steeply decay in the short-wavelength region. These results are, in part, a consequence of the formation of a thin intermediate layer between *p*-InP and Pd. Let us, however, consider in more detail the contribution to photovoltage from two components—the short-circuit photocurrent I_s and resistance R_0 at bias $V \longrightarrow 0$. At not-too-high photocurrents and open-circuit photovoltages, the latter can be represented as

$$V_{\text{ph}} \approx AI_sR_0, \tag{1}$$

where *A* is the active surface area of the diode structure. As shown by experiments, the measured modulated photocurrent falls by six- to eightfold under exposure to unmodulated white light (200-W incandescent lamp). However, the photocurrent under reverse bias decreases by only 30–40%. At the same time, the photovoltage falls by more than two orders of magnitude. Thus, the main change in photovoltage is due to a decrease in differential resistance R_0 (by nearly 1.5 orders of magnitude). Let us consider, in this connection, what carrier characteristics determining the I_s and R_0 values are responsible for their decrease.

Let us, in the first place, reveal the possible mechanism of current transport in the structures studied. Figure 3 presents their *I*–*V* characteristics measured at $T = 100$ and 300 K. The forward currents can be written in the analytical form as

$$I = B\exp\frac{qV}{nkT}, \tag{2}$$

where *B* is a coefficient. At $T = 300$ K, the coefficient $n = 2$ at small biases ($V < 0.3$ V), and, at $T = 110$ K, two

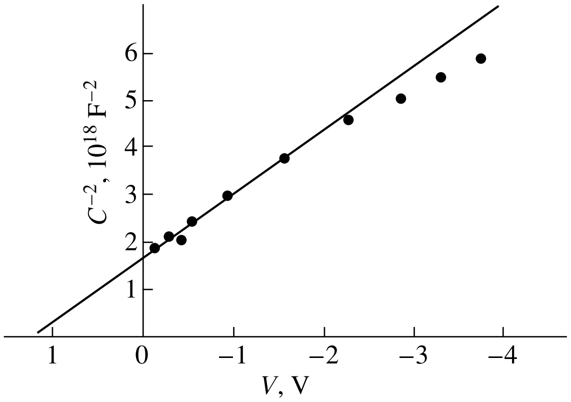

Fig. 1. Capacitance–voltage characteristic of a Pd–*p*-InP diode structure.

slopes can be distinguished, with $n_1 = 30$ and $n_2 = 35$. The reverse current at $T = 300$ K also varies exponentially with voltage ($n = 33$).

Figure 4 presents the temperature dependence of the forward current in the range 110–300 K. The current varies only slightly at 110–230 K and, with T increasing further, can be represented as (Fig. 4, curve *1*)

$$I \propto \exp\left(-\frac{E_a}{kT}\right), \tag{3}$$

with the activation energy $E_a \approx 0.1$ eV.

The presented experimental *I*–*V* characteristics show the predominant contribution to the total current from its two components: generation-recombination ($I_{\text{g–r}}$) and tunnel (I_{tun}) currents, i.e.,

$$I = I_{\text{g–r}} + I_{\text{tun}} + I_{\text{lc}}, \tag{4}$$

where I_{lc} is the leakage current. It should be noted that, although the area A of the diode structures is relatively large, no change in the total current I was observed over the entire range of forward biases upon the structure cleaning operations; i.e., the contribution of I_{lc} is insignificant. Thus,

$$(R_0A)^{-1} = (R_0A)^{-1}_{\text{g–r}} + (R_0A)^{-1}_{\text{tun}}. \tag{5}$$

The generation-recombination current

$$I = \frac{qn_iwA}{2\tau}\exp\left(\frac{qV}{2kT}\right), \tag{6}$$

where n_i is the intrinsic carrier concentration, w is the depletion layer width, and τ is the carrier lifetime in the depletion layer. The corresponding R_0A value can be written as

$$(R_0A)_{\text{g–r}} = \frac{\tau A(V_dN_a)^{1/2}}{n_i(\varepsilon q)^{1/2}}, \tag{7}$$

where V_d is the diffusion potential, ε is the dielectric constant, and q is the elementary charge.

As is known, tunnel currents may be of varied nature. In addition to band-to-band tunneling, various kinds of tunnel transitions are known, which involve impurity levels related to structural defects or chemical impurities. The functional form of tunneling is the same in all cases, and the key factor is the tunneling energy E_{tun}. This energy may be equal to or lower than the energy gap.

As is known, the analytical expression for band-to-band tunneling has the form

$$I_{\text{tun}} = \frac{\sqrt{2}Aq^3(m^*)^{1/2}E_mV}{4\pi^3\hbar^2E_g^{1/2}}\exp\left(-\frac{\pi(m^*)^{1/2}E_g^{3/2}}{2\sqrt{2}q\hbar E_m}\right), \tag{8}$$

where $E_m = \left(\frac{2qN_aV}{\varepsilon}\right)^{1/2}$ is the maximum electric field, and E_g is the energy gap. The general analytical expression, including various kinds of tunneling, can be written as

$$I_{\text{tun}} = C_1V^{3/2}\exp(-C_2/V^{1/2}). \tag{9}$$

Using the proportionality $C_2 \propto (m^*)^{1/2}E_{\text{tun}}^{3/2}$, E_{tun} can be found [5]:

$$E_{\text{tun}} \approx \frac{dE_{\text{tun}}/dT}{dC_2^{3/2}/dT}C_2^{2/3}. \tag{10}$$

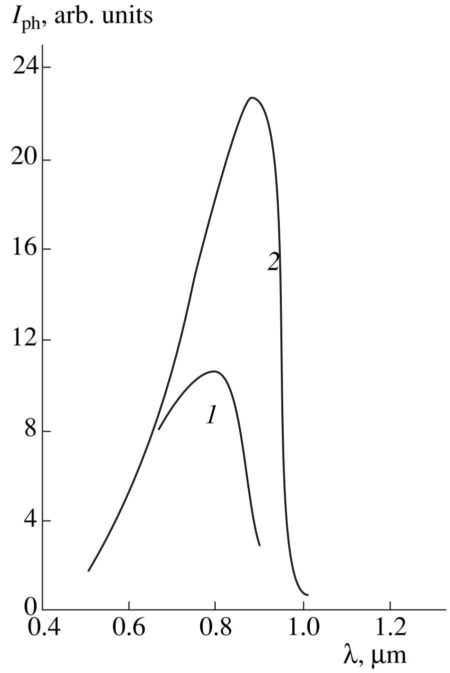

Fig. 2. Photosensitivity spectrum of a Pd–*p*-InP diode structure at temperature *T*: (*1*) 110 and (*2*) 300 K.

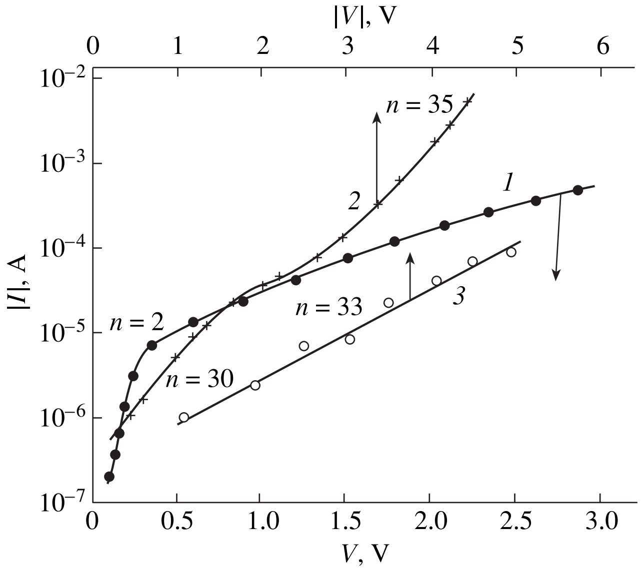

Fig. 3. *I*–*V* characteristics of a Pd–*p*-InP diode structure; forward current: (*1*) $T = 300$ K and (*2*) $T = 110$ K; (*3*) reverse current, $T = 300$ K.

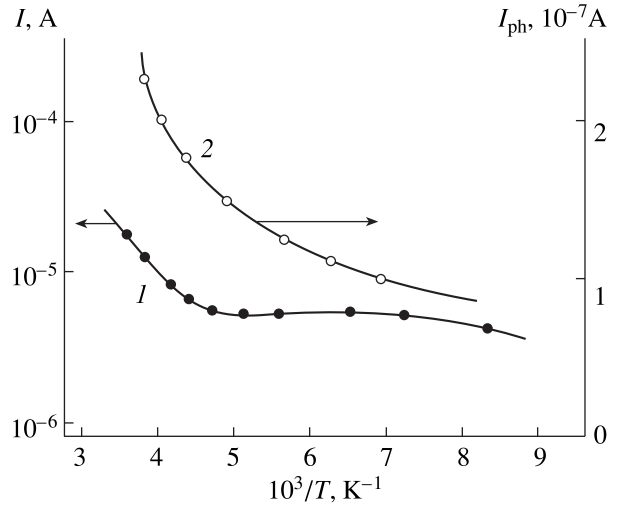

Fig. 4. Temperature dependences of (*1*) forward current and (*2*) photocurrent in a Pd–*p*-InP diode structure.

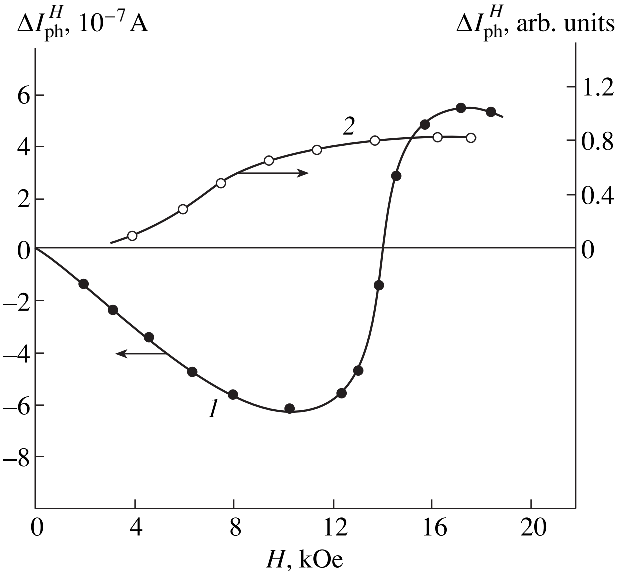

Fig. 5. Variation of photocurrent in a Pd–*p*-InP diode structure with magnetic field H: (*1*) $H \parallel S$ and (*2*) $H \perp S$.

The graphic presentation of the dependence $\ln(I_{tun}/V^{3/2}) = f(V^{-1/2})$ was used to estimate C_2 for two bias ranges for forward current at $T = 110$ K and for reverse current at $T = 300$ K, and E_{tun} was calculated by means of relation (10). Analysis of the spectral dependences of the photovoltage yielded $dE_{tun}/dT \approx 5 \times 10^{-4}$ eV/K. At $T = 110$ K, $E_{tun} \approx 0.28$ eV at low forward voltages and $E_{tun} \approx 0.40$ eV at relatively large biases; at $T = 300$ K, $E_{tun} \approx 0.28$ eV for reverse current. The data obtained suggest that the forward current at small biases is due to tunneling involving the 0.28 eV level (as in the case of the reverse current) and that, at high biases, it is due to tunneling that predominantly involves the 0.40 eV level. The range of intermediate biases is characterized by the joint contribution from both levels.

The analysis performed indicates that, in determining the photovoltage at $T = 300$ K, the second term in (4) should be neglected and the change in V_{ph} be considered exclusively with account of changes in the parameters appearing in (7). Apparently, the principal characteristic, which strongly changes under the influence of external illumination, is the lifetime τ of nonequilibrium carriers. The strong effect of external unmodulated illumination points to the major part played by trapping levels in recombination processes in the depletion layer. On the assumption that the deeper lying level $E_t = 0.40$ eV lies in the lower half of the energy gap and is an effective hole capturing center, we can write [6]

$$\tau_p = \tau_0 \frac{p_0 + n_0}{n_0 + p_0\left[1 + \frac{MN_{vM}}{(N_{vM} + p_0)^2}\right]}, \qquad (11)$$

where τ_p and τ_0 are the lifetimes of majority carriers with and without trapping levels, respectively; M is the concentration of trapping levels; and $N_{vM} = N_v\exp(-E_t/kT)$ is the effective density of states related to the E_t level. In our experiment, τ_p and τ_0 correspond to, respectively, cases with and without external illumination. At $\tau_p/\tau_0 \approx 5 \times 10^{-2}$, $n_i(T = 300\text{ K}) \approx 6 \times 10^6$ cm^{-3}, $N_{vM} \approx 7 \times 10^{10}$ cm^{-3}, the concentration $M \geq 10^{12}$ cm^{-3}, and, for the 0.28 eV level, $M > 10^{14}$ cm^{-3}. The main part of recombination probably goes via deeper levels near the midgap. Thus, the presence of trapping levels makes the lifetime longer and the diffusion length, correspondingly, larger, which raises the efficiency of electron–hole pair separation at the Schottky barrier.

Since the diffusion length $L_n = \sqrt{D_n\tau_n}$, where D_n is the diffusion coefficient, the previously noted change in the short-circuit photocurrent under illumination is in good agreement with the change in τ_n. It becomes understandable now why the photocurrent changes only slightly under reverse bias, since, in this case, the tunneling mechanism of current transport is operative.

The change in photocurrent with temperature is slight (Fig. 4, curve *2*), with the weak rise at low temperature associated with the field- and phonon-and-field-assisted tunneling.

There is reason to believe that impurity-related trapping centers giving rise to levels at 0.28 and 0.40 eV lie in the surface layer of *p*-InP at the interface with the intermediate layer. Additional measurements of the short-circuit photocurrent were carried out in a magnetic field. The measurements were done with frontal illumination of the diode structure (from the Pd side), with the magnetic field parallel to the structure plane (S) ($H \parallel S$) and perpendicular to it ($H \perp S$). The photocurrent variation with magnetic field strength is shown in Fig. 5. A characteristic dependence $\Delta I_{\text{ph}} = f(H)$ is observed at $H \parallel S$ (curve *1*): with increasing magnetic field, the photocurrent first decreases at small H and then grows steeply at around $H \sim 13$ kOe, with subsequent leveling-off.

The photomagnetic current under frontal illumination of a *p*–*n* junction was calculated in [7, 8]; however, only the diffusion mechanism of transport was taken into account. Apparently, a Schottky diode, especially one with generation-recombination current transport, must have its own specific features. Qualitatively, the change in photocurrent in a magnetic field can be understood for our structures by taking the possible changes in the diffusion coefficients $D_{n,\,p}$ and lifetimes $\tau_{n,\,p}$ into account. With $H \parallel S$ and relatively weak magnetic fields, the decrease in photocurrent is associated with a decrease in the diffusion length, since

$$D_{n,\,p} = D_0\left[1 + \left(\frac{\mu_{n,\,p}H}{c}\right)^2\right]^{-1},$$

where μ_n and μ_p are the electron and hole mobilities, and the rate of recombination is high at the heterointerface with the intermediate layer. With H increasing further, the rise in the lifetimes $\tau_{n,\,p}$ starting with $H \approx 13$ kOe will be dominant for a certain part of the flow of nonequilibrium carriers, owing to their magnetodiffusion displacement parallel to the heterostructure plane. This leads to a change of the ΔI_{ph} sign. At $H \perp S$, only the lifetime rise factor is operative and magnetodiffusion displacement parallel to the structure plane occurs, since the magnetic field acts upon the momentum vector components of nonequilibrium electrons being scattered.

It is noteworthy, further, that the steep drop in the spectral curve of photosensitivity in the short-wavelength region also indicates that the rate of surface recombination at the heterointerface is high.

The experiments revealed that, at $T = 110$ K, the relaxation phenomena become more pronounced in forward current measurements. At the same time, reverse currents cannot be measured precisely at all, owing to their instability. These data can be attributed to the nonuniformity of the thickness and composition of the intermediate layer and, correspondingly, the physicomechanical properties of its constituents. The problem of the nature and composition of the intermediate layer in the diode structure invites further physicochemical studies.

REFERENCES

1. M. M. Meredov, G. G. Kovalevskaya, E. V. Russu, and S. V. Slobodchikov, Fiz. Tekh. Poluprovodn. (St. Petersburg) **26** (9), 1590 (1992) [Sov. Phys. Semicond. **26**, 893 (1992)].
2. G. G. Kovalevskaya, L. Kratena, M. M. Meredov, *et al.*, Pis'ma Zh. Tekh. Fiz. **15** (12), 55 (1989) [Sov. Tech. Phys. Lett. **15**, 478 (1989)].
3. G. G. Kovalevskaya, M. M. Meredov, E. V. Russu, *et al.*, Fiz. Tekh. Poluprovodn. (St. Petersburg) **26** (10), 1750 (1992) [Sov. Phys. Semicond. **26**, 978 (1992)].
4. E. Hökelek and G. J. Robinson, Appl. Phys. Lett. **40**, 426 (1982).
5. N. Tabatabaie and G. E. Stillman, Appl. Phys. Lett. **40** (5), 415 (1982).
6. S. M. Ryvkin, *Photoelectric Effects in Semiconductors* (Fizmatgiz, Moscow, 1963; Consultants Bureau, New York, 1964), Chap. 6.
7. Z. S. Gribnikov, Radiotekh. Élektron. (Moscow) **10** (6), 1110 (1965).
8. I. P. Zhad'ko and V. V. Romanov, Fiz. Tekh. Poluprovodn. (Leningrad) **12** (9), 1789 (1978) [Sov. Phys. Semicond. **12**, 1059 (1978)].

Translated by M. Tagirdzhanov